MEMS Harsh Environment Sensors for Earth and Space Exploration

by

Jonathon Oiler

A Dissertation Presented in Partial Fulfillment
of the Requirements for the Degree
Doctor of Philosophy

Approved March 2013 by the
Graduate Supervisory Committee:

Hongyu Yu, Chair
Ariel Anbar
Evan Scannapieco
Hilairy Hartnett
Francis Timmes

ARIZONA STATE UNIVERSITY

May 2013

ABSTRACT

Harsh environments have conditions that make collecting scientific data difficult with existing commercial-off-the-shelf technology. Micro Electro Mechanical Systems (MEMS) technology is ideally suited for harsh environment characterization and operation due to the wide range of materials available and an incredible array of different sensing techniques while providing small device size, low power consumption, and robustness.

There were two main objectives of the research conducted. The first objective was to design, fabricate, and test novel sensors that measure the amount of exposure to ionizing radiation for a wide range of applications including characterization of harsh environments. Two types of MEMS ionizing radiation dosimeters were developed. The first sensor was a passive radiation-sensitive capacitor-antenna design. The antenna's emitted frequency of peak-intensity changed as exposure time to radiation increased. The second sensor was a film bulk acoustic-wave resonator, whose resonant frequency decreased with increasing ionizing radiation exposure time.

The second objective was to develop MEMS sensor systems that could be deployed to gather scientific data and to use that data to address the following research question: do temperature and/or conductivity predict the appearance of photosynthetic organisms in hot springs. To this end, temperature and electrical conductivity sensor arrays were designed and fabricated based on mature MEMS technology. Electronic circuits and the software interface to the electronics were developed for field data collection. The sensor arrays utilized in the hot springs yielded results that support the hypothesis that temperature plays a key role in determining where the photosynthetic

organisms occur. Additionally, a cold-film fluidic flow sensor was developed, which is suitable for near-boiling temperature measurement. Future research should focus on (1) developing a MEMS pH sensor array with integrated temperature, conductivity, and flow sensors to provide multi-dimensional data for scientific study and (2) finding solutions to biofouling and self-calibration, which affects sensor performance over long-term deployment.

DEDICATION

To Marybeth – Thank you for everything.
To Baxter, Madison, and Rocco – Woof.

ACKNOWLEDGMENTS

I would like to express my deepest gratitude to my advisor, Hongyu Yu, for providing the opportunity to focus on my research interests related to the sensor development for the hot springs and helping to find interested undergraduate students to advance those projects faster than I could work on my own. I would also like to thank him for his support and guidance throughout my years in graduate school. I would like to thank members of the MEMS research group – Hai, Rui, Teng, Ruirui, and Mengbing for their friendship and help with various projects. I would like to thank the CSSER cleanroom staff – Todd, Jon, Carrie, and Paul for their help with training on and using the equipment and teaching the ways of cleanroom processing and safety.

I would like to thank Hilairy Hartnett for her input on my research projects and dissertation. I would like to thank Everett Shock for supporting my research interests and providing guidance and the opportunity to work with his team and collect data at Yellowstone National Park and the Nevada site.

I would like to thank Hugh Barnaby for advising me on the radiation projects and Keith Holbert for allowing the radiation testing in his lab.

I would like to thank my parents, Dave and Jean - for their continuous love and support throughout the years.

Finally, and most importantly, I would like to thank my wonderful wife, Marybeth, without whom I would never have even considered following my dreams and going to graduate school. Thank you for riding at my side on this roller coaster adventure.

TABLE OF CONTENTS

Page

LIST OF FIGURES viii

CHAPTER

1 INTRODUCTION 1

1.1 Photolithography 6

1.2 Deposition 9

1.3 Etching 12

1.4 Lift-off 16

1.5 MEMS Fabrication 17

2 MEMS IONIZING RADIATION SENSORS 23

2.1 MOSCAP-Antenna Passive Ionizing Radiation Sensor 30

2.2 FBAR Ionizing Radiation Sensors 40

2.3 Conclusion 57

3 MEMS TEMPERATURE SENSOR ARRAYS 59

3.1 Resistance Temperature Detectors 65

3.2 Silicon Substrate RTD Arrays 69

3.3 Printed Circuit Board-based RTD Arrays 75

3.4 Comsol Multiphysics Modeling 77

3.5 Fused Quartz Substrate RTD Arrays 80

3.6 Electronic Read-Out 83

3.7 Hot Spring Measurement Locations 88

3.8 Hot Spring Data from China 90

CHAPTER Page

3.9 Hot Spring Data from Yellowstone National Park 93

3.10 Long-term Temperature Monitoring Station 110

3.11 Conclusion 120

4 MEMS ELECTRICAL CONDUCTIVITY SENSOR ARRAYS 123

4.1 Electrical Conductivity Sensors 126

4.2 Electrical Conductivity Arrays 135

4.3 Electronic Read-Out 145

4.4 Hot Spring Data from Gerlach, NV 151

4.5 Hot Spring Data from Yellowstone National Park 153

4.6 Current and Future Work 160

4.7 Conclusion 160

5 MEASUREMENTS AT GEYSER CREEK BASIN 163

5.1 Data from Geyser Creek Hot Springs 163

5.2 Conclusion 194

6 THERMOELECTRIC COOL-FILM FLOW SENSOR 196

6.1 Cool-film Flow Sensor Experiment Setup 208

6.2 Cool-film Flow Sensor Experiment Results 215

6.3 Conclusion 218

7 CONCLUSION 220

7.1 pH Sensor Development 222

7.2 Biofouling 226

CHAPTER Page

7.3 Conclusion 229

References 230

LIST OF FIGURES

Figure Page

1.1 Image of a 100 mm diameter polished silicon wafer (photo courtesy of npl.co.uk). 5

1.2 (left) Topside schematic of a photomask with ‘plus’ shape. The black represents areas of the UV-opaque film. Below the photomask pattern is transferred onto the wafer surface where red is the positive photoresist and gray is the silicon wafer. (right) Schematic cross-section of the photomask and wafer showing where the UV light is transmitted and absorbed by the positive photoresist. Areas of positive photoresist that do not absorb UV remain on the surface after development. 7

1.3 (left) Topside schematic of a photomask with ‘plus’ shape. The black represents areas of the UV-opaque film. Below the photomask pattern is transferred to the wafer surface where red is the negative photoresist and gray is the silicon wafer. (right) Schematic cross-section of the photomask and wafer showing where the UV light is transmitted and absorbed by the negative photoresist. Areas of negative photoresist that do not absorb UV are removed during development. 8

Figure Page

1.4 Figure 1.4: Schematic cross section of an isotropically etched silicon wafer (gray) with photoresist mask (red) pattern on top. A common silicon wet isotropic etch recipe uses water and hydrofluoric, nitric, and acetic acids. 14

1.5 Schematic cross section of an anisotropically etched silicon wafer. A potassium hydroxide and water solution will anisotropically etch silicon at a high rate. The high selectivity between the <100> and <111> plane creates a 54.7 °. 14

1.6 A schematic cross-sectional depiction of the liftoff process. (top) A thin film (blue) is directionally-deposited onto the wafer covering the positive photoresist (red) and exposed silicon wafer surface (gray). (bottom) Same process as the top, however, the negative photoresist shape makes liftoff easier as less of the thin film is deposited on the sidewalls. 17

1.7 Scanning electron micrograph of a MEMS micro-motor (Yasseen et al. 2000). 18

1.8 Scanning electron micrograph of a cantilevered beam (Koev 2006). 19

1.9 Scanning electron micrograph of comb drive accelerometer (Abdolvand et al. 2007). 20

Figure Page

1.10 A fully integrated time-of-flight mass spectrometer. (left) A scanning electron micrograph showing the mass filter. (right) The packaged mass spectrometer shown next to a penny for scale (Wapelhorst et al. 2007). 21

2.1 Schematic cross-section drawing showing a p-channel MOSFET before (top) and after (bottom) ionizing radiation. The radiation-induced trapped charge in the oxide changes the device electrical characteristics. The gray n+ and blue p+ regions are doped into the silicon. The white area is silicon dioxide. The bright blue regions are metals. 29

2.2 Schematic cross-section drawing of a MOS capacitor. Most commonly, a layer of silicon dioxide thermally grown on a layer of silicon is sandwiched between two aluminum electrodes. 32

2.3 Capacitance-Voltage curve for a p-doped MOSCAP. 34

2.4 A schematic of the fabrication of the MOSCAP in cross-section. (a) Photoresist is patterned over silicon nitride (SiN) at the bottom of the SOI wafer. (b) The SiN is etched and the SiN is used as a mask for the anisotropic etching of the handler layer Si. (c) Photoresist is patterned and the SiN is etched over a region of device layer Si. (d) Aluminum is deposited on both sides of the wafer. (e) Finally, the aluminum is wet etched on the top of the wafer to form the top electrode and bond pad. 36

Figure Page

2.5 Radiation testing equipment in Professor Holbert's laboratory. Devices are exposed to 1.2 MeV photons from a ^{60}Co source in the belly of the lead-shielded machine. 38

2.6 Capacitance-Voltage curve for the fabricated p-doped MOSCAP devices at different total ionizing doses. 39

2.7 Plot of reflected intensity from inside an anechoic chamber with a capacitor-loaded antenna device in the chamber. The peak at > 9 GHz is a response from the antenna. 40

2.8 Schematic drawing of a typical FBAR device in cross-section. 42

2.9 A schematic of the fabrication of the MOSCAP in cross-section. (a) LPCVD SiN is deposited over the entire Si wafer. (b) Photoresist is patterned over an area of silicon nitride (SiN) at the bottom of the SOI wafer and the SiN is etched (c) The SiN is used as a mask for the anisotropic etching of the Si. (d) Gold is deposited on the backside of the wafer and ZnO on the top side. (e) Photoresist is patterned overtop the ZnO and the ZnO is wet etched. (f) Photoresist is patterned overtop the SiN diaphragm and a via is etched through the SiN. (g) Photoresist is patterned for liftoff and gold is deposited and lift off performed for the final device structure. 43

2.10 Magnified photograph of the top side of the FBAR device deposited over a square diaphragm (seen as the lighter orange color). 44

Figure Page

2.11 Probe station with attached temperature-controlled hot chuck system for performing frequency-scattering parameter measurements with a network analyzer. 46

2.12 Schematic circuit layout for the modified Butterworth-Van Dyke model used to model the FBAR device. 47

2.13 Plot showing FBAR cumulative frequency shift with increasing ionizing dose. Error bars represent uncertainty based on resolution of frequency measurement. 48

2.14 A schematic of the fabrication of the MOSCAP in cross-section. (a) LPCVD SiN is deposited over the entire Si wafer. (b) Photoresist is patterned over an area of silicon nitride (SiN) at the bottom of the SOI wafer and the SiN is etched (c) The SiN is used as a mask for the anisotropic etching of the Si. (d) Gold is deposited on the top side of the wafer, followed by photoresist patterning and etching of the Au. (e) ZnO is deposited on the top side of the wafer and photoresist is patterned overtop the ZnO and the ZnO is etched. (f) PECVD SiN is deposited on the top side of the wafer, followed by photoresist patterning and etching of the PECVD SiN. (g) Photoresist is patterned for liftoff and gold is deposited and lift off performed for the final device structure in (h). 50

Figure Page

2.15 Magnified image of the top side of the FBAR device deposited over a square diaphragm. The diaphragm is wrinkled due to stress in the LPCVD SiN. 52

2.16 Schematic drawing of the FBAR mason model for the 2nd generation device structure. 54

2.17 Matlab plot of the impedance magnitude of the 2nd generation FBAR for different parallel plate capacitances (C_0) around the series (minimum) and parallel (maximum) resonant frequencies. 55

2.18 Matlab plot of the impedance magnitude of the 2nd generation FBAR for different stiffness (Young's modulus) around the series (minimum) and parallel (maximum) resonant frequencies. 56

2.19 Plot showing the decrease in the series resonant frequency for increasing DC voltage offset. 57

3.1 Photograph of hot spring source pool and outflow channel at Yellowstone National Park. 59

3.2 *(left)* Photograph of water from a boiling spring (upper right, dark blue) flowing toward the viewer. Total width of outflow channel is ~1.5m. Note the sharp transition in the appearance of photosynthesis where color changes from off-white to bright green. (*right)* Photograph of different zones of photosynthetic microbes. Different communities can be distinguished by the sharp change in colors from orange to yellow to green. 62

Figure Page

3.3 Plot from Cox et al. (2011) showing the dashed curve where the transition to photosynthesis occurs as a function of pH and temperature. Filled circles indicate locations where photosynthetic pigments were visible. Open circles indicate locations where no photosynthetic pigments were visible. 64

3.4 A schematic of the fabrication of the silicon substrate temperature array in cross-section. A layer of Ti/Pt is deposited and patterned on the Si wafer to create the resistor in (a) and (b). Next a layer of Cr/Cu is deposited and patterned to create the bond pads and leads connecting pads to the resistors in (c) and (d). Finally, Parylene-C is deposited over the entire wafer in (e). 71

3.5 The top photograph shows a silicon substrate temperature array. Copper leads connect the RTDs to the bond pads at the bottom of the sensor (left). After soldering wires to the bond pads, the area is covered in an epoxy for stronger adhesion. The bottom photograph shows a magnified view of one of the 15 fabricated RTDs. 73

3.6 Silicon substrate temperature array calibration curve showing five platinum-based RTDs. Arrays were calibrated in water between the ranges of temperature expected in the hot springs. 75

3.7 Diagram of commercial platinum RTD used in temperature array. Image courtesy of Omega Engineering, Inc. The RTD is 2mm on a side. 76

Figure Page

3.8 Printed circuit board temperature array calibration showing 15 commercially purchased (Omega Engineering, Inc.) platinum-based RTDs. Arrays were calibrated in water between the ranges of temperature expected in the hot springs. 77

3.9 Schematic of silicon substrate RTD array simulated with Comsol Multiphysics® heat transfer package (not to scale). 78

3.10 Comsol® Multiphysics model results for the silicon substrate RTD array. Blue lines show the temperature at the center of the platinum metal resistors under heating from reservoirs of water at 45 °C (318 K), 55 °C (328 K), 65 °C (338 K), and 75 °C (348 K) which are represented by the red dots. The unit of time on the x-axis is seconds. The arrows show which resistor is associated with its corresponding reservoir. 79

3.11 Comsol® model results for the fused quartz substrate RTD array. Blue lines show the temperature at the center of the platinum metal resistors under heating from reservoirs of water at 45 °C (318 K), 55 °C (328 K), 65 °C (338 K), and 75 °C (348 K) which are represented by the red dots. The unit of time on the x-axis is seconds. 80

Figure Page

3.12 A schematic of the fabrication of the fused quartz substrate temperature array in cross-section. A layer of Ti/Ni is deposited and patterned on the Si wafer to create the resistor in (a) and (b). Next a layer of Cr/Cu is deposited and patterned to create the bond pads and leads connecting pads to the resistors in (c) and (d). Finally, Parylene-C is deposited over the entire wafer in (e). 81

3.13 Photograph of the fused quartz substrate temperature array with nickel RTDs. The length of the array is 9.5 cm. 82

3.14 Resistance measurements from a platinum and nickel RTD over a wide range of temperature. The nickel RTD has a higher TCR of ~1600 ppm/°C compared to just 500 ppm/°C for the platinum RTD. 82

3.15 Circuit schematic to measure the resistance of one of the RTDs on an array. 84

3.16 Printed circuit board for the high precision, low-TCR constant resistors required to determine the current in the measurement circuit. The keyboard in the background is provided for scale. 86

3.17 Photograph of the multifunction data acquisition device (USB-6289) from National Instruments. 87

3.18 Screenshot from the LabVIEW software showing a portion of the temperature array measurement program. 88

3.19 The hydrothermal systems are located in southwest China near the city of Tengchong in the Yunnan Province (red dot). 89

Figure Page

3.20 Map of Yellowstone National Park showing the location field sites referenced in this chapter. 90

3.21 Photograph of the temperature array being placed vertically into the hot spring to a depth of about 4 cm at nine different locations. 91

3.22 Plot of temperature at various depths along different spatial locations at the 'Geothermal Explosion Site' hot spring in Tengchong, China. Error bars on all temperature plots represent the uncertainty of ±1 °C due to sensor system noise and calibration error. 92

3.23 Photograph of a hot spring outflow channel where a yellowish photosynthetic community can be seen at the left hand side of the channel and a green community seen at the right. A plot of the temperature distribution across the channel is also provided. Dashed lines in the image and plot mark the approximate locations where the visually distinct photosynthetic communities appear. Error bars on all temperature plots represent the uncertainty of ±1 °C due to sensor system noise and calibration error. The length of the array is 18.5 cm for scale. 94

3.24 Photograph of a bubbling spring source surrounded by yellow sulfur streamers which are, in turn, surrounded by a purple photosynthetic mat community. A plot of the temperature distribution across one region of the photosynthetic transition zone (feature) is provided. The yellow star on the array signifies the zero position in the plot. The dashed line in the image and plot mark the approximate location where the visually purple mat appears. The length of the array is 18.5 cm for scale. 95

3.25 Photograph of a hot spring source pool (at the left) and the transition to different photosynthetic communities with distance from the source pool. Black dashed lines approximate where the transitions to different microbial communities occur, red dots indicate the locations of temperature sensors. The yellow star marks the zero position for the next figure plot. The length of the array is 18.5 cm for scale. 96

3.26 Plot of temperature as a function of distance away a source pool (at the left). The dashed lines mark the apparent boundaries of the different colored microbial communities. 97

3.27 Photograph of an area where two different hot spring outflow channels merge and a sharp photosynthetic boundary occurs. Arrows show the direction of flow from the different outflow channels. The length of the plastic box is 30 cm for scale. 98

Figure Page

3.28 Photograph of a hot spring stream where two channels from different sources merged and a photosynthetic boundary appears sharply at about the center of the stream. 99

3.29 Plot of temperature across the stream below the confluence of two outflow channels. The clear side of the stream (no photosynthesis) is hotter than the green side (photosynthesis) of the stream. The dashed line marks the approximate transition to photosynthesis at this location. 100

3.30 Photograph of two outflow channel merging (yellow arrows). In the upper channel the green photosynthetic community is clearly apparent. In the lower stream there is no visible community and where they merge a sharp boundary occurs. The length of the plastic box is 30 cm for scale. 101

3.31 Photograph of the stream conversion zone where the photosynthetic mat sharply ends. The yellow star marks the zero position in the temperature plot. The black dashed line represents the approximate location where the transition to photosynthesis occurs. The length of the array is 18.5 cm for scale. 102

3.32 Photograph of a temperature array connected to a fishing pole in order to measure temperature at depth in a hot spring source pool. 103

3.33 Average temperature measurements averaged between depths from the bottom of the pool (at this particular location) to the surface. 104

Figure Page

3.34 Photograph of a geyser hot spring in Imperial Geyser Basin where the water level oscillates. The water periodically recedes below the edge of the source pool and becomes heated and then rises to a point at which the water overflows and runs down into the outflow channel (shown by black arrow). 105

3.35 Close-up photograph of the temperature array in the outflow channel of a geyser in Imperial Geyser Basin. The length of the array is 18.5 cm for scale. 106

3.36 Time-series photographs showing the flow of water down the outflow channel. The numbers at the bottom left of each picture show the order of the picture series. Water begins flowing over the sensor at picture 8 approximately 10 minutes after the data started recording. The length of the array is 18.5 cm for scale. 107

3.37 Plot of temperature over time for selected sensors in the temperature array. The black line designates when water begins flowing over the array. 108

3.38 Google satellite image of Great Boiling Spring hydrothermal system. Data are being collected from the GBS pool and from the Great Boiling Springs hot spring (GBS16) pool (Costa et al. 2009) along the edge near the bathing pool (yellow oval). 112

Figure Page

3.39 Photographs of Great Boiling Spring hot spring (GBS), Gerlach, NV, from two different directions where the first long-term monitoring station was set up. The red dots represent the locations where 16 individual RTDs were placed in the hot spring. The numbers correspond to the sensor numbers provided in the following plot. Arrows pointing north are provided for orientation. The GBS pool is ~6.5 m in diameter. 113

3.40 A plot of temperature as a function of time for the 16 RTDs over a 3 month period between March, 2012 and June, 2012 for the GBS pool. 115

3.41 (left) Photograph of the Great Boiling Spring pool after sensor installation. (right) Photograph of Great Boiling Spring pool on 4/18/12 showing receded water level. The GBS pool is ~6.5 m in diameter. 116

3.42 Photograph and location of the 14 RTDs located around GBS16 pool. The inset shows the location of the sensors relative to the GBS source pool. The yellow oval is the same oval from Figure 3.38 showing the satellite image. Arrow pointing north is provided for orientation. The GBS16 pool is ~25 m in diameter. 117

3.43 Temperature data for 11 RTDs located in GBS16 (adjacent to GBS) over the previous 10 months. 119

Figure Page

4.1 Illustration depicting the underlying processes responsible for the biogeochemical conditions found in the hot springs. (Credit: Ed Garnero and Everett Shock). 124

4.2 Schematic of the electrical conductivity measurement. Current is passed between the two black square electrodes. The ions in the solution act as a resistor, and the resistance value is proportional to the number of ions between the electrodes. 127

4.3 Schematic drawing of a two-point conductivity sensor. The electrodes are located at the top of the image and the square bond pads at the bottom with leads to connecting the bond pads to the electrodes. Measurement of both the current that is passed and the voltage drop is performed at the same electrodes and leads. The small shapes to the left of the electrodes are alignment marks for fabrication. Distance between the outer is ~1 cm. 128

4.4 Schematic drawing of a four-point conductivity sensor. The electrodes are located at the top of the image and the square bond pads at the bottom with leads to connecting the bond pads to the electrodes. Current is passed between the outer electrodes and the voltage drop across the solution is measured at the inner electrodes. The small shapes to the left of the electrodes are alignment marks for fabrication. Distance between the outer electrodes is ~1 cm..... 130

Figure Page

4.5 Schematic of charged electrodes in solution of mobile ions. Negative ions are attracted to positively charged electrodes and vice versa. The charge layer sets up the double layer capacitance. 133

4.6 Electrical model of the electrode polarization impedance shows the Faraday impedance (Z_F) in parallel with the double layer capacitor (C_{DL}). 134

4.7 Electrical model of the four-point probe. The resistances of the liquid solution between the outer force electrodes and the inner sense electrodes are given as R_1 and R_2. The resistance between the inner sense electrodes is given as R_{SOL} and is the desired measurement of the solution resistance. The electrode polarization impedances are labeled as E1-E4. The voltage (*V*) is measured between the inner sense electrodes and the current (*A*) is passed between the outer force electrodes. 135

4.8 Schematic of the four-point probe electrode geometry and variables determined for a cell constant of 6 cm^{-1}. 138

4.9 A schematic of the fabrication process flow for the conductivity array in cross-section. A layer of Ti/Pt is deposited and patterned on the wafer to create both the electrodes and the RTD in (a) and (b). Next a layer of Parylene-C is deposited over the entire wafer and selectively etched over the conductivity electrodes and bond pads (c) and (d). A platinum resistance temperature detector fabricated between the sense electrodes remains covered by the Parylene-C. 140

4.10 Photograph of a completed conductivity sensor array fabricated on fused quartz. 142

4.11 Photograph of the corroded electrode following operation for a few hours in a hot spring. One of the outer force electrodes is at the right of the image with the sense electrode located to its left. The non-corroded metal should appear black in this image as is seen at the bottom of the electrodes and in the meandering RTD to the left of the sense electrode which is covered by the transparent polymer Parylene-C. Epoxy covers a portion of the RTD in this image. The width of the outer right electrode is 215 μm. 143

4.12 Calibration curve for the nickel-based electrode conductivity arrays used in Gerlach, NV. 143

4.13 Calibration curve for the platinum-based electrode conductivity arrays used at Yellowstone National Park. 145

Figure Page

4.14 Circuit layout schematic for the conductivity measurement. The green shape represents the four-point probe. The sinusoidal excitation voltage V_{EX} is input to the outer force electrodes. The voltage drop (V_S) across the solution is measured at the inner sense electrodes. The current through the solution is determined by taking V_{REF} and dividing by the resistance R_{REF}. V_{CC+} and V_{CC-} are the voltage supplies to power the operational amplifier (triangle). 146

4.15 Photograph of printed circuit board built for making conductivity measurements. Around the outside of the board are screw terminal for the input wires from the conductivity array. The keyboard in the background is provided for scale. 150

4.16 Conductivity measured by each sensor in the conductivity array at different locations downstream of the main source of Rick's Hot Creek. Locations are not equidistant. Error bars on all conductivity plots represent the uncertainty of 10% due to sensor system noise and calibration error. 152

4.17 Photograph of two hot spring outflow channels (yellow and green) merging. The length of the plastic box is 30 cm for scale. 154

Figure Page

4.18 Photograph of boundary where two hot springs merge where green photosynthetic bacteria are juxtaposed with a region containing a yellow sulfur precipitate. Temperature (red circles) and conductivity (blue triangles) measurements were taken across the boundary. Yellow stars mark the zero positions for the next two figure plots. The long dimension of the conductivity array is ~6 cm for scale. 155

4.19 Plot of temperature across the photosynthetic transition zone. The sulfur region is at the left of the plot and the appearance of green bacteria occurs approximately where the dashed line appears and continues to the right of the line. The zero position corresponds to the yellow star in Figure 4.18. Error bars on all temperature plots represent the uncertainty of ±1 °C due to sensor system noise and calibration error. 156

4.20 Plot of conductivity across the photosynthetic transition zone. The sulfur region is at the left of the plot and the appearance of bacteria occurs approximately where the dashed line appears and continues to the right of the line. The zero position corresponds to the yellow star in Figure 4.18. 157

4.21 Photograph of a hot spring source pool in Norris Geyser Basin. The orange color around the pool is oxidized iron. The width of the source pool is ~1.5 m for scale. 158

Figure Page

4.22 Measurements of temperature and conductivity in each of four small source pools at Norris Geyser Basin. The length of the array is 18.5 cm for scale. 159

5.1 Photograph of a hot spring in Geyser Creek Basin. 163

5.2 Photograph of the microbial mat community found in the alkaline outflow channel. The temperature array is 2.4 cm by 18.5 cm. 164

5.3 Photo-mosaic (courtesy of Andrew Dombard) of the acidic stream (bottom) and alkaline stream (top). A zoomed-in image of the region within the yellow oval is provided in Figure 5.4. A 1.2 m thin brown stick located between the two streams is provided for scale. Black arrows show the direction of the fluid flow in the two streams. 166

5.4 Close-up photograph of the 'microbial striping zone' where the water from each of the two channels mixed. Black arrows show the approximate direction of flow for each stream before mixing. The sensor array at the right is 2.4 cm by 18.5 cm. The dashed lines indicate where the colored zones change. 168

5.5 Photograph of an 18.5 cm long temperature array placed across the microbial striping zone with dashed lines outlining four distinct color regions. The yellow star marks the zero position in the temperature plot. 169

Figure Page

5.6 Plot of temperature across the microbial striping zone. Dashed lines approximate the locations where the transitions occur. Left on the plot is closer to the acidic stream. Error bars on all temperature plots represent the uncertainty of ±1 °C due to sensor system noise and calibration error. 170

5.7 ArcMap™ image showing the photo-mosaic of the two streams and the temperature and conductivity measurement points over top. Red circles represent temperature measurements, blue triangles represent conductivity measurements. A 1.2 m thin brown stick located between the two streams is provided for scale. 172

5.8 Close-up image showing the location of the temperature and conductivity measurements around the mixing zone. Red circles represent temperature measurements, blue triangles represent conductivity measurements. 173

5.9 Temperature color map of the acidic and alkaline outflow channels created in ArcMap™. Temperatures range from 31 °C to 60 °C with blue representing cooler temperatures than red colors. The acidic stream is at the bottom of the image and the alkaline stream is at the top. A 1.2 m thin brown stick located between the two streams is provided for scale. 174

5.10 (top) Close-up image of the mixing zone where the two streams merge. Red circles represent temperature measurements. The acidic stream is flowing in the direction of the bottom left yellow arrow and the alkaline stream is flowing in the direction of the top left yellow arrow. (bottom) Close-up of the temperature color map overlaid on the image. 176

5.11 Conductivity color map of the acidic outflow channel (bottom of image) and alkaline outflow channel (top of image) created in ArcMap™ with blue colors that are lower conductivity than red colors. Conductivities range from 830 μS/cm to 4300 μS/cm. The acidic stream is at the bottom of the image and the alkaline stream is at the top. A 1.2 m thin brown stick located between the two streams is provided for scale. 178

5.12 (top) Close-up image of the mixing zone between the alkaline and acidic channels. Blue triangles represent conductivity measurements. The acidic stream is flowing in the direction of the bottom left yellow arrow and the alkaline stream is flowing in the direction of the top left yellow arrow. (bottom) Close-up of the conductivity color map overlaid on the mixing zone. 180

Figure Page

5.13 Image showing the microbial striping zone with the location of the temperature (red circles) and conductivity (blue triangles) measurements overlaid on it. The yellow oval shows the two sets of data to be compared. The two sets of data are separated by ~5 cm. 182

5.14 Plot of temperature and conductivity across the microbial striping zone. The zero position in this plot is located at the bottom of the image in Figure 5.13. Error bars on all conductivity measurements represent the uncertainty of 10% due to sensor system noise and calibration error. 183

5.15 Plot of the measured temperature and conductivity predicted by the two-end member mixing model across the mixing zone. 185

5.16 Plot of the measured and predicted conductivity across the mixing zone. 186

5.17 Predicted conductivity color map of the acidic outflow channel (bottom of image) and alkaline outflow channel (top of image) created in ArcMap™ with blue colors that are lower conductivity than red colors. Conductivities range from 810 μS/cm to 4200 μS/cm. A 1.2 m thin brown stick located between the two streams is provided for scale. 187

Figure Page

5.18 Percent error color map of the acidic and alkaline outflow channels created in ArcMap™. Blue colors are low error and red high error. The acidic stream is at the bottom of the image and the alkaline stream is at the top. Error ranges between ~0% and ~190%. 189

5.19 Close-up image of the percent error color map in the mixing zone. The blue triangles represent locations where the conductivity measurements were taken. The map highlights only areas where the percent error is below 30%. Yellow circles show conductivity measurements where the percent error > 30%. 190

5.20 Predicted pH based on temperature values in the range of those measured in the acidic-alkaline hot spring system. 192

5.21 Measured and predicted pH values plotted as a function of temperature across the mixing zone. Error bars for the uncertainty in pH (0.01) are smaller than the data markers. 193

6.1 Schematic drawing of an arterial bifurcation with flow fields highlighting distinct regions of wall shear stress. 199

6.2 Schematic diagram showing a fluid moving across a plate with a heated sensing element on top. The velocity profile shows the shape of the velocity boundary layer and the thermal profile shows shape of the thermal boundary layer. 201

6.3 Schematic diagram showing a fluid moving across a plate with a cooled sensing element on top. The velocity profile shows the shape of the velocity boundary layer and the thermal profile shows shape of the thermal boundary layer. 206

6.4 Schematic diagram showing how the Peltier cooling effect pumps heat from the top of the device to the bottom under an applied voltage. Red arrows represent the flow of heat. 207

6.5 Image of a potted micro thermoelectric cooler (TE Technology, Inc.) with edges covered in waterproof marine epoxy. The cooler is approximately 3.4 mm length on a side. 209

6.6 A schematic of the fabrication process flow for the flexible micro RTD in cross-section. (a) A layer of SiO_2 is thermally grown on the wafer and a layer of sacrificial amorphous Si is deposited overtop the SiO_2. (b) Photoresist is deposited and patterned and a layer of Ti/Pt is deposited and lifted off. (c) Parylene-C is deposited over the entire wafer and removed over an area of the Ti/Pt using a photoresist mask. (d) Photoresist is deposited and patterned and a layer of Cr/Au is deposited and lifted off over the Parylene-C opening. (e) A second layer of Parylene-C is deposited over the entire wafer. (f) The Parylene-C removed over an area of the Cr/Au and an area exposing the sacrificial Si. (g) Finally, the sacrificial Si is etched away underneath the Parylene-C, releasing the device. 210

Figure Page

6.7 (left) Close-up image of the resistive sensing element on the micro RTD. (right) Schematic drawing of RTD in cross-section. 211

6.8 (left) Close-up image of the cooler with the micro RTD bonded to the cold-side junction. Bubbles are present in the PDMS due to non-vacuum curing. (right) Schematic drawing of the embedded cooler and RTD in a flow channel. 212

6.9 The flow channel with embedded sensor were placed entirely underwater. Flow speed was controlled by a peristaltic pump and flow controller. Power input to the thermoelectric cooler was monitored with the voltage controller and RTD resistance was monitored with a high-precision multimeter. 213

6.10 Temperature-resistance calibration curve for the micro RTD. The device TCR was ~1000 ppm/°C. 214

6.11 Plot showing the increase of power input to the thermoelectric cooler required to maintain a constant RTD temperature for increasing wall shear stress (flow speed). 215

6.12 Plot showing the increase of RTD temperature (at constant power input) for increasing wall shear stress (flow speed). 216

6.13 Screenshot image of Comsol® 3D model of a cooled RTD in flow channel. 217

6.14 Plot comparing the change in RTD temperature with increasing shear stress (flow speed). 218

Figure Page

7.1 Plots from Bergveld (2002). (a) ISFET response as a function of increasing pH. (b) ISFET response as a function of increasing salt content. 224

7.2 Schematic drawing of the pH-sensitive ISFET (top) and the non-pH-sensitive REFET (bottom). 225

7.3 Schematic depiction of microbial adhesion to a material surface in aqueous solution from Al-Juboori and Yusaf (2012). 227

CHAPTER 1: INTRODUCTION

The overall goal of the research presented in this dissertation was to develop new technology, specifically sensor systems, that could be used for the scientific exploration of harsh environments with an eye toward future Earth study and space exploration missions. In a couple of instances, the developed sensor systems were deployed in harsh environments and were used to collect data presented in this dissertation. The term "harsh environment" is often used, but there is no clear definition. For this dissertation, "harsh environment" is defined as an environment in which collecting scientific data is difficult with existing commercial-off-the-shelf technology. The sensors developed were designed to either characterize parameters which make an environment harsh or collect data within a harsh environment. For example, one sensor was developed measure the cumulative amount of energy deposited in a material by exposure to ionizing radiation which can be damaging to biology and electronics. Alternatively, the electrical conductivity sensor arrays were developed to provide a measure of bulk ion chemical concentration across zones of different microbial communities while operating in a harsh environment of high temperature water with high acidity or alkalinity as are found in hydrothermal systems on Earth.

Earth-based research often involves traveling to remote locations for data collection. In some cases, utilizing remote sensing can minimize this requirement; however, remote sensing is often used to monitor changes of large-scale features, for example measuring global ocean surface temperature via satellite infrared imagery. For many environments though, *in-situ* sensors are the best and possibly only way for characterization, due to the small spatial size of the environment, its physical location, the

type of measurement needed, or cost restrictions. Researchers are often required to carry equipment into these remote areas, which limits the instruments that can be brought into the field due to weight and size limitations. Furthermore, continuous or long-term power is often not available at these sites; therefore most of the equipment require batteries which further limit the available instruments and impose a measurement lifetime. The size, weight, and power requirements of instruments used to carry out remote *in-situ* science dictate that the technology is small, lightweight, and low power. Those factors are the driving force behind the sensor system development carried out for these applications.

In space exploration applications, a primary mission limitation is cost. There are a number of different factors that affect the cost of a mission. Clearly, the cost of designing and building a suite of instruments is a major factor on the cost of the overall mission. A scientific instrument typically consists of the sensor, the associated electronics, and the packaging. Instruments are the most critical part of any mission, as they are the means by which scientific data is collected. Therefore, the goal of any mission is to maximize the amount of scientific data that can be collected. Often times, limited mission funding leads to a trade-off between the desire to have a number of different instruments in order to address a broad range of scientific questions and having the most advanced and capable (and therefore costly) instrument for making the best possible specific observation.

Another major mission expense is the launch vehicle. For space missions, the National Aeronautics and Space Administration (NASA) currently utilizes the United Launch Alliance (ULA) Atlas V and Delta IV rockets, Space Exploration Technologies Corporation (Space-X) Falcon 9 rocket, Orbital Science Corporation Taurus 2 rocket, and the soon-to-be permanently retired Delta II rocket from ULA for geostationary transfer

orbit launches. The Falcon 9 (Space-X, 2009), Taurus 2 (Orbital Sciences 2006), and Delta II (United Launch Alliance 2012) are capable of launching intermediate-size payloads (880-4500 kg). Large payloads (4300-13000 kg) are launched with the Atlas V or Delta IV vehicles (United Launch Alliance 2012). Although launch expenses are variable depending on the mission, costs are typically estimated to be ~$22,000/kg for launch to geostationary transfer orbit, depending on launch vehicle and payload mass (Futron 2002). The high launch cost combined with a limited payload size place further constraints on the spacecraft mission design. In addition, the spacecraft needs to carry enough fuel to deliver itself to the intended destination after separation from the launch vehicle. Higher spacecraft masses require more fuel to increase and decrease velocity during the trip to the target or while in orbit. Therefore, there are large costs associated with just launching the fuel, which ultimately places constraints on the spacecraft instrumentation.

A third major cost factor to a mission is power. Any spacecraft must be able to provide enough power to operate all the science instruments when they need to be turned on as well as operating the internal electronics that collect and store the data and transmit the data back to Earth. Typically, spacecraft power generation comes from either solar panels or radio-isotope thermoelectric generators (RTGs). Solar panels are typically satisfactory for missions staying within the inner solar system or low-cost missions to the outer solar system. Solar panels, however, are bulky and can take up a lot of the space in the payload fairing of the rocket, limiting the space available for instruments. Increasing the number of instruments increases the power consumption and requires in larger, heavier, and more costly solar panels. Larger spacecraft with more instrument capabilities

may require the use of a RTG, especially if traveling to the outer solar system where the solar radiation flux is diminished. However, the use of RTGs is becoming less frequent due to a dwindling supply of nuclear material (National Research Council 2009) and therefore low-power instruments are currently at a premium. Taking all of these cost forces into effect, an ideal space instrument would be small in size, lightweight, and low power, without sacrificing scientific capability or engineering reliability. These space exploration requirements are also similar to those described above for the remote Earth-based field-capable sensors that require small size, low mass, and low power for field-portability and long-term monitoring.

Micro Electro Mechanical Systems (MEMS) technology is ideally suited for conducting research under these constraints. Micro Electro Mechanical Systems stand for a class of batch-fabricated devices which may consist of electrical, mechanical, chemical, and other components to perform macroscopic functions on a micro scale. The small size of the MEMS devices naturally make them lightweight. They also consume very little power due to their size and the wide range of materials available for fabrication. This technology was developed by expanding upon techniques used by the microelectronics industry which give MEMS a high degree of engineering reliability. Initially, the materials used in MEMS fabrication were the same as those used in microelectronics fabrication – the bulk semiconductor silicon wafer (Figure 1.1), the doped poly-crystalline silicon (poly-silicon) gate, gate-oxide insulators such as silicon dioxide or silicon nitride, and interconnect metals such as aluminum or copper. As MEMS fabrication techniques have expanded, a greater swath of semiconductor, insulator, and metal materials have been employed, as well as a number of different classes of

materials, including piezoelectrics (Ballato 1995), polymers (Zhou et al. 2004), ceramics (Mehregany et al. 1998), and thermoelectric (Gross et al. 2011) and superconducting materials (Hijazi et al. 2003).

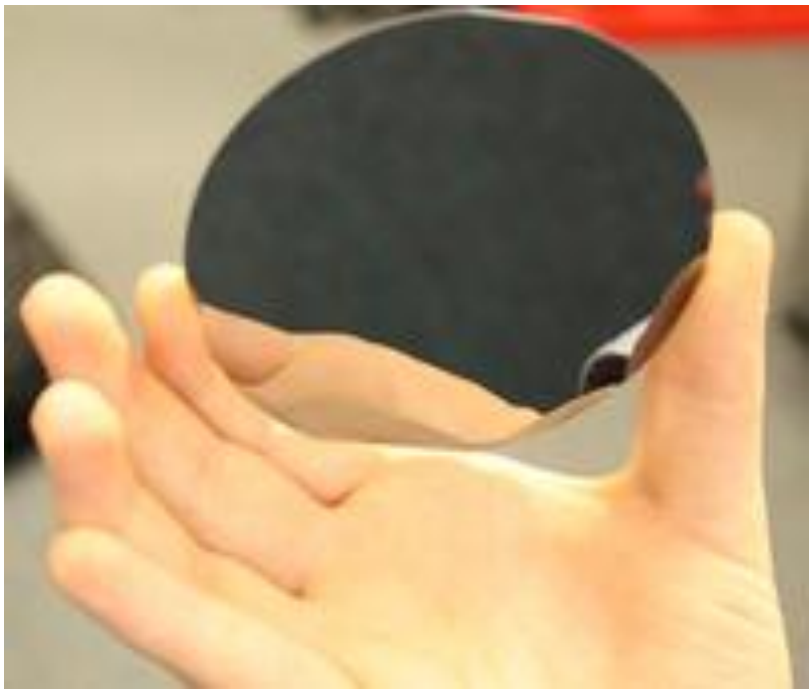

Figure 1.1: Image of a 100 mm diameter polished silicon wafer (photo courtesy of npl.co.uk).

There are two main processes by which MEMS devices are made – bulk micromachining and surface micromachining. Bulk micromachining consists of selectively etching (removing) material to form structures within the bulk substrate of typically a silicon wafer. Surface micromachining consists of depositing and selectively etching materials on top of the bulk substrate. In order to perform the selective deposition or etching of a material, photolithography is employed. A brief discussion of photolithography, deposition, and etching techniques are provided below and is focused on those techniques employed in the fabrication of the sensors described in this dissertation.

1.1 Photolithography

Photolithography is the process of using high energy light (or charged particles) to transfer a pattern from a photomask to a light (or charged particle) sensitive compound called photoresist that is typically spin-deposited on top of the wafer surface. The photoresist consists of resin and solvent chemicals. Liquid photoresist is poured over the surface of the wafer and the wafer is spun at a high revolution rate (typically 1000's of rpm) to create a smooth layer of uniform thickness photoresist. The wafer is then heated at a temperature around 90 °C to evaporate the solvent component of the photoresist. The photoresist is then at its most responsive state for processing. The photomask is typically glass (or quartz) that is transparent to the emitted light with areas where opaque films (mask) cover the surface with a user-designed pattern. This photomask pattern is then transferred into the exposed photoresist. For the sake of brevity, only ultraviolet (UV) light sensitive processes are discussed but the same concepts can explain higher energy photons and charged particle lithography. There are two types of photoresist; where the transmitted UV light is absorbed by *positive* photoresist, the photoresist becomes weakened and soluble and is removed after immersion in a developer solution. Areas where the *positive* photoresist was not exposed to UV light (due to the opaque areas of the mask) remain intact after immersion in the developer. Thus, the remaining positive resist matches the pattern in opaque parts of the mask. The wafer surface is exposed where the photoresist was removed. For *negative* photoresists, the reverse is true. Areas where the *negative* photoresist absorbs UV light become stronger and insoluble in the developer solution. Areas not exposed to UV are weak and soluble in the solution. Thus, after development the reverse or negative image of the mask is patterned to the wafer

surface. Figure 1.2 shows the positive photolithography result using a photomask with a 'plus' shape. Figure 1.3 shows the negative photolithography result using the same photomask. Following development, the wafer can be heated to an elevated temperature (typically 100-130 °C) to make the photoresist more chemically inert in later etch steps. Photoresist can be completely removed from the wafer surface by immersion in acetone.

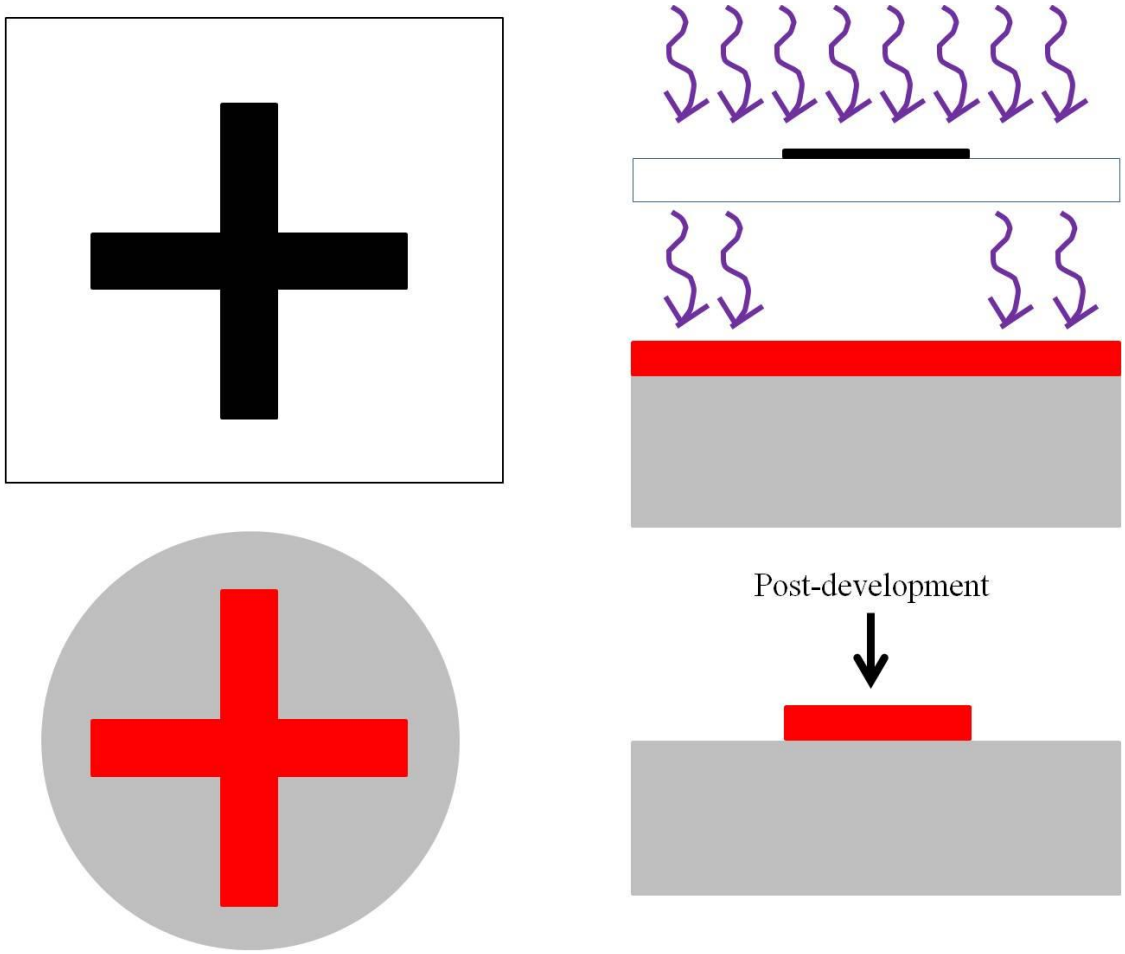

Figure 1.2: (left) Topside schematic of a photomask with 'plus' shape. The black represents areas of the UV-opaque film. Below the photomask pattern is transferred onto the wafer surface where red is the positive photoresist and gray is the silicon wafer. (right) Schematic cross-section of the photomask and wafer showing where the UV light is transmitted and absorbed by the positive photoresist. Areas of positive photoresist that do not absorb UV remain on the surface after development.

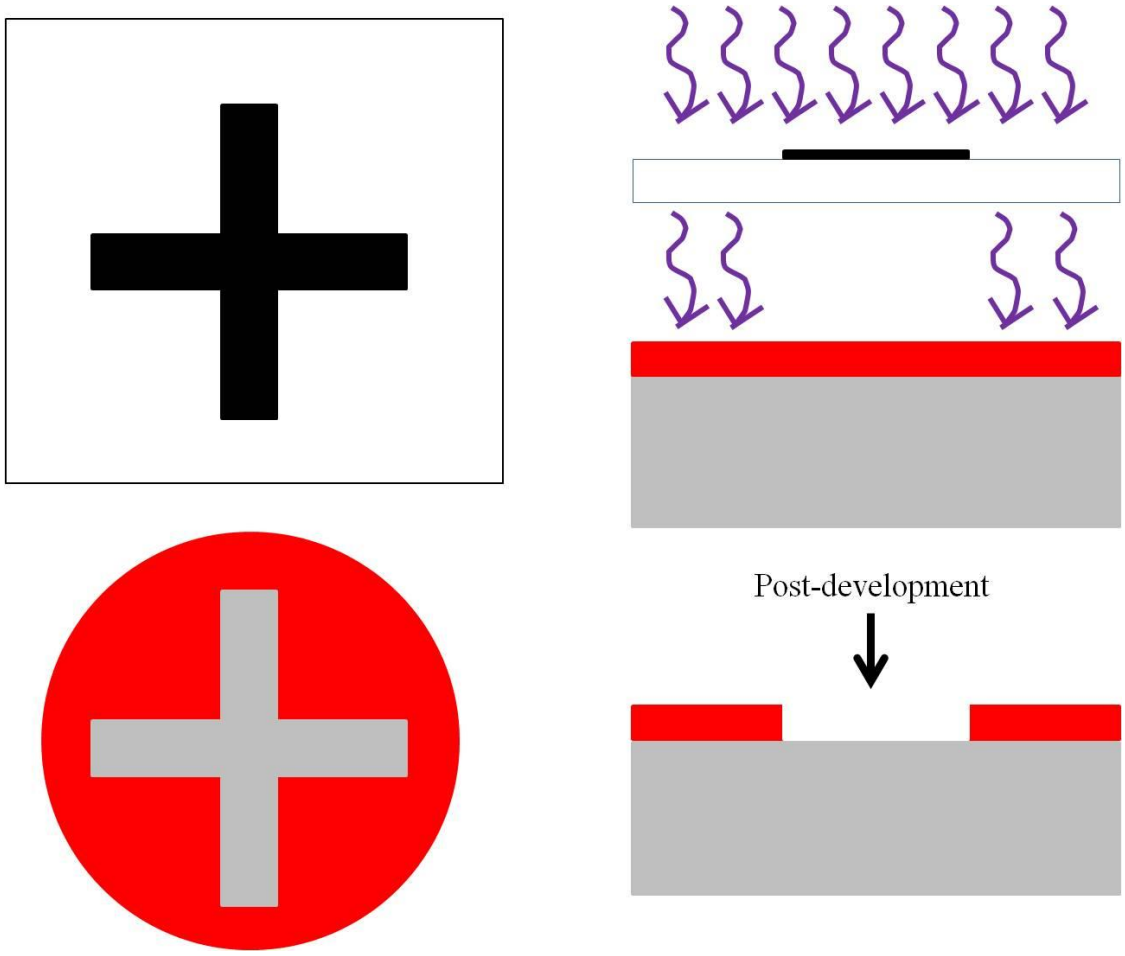

Figure 1.3: (left) Topside schematic of a photomask with ‘plus’ shape. The black represents areas of the UV-opaque film. Below the photomask pattern is transferred to the wafer surface where red is the negative photoresist and gray is the silicon wafer. (right) Schematic cross-section of the photomask and wafer showing where the UV light is transmitted and absorbed by the negative photoresist. Areas of negative photoresist that do not absorb UV are removed during development.

Following the photoresist development, a deposition or etching process is carried out. The choice of using positive or negative photoresist typically depends on the processing step following the photoresist development. For example, negative photoresist is better suited when the next process step involves the lift-off deposition technique (to be discussed later). Photoresist has a temperature limit. The maximum temperature is dependent on the type of photoresist being used; however, generally, it cannot withstand

temperatures greater than 200 °C over an extended period of time and therefore is limited in its use to low temperature processing. The next two sections will discuss deposition and etching.

1.2 Deposition

For almost any material used in the MEMS fabrication process, there is a method by which it can be deposited on a wafer surface. Some deposition processes can be carried out while keeping the substrate at room temperature while others require much higher temperatures. For instance, most metals can be evaporated under vacuum using thermal, electron beam, or sputter evaporation and will condense on the wafer surface; these processes are collectively known as physical vapor deposition. All of these deposition processes are typically performed under high vacuum conditions for high film quality and to ensure that the deposited material does not become oxidized.

In the thermal evaporation process, a high current is passed through an inert filament with the target deposition metal overtop. The resistance to current in the metal filament causes it to heat up and evaporate the target metal which then condenses on the much cooler wafer surface. Typically, the filament is made from a metal (e.g., tungsten) with a much higher evaporation temperature than the desired target metal.

Electron beam evaporation is similar to thermal evaporation except that a beam of electrons generated at a cathode is directed into a crucible containing the desired target metal at the anode. The electrons are accelerated under a very high potential and their kinetic energy is transformed into thermal energy in the target metal as they travel through the crucible to the anode. The evaporated metal condenses on the room temperature wafer in the deposition chamber. The high current generated for electron

beam deposition along with active cooling of the crucible containing the target metal allows for deposition of most metals and a number of other materials as well (e.g., silicon or silicon dioxide).

In the sputter process, the material to be deposited on the wafer is in the form of a thin circular plate called the target. In a simple sputter process, argon gas is flowed into the evacuated chamber and under a high potential forms a plasma. Positively charged argon atoms are accelerated into the metal target cathode. These argon ions slam into the target metal and eject the target metal atoms which then move about the chamber and condense on the wafer. The sputter process can incorporate direct current or alternating current potentials to expand the range of target materials to insulators or semiconductors. During the sputter process, the substrate can be heated to a high temperature which allows for more crystalline films – as in the case of the piezoelectric semiconductor material zinc oxide. Physical vapor deposition on a substrate at room temperature typically leads to amorphous films and in the thermal, electron beam, and sputter processes, deposition is mostly directional – meaning surfaces in line of sight of the filament, crucible, or metal target will undergo the largest amount of deposition.

The other main deposition process category is called chemical vapor deposition. Chemical vapor deposition (CVD) typically occurs at elevated temperatures but can also occur at room temperature. In chemical vapor deposition, gases are flowed into a chamber and after a chemical reaction one or more of the products are deposited on the surface. Deposited films can be mono-crystalline, poly-crystalline, or amorphous and are conformal coatings – meaning the deposition is uniform over the entire wafer. There are a number of different methods for performing chemical vapor deposition, but the two main

techniques used for the fabricated sensors were low pressure CVD and plasma-enhanced CVD.

In low pressure CVD gases are flowed through furnace tube under high temperature (> 500 °C) for most materials. For example, low pressure CVD silicon nitride films are deposited at temperatures around 800 °C (Temple-Boyer et al. 1997). The tube is maintained at low pressure by flowing gas in at one end of the tube and pumping out the reaction products at the other end which results in high quality (minimal defects and low roughness) films. The most common films deposited by low pressure CVD are silicon dioxide, silicon nitride, silicon, and poly-silicon. Poly-silicon can be doped during low pressure CVD by introducing additional gases containing the desired dopant element. In addition, the deposition of the polymer Parylene-C is a low pressure CVD process, although it is deposited differently than described above. Parylene-C begins as a solid dimer and is vaporized at a temperature around 150 °C. The vapor passes through a high temperature furnace at ~690 °C which splits the molecule into two monomers. These monomers then travel into a low-vacuum room temperature chamber where they adsorb and polymerize on the surface of the wafer, creating a conformal coating.

In plasma enhanced CVD, the films are deposited at lower temperatures than for low pressure CVD (< 500 °C). Typically, insulators such as silicon dioxide or silicon nitride are deposited via this technique. Reactant gases are mixed under a high radio-frequency potential field generating a plasma. The plasma environment allows high yield chemical reactions to occur at much lower temperatures than without the plasma. For example, a low-stress silicon nitride film that required 800 °C for deposition in a low

pressure CVD process could be completed at 350 °C in a plasma enhanced process. However, the plasma enhanced process delivers a lower film quality (more defects and higher roughness) compared to low pressure CVD due to the lower temperature and wafer interaction with energetic plasma ions.

Finally, although not technically a deposition process, new material can be grown from other materials. Most commonly, a layer of silicon dioxide can be grown on the surface of a silicon substrate. Silicon will naturally react with oxygen to form silicon dioxide. At room temperature, this reaction can create a layer of silicon dioxide called native oxide about 2-3 nm thick on top of silicon. Under high temperature and higher partial pressures of oxygen, the layer of silicon dioxide can grow much thicker – usually no more than 10 μm. The film formed by thermal oxidation is the highest quality (has the lowest number of defects) silicon dioxide of any process. This is the method used primarily by the microelectronics industry for creating the gate oxide for solid-state transistors.

1.3 Etching

Removing material from the surface or from the bulk substrate of the wafer can be done through a wet or dry process. The wet process involves immersing the wafer in a liquid solution of chemicals that react with and remove the target material. The dry process involves placing the wafer in a chamber and using gases to remove the target material via a chemical reaction or sputter process (or combination of the two). For either of these processes, photoresist or another material is used to cover and prevent (mask) certain areas of the surface or bulk substrate from being etched. Therefore, choice of the masking material should have strong adhesion to the surface underneath and have high

etch selectivity. Etch selectivity is the ratio of how much material of the mask is removed relative to the target material per unit time. Most MEMS etching recipes (wet and dry) are designed so that photoresist can be used as the masking layer for ease of process and time considerations. Typically, photoresist has some non-zero etch rate in most etch processes so the thickness of the photoresist mask is a critical parameter.

Wet etchant solutions are typically acidic, alkaline, or oxidizing in nature and have higher etching rates than dry processes. Most wet etchants remove material isotropically (the amount of material removed is the same in all directions) (Figure 1.4); however, there are solutions that can etch anisotropically (certain crystal-plane directions have faster etch rates) as well. One of the most frequently used anisotropic etchants is a potassium hydroxide (KOH) and water solution for etching single-crystal silicon due to its extremely high etch rate (1400 nm/min, Williams and Muller 1996). This etchant will react strongly with photoresist; however, silicon nitride has a high selectivity to KOH and therefore can be used as the mask. The solution etches different silicon crystal planes at different rates – the <100> plane will etch much faster than the <111> plane, creating a trapezoidal etch cavity with sidewalls angled at 54.7 ° (Figure 1.5).

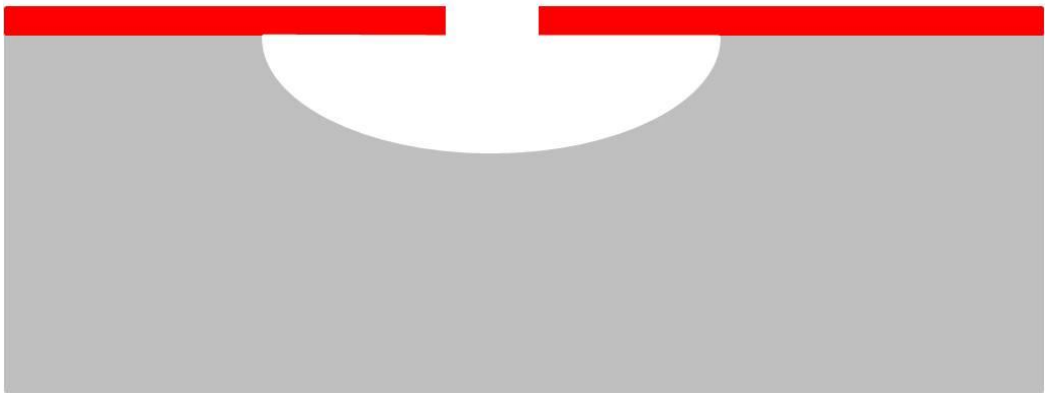

Figure 1.4: Schematic cross section of an isotropically etched silicon wafer (gray) with photoresist mask (red) pattern on top. A common silicon wet isotropic etch recipe uses water and hydrofluoric, nitric, and acetic acids.

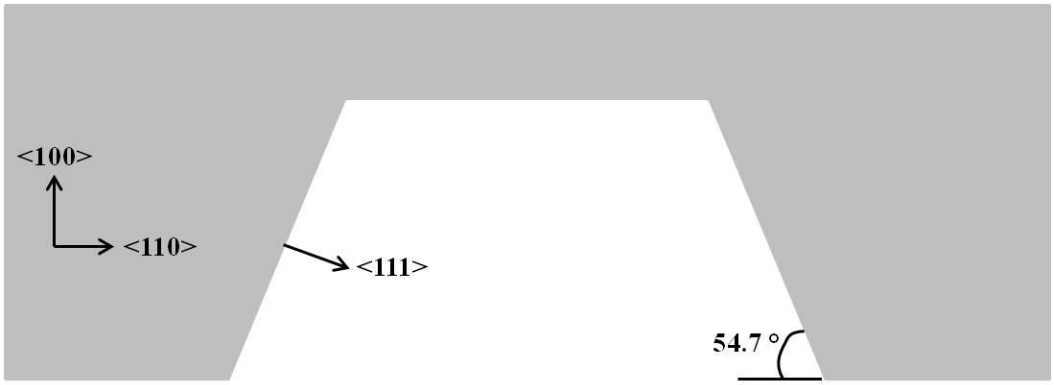

Figure 1.5 Schematic cross section of an anisotropically etched silicon wafer. A potassium hydroxide and water solution will anisotropically etch silicon at a high rate. The high selectivity between the <100> and <111> plane creates a 54.7 °.

Unaltered, dry etching processes would be almost exclusively isotropic chemical etches via reactive gas species. However, due to the ability to add directionality with charged gas species under an electric field, dry etching has become the best way to perform most anisotropic etches, specifically for creating high aspect ratio features. There are a number of different techniques for dry etching, but the most critical ones for creating tall and narrow structures are reactive ion etching, which can be carried out on

most semiconductors, insulators, and metals and deep reactive ion etching which is primarily used on silicon.

Reactive ion etching (RIE) is a method by which the targeted material to be etched is vertically bombarded by chemically reactive gas particles. The impact from the gas species may sputter off material and due to the vertical motion, the gas species is most likely to make initial contact and react with material perpendicular to the direction of travel. In the etch chamber, the chemically reactive gas species is ionized and forms a plasma under a strong radio frequency potential and the ionized gas particle vertical motion is due to the strong vertical electric field. Photoresist is usually an acceptable mask material for most RIE processes.

Deep reactive ion etching (DRIE) is one of the most recent MEMS breakthrough processing technology advances. Similar to RIE, DRIE utilizes directional chemical etching. In the RIE process, the directionality is not perfectly vertical. Therefore, there is some maximum aspect ratio that can be created before the chemical species will begin to bombard and etch the sidewalls of a cavity as well as its bottom. The DRIE technique uses a modified process whereby the directional etching is alternated with deposition of a passivation layer. After a directional etching step, a layer of chemically-inert material is deposited conformally over the wafer (including the sidewalls and bottom of the trench being etched). When the next etching step begins, the mostly vertical motion of the etch gas species will sputter off the passivation layer at the bottom of the trench, but does not have enough lateral energy to do the same on the sidewalls. Therefore, the gas species can chemically react with material at the bottom of the trench but not at the sidewalls.

This method allows for deep trench etching through the entire wafer, greatly expanding the capability to create unique and novel MEMS structures.

1.4 Lift-off

The last MEMS processing technique to be described here is called lift-off and accomplishes the same result as selectively etching a material, without utilizing a wet or dry etching process. Lift-off is typically an easier process to selectively deposit a thin film (usually a metal). Lift-off requires photoresist and therefore can only be used when the following deposition occurs at low temperature (ideally room temperature) and is directional. In the lift-off process photoresist is spun on the wafer surface and patterned with a photomask and the photoresist must be removed in the areas where the film is to be deposited on the wafer surface. The photoresist thickness typically needs to be at least five times greater than the film to be deposited. Next, the directional deposition is carried out; the film covers the photoresist and areas of the wafer surface where the photoresist was removed. Conformal deposition processes cannot be used with lift-off. In the final step, the wafer is placed in an acetone bath and the photoresist is removed – along with the metal deposited on top of it, leaving only the metal deposited directly to the wafer surface. Both positive and negative photoresist can be used to complete this process, but negative photoresist is easier to lift-off (Figure 1.6). This is due to the fact that when negative photoresist is developed and removed, an undercut is created.

Figure 1.6: A schematic cross-sectional depiction of the liftoff process. (top) A thin film (blue) is directionally-deposited onto the wafer covering the positive photoresist (red) and exposed silicon wafer surface (gray). (bottom) Same process as the top, however, the negative photoresist shape makes liftoff easier as less of the thin film is deposited on the sidewalls.

1.5 MEMS Fabrication

The combination of surface and bulk substrate deposition and etching of a wide variety of materials can be used to create some really amazing MEMS devices. In this section, a few of the more famous or common structures will be discussed. One of first notable devices fabricated with MEMS technology was the micro-motor (Fan et al. 1988). Although the first motor did not have a direct application, the proof-of-concept creation of an electro-mechanical device at the micro-scale generated a lot of buzz and

had coverage in the New York Times declaring the "advent of the age of micro-machines" (Pollack 1988). Today, micro-motor (Figure 1.7) applications are still few and far between, mainly used for driving small fans or providing propulsion for micro-scale vehicles (Livermore et al. 2004).

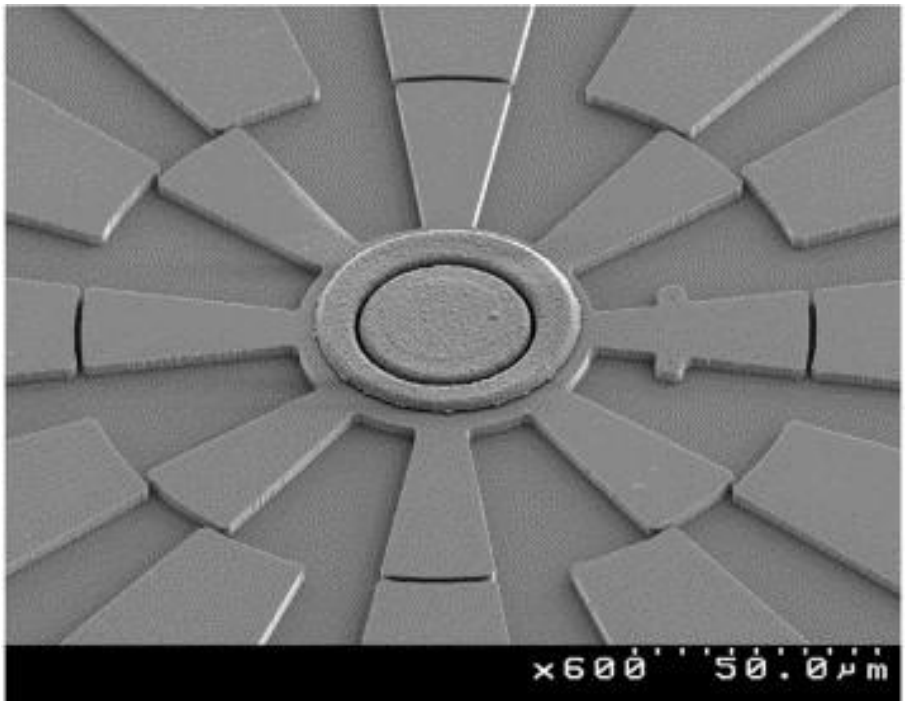

Figure 1.7: Scanning electron micrograph of a MEMS micro-motor (Yasseen et al. 2000).

On the other hand, the cantilevered beam may be the most common and widely used structure in the MEMS research community and industry (Figure 1.8) due to its application versatility. The cantilevered beam has been used in switches (Shalaby et al. 2009), resonators (Lo and Fedder 2007), accelerometers (Yang et al. 2005), atomic force microscopy (Tortonese 1997), and molecular sensing (Koev 2006). It can also be combined with piezoelectric or piezoresistive materials for measuring pressure (Sohgawa et al. 2007), fluid flow properties (Young-Min et al. 2003) or energy harvesting (Kulah and Najafi 2008).

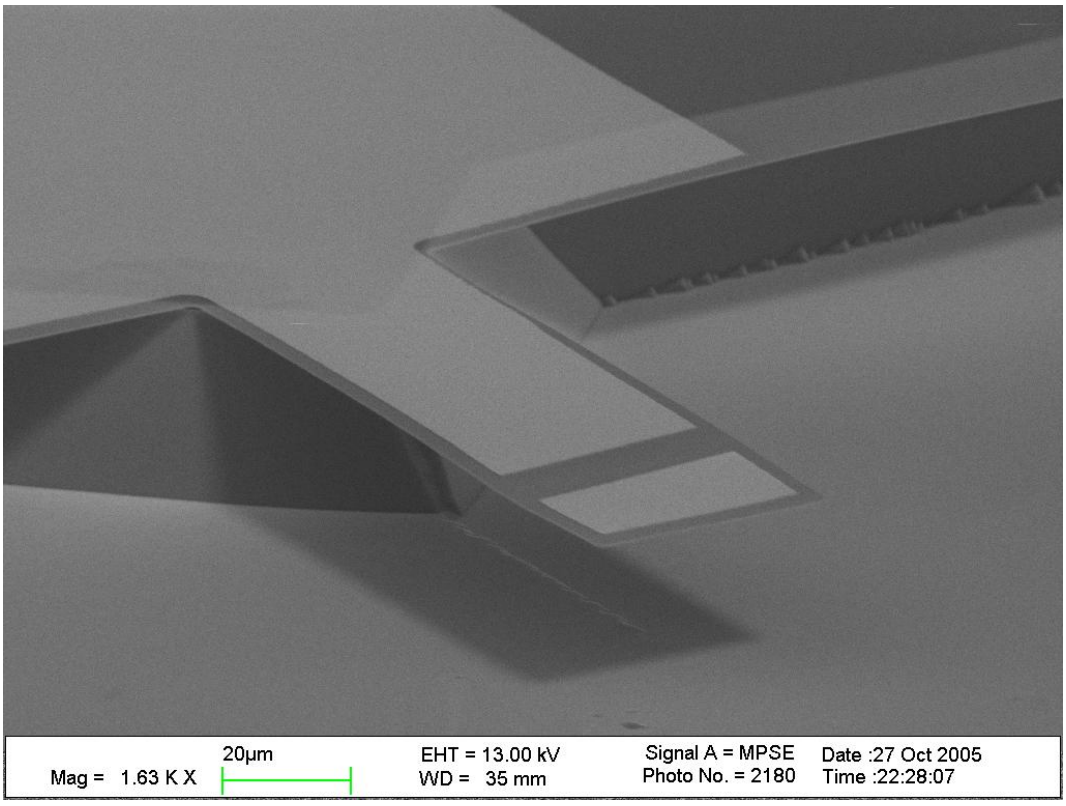

Figure 1.8: Scanning electron micrograph of a cantilevered beam (Koev 2006).

One of the most successful commercial MEMS products is the accelerometer. Most micro-accelerometers have incorporated a mass-spring system for measuring acceleration. Typically, the mass is made from single-crystal silicon and acceleration sensing is provided through the bending of piezoresistive springs or, more commonly, capacitive changes of comb-drive fingers (Abdolvand et al. 2007). From a parallel plate capacitor point-of-view, the comb drive proof mass system can exploit changes in the distance between plates and/or in surface area (Figure 1.9).

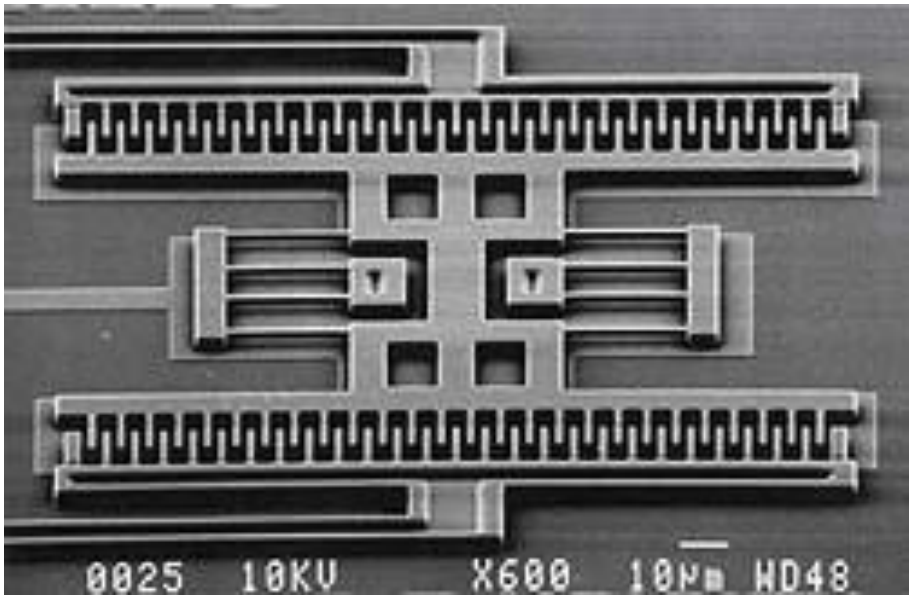

Figure 1.9: Scanning electron micrograph of comb drive accelerometer (Abdolvand et al. 2007).

Finally, to get a sense of how various MEMS technologies can be integrated in order to develop a complicated instrument at the micro-scale, an example of a mass spectrometer will be discussed (Wapelhorst et al. 2007). Mass spectrometers are required for identifying the presence and quantity of atomic species in a given sample of material. These devices are common in university research labs but are often large and extremely expensive. A fully integrated MEMS time-of-flight mass spectrometer was fabricated and is shown in Figure 1.10.

Figure 1.10: A fully integrated time-of-flight mass spectrometer. (left) A scanning electron micrograph showing the mass filter. (right) The packaged mass spectrometer shown next to a penny for scale (Wapelhorst et al. 2007).

The key principles of a time-of-flight mass spectrometer are inputting a sample, ionizing the atomic species, filtering out undesired species, and collecting and indentifying the arrival of the atomic species. The gas sample is input into the ionizing chamber through the thin tubes at the right of Figure 1.10 and the atomic species are ionized via electron impact ionization. Through this process, all the ionized atomic species have the same kinetic energy. The species are delivered into the mass filter via electric potentials and the filter electrodes located at specific locations turn on and off at a set frequency as a means to allow the traversal of ions of a unique velocity (and therefore specific elemental mass given all species have the same kinetic energy). Finally, these ions are collected and counted by Faraday cups to provide the abundance of the element of interest. While MEMS sensors may never be as sensitive as their larger counterparts, their small size, low power, and mass production capability provides the opportunity to be utilized in areas where mass, power consumption, and cost are critically important.

After approximately three decades of research and development, MEMS technology is finally mature and sensitive enough to begin to be incorporated into space

exploration missions. A few notable space mission applications where MEMS were or will be utilized are as an atomic force microscope in the Mars Phoenix Lander (de Rooij et al. 2009), a micro-mirror array for an infrared spectrometer on the Lunar CRater Observation and Sensing Satellite, a short-period seismometer on the upcoming Mars InSight mission (Mimoun et al. 2012), and a micro-shutter array for an infrared spectrograph on the upcoming James Webb Space Telescope (Li et al. 2010). Incorporating MEMS devices into space exploration is still in its infancy, however, as the costs of space exploration become more prohibitive and budgets get tighter, MEMS stands to play an increasing role and therefore it is critical to continue expanding the areas in which MEMS devices can contribute.

The various projects described in the upcoming chapters are geared toward operating in or characterizing harsh environments on Earth that may be analogs to those that once existed or currently exist on a planetary body in this solar system. Chapter 2 will discuss MEMS ionizing radiation sensors, Chapter 3 will discuss MEMS temperature sensor arrays, Chapter 4 will discuss MEMS electrical conductivity sensor arrays, Chapter 5 will discuss sensor array data collected at a specific hot spring system, Chapter 6 will discuss a MEMS thermoelectric flow sensor, and Chapter 7 will conclude the dissertation with a discussion of future research directions.

CHAPTER 2: MEMS IONIZING RADIATION SENSORS

Exposure to ionizing radiation is primarily discussed as it pertains to the effects on biology. As the Chernobyl and Fukushima nuclear reactor accidents made so clear, ionizing radiation poses a real danger to humans. This is also true in space, where astronauts are exposed to higher amounts of radiation and is one of the major limitations for future deep space human exploration (White and Averner 2001). Ionizing radiation also poses a major limitation to the lifetime of electronics, especially for space exploration. Currently, NASA has a plan to develop a spacecraft to study the atmosphere and geology of Europa. However, Europa being the second closest moon to Jupiter, has an extremely high flux ionizing radiation environment and even with shielding, the proposed spacecraft would only orbit Europa for nine months before radiation damage was expected to end the mission (Clark et al. 2011). Therefore, ionizing radiation environments are harsh environments as it pertains to both sensors and biology and being able to monitor the exposure to it is extremely important.

Ionizing radiation is defined as photons and particles with enough energy to strip electrons from atoms or break molecular bonds and possibly create highly reactive (charged) species that can further damage materials through chemical reactions. Since different molecules and atoms have different thresholds for breaking up or becoming ionized, there is no absolute definition for ionizing radiation in terms of an energy threshold. However, for particles and photons, the ionizing radiation level is commonly accepted at energies starting at ~10 eV, which is in the far UV region of the electromagnetic spectrum (Snow et al. 1967). The standard measurement unit for ionizing radiation is the rad which is defined as 100 ergs of deposited energy per unit gram of

material. The energy deposited by ionizing radiation is dependent on the charge, mass, and energy of the particle as well as the incident material and is called linear energy transfer.

There are a number of different sources of ionizing radiation. Extraterrestrial sources include the Sun, which continuously emits ionizing electromagnetic radiation and can deliver high energy particles at large fluxes during solar particle events, high energy particles delivered from the Van Allen radiation belts (Jorgensen et al. 2006), and a very low flux of extremely high energy particles called galactic cosmic rays. Most of the ionizing radiation from space is shielded from Earth by the magnetosphere or absorbed in the upper atmosphere (Dalgarno and McElroy 1966). The primary terrestrial source of ionizing radiation involves the inhalation of radon gas emitted from soil and rocks. Lower contributions come from gamma rays from the decay of uranium, thorium, and radon. Trace amounts of terrestrial radiation come from sources such as atmospheric nuclear testing and the Chernobyl accident. Artificial radiation (e.g., medical testing equipment) contributes approximately the same amount as galactic cosmic rays (Charles 2001).

There are two main ways that ionizing radiation can physically damage non-biological materials as described from an electrical properties perspective: total ionizing dose and displacement damage. Additionally, ionizing radiation can also cause single event effects, which are an issue in digital electronics and therefore will not be discussed here. The first physical effect, total ionizing dose, occurs when charged particles of substantially high energy enter a material. A charged particle will travel through the material and interact with negatively charged electrons and positively charged holes via the Coulomb force governing the attraction (or repulsion) between particles of dissimilar (or similar)

polarity. Holes, which are treated as positively charged particles, are essentially the absence of electrons in an otherwise filled valence shell. If the energy transferred to electrons (or holes) is high enough to move the valence bound electron into the conduction band, then an electron-hole pair is created. These secondary electrons can emit a photon and drop back into the valence shell and recombine with its corresponding hole, or, with high enough energy, can travel through the material and create additional electron-hole pairs. In this way, the higher the incident charged particle energy, the more electron-hole pairs are created (Summers et al. 1994). In certain materials, the electrons and holes will not all recombine and there will be an excess in electrons or holes, creating a net charge buildup somewhere, such as in material defect regions. As these devices receive increasing total ionizing dose, the electron or hole excess will become larger, and the net charge accumulates. The charge buildup can change the electronic properties of a device incorporating these materials. An example showing the effects of total ionizing dose will be provided later in the chapter. This discussion was related to charged particles and not photons. However, while photons do not have charge, they can generate energetic secondary electrons via the photoelectric effect, Compton scattering, or pair-production depending on the energy of the impinging photons. These secondary electrons will have the same effect as described above.

The second main method of radiation damage is called displacement damage. Displacement damage primarily occurs when neutrally charged particles (e.g., neutrons) collide with an atom within a lattice (massive ionized particles can do this as well). The effects on a semiconductor material such as silicon are that the atom will be knocked out of the lattice and move to an interstitial location, leaving a vacancy behind. These

vacancy-interstitial pairs are sources of traps and recombination centers in the semiconductor, affecting its electrical properties. Specifically, the traps and recombination centers have the effect to reduce minority carrier lifetime, change carrier density, and reduce charge carrier mobility in the semiconductor (Messenger 1992).

Ionizing radiation effects on biology are caused by the same physics as described above, however, from a biological context, the ramifications are different. As mentioned previously, incident ionizing radiation will serve to ionize atoms and break molecular bonds. With the DNA molecule, the most damaging effects occur when the ionizing radiation breaks both strands of the double helix structure, making it incapable of repairing itself before replication (Martin et al. 2010). However, DNA occupies a small part of the cell and other radiation effects such as breaking the bonds of water molecules in the cell, some of which may recombine into toxic substances such as hydrogen peroxide, can be just as deleterious (Zastawny et al. 1998). There are also stochastic effects, such as developing an increased risk for cancer or heart disease. Ionizing radiation is also used in medical treatments of a number of different cancers. Typically, a cancer-based radiation treatment may require a total cumulative dose of 2000-8000 rads at daily intervals of 100 rads (Ahmad et al. 1993).

There are two main types of ionizing radiation sensors. The first type measures the energy of the incident radiation and is known as a spectrometer. Spectrometers are important for using the energy information to identify the source of the radiation, such as detecting uranium or plutonium from smuggled nuclear weapons (Phlips et al. 2004). This technique does not provide information about how much cumulative energy is deposited into a material. Sensors measuring the cumulative dose of energy absorbed by a

particular material over a period of time are called dosimeters. Some dosimeter technologies were developed for measuring low levels of radiation deposited in the human body from the natural background and working with nuclear materials such as in nuclear power plants, nuclear research labs, and operating certain medical devices. A second class of dosimeters is used to measure radiation doses in the high dose range such as in space applications (Georgiou 2008) and certain biomedical applications (Son and Ziaie 2008). Measurement of dosimetry in the higher dose range is the focus of this research.

Radiation absorption in space is a major concern for both spacecraft electronics and astronauts. While Earth's magnetic field provides some protection, ionizing radiation in the form of galactic cosmic rays or solar particle events (Baker et al. 2007) is strong enough to degrade the performance of electronic equipment such as space telescopes (Yamashita et al. 1997) and human radiation exposure in space has been shown to increase the risk of developing cataracts in astronauts (Cucinotta et al. 2001).

For biomedical applications, small sensor size is needed to make the placement or insertion of the device minimally-invasive. In cancer treatments, placing a radiation sensor close to the irradiated target to provide accurate information about the dose received could help improve tumor targeting and eradication and reduce side effects such as radiation-induced second cancers (Xu et al. 2008). In addition, wireless readout capability would allow possible *in-vivo* insertion next to the tumor. Highly sensitive solid-state metal-oxide-semiconductor field-effect transistor (MOSFET) dosimeters (e.g., RADFETs) have been developed over the past decade and have the capability to be implanted as biomedical dosimeters (Beyer et al. 2008). However, these devices, when

paired with an inductor, have limited sensitivity in wireless applications due to lower resonant frequencies.

The operating principle of the RADFET is based on the MOSFET device structure which consists of doped silicon with a layer of silicon dioxide (SiO_2) on top. On top of the SiO_2 is a layer of metal. During irradiation, electrons in the metal are already in the conduction band and the additional energy given to the conduction band electrons has little effect. For silicon, there are electrons in both the valence and conduction bands. The energy required for an electron to jump the bandgap to move from the valence shell to the conduction shell is relatively small (1.12 eV), therefore ionizing radiation will cause a large increase in conduction band electrons (and valence band holes) and thus temporarily increase the conductivity. However, the relaxation time (the time it takes for the conduction electrons to fall back into the valence band) is short, so recombination rates are high causing little permanent damage. However, for SiO_2 (and other insulators as well), the band gap is large (8.9 eV) and thus before irradiation there are no conduction band electrons (Schwank et al. 2008). Ionizing radiation will excite electrons into the conduction band of the SiO_2. While some recombination will occur, many of the electrons will migrate toward the metal gate via drift and diffusion and be liberated from the oxide. The excess holes, which have a significantly lower mobility than the electrons, can be trapped in the oxide or will migrate away from a positively charged gate to the oxide-semiconductor interface and can become trapped there as well. The net result is the build-up of positive charge in the oxide which will change the device characteristics (Barnaby 2006).

For a p-channel MOSFET, the pre and post-radiation effects can be shown schematically in Figure 2.1.

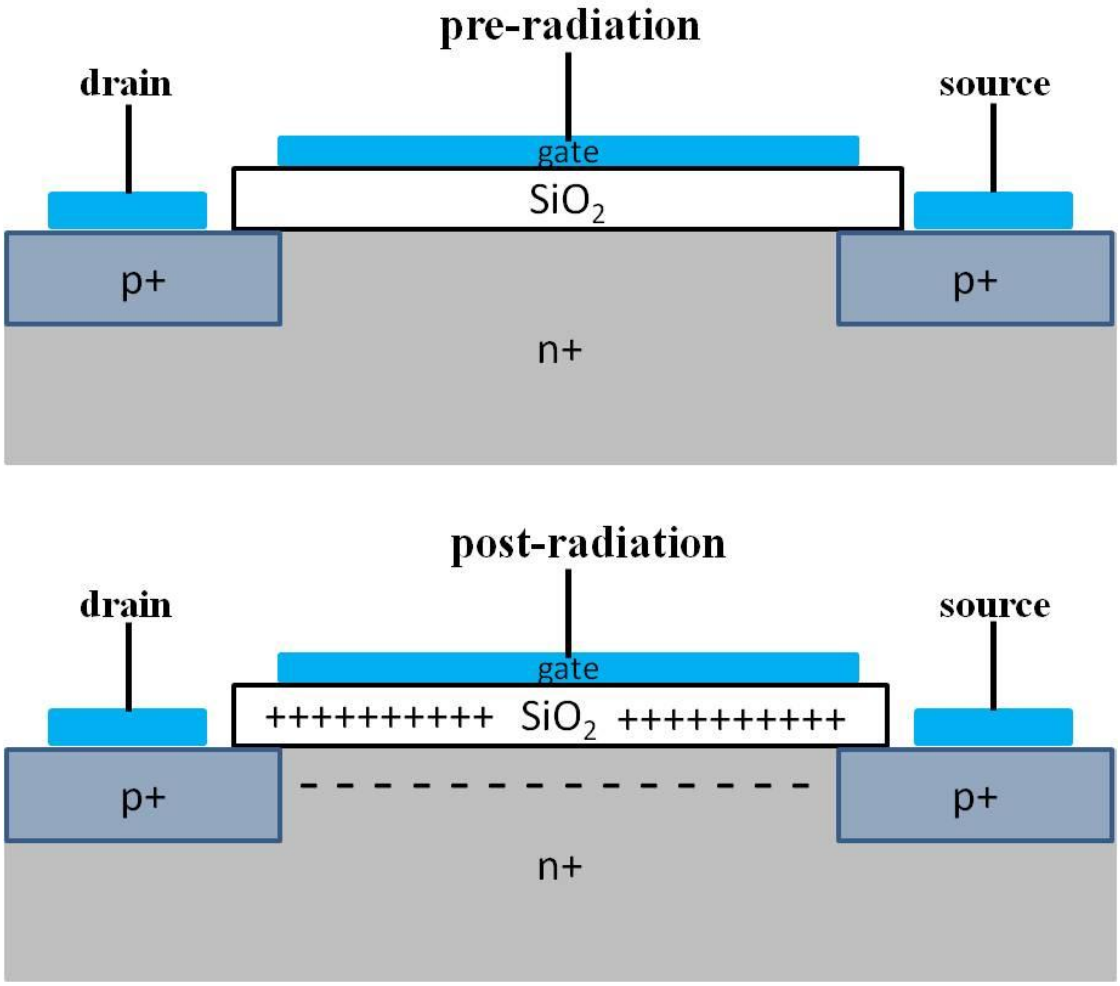

Figure 2.1: Schematic cross-section drawing showing a p-channel MOSFET before (top) and after (bottom) ionizing radiation. The radiation-induced trapped charge in the oxide changes the device electrical characteristics. The gray n+ and blue p+ regions are doped into the silicon. The white area is silicon dioxide. The bright blue regions are metals.

The MOSFET devices are very simple voltage controlled switches. In a normal pre-radiation state, with no metal gate voltage (or a positive gate voltage), the majority carriers (holes) in the silicon cannot flow between the heavily doped source and drain regions (under a voltage differential), as the positively charged holes will combine with

the negatively charged electron majority carriers in the silicon channel between the diffusion wells. Thus, the device is OFF. When a negative gate voltage is applied, the negative charge of the gate will repel the negatively charged electrons in the channel between the two p+ regions. At a certain negative threshold voltage, enough electrons have been forced from the channel that the holes can flow between source and drain p+ regions (under a source-to-drain voltage differential). When this occurs, the device has switched from OFF to ON.

After the ionizing radiation, the p-channel MOSFET electrical characteristics will change. The trapped positive charge in the silicon dioxide (white) will attract the majority carrier electrons within the silicon channel. Thus, it will take a larger negative gate voltage to remove the excess electrons in the channel and turn the device ON. In this way, the p-channel threshold voltage becomes more negative (Kelleher et al. 1995). As the total ionizing dose is increased, the trapped charge accumulates, changing the threshold voltage (Gopalan 2010).

2.1 MOSCAP-Antenna Passive Ionizing Radiation Sensor

MOSFETs are active devices since they require power to be operated. Therefore, any wireless RADFET sensor package must also include a power source such as a small battery and electronics package for operation. The need for the power source and electronics not only increases the device size, but makes it more complicated to be utilized *in-vivo*, increases the cost, decreases the lifespan, and limits the number of applications. Passive devices on the other hand, require no power for operation and therefore can overcome all of the disadvantages of the RADFET device. Therefore, in order to take advantage of the high radiation sensitivity of the RADFET while operating

the sensor passively, a wireless antenna based dosimeter was researched. The device consisted of a patch antenna coupled to a radiation-sensitive metal-oxide-semiconductor capacitor (MOSCAP).

Patch antennas are simple structures consisting of a thin sheet (patch) of metal mounted over top of a metal ground plane separated by a dielectric medium. The patch antenna resonates when its length is approximately half the wavelength of the incoming RF wave. An electric field travels through the dielectric material between the patch metal and the ground plane. The electric field continues beyond the edges of the metal sheets, and these fringing fields are responsible for the antenna radiating back to the environment (Denlinger 1969). By using a receiver, the returned (radiated) signal from the antenna can be measured in frequency and intensity. The frequency of highest intensity is associated with the resonant frequency of the patch antenna. However, the antenna's resonant frequency can be changed via capacitive loading. Capacitive loading simply means that a capacitor is placed at the edge of the patch antenna (where the fringing occurs), connecting the patch metal and ground plane. The antenna's resonant frequency (of strongest signal) will decrease with increasing capacitance (Ferrari et al. 2007). Therefore, a radiation-sensitive capacitor-loaded antenna will change its resonant frequency with total ionizing dose which can be monitored passively using an interrogator/receiver system.

The MOSCAP consists of a layer of SiO_2 (or another insulator) on top of a layer of monocrystalline silicon, both of which are sandwiched between two metal layers (Figure 2.2).

Figure 2.2: Schematic cross-section drawing of a MOS capacitor. Most commonly, a layer of silicon dioxide thermally grown on a layer of silicon is sandwiched between two aluminum electrodes.

The MOSCAP material layers respond to the radiation exactly the same as the RADFET, with the buildup of radiation-induced charge in the oxide layer (and at the oxide-silicon interface) proportional to the dose. The difference here is that instead of changing the device threshold voltage, the device capacitance is changed. In a MOSCAP, the equivalent electrical circuit has two capacitors in series between the top and bottom metal pads. Therefore, the total capacitance of the MOSCAP (C_{tot}) is given by:

$$C_{tot} = \frac{1}{\frac{1}{C_{ox}} + \frac{1}{C_{Si}}}, \quad \text{(Eq. 2.1)}$$

where C_{ox} is the parallel plate capacitance of the SiO_2 and C_{Si} is the semiconductor capacitance. The capacitance C_{ox} is given by:

$$C_{ox} = \frac{\varepsilon_0 \varepsilon_{ox} A}{t_{ox}}, \quad \text{(Eq. 2.2)}$$

where ε_0 is the permittivity of free-space, ε_{ox} is the dielectric constant of silicon dioxide, A is the surface area of the oxide underneath the metal electrodes, and t_{ox} is the thickness of the oxide layer. This capacitance does not change as a result of the radiation. The semiconductor capacitance, $C_{Si,}$ is given by:

$$C_{Si} = \frac{\varepsilon_0 \varepsilon_{Si} A}{W_{dep}}, \quad \text{(Eq. 2.3)}$$

where ε_0 is the permittivity of free-space, ε_{Si} is the dielectric constant of silicon, A is the surface area of the oxide underneath the metal electrodes, and W_{dep} is the width (thickness) of the depletion region. In a PMOS device, the silicon is doped with an excess of holes. The depletion region in the silicon is formed when a positive voltage is applied at the top metal electrode and the positively charged majority carrier holes in the silicon are repelled away from the Si-SiO_2 interface, forming a region of silicon essentially free of the majority carrier charge. The depth at which the majority carrier holes are located forms essentially the bottom electrode of the semiconductor capacitor and the non-conducting region in between drives the semiconductor capacitance. The depth of the depletion region is proportional to the voltage at the top electrode. Therefore, radiation-induced positive charge trapped in the oxide (or at the interface) will act as a positive voltage and increase the depletion region width. In this way, the semiconductor capacitance (and thus the total capacitance) is proportional to ionizing dose. Normalizing the total capacitance by the surface area and the permittivity of free space (C'_{tot}), Eq. 6.1 can be rewritten as:

$$C'_{tot} = \frac{1}{\frac{t_{ox}}{\varepsilon_{ox}} + \frac{W_{dep}}{\varepsilon_{Si}}} \quad \text{(Eq. 2.4)}$$

A plot showing the capacitance change of a MOSCAP with varying top electrode voltage is shown in Figure 2.3.

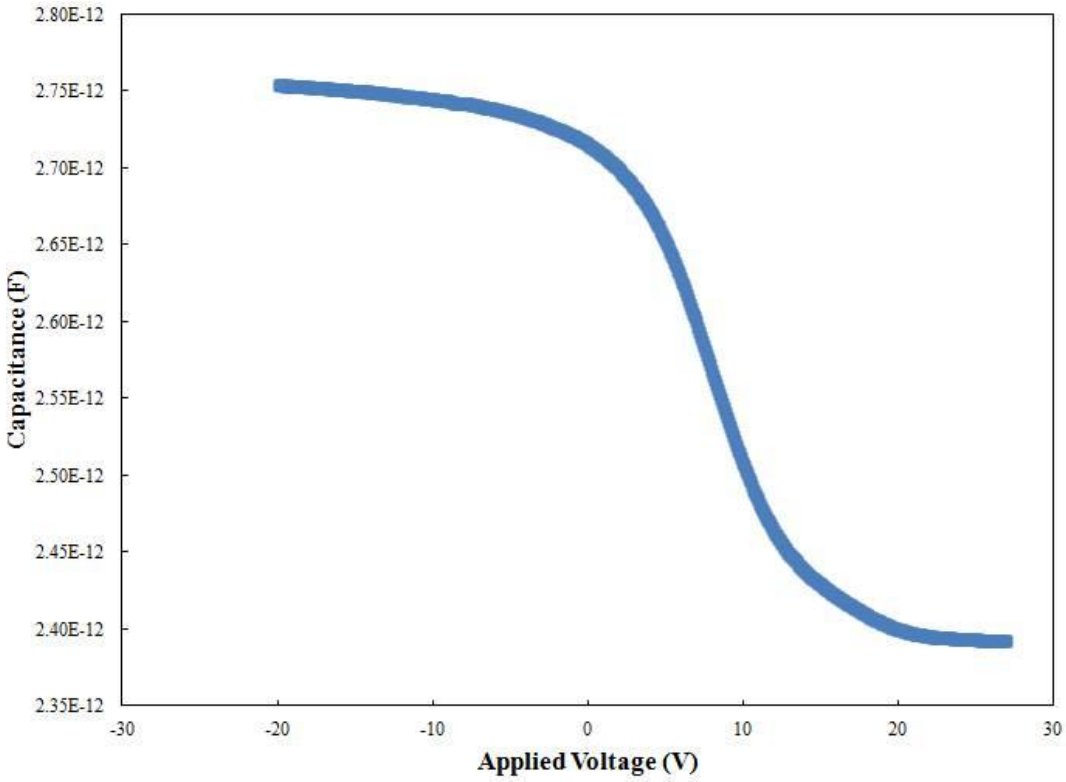

Figure 2.3: Capacitance-Voltage curve for a p-doped MOSCAP.

At a negative voltage, the positively charged majority carrier holes in the silicon are attracted toward the top electrode and move toward to Si-SiO_2 interface, minimizing the depletion region such that the total capacitance is only a function of the SiO_2 parallel plate capacitor. At this stage the device is said to be in accumulation. As the voltage becomes less negative (or more positive), the total capacitance decreases as the depletion region becomes wider (holes move farther away). At this stage, the device is said to be in depletion. Finally, when the voltage is increased enough such that the holes are repelled and the positive top electrode charge has attracted and accumulated all of the minority carrier electrons toward the interface, then the device is said to be in inversion (since the polarity of charge at the oxide interface has flipped). Any further increase in voltage will not change the capacitance value. Radiation-induced positive charge trapped in the oxide

and at the oxide-semiconductor interface will serve to drive the MOSCAP into depletion at a more negative voltage (shifting the curve to the left). Thus, a device operated at a constant voltage will decrease in capacitance as the total ionizing dose increases.

The fabrication of the MOSCAP was a critical design aspect due to the fact that when used with a patch antenna a large resistance through the silicon portion of the MOSCAP would decrease the intensity of the radiated signal from the antenna. Therefore, a standard MOSCAP using the entire silicon wafer thickness would kill the reflected signal. Also, a thin layer of moncrystalline silicon is difficult to deposit on top of silicon dioxide. Therefore, the MOSCAP was fabricated using a silicon-on-insulator (SOI) wafer. The SOI process creates a wafer consisting of a thick monocrystalline substrate (handle layer), on top of which is a layer of thermally-grown SiO_2 (box layer), on top of which is a thin layer of monocrystalline silicon (device layer) which can be doped heavily to lower its resistance. The fabrication process flow of the MOSCAP is provided in Figure 2.4.

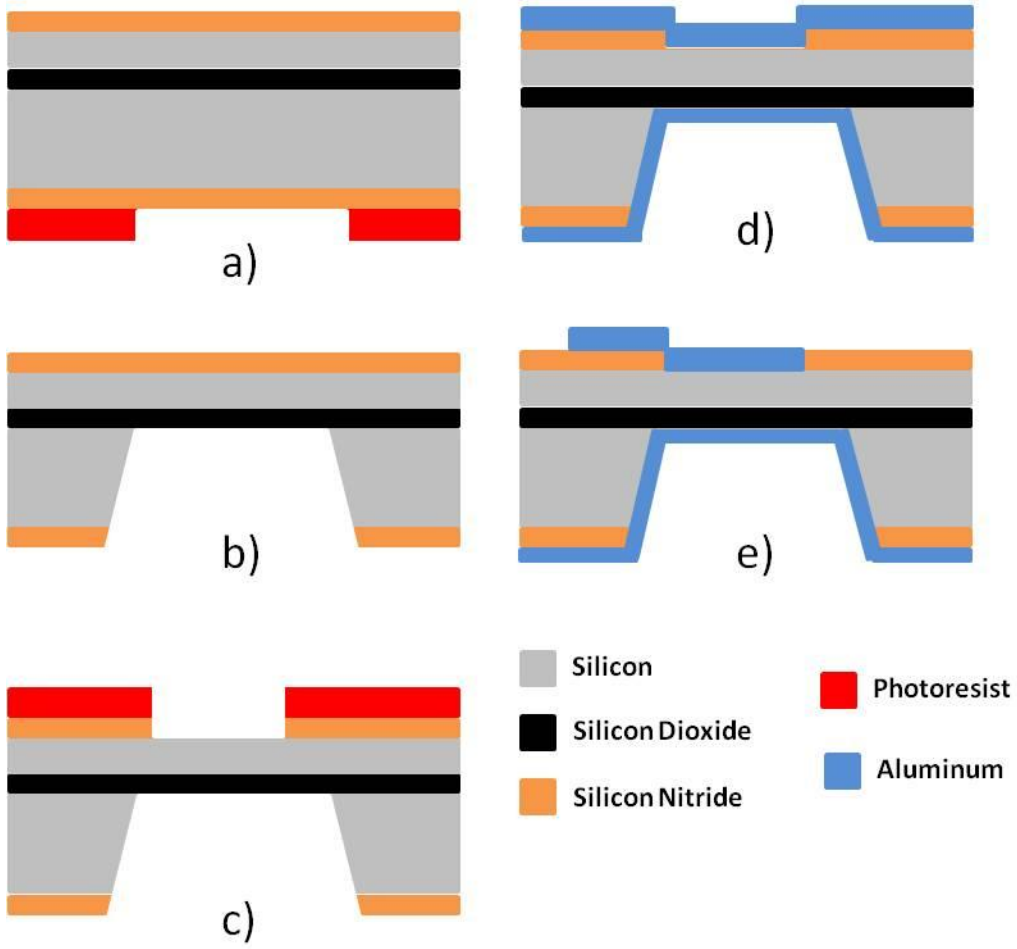

Figure 2.4: A schematic of the fabrication of the MOSCAP in cross-section. (a) Photoresist is patterned over silicon nitride (SiN) at the bottom of the SOI wafer. (b) The SiN is etched and the SiN is used as a mask for the anisotropic etching of the handler layer Si. (c) Photoresist is patterned and the SiN is etched over a region of device layer Si. (d) Aluminum is deposited on both sides of the wafer. (e) Finally, the aluminum is wet etched on the top of the wafer to form the top electrode and bond pad.

The fabrication of the MOSCAP started with an SOI wafer with a handle layer thickness of 500 µm, a box layer thickness of 2 µm, and a heavily p-doped device layer of 5 µm. A 1 µm layer of low-stress low pressure chemical vapor deposition (LPCVD) silicon nitride (SiN) was deposited on both sides. At the bottom of the wafer (the side with the Si handle layer), positive photoresist was deposited and patterned over a region of the SiN. The SiN was dry etched using reactive ion etching (RIE). The photoresist was

removed in acetone and the wafer was submerged in a potassium hydroxide (KOH) solution to anisotropically wet etch the silicon handle layer. The SiN is not etched in KOH. Etching stops at the silicon dioxide box layer forming a thin diaphragm of 2 µm SiO_2 and 5 µm Si. Next, positive photoresist is deposited and patterned over the top side SiN. The exposed SiN is removed using RIE. A 400 nm thick aluminum layer is electron-beam deposited on the top and bottom of the wafer. Finally, a positive photoresist is deposited and patterned over the top side aluminum. The top side aluminum is wet etched in a phosphoric-acetic-nitric acid solution. The resulting device is an 'upside-down' MOSCAP over the device diaphragm. The device layer Si was heavily doped and therefore provided a very small resistance which was desired. The bond pad connection to the top side metal sat on a layer of SiN and therefore also contributed to the overall capacitance, however it was just a small fraction of the total.

The MOSCAPs were irradiated to different levels of total ionizing dose from ~1.2 MeV gamma rays from a ^{60}Co source in Professor Keith Holbert's Radiation Damage Laboratory at Arizona State University (Figure 2.5).

Figure 2.5: Radiation testing equipment in Professor Holbert's laboratory. Devices are exposed to 1.2 MeV photons from a ^{60}Co source in the belly of the lead-shielded machine.

Capacitance measurements were taken over a range of voltages before radiation and after different doses (Figure 2.6).

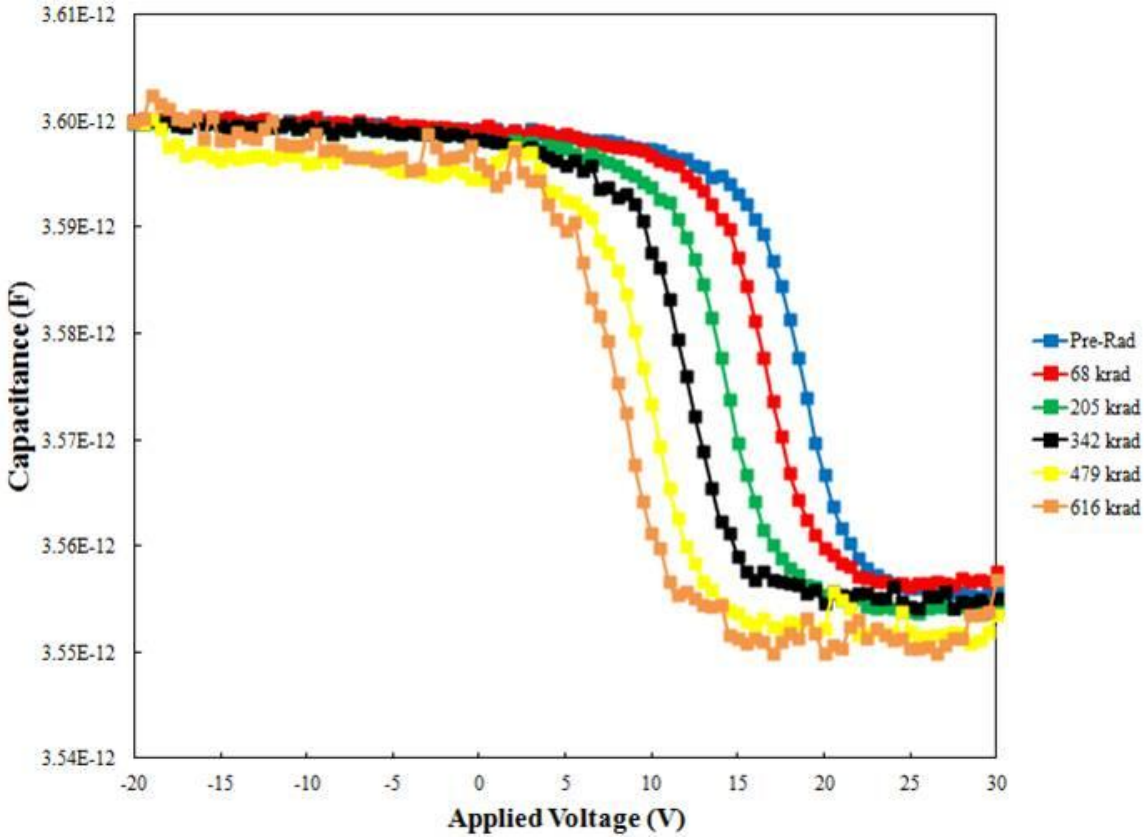

Figure 2.6: Capacitance-Voltage curve for the fabricated p-doped MOSCAP devices at different total ionizing doses.

As seen in the plot, the capacitance-voltage curve shifts to the left under increasing total ionizing dose as a result of the trapped charge in the SiO_2 box layer. The dose range for this testing started at a high radiation dose, which would be important for nuclear materials monitoring or space applications.

In addition, the capacitor-loaded antenna concept was tested by a group of electrical engineering senior design students under my lead. While the MOSCAP devices were being fabricated, the senior design group purchased small non-radiation sensitive capacitors of similar capacitance to that which was being designed for and bonded them to miniature patch antennas. The devices were placed in an anechoic chamber and interrogated with an RF signal. A receiver recorded the reflected intensity from the room

and one such plot is provided, showing a weak but noticeable intensity peak from the device above the noise at slightly greater than 9 GHz (Figure 2.7).

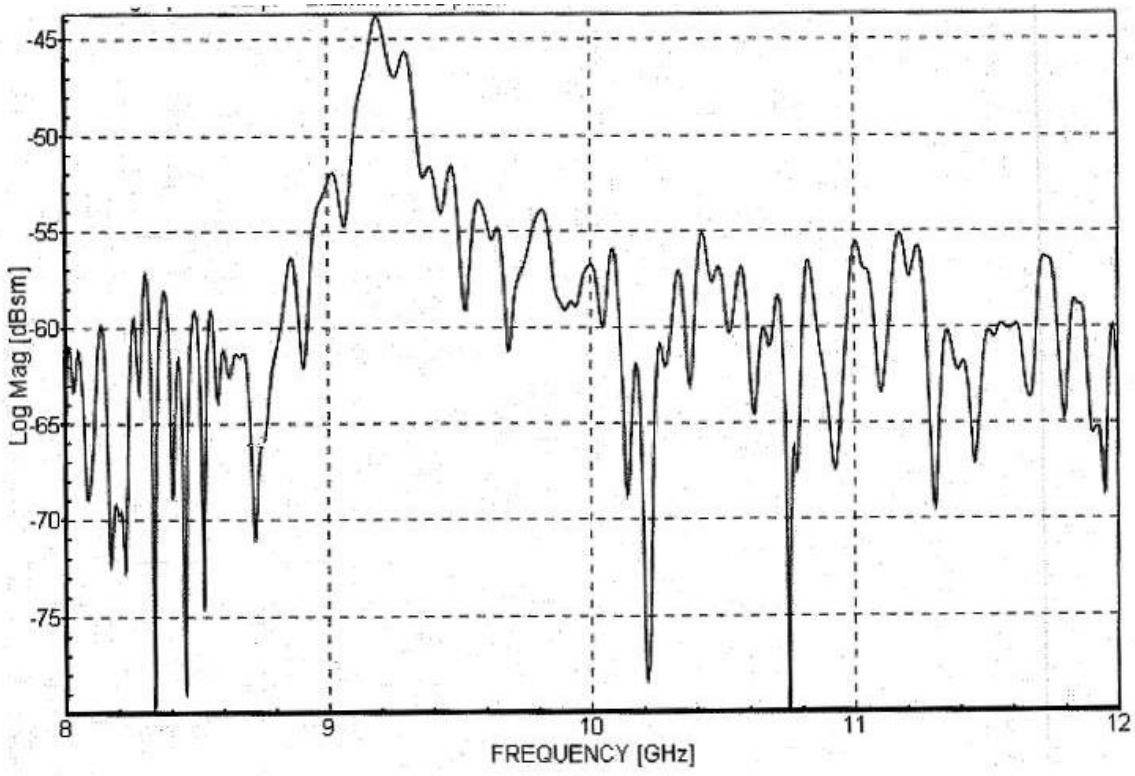

Figure 2.7: Plot of reflected intensity from inside an anechoic chamber with a capacitor-loaded antenna device in the chamber. The peak at > 9 GHz is a response from the antenna.

During the research, a patent application was pursued for this concept; however, another patent was discovered that proposed a very similar concept, so further work on this device was discontinued.

2.2 FBAR Ionizing Radiation Sensors

At the same time, another type of device was being pursued as a potential wireless ionizing radiation sensor. This sensor utilizes a RF resonator as the sensor. Resonators are devices that use piezoelectric materials to turn electrical energy into mechanical energy (or vice versa). The mechanical energy is manifested as acoustic waves that can

travel in the thickness-direction of the piezoelectric material. The acoustic waves will reflect at the boundaries between materials when the reflection coefficient is high. A standing wave will form if the thickness of the piezoelectric film from which the acoustic wave is propagating back and forth is an integer multiple of half of the acoustic wavelength. The fundamental resonant frequency of the film material is given as:

$$f_0 = \frac{v}{2t}, \qquad \text{(Eq. 2.5)}$$

where v is the velocity of the acoustic wave in the material, and t is the thickness of the material. The acoustic wave will modify the distribution of the electric field within the piezoelectric material which changes the electrical impedance of the device. Therefore the electrical impedance of the sensor will vary with frequency (Qiu 2011). For resonating devices operating in the gigahertz (GHz) frequency range, the piezoelectric film must be less than a few micrometers thick and therefore these devices are called film bulk acoustic-wave resonators (FBARs). A typical FBAR involves a piezoelectric material (e.g., zinc oxide [ZnO]) sandwiched between metal electrodes (e.g., Au) on a supporting diaphragm typically made of SiN (Figure 2.8) although some of the devices described in this chapter have slightly different structures.

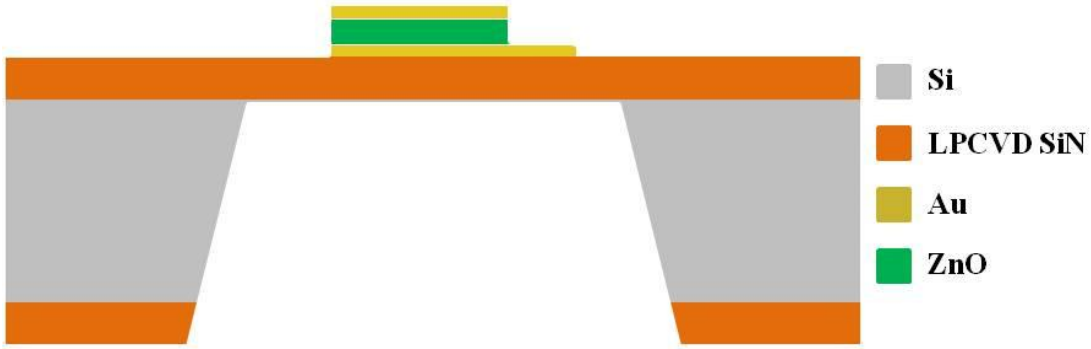

Figure 2.8: Schematic drawing of a typical FBAR device in cross-section.

These devices have operational frequencies between 0.5 and 10 GHz and have high quality factors (*Q*) which describes the rate of energy loss of a vibrating oscillator relative to its stored energy.

Film bulk acoustic-wave resonators are MEMS devices that have previously been developed for the applications of high sensitivity mass sensors (Zhang and Kim 2005) and ultraviolet sensors (Qiu et al. 2009). The ultraviolet (UV) sensing effect was owed to the piezoelectric film density change that occurred only during exposure to UV and was not permanent. These devices also have the capability to be read-out wirelessly (Ruby et al. 2001). The sensors described in this chapter incorporate ZnO as the piezoelectric film for the FBAR structure.

The first ionizing radiation tests of the FBAR structure were exploratory in nature. The FBAR quality factor is very sensitive to the device fabrication and depends on high quality electrodes and piezoelectric film and smooth and low-stress depositional surfaces such as the SiN diaphragm. Any of these factors might have been affected from either displacement damage or total ionizing dose of the ionizing radiation which may affect its resonating properties.

The schematic fabrication flow drawing of the original FBAR structure is shown in Fig. 2.9.

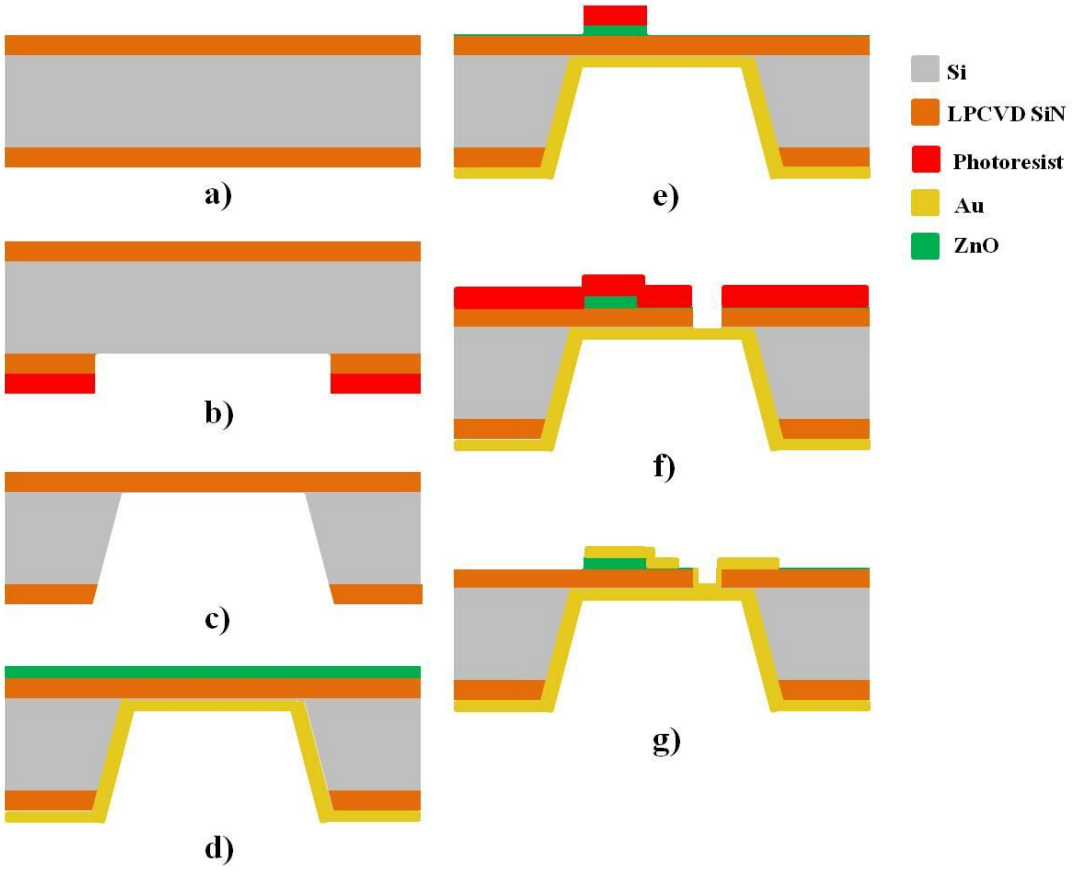

Figure 2.9: A schematic of the fabrication of the FBAR in cross-section. (a) LPCVD SiN is deposited over the entire Si wafer. (b) Photoresist is patterned over an area of silicon nitride (SiN) at the bottom of the Si wafer and the SiN is etched (c) The SiN is used as a mask for the anisotropic etching of the Si. (d) Gold is deposited on the backside of the wafer and ZnO on the top side. (e) Photoresist is patterned overtop the ZnO and the ZnO is wet etched. (f) Photoresist is patterned overtop the SiN diaphragm and a via is etched through the SiN. (g) Photoresist is patterned for liftoff and gold is deposited and lift off performed for the final device structure.

In this structure, 0.6 μm LPCVD SiN is conformally deposited over the entire Si wafer. Next, positive photoresist is deposited on the bottom of the wafer and patterned over the SiN. The SiN is dry etched using RIE and the photoresist removed in acetone. The SiN is used as a mask for the anisotropic wet etching of the Si substrate using a potassium

hydroxide solution. The wet etching ends when the SiN layer is reached. Next, 0.1 µm Au is electron-beam (e-beam) evaporated on the backside. Following that, 0.6 µm ZnO is sputter deposited over the LPCVD SiN on the top side of the wafer. Positive photoresist is deposited and patterned over the top side ZnO. The ZnO is wet etched using a phosphoric acid solution. Next, positive photoresist is deposited and patterned over the top side SiN and a via through the SiN is dry etched with RIE down to the backside gold. Finally, a negative photoresist is deposited and patterned for liftoff on the top side. Gold is deposited via e-beam evaporation and lifted off in acetone creating the final structure and connecting the bottom side gold to pads on the top side. An image of the top side of the FBAR is provided in Figure 2.10.

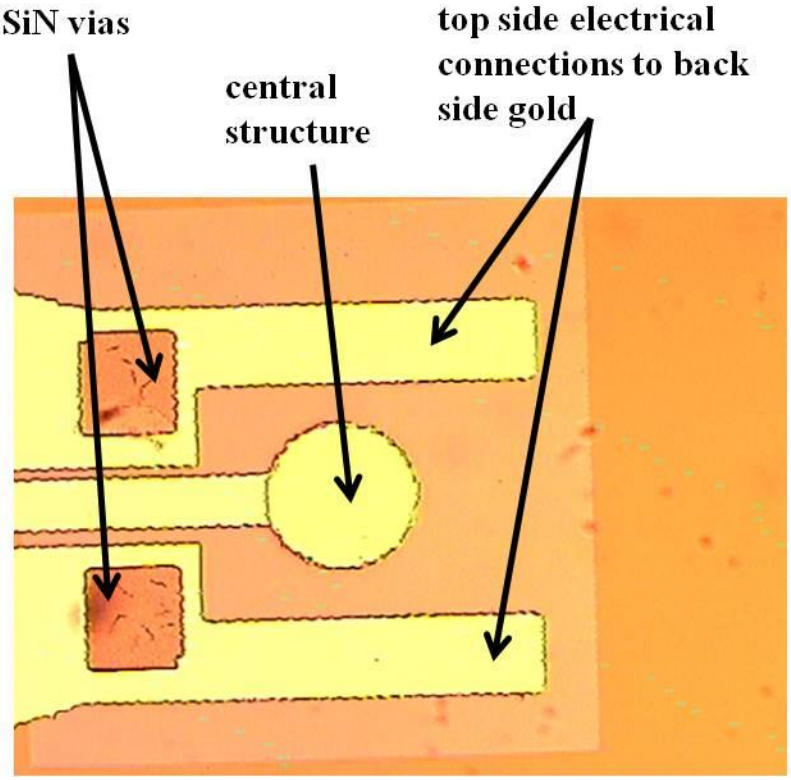

Figure 2.10: Magnified photograph of the top side of the FBAR device deposited over a square diaphragm (seen as the lighter orange color).

The key structure over the diaphragm is metal/insulator/ZnO/metal. Since ZnO is also a semiconductor, the device resembles the MOS-type structure described earlier, however, the deposited ZnO is polycrystalline and therefore the may not operate as such. Capacitance-voltage measurements were attempted on these devices, however, the high frequency necessary to output low-noise capacitance data stimulated the piezoelectric qualities of the ZnO and made the measurements inconclusive.

A number of devices on a single sample were irradiated using the ^{60}Co gamma ray source. Frequency-scattering parameter measurements were made before irradiation and after doses of 20 krad, 100 krad, and 200 krad using an E5071C network analyzer (Figure 2.11). A HCC214S hot chuck system (INSTEC, Boulder, CO) attached to the probe station was employed to maintain a constant temperature of the device during measurement.

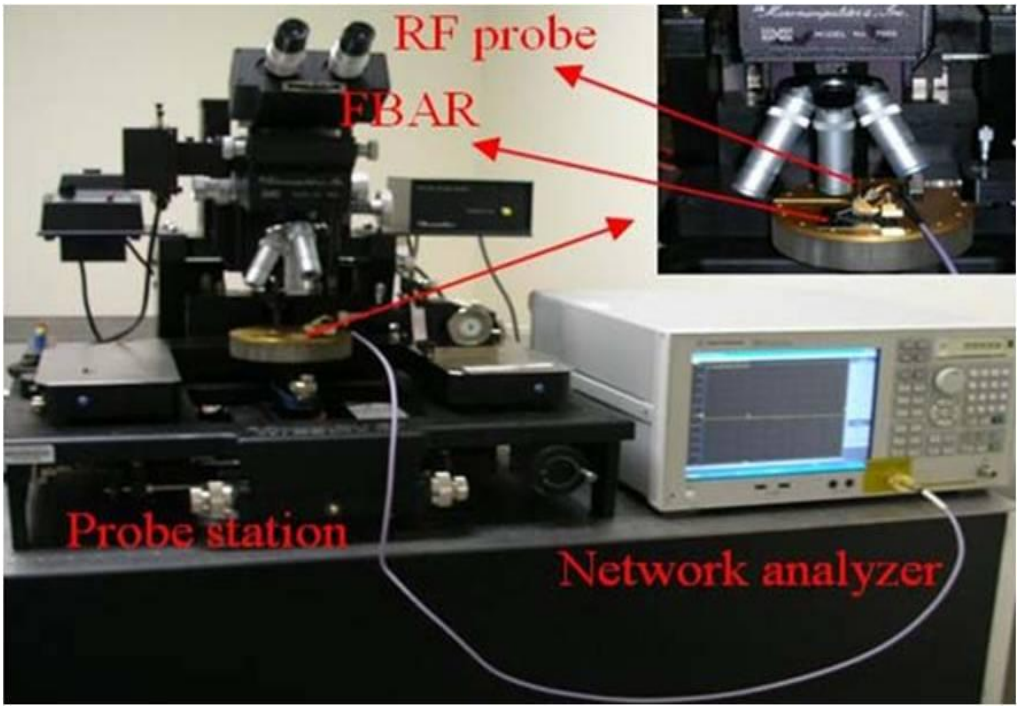

Figure 2.11: Probe station with attached temperature-controlled hot chuck system for performing frequency-scattering parameter measurements with a network analyzer.

In fact, there are two resonant frequencies located on either side of the fundamental resonant frequency described by Eq. 2.5. These two frequencies are the series and parallel resonant frequencies and are caused by the fact that the FBAR acts as a series connection of a resistor, inductor, and capacitor which is in parallel with a resistor and capacitor. The equivalent circuit describing this setup is called the modified Butterworth-Van Dyke (mBVD) model (Figure 2.12).

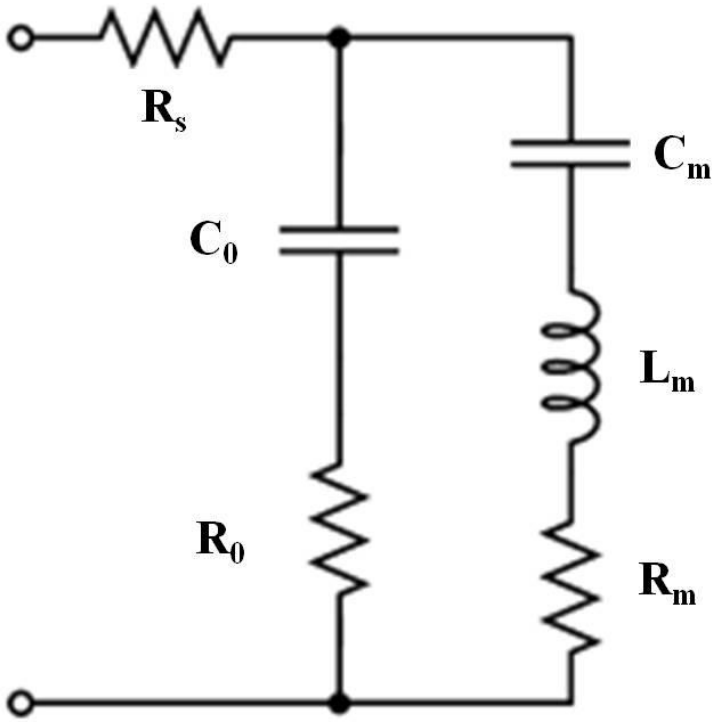

Figure 2.12: Schematic circuit layout for the modified Butterworth-Van Dyke model used to model the FBAR device.

Each of the circuit elements in the mBVD model were extracted following the method in Larson III et al. (2000) for each device before and after all of the ionizing radiation doses. The parallel and resonant frequencies can be determined directly using the S_{11} scattering parameter data.

The results showed that FBAR device parallel and series resonant frequencies decreased due to the ionizing radiation (Figure 2.13).

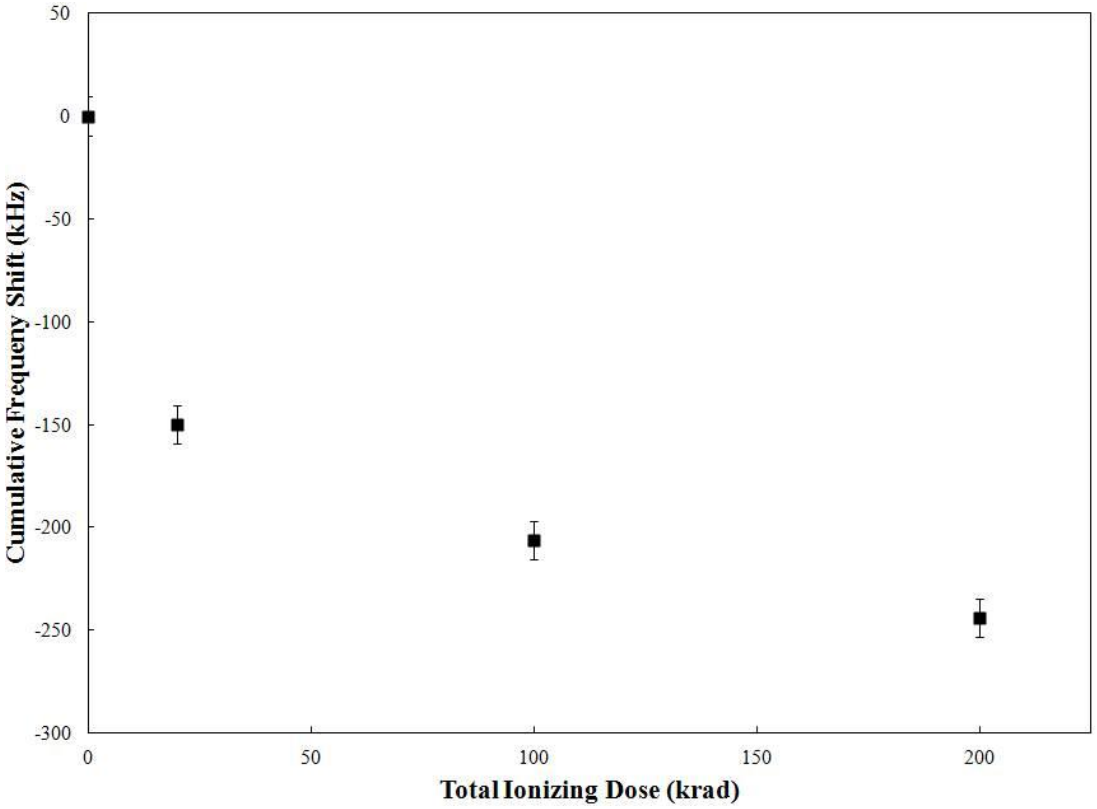

Figure 2.13: Plot showing FBAR cumulative frequency shift with increasing ionizing dose. Error bars represent uncertainty based on resolution of frequency measurement.

The total shift represents about a 100 ppm change in frequency. From the extraction of the mBVD circuit element parameters, it appeared the shift was possibly due to a change in plate capacitance, C_0, of the model. However, the mBVD electrical model is unphysical, meaning that the circuit element changes do not necessarily describe what is physically happening to the device structure. However, based on the possibility that the plate capacitance change was real, a second set of devices were fabricated that would have enhanced sensitivity to radiation from a capacitive standpoint.

The next set of devices that were fabricated used a different type of SiN insulator above the ZnO (forming the insulator-semiconductor pair). The insulator material in contact with the ZnO was changed to plasma-enhanced chemical vapor deposition

(PECVD) SiN since it has more charge-trapping defects than LPCVD SiN (Dun et al. 1981). Defect abundance is higher in PECVD than LPCVD primarily due to the deposition temperature. For LPCVD, the deposition temperature was 830 °C and PECVD deposition temperature was 300 °C. For the low-temperature PECVD, hydrogen-based defects, as well as other defects, are incorporated into the film at much higher levels than in the higher temperature LPCVD. These defects (e.g., SiH bonds) will trap a larger amount of charge than the LPCVD film, which does not incorporate as much hydrogen (Tsu et al. 1986).

The schematic fabrication flow drawing of the second generation FBAR structure is shown in Fig. 2.14.

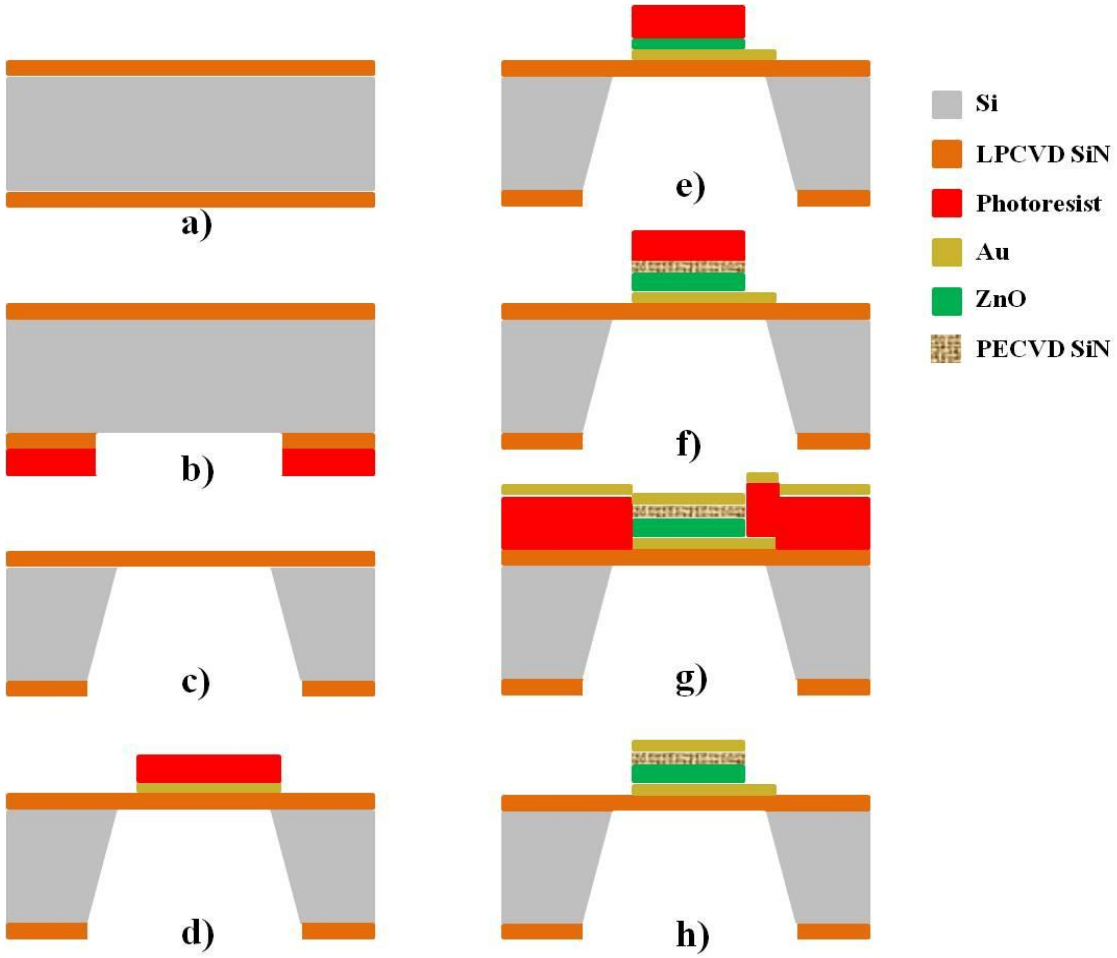

Figure 2.14: A schematic of the fabrication of the second generation FBAR in cross-section. (a) LPCVD SiN is deposited over the entire Si wafer. (b) Photoresist is patterned over an area of silicon nitride (SiN) at the bottom of the Si wafer and the SiN is etched (c) The SiN is used as a mask for the anisotropic etching of the Si. (d) Gold is deposited on the top side of the wafer, followed by photoresist patterning and etching of the Au. (e) ZnO is deposited on the top side of the wafer and photoresist is patterned overtop the ZnO and the ZnO is etched. (f) PECVD SiN is deposited on the top side of the wafer, followed by photoresist patterning and etching of the PECVD SiN. (g) Photoresist is patterned for liftoff and gold is deposited and lift off performed for the final device structure in (h).

In this structure, 1.2 µm LPCVD SiN is conformally deposited over the entire Si wafer.

Next, positive photoresist is deposited on the bottom of the wafer and patterned over the

SiN. The LPCVD SiN is dry etched using RIE and the photoresist removed in acetone.

The LPCVD SiN is used as a mask for the anisotropic wet etching of the Si substrate

using a potassium hydroxide solution. The wet etching ends when the SiN layer is reached. Next, 0.1 µm Au is electron-beam (e-beam) evaporated on the top side. Positive photoresist is patterned over the Au and the Au is wet etched in a potassium-iodide solution. Following that, 1.2 µm ZnO is sputter deposited over the LPCVD SiN on the top side of the wafer. Positive photoresist is deposited and patterned over the top side ZnO. The ZnO is wet etched using a phosphoric acid solution. Next, variable thickness PECVD is deposited on the top side of the wafer and a positive photoresist is deposited and patterned over the top side PECVD SiN the PECVD SiN is dry etched with RIE. Finally, a negative photoresist is deposited and patterned for liftoff on the top side. Gold is deposited via e-beam evaporation and lifted off in acetone creating the final structure and connecting the bottom side gold to pads on the top side. The PECVD thickness of the samples were 0, 0.1 µm, 0.2 µm, and 0.3 µm. An image of the top side of the FBAR is provided in Figure 2.15.

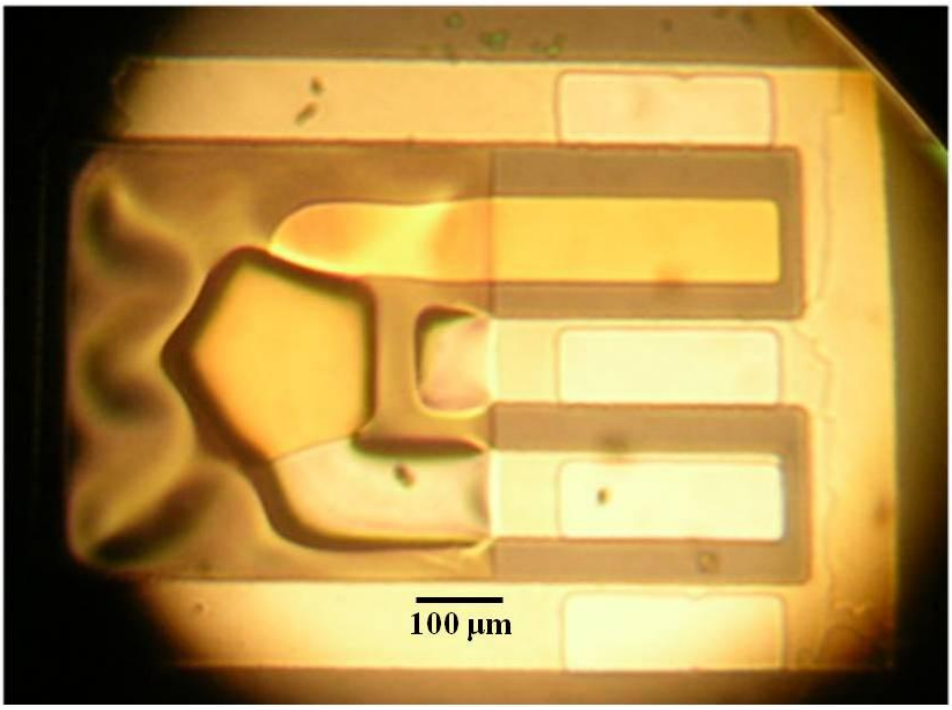

Figure 2.15: Magnified image of the top side of the FBAR device deposited over a square diaphragm. The diaphragm is wrinkled due to stress in the LPCVD SiN.

A number of devices on different sample substrates were irradiated using the ^{60}Co gamma ray source. Frequency-scattering parameter measurements were made before irradiation and after different doses of 10 krad, 20 krad, 40 krad, and 100 krad using the network analyzer and hot chuck system to maintain a constant temperature of the device during measurement. The measured frequency range was increased to allow for measurement of larger frequency shifts due to radiation exposure, however, due to a limit on the number of samples taken across the frequency range, the frequency increment in these tests were too large to resolve the shifts reported from the previous experiment. The data show essentially no clear shift in frequency for the 0, 0.1 µm, 0.2 µm thick PECVD SiN samples. However, the data for three different 0.3 µm devices showed a huge negative shift in frequency of ~23,000 kHz after each of the first two doses (10 krad and

20 krad). No more shifts were seen after the 20 krad dose. For each of the devices, the quality factor, *Q*, changed drastically from ~200-300 before the testing to ~20-50 after the 20 krad dose and stayed at this level after the remaining doses.

The change in *Q* signified that most likely the ZnO was damaged and accounted for the negative resonant frequency shift. However, no explanation could be determined for why the 0.3 μm samples were affected so strongly from the radiation exposure and not the other samples. Damage to the sample containing the devices could not be ruled out although the data and visual appearance of the devices did not appear to show any noticeable damage and the shift appeared over two sets of measurements.

A third set of devices having the same structure as the 2nd generation FBARs were fabricated by a colleague Qian Zhang and had PECVD thicknesses of 0, 0.1 μm, 0.2 μm, 0.3 μm, 0.4 μm, 0.5 μm, and 0.6 μm. Again, the measured frequency range was large so that big shifts in frequency could be seen at the expense of resolving the smaller shifts seen in the first experiment. Measurements were taken before irradiation and after doses of 10 krad, 20 krad, 40 krad, and 100 krad. From this experiment, no clear frequency shifts were seen in all of the devices at any PECVD SiN thickness, thus confusing the previous results.

A more physical representation of the FBAR resonating structure can be realized with the Mason model (Jamneala et al. 2008), which approaches the FBAR from an acoustic impedance perspective. Therefore, changes to the structure in terms of stiffness, density, and even plate capacitance can be simulated. A schematic representation of the model is shown in Figure 2.16.

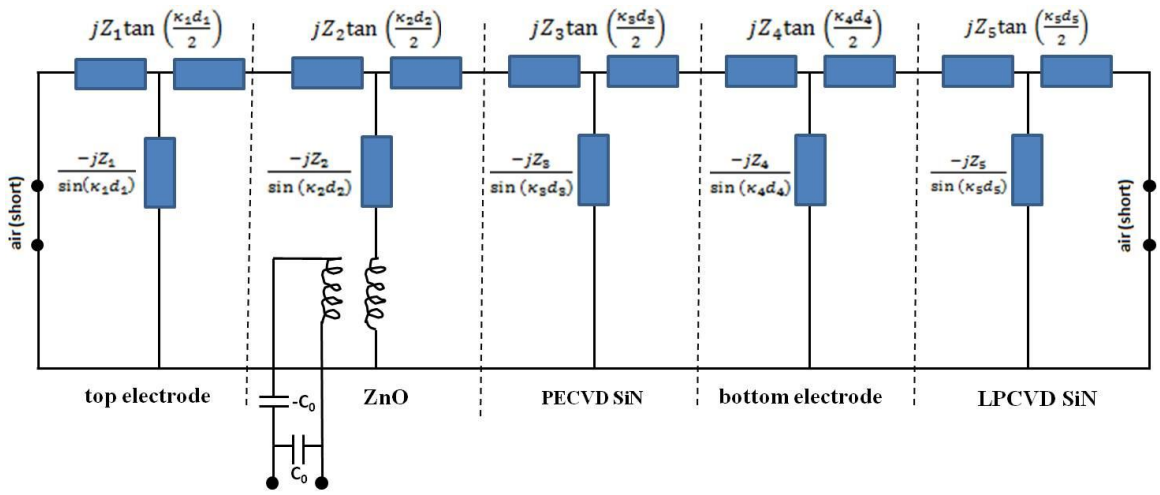

Figure 2.16: Schematic drawing of the FBAR mason model for the 2nd generation device structure.

The blue square elements in the model represent impedances to the acoustic wave and the squiggly lines represent a transformer used to link the mechanical properties to the electrical properties of the device in terms of the parallel plate capacitance. The dashed lines are for appearance and show where each layer of the structure fits within the model.

The Mason model was simulated in Matlab® and shows that changes to the parallel plate capacitance, C_0, do not cause a shift in resonant frequency, but rather a decrease in the S_{11} scattering-parameter impedance magnitude (Figure 2.17). Therefore, radiation-induced changes to the parallel plate capacitance cannot cause the resonant frequency reduction seen in the data.

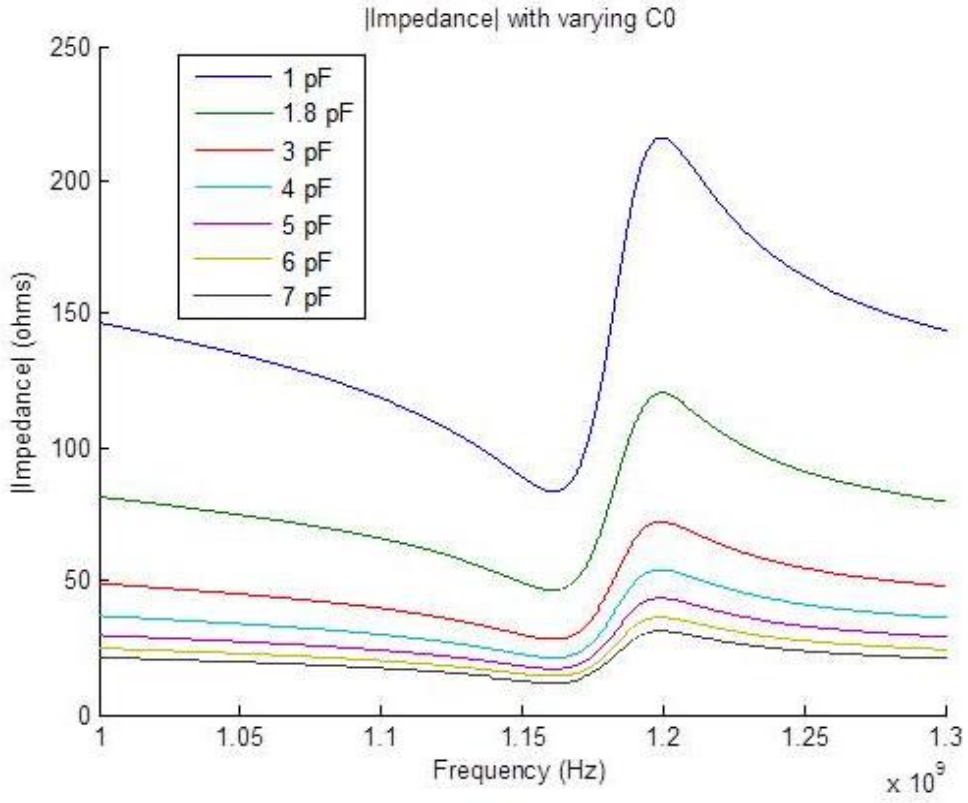

Figure 2.17: Matlab plot of the impedance magnitude of the 2nd generation FBAR for different parallel plate capacitances (C_0) around the series (minimum) and parallel (maximum) resonant frequencies.

Another possibility was that the charges trapped in the SiN layer similar to a DC offset voltage applied to the piezoelectric material. An applied DC voltage would change the stiffness (Young's Modulus) of the piezoelectric material, which in turn would affect the acoustic velocity through the material and thus change the resonant frequency (Aigner et al. 2005). Stiffness changes were applied to the Mason model and the results shown in Figure 2.18.

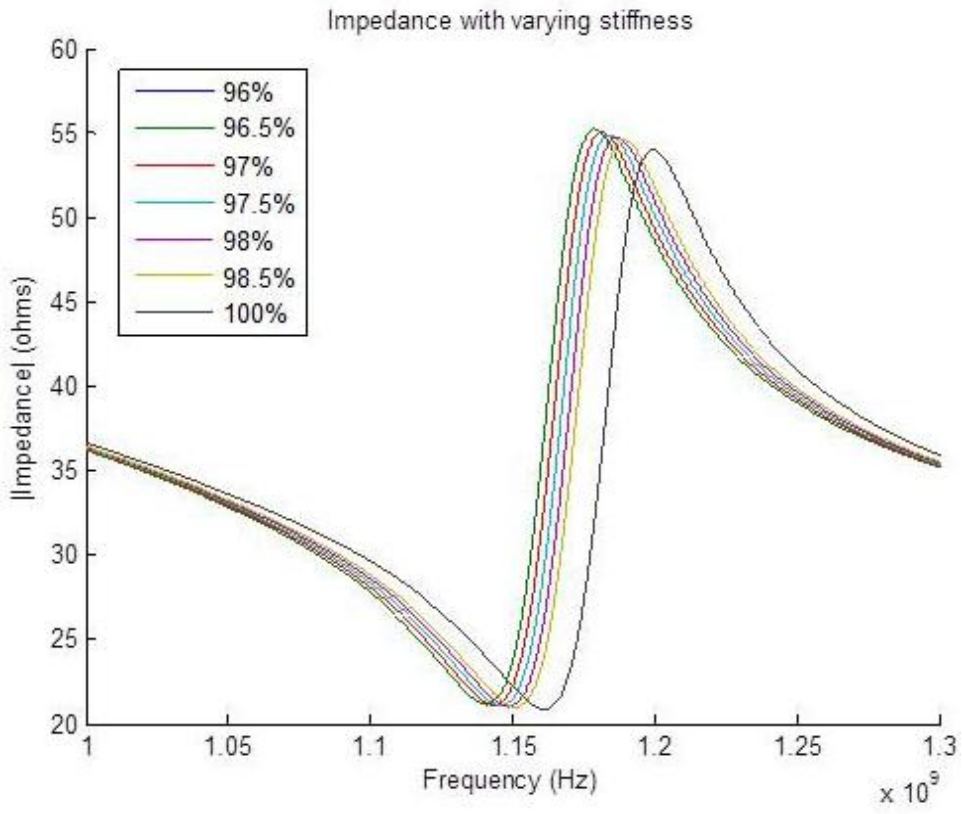

Figure 2.18: Matlab plot of the impedance magnitude of the 2nd generation FBAR for different stiffness (Young's modulus) around the series (minimum) and parallel (maximum) resonant frequencies.

The plot shows that changes to the stiffness can induce a resonant frequency shift. Based on this data, a radiation-induced negative frequency shift would require a corresponding decrease in the film stiffness. To test this concept, the series resonant frequency of a 0.2 µm FBAR device was monitored under an applied DC voltage offset (Figure 2.19).

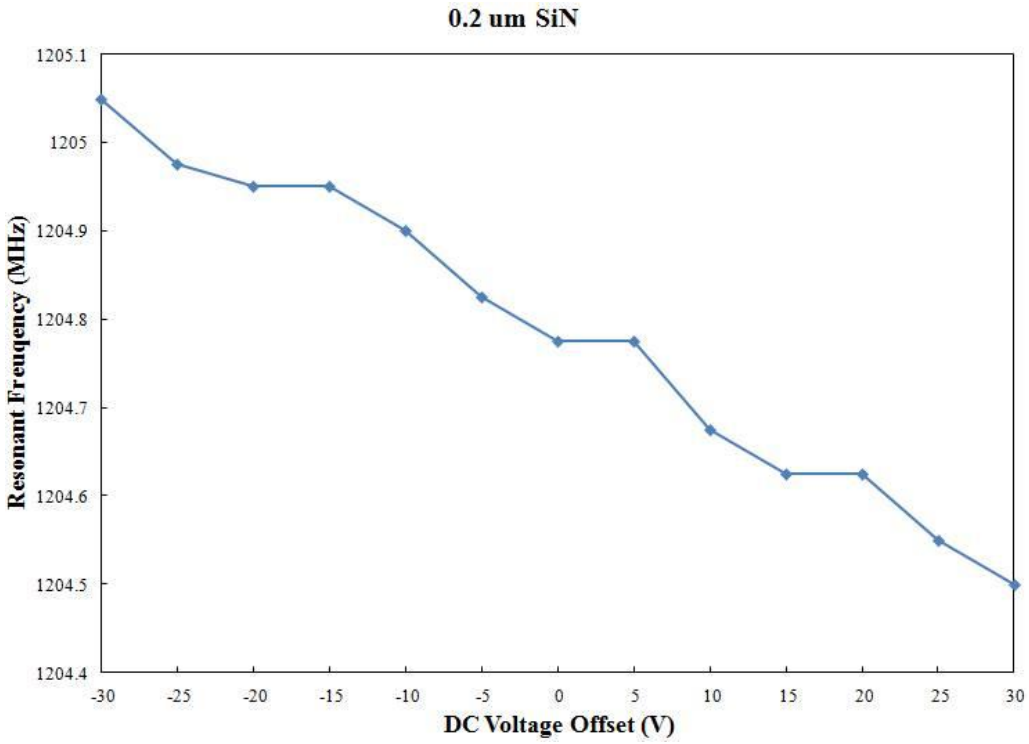

Figure 2.19: Plot showing the decrease in the series resonant frequency for increasing DC voltage offset.

The plot shows that the series resonant frequency of the FBAR device decreases approximately linearly with an increase in applied DC voltage. The frequency change was approximately 8 ppm/V. Therefore, a possible explanation for the first FBAR experiment was that the radiation-induced charge trapped in the insulating SiN acted as a positive DC voltage offset, causing a reduction in the stiffness of the ZnO which resulted in a decrease in the resonant frequency. However, this method cannot explain the results from the second experiment with the huge frequency shift and Q degradation and the cause of that result remains unknown.

2.3 Conclusion

Ionizing radiation sensing is important for characterizing harsh environment effects on biology and electronics. Two different ionizing radiation dosimeters were

developed. One device was a passive sensor based on an antenna-MOSCAP design where the MOSCAP was sensitive to ionizing radiation. The radiation-induced decrease in the capacitance changes the resonant frequency at which the antenna radiates. The second device was an active sensor based on a film bulk acoustic wave resonator. The most likely explanation causing the radiation shift seen in the first experiment is due to a stiffness change caused by the voltage offset of the radiation-induced trapped charge in the SiN layer.

CHAPTER 3: MEMS TEMPERATURE SENSOR ARRAYS

Hydrothermal ecosystems are some of the most naturally harsh environments on Earth. Hot springs occur when meteoric water is circulated through hot rock; typically, this rock surrounds magma chambers associated with volcanically or tectonically active regions. The water is delivered back to the surface at very high temperatures (often boiling; i.e., near 100 °C). Large amounts of emerging water can form source pools. Water that rises above the rim of the source pool can spill out and form an outflow channel that carries water away from the source (Figure 3.1). These outflow channels host an enormous collection of diverse organisms, from chemosynthetic microbes in the hottest zones nearest the source to photosynthetic bacteria and eukarya in lower temperature regions farther away from the source.

Figure 3.1: Photograph of hot spring source pool and outflow channel at Yellowstone National Park.

The hot spring environments are of immense interest to scientists for a number of reasons. From a biological standpoint, some of the organisms found in the hot springs

may be genetically similar to the first life to appear on the Earth. Oxygen isotope data (Knauth and Lowe 2003) point to the fact that the early Earth oceans may have been significantly warmer - gradually cooling to current temperatures. Additionally, ancestral elongation gene studies (Gaucher et al. 2010) are used to argue that the organisms hosting these genes lived in environments that progressively cooled from the Archaean to the present. Results from gene studies and isotopic studies both predict similar temperatures. The genetic diversity seen in these hot springs is much higher than that of almost any other environment found on Earth (Barns et al. 1994). Researchers investigate these organisms to understand aspects of genetic evolution such as gene transfer to and compare and contrast organisms found in adjacent hot springs. The hot springs are also interesting from a geochemical perspective. These hot springs are locations of fluid mixing, dynamic cooling, as well as mineral dissolution and precipitation. The focus of this research, then, is to understand the interplay between the geochemical environment and the appearance of certain types of biology. The biology that thrives in the hot spring does so because it can most effectively utilize the molecules and ions available in the water or sediment (Shock et al. 2005).

Measurements of the chemical and physical properties of the hot spring are therefore critical for understanding the biogeochemical environment. Data such as pH, conductivity, and temperature can be used to calculate the energetics of metabolic processes (Amend and Shock 2001). However, conducting research in the hot springs is challenging. Measurements are taken in water where temperatures can reach boiling and the pH can be anywhere from <2 to >9 (however, any individual hot spring will either be acidic or alkaline). The geochemical parameters of the water are very dynamic and can

change over short length scales. Additionally, hot spring outflow channels can become very narrow and shallow as they transport water away from the source making it difficult for large instruments to take measurements.

These combined conditions make this harsh environment highly specialized and requires costly instrumentation to determine the geochemical properties of the fluid. Most of the existing geochemical information comes from bulk sampling of fluids, sediments, and gases. However, in many cases, the amount of water, sediment, or soil samples needed for laboratory analysis is larger than the length-scale over which the changes occur. In hot springs, high spatial resolution is necessary to characterize the sharp transitions between high-temperature regions that support chemoautotrophic organisms and lower-temperature portions that support photosynthetic organisms or between different photosynthetic microbial communities, many of which can be distinguished by a sharp change in color (Figure 3.2).

Figure 3.2: *(left)* Photograph of water from a boiling spring (upper right, dark blue) flowing toward the viewer. Total width of outflow channel is ~1.5m. Note the sharp transition in the appearance of photosynthesis where color changes from off-white to bright green. (*right)* Photograph of different zones of photosynthetic microbes. Different communities can be distinguished by the sharp change in colors from orange to yellow to green.

Transitions at the photosynthetic fringe not only have a dramatic appearance, but also can be accompanied by extreme changes in microbial communities. These transitions can occur in <1 cm, which is too small a spatial scale for measurement with current bulky commercial instruments. Long duration measurements are also important because these ecosystems are not isolated from external effects (e.g. weather) that can change flow parameters and concentrations of the chemical constituents within the spring through dilution by rainwater. The questions driving the development of the MEMS temperature arrays are: *Is temperature the key variable responsible for the transition to photosynthesis or appearance of different photosynthetic communities in hot spring outflow channels?* Temperature and pH have been explored to address the transition between where photosynthesis first appears (Cox et al. 2011). Temperature and pH sensors were placed

on either side of these transitions zones and the data were used to generate the plot shown in Figure 3.3. Clearly, both temperature and pH play a role. However, the sizes of these sensors do not allow measurement across the sharp transition zone. Therefore, one may ask: *Is the temperature gradient across the photosynthetic boundary linear or does it resemble a step function as is assumed with Figure 3.3?* Furthermore, Cox et al. (2011) did not address the characteristic causing the change in appearance of adjacent but visibly different photosynthetic communities. Finally, most of the measurements taken at the hot spring sites are singular in location and time. These measurements are like a snapshot of the hydrothermal system. However, we know that these systems are dynamic in and of themselves and are also affected by extraneous input such as the weather. *How dynamic are hot spring environments over short and long periods of time?*

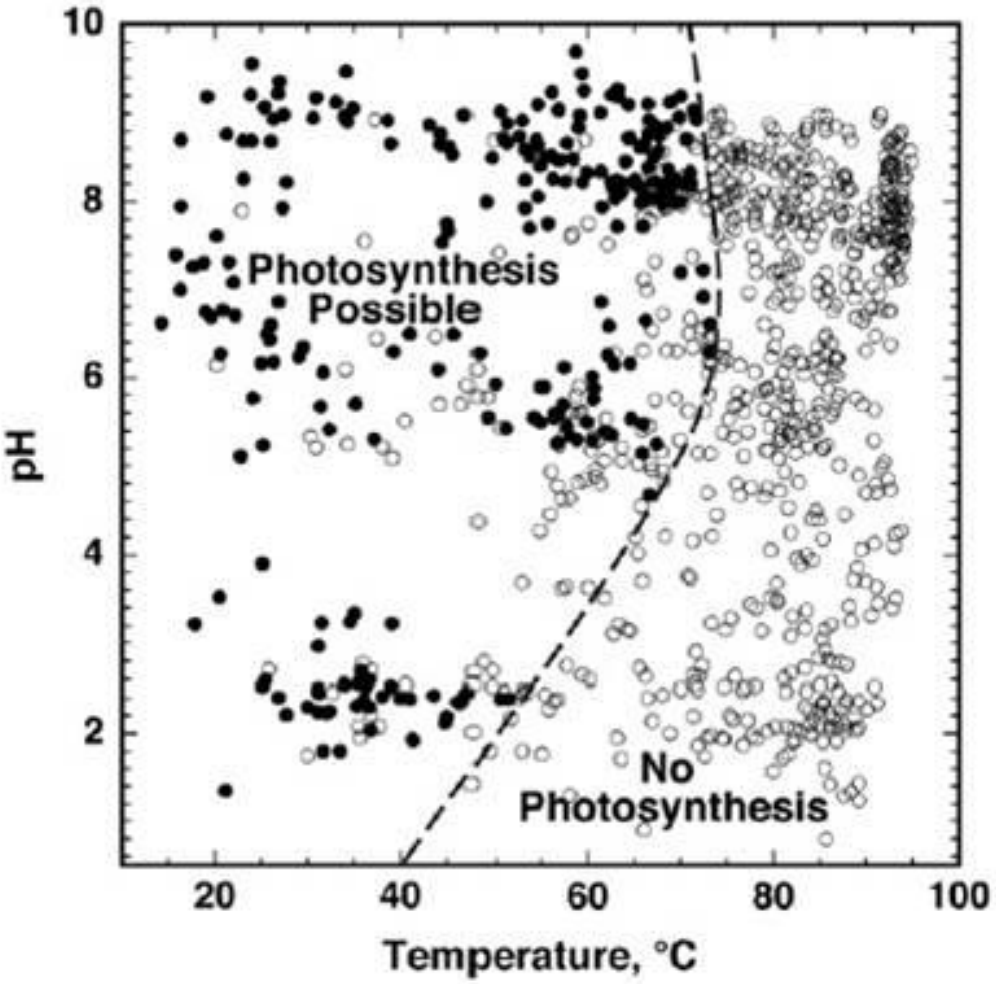

Figure 3.3: Plot from Cox et al. (2011) showing the dashed curve where the transition to photosynthesis occurs as a function of pH and temperature. Filled circles indicate locations where photosynthetic pigments were visible. Open circles indicate locations where no photosynthetic pigments were visible.

With recent advances in materials and fabrication techniques, MEMS temperature sensors can be developed to be both chemically and thermally-tolerant to the conditions present in the hot springs. The small size of the sensing elements (micron scale) provides the high spatial resolution necessary to interrogate the sharp transition zones between the chemotrophic and photosynthetic communities. Moreover, MEMS sensors have high temporal resolution on the order of milliseconds and low drift for long period measurements. Due to the ability to batch fabricate sensors, an array of temperature

sensors can be deployed throughout the hot spring, providing the capability to perform simultaneous mapping of the environment.

3.1 Resistance Temperature Detectors

Sensors incorporating MEMS technology have been developed previously for measuring temperature (Clayton 1988). One class of temperature sensors, known as, resistance temperature detectors (RTDs) are a mature technology and are ideally suited for this application due to the small size, low power, robustness, and simple design. The basic principle behind the RTD involves passing a known current (or voltage) through a resistor (made of any temperature sensitive material) that changes resistance with temperature. By measuring the voltage drop (or current) across the resistor, the resistance can be determined by Ohm's Law:

$$V = IR, \qquad \text{(Eq. 3.1)}$$

where I is the current passing through the resistor R and V is the voltage drop measured across the resistor.

The physics that explain why a material will change resistance with temperature are straightforward. As electrons pass through a material, they are passed from one atom to the next. Sometimes those electrons will collide with an atom. When that happens, the kinetic energy of the electron is transferred to the atom which then vibrates. The electron will gain its kinetic energy back as it accelerates under the force of the electric field until it slams into another atom. The more atoms 'in the way' of the traveling electron, the more the electron is impeded from its flow. The measure of a material's ability to impede electron flow is defined as its resistance. Temperature, on the other hand, is a measure of the amount of vibration of an atom. As a material is heated, its atoms will have higher

vibration amplitudes and therefore will collide more frequently with electrons and impede their flow which is tantamount to having a higher resistance. Since resistance is also function of the length of a material, the more appropriate material property to discuss is resistivity, which is the material resistance per unit length.

The resistivity of a specific material is a function of temperature. For a given material, the characteristic equation describing the temperature dependence (for T > 0 °C) of its resistivity over a particular temperature range is given by the Callendar-van Dusen equation:

$$\rho = \rho_0[1 + AT - BT^2], \quad \text{(Eq. 3.2)}$$

where ρ is the material resistivity (resistance per unit length) at a given temperature T, ρ_0 is the bulk resistivity of the bulk material (thick film) at 0 °C, and A and B are constant coefficients, typically determined empirically (Lacy 2011). At temperatures below 0 °C, the material temperature dependence equation is given as:

$$\rho = \rho_0[1 + AT - BT^2 - C(T - 100)T^3], \quad \text{(Eq. 3.3)}$$

where an additional temperature term is required (Estrada 1990). The main considerations for choosing an RTD material are linearity in resistance change with temperature, high sensitivity to temperature, and compatibility with MEMS fabrication. Based on these driving forces, metals are often chosen as the resistor material due to their high linearity over a wide range of temperatures. For metals such as platinum (Pt) and nickel (Ni), the quadratic coefficient B is negligibly small over a large temperature range (ΔT_{Pt} > 800 °C; ΔT_{Ni} > 300 °C), making these metals highly linear. Additionally, at temperatures below 0 °C, both the nickel and platinum metal C coefficients are negligible safely through -50 °C for nickel and -200 °C for platinum (Trietley 1986). Using metal resistors in the operating

temperature range for hot spring measurements, the Callendar-van Dusen equation can then be rewritten as:

$$\rho = \rho_0[1 + \alpha(T - T_0)], \quad \text{(Eq. 3.4)}$$

where ρ_0 is now the bulk resistivity at the temperature T_0, and the coefficient A from is now rebranded as α, and is defined as the temperature coefficient of resistivity or resistance (TCR). Rewriting this equation in terms of the resistance, R, gives:

$$R = R_0[1 + \alpha(T - T_0)], \quad \text{(Eq. 3.5)}$$

where R_0 is the resistance at T_0. Rewriting the equation by setting R - R_0 = ΔR and T - T_0 = ΔT, the RTD sensitivity is:

$$\Delta R/\Delta T = R_0\alpha, \quad \text{(Eq. 3.6)}$$

therefore, the TCR and the R_0 value determine the sensitivity of the RTD. For platinum and nickel, the TCRs are ~3900 ppm/°C and ~6400 ppm/°C, respectively (Belser and Hicklin 1959). Although nickel has the higher TCR, platinum is used almost exclusively in commercial MEMS RTDs due to its almost perfect linearity over a much larger range of temperatures and has greater thermal stability compared to nickel.

While the bulk resistivity, ρ_0, is constant over the given temperatures ranges, ρ_0 will take on different values depending on the metal layer (film) thickness and film quality. Specifically, the bulk resistivity of a material is governed by a number of factors including film thickness, grain size, and thermal expansion mismatch between metal film and substrate. Along with film thickness, the fabrication process can affect the film grain size diameter, which is affected by parameters such as deposition chamber pressure, substrate temperature during deposition, and the rate of deposition (Singh 1973). Due to

all of these process-related factors, fabricated RTDs have TCRs significantly lower than the bulk values.

Since the sensitivity is also dependent on R_0, it may seem prudent to design an RTD with very high resistance to get high sensitivity. While this is true, the major issue involved with using large resistors as RTDs is self-heating, otherwise known as joule heating. The power input to a resistor is the product of the current through the resistor and the voltage drop across it. The power equation in terms of the resistance can be rewritten using a simple substitution from ohm's law:

$$P = IV = I^2R. \quad \text{(Eq. 3.7)}$$

From this equation, it's clear that with a constant current flow, a larger resistor will consume more power. For a resistor, the power consumption results in the generation of heat. The heat generated in the resistor will be dissipated to the surroundings. To get an idea about the effects of joule heating, a simple model can be created. For this model, the heat dissipated in the resistor is removed to the water environment through convection. The convective heat transfer equation can be written in the form:

$$P = hA\Delta T, \quad \text{(Eq. 3.8)}$$

where P is the power dissipated by the resistor to the ambient environment, h is the convective heat transfer coefficient, A is the surface area over which the heat is convected, and ΔT is the temperature difference between the resistor and the ambient environment. If a typical current of 100 μA is passed through a resistor of 1000 Ω, the power is 10 μW. If this power is dissipated over a resistor of typical surface area 100 x 100 μm^2, and the desired self-heating needs to be kept to 0.1 °C or less for measurement accuracy, then the convective heat transfer coefficient between the sensor and

environment needs to be 10,000 W/m^2-°C at a minimum. For free or forced convection in water, the heat transfer coefficient is on the order of a few thousand W/m^2-°C; therefore, joule heating can be a significant constraint in RTD design. Reducing the power dissipated through the resistor by decreasing the current is possible; however, measuring very low voltage drops can be difficult due to the noise in the system. Fortunately, heat can be dissipated through the substrate on which the resistor is fabricated. A substrate such as silicon (Si) has a high thermal conductivity and therefore reduces the amount of joule heating. However, the high thermal conductivity of silicon poses another problem that will be discussed later.

3.2 Silicon Substrate RTD Arrays

To address questions about the role of temperature in the transition to photosynthesis and between adjacent photosynthetic communities, a temperature array was designed that incorporated a linear arrangement of RTDs at spatial separations of 5 mm. Due to a limit of the data acquisition technology (to be discussed later), 15 different RTDs were used in each array. Each RTD was designed as a meandering resistor. The metal chosen for the RTD was platinum because of its excellent linearity and high TCR. In targeting a resistance of approximately 1500 Ω (for high sensitivity with minimal joule heating effects), a typical thickness around 100 nm, and a line width of 10 μm for ease of fabrication, then the overall length of resistor is ~15000 μm which is why the meandering shape is utilized to maintain a small footprint so as to measure temperature at a 'point-source' location.

After each array is fabricated, wires must be connected from the array to the data acquisition device which provides the input voltage and measures the corresponding

voltage drop across the sensors. The easiest way to connect the external wires was to solder them to large bond pads fabricated on the RTD array. Soldering involves bonding two separate metals together through the use of a third metal that is melted with a soldering iron and which adheres to the other two metals. The bond pads are rectangular areas of copper metal that must be at least as wide as the diameter of the wire for successful soldering. The bond pads for each RTD were located adjacent to one another along the bottom of the array to keep the array as flat as possible. Thick (300 nm) copper leads were fabricated on the array to connect the RTDs to the bond pads and provide minimal resistance ($< 20\ \Omega$) contribution to the overall RTD resistance. Thin external wires (AWG 30) were utilized to maintain small bond pads and therefore keep the width of the array to a minimum. To limit the number of wires soldered to the array, each RTD was connected to a shared ground connection.

The fabrication flow process of the temperature array is depicted schematically in cross-section in Figure 3.4.

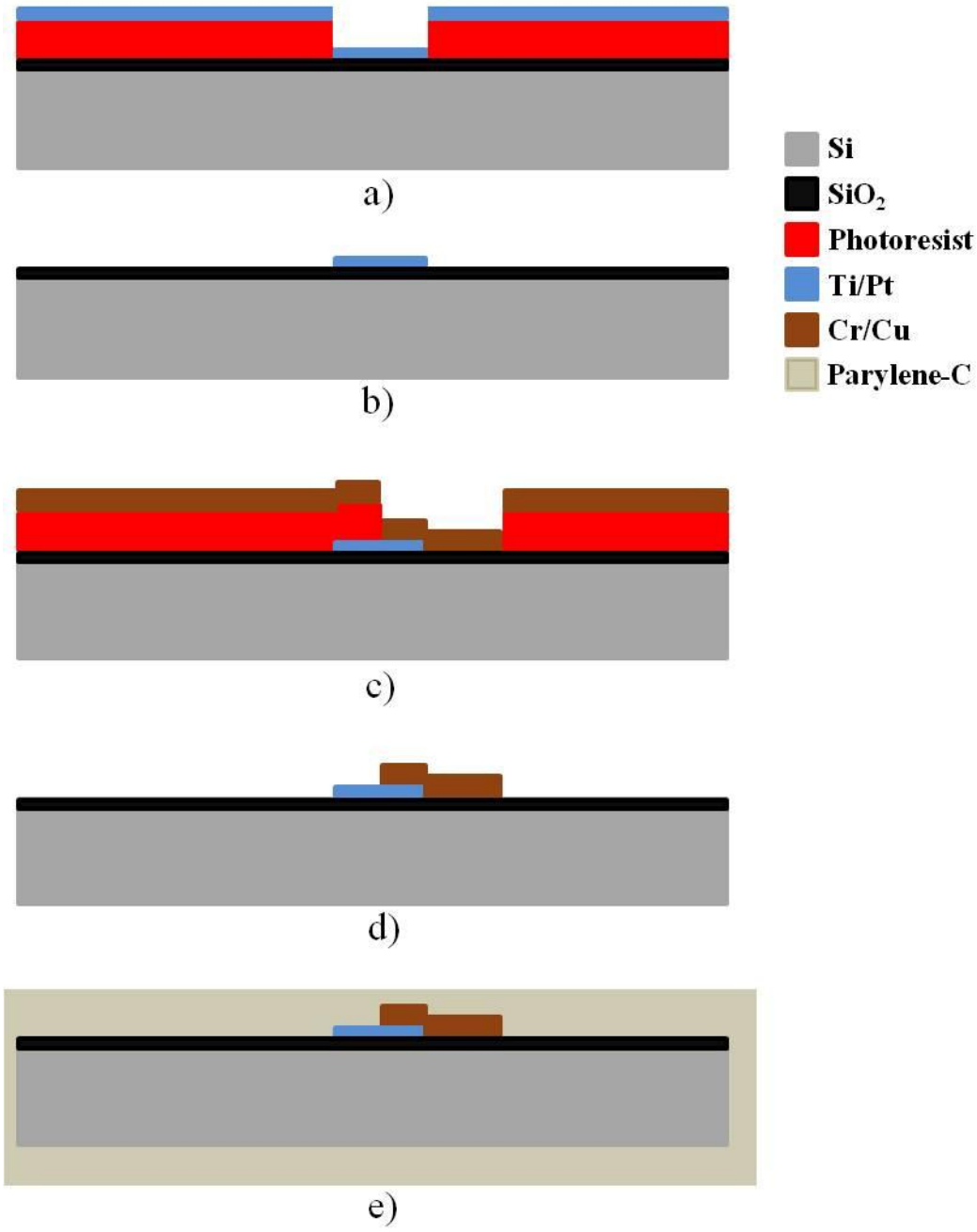

Figure 3.4: A schematic of the fabrication of the silicon substrate temperature array in cross-section. A layer of Ti/Pt is deposited and patterned on the Si wafer to create the resistor in (a) and (b). Next a layer of Cr/Cu is deposited and patterned to create the bond pads and leads connecting pads to the resistors in (c) and (d). Finally, Parylene-C is deposited over the entire wafer in (e).

In the first step, a 250 nm layer of silicon dioxide (SiO_2) is deposited on top of the silicon

(Si) wafer via chemical vapor deposition in order to electrically insulate the resistor from

the silicon semiconductor substrate. Next, a negative photoresist is deposited and the meandering resistor geometry is patterned on top of a bare silicon (Si) wafer. Then, a 15 nm layer of titanium (Ti) is deposited followed by a 100 nm layer of platinum (Pt) using electron-beam evaporation. The thickness was chosen to create a ~1500 Ω resistor. The titanium layer provides stronger adhesion between the platinum and the silicon surface. After metal deposition, the wafer is immersed in acetone in order to dissolve the photoresist which lifts-off metal on top of it. Another layer of negative photoresist is deposited on top of the existing structure and patterned to designate the location for the bond pads and the leads connecting the meandering resistors to the bond pads. Next, a 20 nm layer of chromium (Cr) is deposited followed by a thick 300 nm layer of copper (Cu). The thick copper is necessary in order to contribute very little overall resistance to the RTD (~1 %). Following the last metal deposition, the wafer is prepared for Parylene-C deposition. Parylene-C is an electrically insulating transparent polymer with excellent chemical resistance and extremely low water leakage rate. This material is used to prevent the electrical components from shorting in the water and to protect the array materials from chemical attack in the hot springs. To create a strong bond between the Parylene-C and wafer, the wafer is immersed in an adhesion promoter wet bath of A-174 silane and isopropyl alcohol. Following this step, the wafer is placed in the Parylene deposition chamber and undergoes a 5 μm thick deposition. The final step (not shown in the figure) is to deposit and pattern positive photoresist over the bond pads and remove the Parylene-C over top the bond pads using a dry O_2 plasma etch.

Following the cleanroom fabrication the wafer is diced using a dicing saw – creating four separate 15-sensor arrays. Next, wires are soldered to the bond pads for

each resistor and the ground plane. Since the wires are often exposed to the hot spring environment, a wire sheathing made from polytetrafluoroethylene (PTFE), also known as Teflon, which has very high temperature tolerance and high chemical resistance was used. The bond strength between the wire and bond pad is still weak after soldering; a strong tug can remove the wire from the device. Therefore, a semi-chemically-resistant epoxy with high temperature tolerance (Epoxy Technologies, H77 Epoxy) is poured over top the solder connections and cured at 60 °C overnight. Finally, the entire array with wires is coated in another 20 μm of Parylene-C for added chemical and water-leakage protection (Figure 3.5).

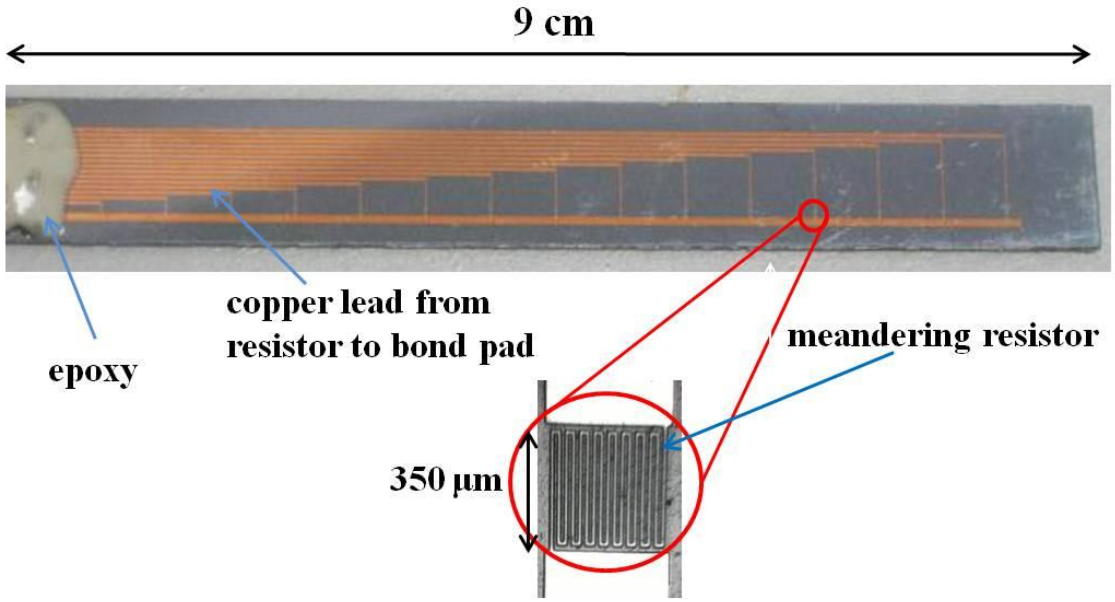

Figure 3.5: The top photograph shows a silicon substrate temperature array. Copper leads connect the RTDs to the bond pads at the bottom of the sensor (left). After soldering wires to the bond pads, the area is covered in an epoxy for stronger adhesion. The bottom photograph shows a magnified view of one of the 15 fabricated RTDs.

Since the RTDs ultimately provide a measure of resistance, the array must be calibrated so that every resistance measurement corresponds to a particular temperature. Typical calibration involves using a temperature-controlled water bath. For this initial

calibration, a lack of access to a water bath required that a glass dish filled with water and heated by a hot plate was used. The temperature of the fluid was monitored using a high-precision thermocouple. Since the water was heated from below, before measurements were taken, the hot plate was turned off and the water stirred until well mixed. Water has a high heat capacity and therefore has good temperature stability. Temperature and resistor measurements were recorded every 2 minutes. An example calibration showing five simultaneous RTD measurements is shown in Figure 3.6. Calibration curves were generated for each sensor and all had very high linearity ($R^2 > 0.999$). The curves were fit with linear trendlines and the equations were used to provide real-time *in-situ* monitoring. The relatively large resistance difference between different RTDs was unexpected but seen in every fabricated array. This difference is attributed to fabrication process variations (e.g., deposited metal thickness) across different locations of the wafer. An optimized fabrication process with commercial-grade equipment and process capability would remove these variations. The average TCR for these RTDs was only 450 ppm/°C. For bulk platinum, the TCR is ~3900 ppm/°C. The low TCR value is attributed to both the thin (100 nm) layer of platinum as well as the process conditions leading to small grain size as discussed earlier.

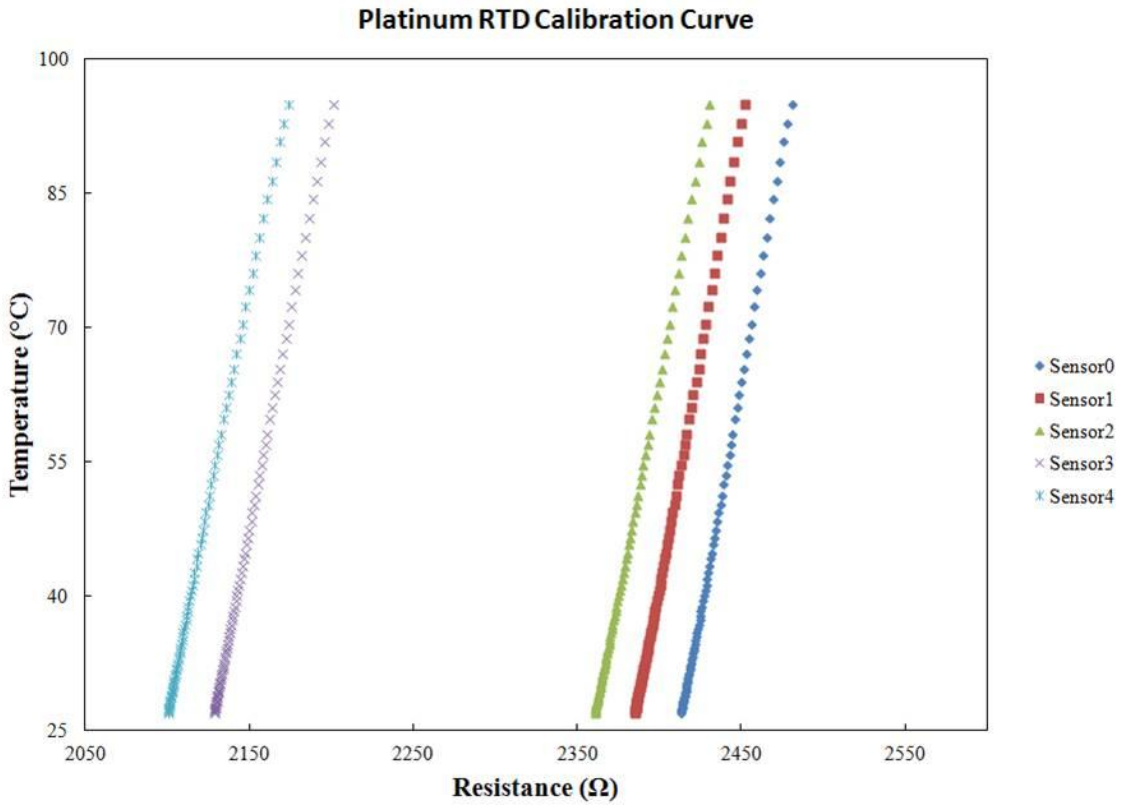

Figure 3.6: Silicon substrate temperature array calibration curve showing five platinum-based RTDs. Arrays were calibrated in water between the ranges of temperature expected in the hot springs.

3.3 Printed Circuit Board-based RTD Arrays

Another type of temperature sensor array was designed and built incorporating commercially fabricated RTDs from Omega Engineering, Inc. Similar to the cleanroom fabricated devices, the commercial RTDs are fabricated using a meandering resistor geometry and made from platinum (Figure 3.7). The RTDs are sold individually and have a resistance of 1000 Ω at 0 °C. The TCR of these sensors matches that of bulk platinum ~3900 ppm/°C.

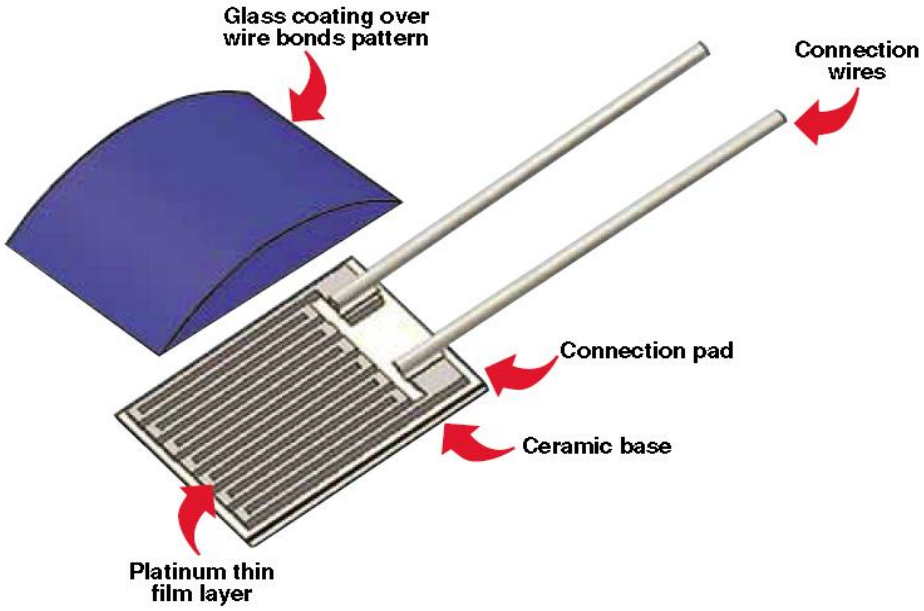

Figure 3.7: Diagram of commercial platinum RTD used in temperature array. Image courtesy of Omega Engineering, Inc. The RTD is 2mm on a side.

In order to create a temperature array, a printed circuit board (PCB) layout was designed to hold 15 of these commercial RTDs at spatial intervals of 1 cm. The PCBs were ordered through a company called ExpressPCB. Similar to the cleanroom devices the PCB arrays were designed with bond pad wire connections at the bottom of the array. Again, wires were soldered to the array and the pads were covered in the same epoxy to increase the bond strength. Following the epoxy cure, the PCB arrays were coated with a layer of 20 μm thick Parylene-C. Again, the PCB arrays must be calibrated to relate temperature to the measured resistance. As seen in the calibration curve (Figure 3.8), the advantage of using the commercial RTDs over the cleanroom fabricated RTDs is the sensitivity due to the high TCR. The disadvantage is the size. The RTD packaging is 2 mm x 2 mm and including the leads makes it difficult to have separations any less than the 1 cm used in the array.

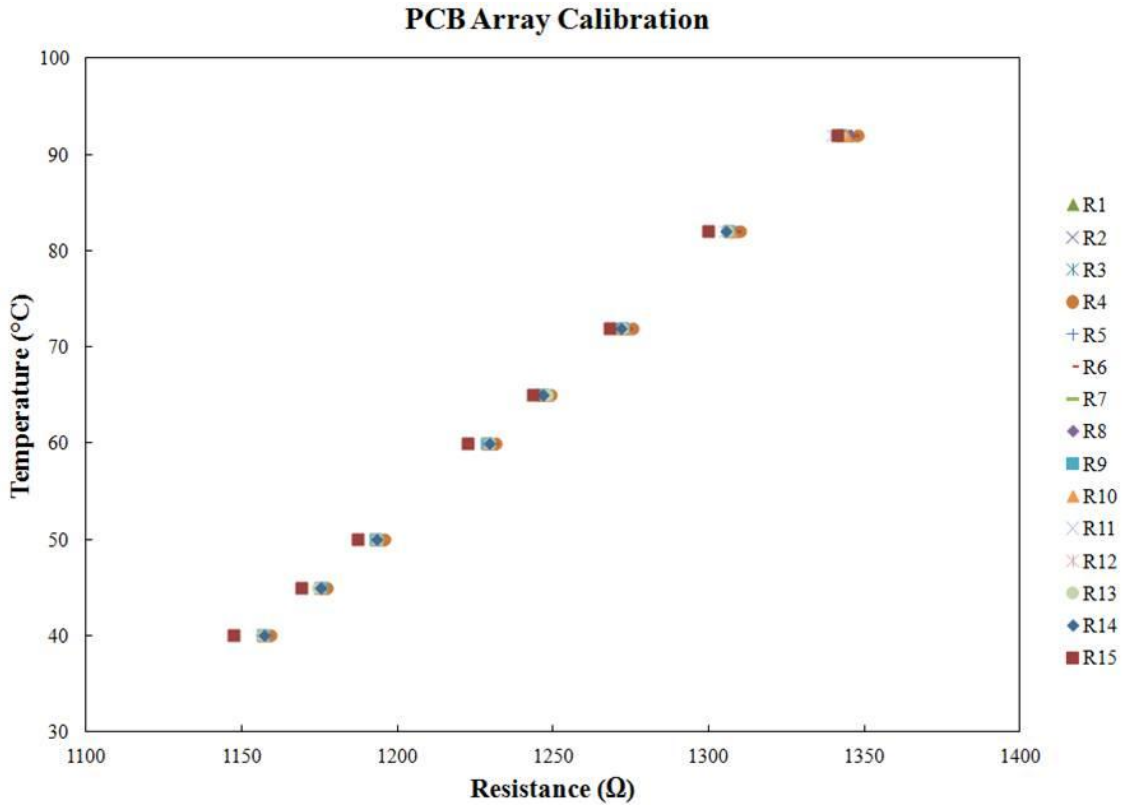

Figure 3.8: Printed circuit board temperature array calibration showing 15 commercially purchased (Omega Engineering, Inc.) platinum-based RTDs. Arrays were calibrated in water between the ranges of temperature expected in the hot springs.

3.4 Comsol Multiphysics Modeling

The motivation behind modeling the RTD array was due to the fact that, qualitatively, the silicon substrate array seemed to measure *in-situ* temperature gradients between adjacent RTDs smaller than what was measured when the array was lifted up and set back down at the same separation. The silicon substrate RTD array was modeled in Comsol Multiphysics® with the heat transfer package. Comsol Multiphysics® is a finite element analysis software package for engineering and physics applications. An array consisting of four RTDs separated by 5 mm were modeled using a 2-D simulation of the device cross-section. The model consisted of a 500 μm silicon substrate with a 500 nm layer of silicon dioxide (insulator) on top with 500 nm thick platinum metal (resistor)

on top of that followed by 20 μm thick Parylene-C covering the platinum. Four different reservoirs of water at temperatures of 45 °C, 55 °C, 65 °C and 75 °C were placed above and below each of the four RTDs to simulate a temperature gradient in the hot spring (Figure 3.9).

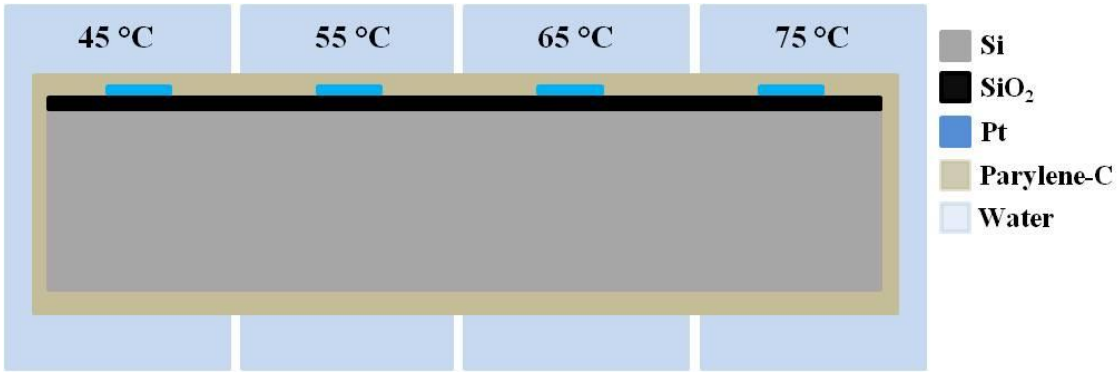

Figure 3.9: Schematic of silicon substrate RTD array simulated with Comsol Multiphysics® heat transfer package (not to scale).

The results of the simulation indicate that at steady state none of the RTDs measure the temperature of the water reservoir that they sit beneath. This is due to the fact that silicon has a very high thermal conductivity coefficient of ~150 W/m-K (Hopkins et al. 2011) which is more than two orders of magnitude higher than the Parylene-C and silicon dioxide. The metal resistors located below the cooler water reservoirs ended up warmer and the resistors below the warmer reservoirs ended up cooler (Figure 3.10). Varying the thickness of the silicon dioxide or the Parylene-C had no effect. Additionally, the model was run where the silicon directly below each resistor was removed (this can be done in fabrication with deep reactive ion etching), but no change was seen because most of the silicon thermal mass was not removed. Removing most or the entire silicon substrate is not possible due to the fact that this makes the array very fragile.

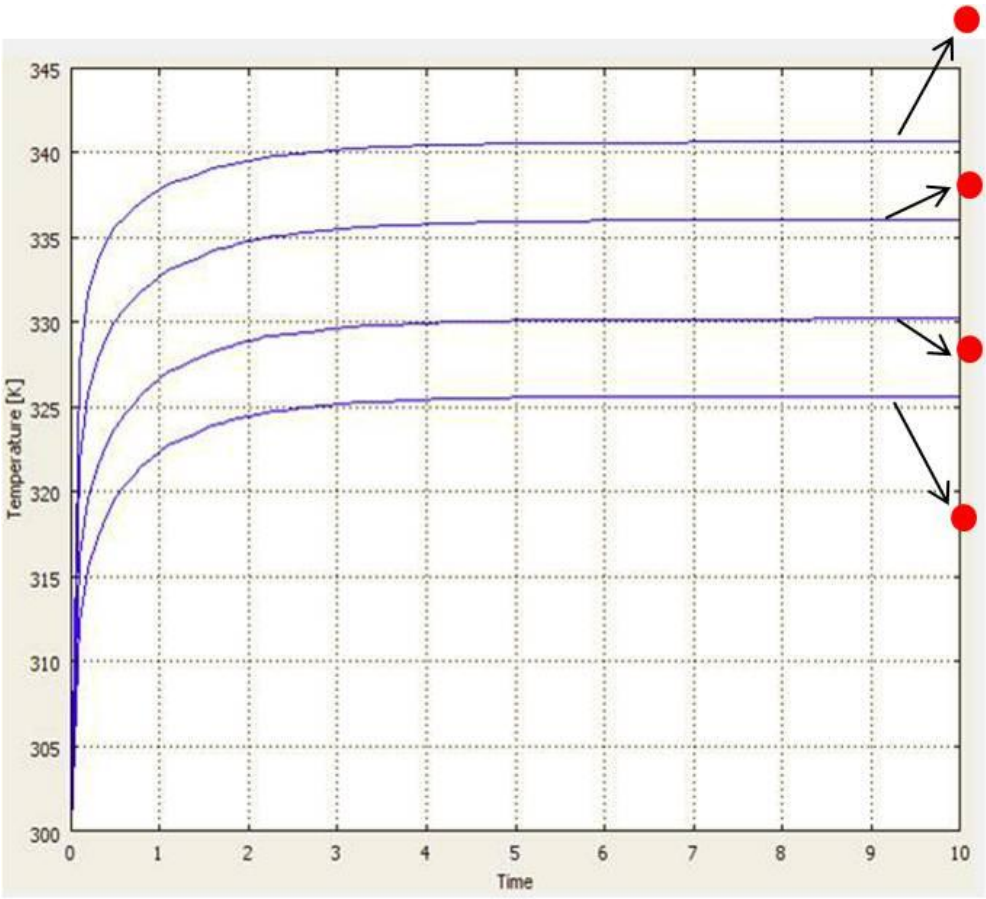

Figure 3.10: Comsol® Multiphysics model results for the silicon substrate RTD array. Blue lines show the temperature at the center of the platinum metal resistors under heating from reservoirs of water at 45 °C (318 K), 55 °C (328 K), 65 °C (338 K), and 75 °C (348 K) which are represented by the red dots. The unit of time on the x-axis is seconds. The arrows show which resistor is associated with its corresponding reservoir.

Alternatively a less thermally conductive substrate could be used instead of silicon. One such option is a fused quartz substrate. Fused quartz (SiO_2) is a synthetic form of quartz and has a thermal conductivity coefficient more than two orders of magnitude lower than silicon. Changing the substrate from silicon to silicon dioxide (and removing the now unnecessary 300 nm SiO_2 insulator layer) but keeping the rest of the model parameters unchanged showed that the resistors would measure the water reservoir temperature accurately (Figure 3.11).

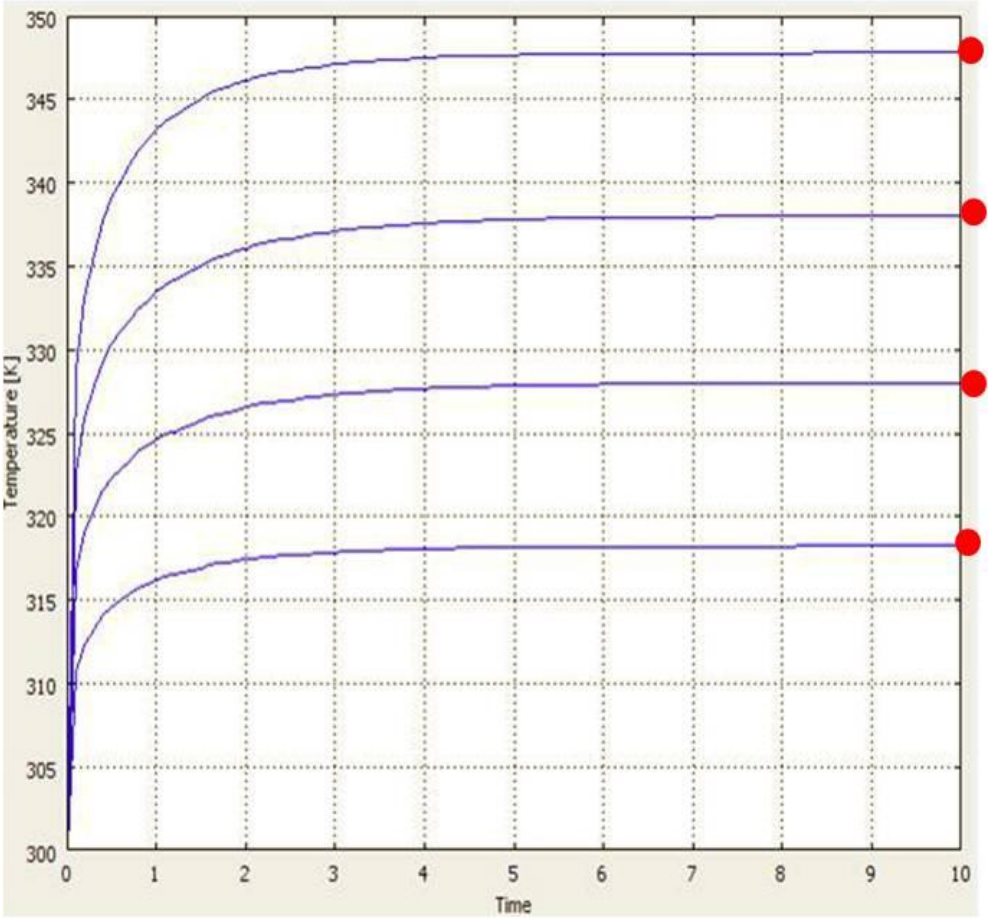

Figure 3.11: Comsol® model results for the fused quartz substrate RTD array. Blue lines show the temperature at the center of the platinum metal resistors under heating from reservoirs of water at 45 °C (318 K), 55 °C (328 K), 65 °C (338 K), and 75 °C (348 K) which are represented by the red dots. The unit of time on the x-axis is seconds.

3.5 Fused Quartz Substrate RTD Arrays

Based on these results a new batch of temperature arrays were designed and fabricated. The fabrication process is shown in Figure 3.12.

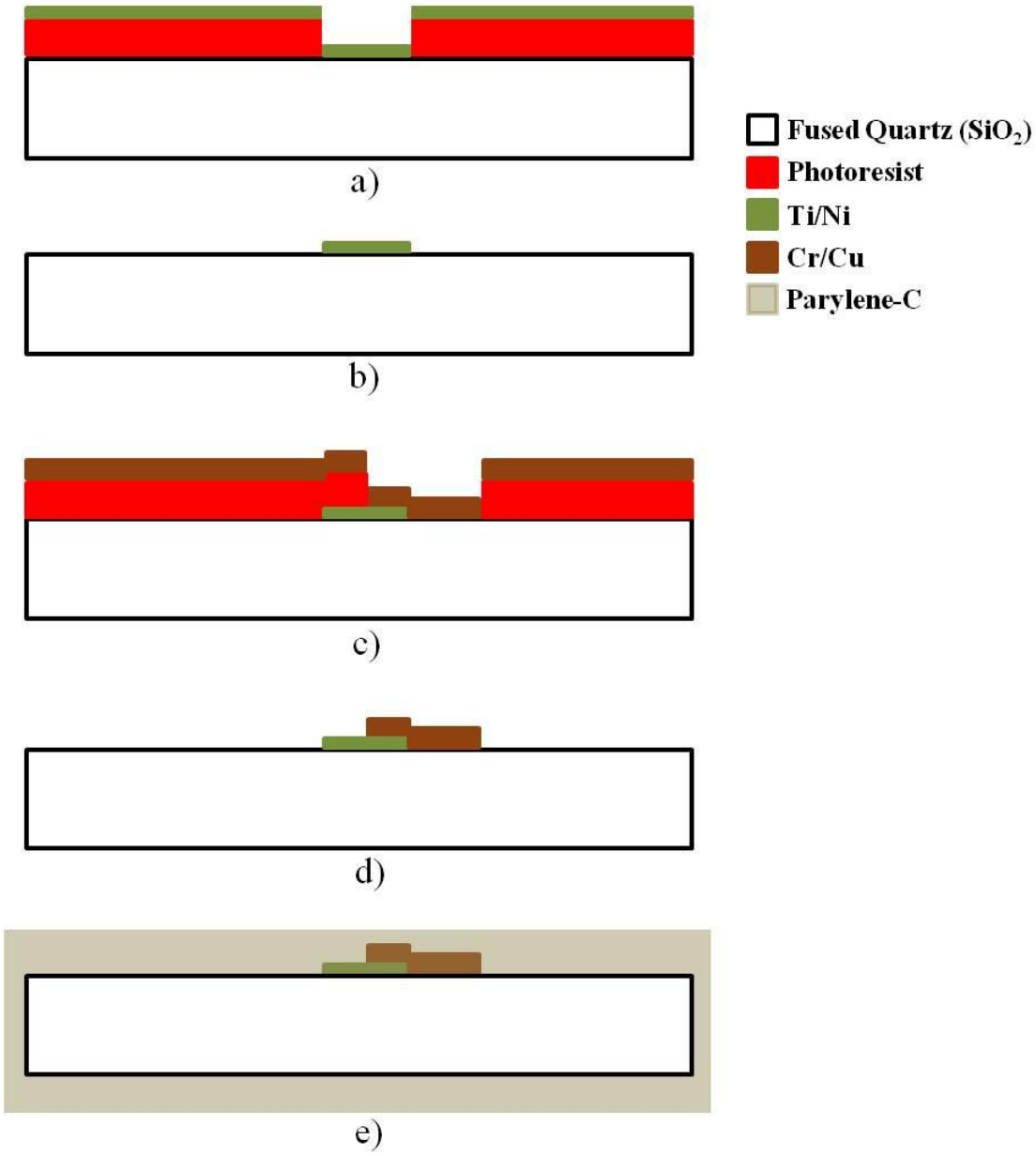

Figure 3.12: A schematic of the fabrication of the fused quartz substrate temperature array in cross-section. A layer of Ti/Ni is deposited and patterned on the Si wafer to create the resistor in (a) and (b). Next a layer of Cr/Cu is deposited and patterned to create the bond pads and leads connecting pads to the resistors in (c) and (d). Finally, Parylene-C is deposited over the entire wafer in (e).

The process is the same as that for the silicon substrate RTD except that the substrate is changed to fused quartz and nickel is used in place of platinum to increase the TCR and therefore increase sensitivity. The fabricated array is shown in Figure 3.13.

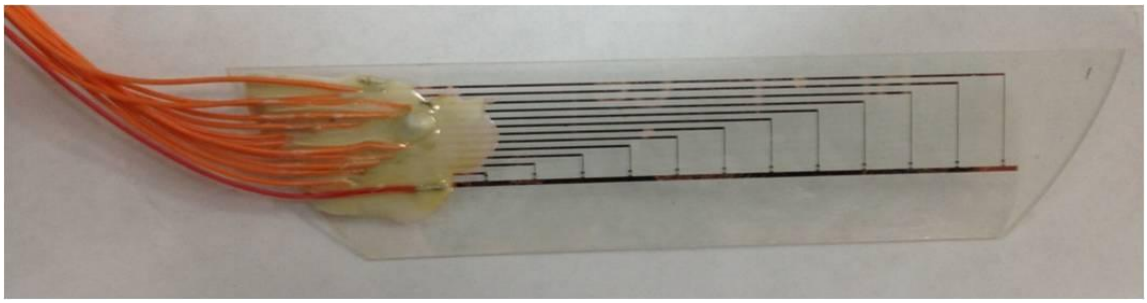

Figure 3.13: Photograph of the fused quartz substrate temperature array with nickel RTDs. The length of the array is 9.5 cm.

A comparison between a silicon substrate platinum RTD and a fused quartz substrate nickel RTD is shown in Figure 3.14.

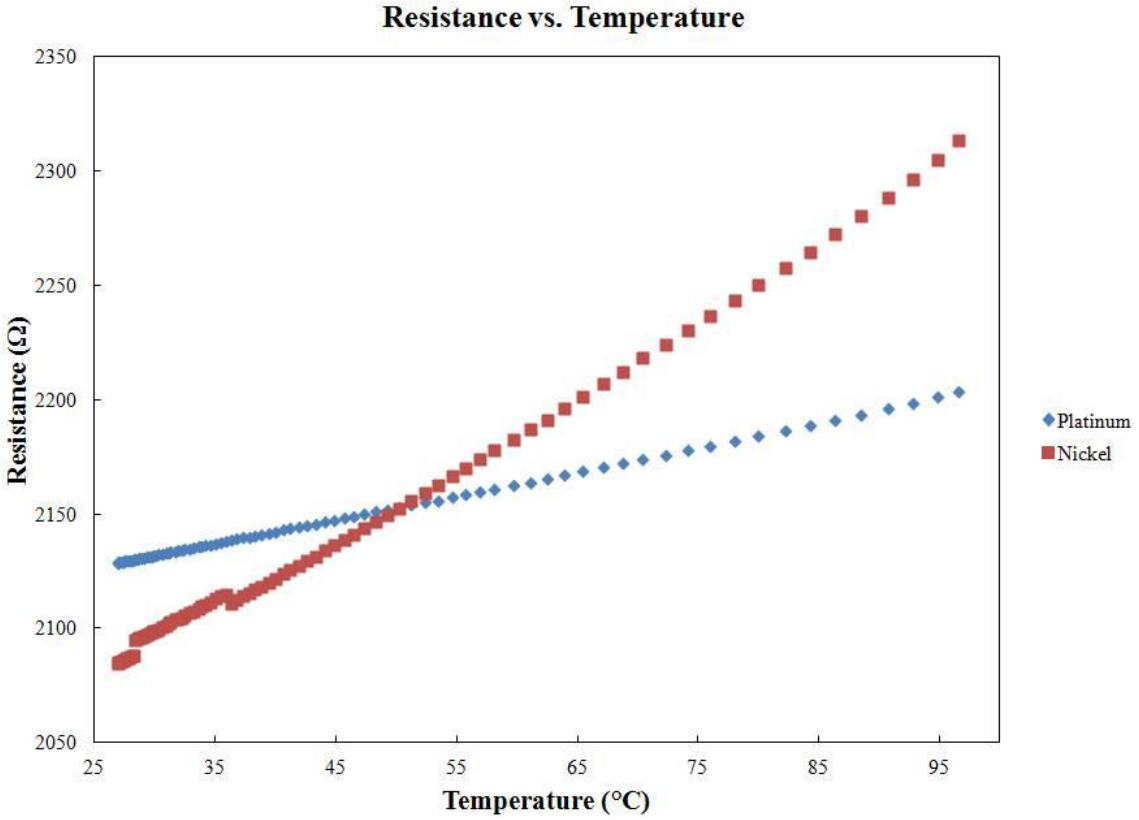

Figure 3.14: Resistance measurements from a platinum and nickel RTD over a wide range of temperature. The nickel RTD has a higher TCR of ~1600 ppm/°C compared to just 500 ppm/°C for the platinum RTD.

Here, the starting resistances are almost the same – so the difference between the two sensitivities is driven by the TCR differences between nickel and platinum. The TCR measured for the platinum element was 500 ppm/°C and for the nickel element was 1600 ppm/°C**.** The nickel plot has a 'bump' of increased resistance between 26 °C and 35 °C and is attributed to a software glitch in the recording program. The comparison is not just one of difference in choice of metal. Not only is the resistor material changed, but the substrate is different as well. In fact, the substrate change may be the largest reason for the increased sensitivity. This is due to the fact that fused quartz is a poor thermal conductor; during e-beam evaporation of the metal, the substrate is heated to a much higher temperature as it does not efficiently conduct heat radiated from the hot crucible into the large metal plate that the substrate is attached to. This higher temperature allows for larger metal grain size which improves TCR. In fact, platinum was deposited at a similar thickness as the nickel-RTD and on a fused quartz substrate and its TCR was measured to be ~1000 ppm/°C, double that of the silicon substrate. Due to the thermal insulating properties of the fused quartz substrate, the maximum current through the resistor must be decreased because joule heating is more likely.

3.6 Electronic Read-Out

In order to monitor the temperature change of the arrays, a circuit was designed and constructed to measure the resistance values of the RTDs. Using ohm's law (Eq. 3.1), the current through the resistor and voltage drop across it must be known in order to determine the resistance. Measuring the voltage drop across the resistor is a simple task carried out by the data acquisition device (to be discussed next). However, directly measuring the current flow through the resistor is a much more complicated measurement

that could not be carried out using the data acquisition device. Therefore, the current through the RTD was measured indirectly, using another resistor in series with the RTD (Figure 3.15).

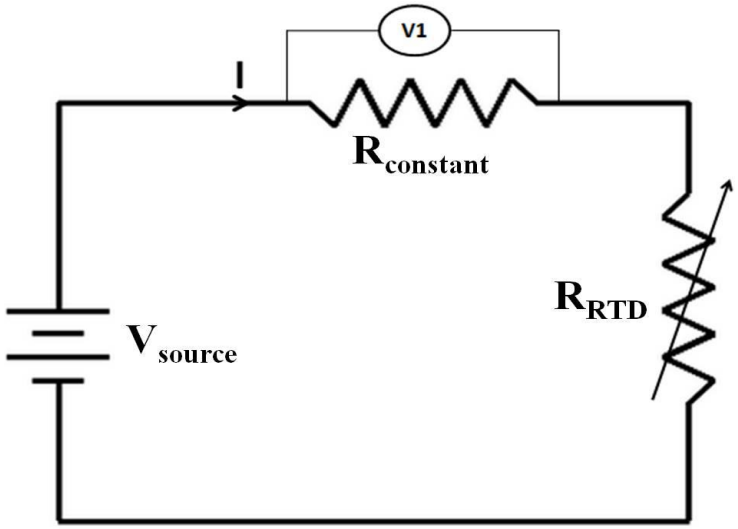

Figure 3.15: Circuit schematic to measure the resistance of one of the RTDs on an array.

In this circuit, the source voltage (V_{source}) is generated by the data acquisition instrument and is set to a constant 2 V. The voltage magnitude was set so that the current through the RTD was high enough to be easily measured above the noise floor, but low enough so that it does not cause joule heating. The first resistor in the circuit is used to determine the current through the entire circuit. Since the two resistors are in series, the current through one of the resistors is the same as that through the other resistor. Measuring the voltage drop, ($V1$) across the constant resistor ($R_{constant}$) provides the current (I) through that resistor via Ohm's Law and is the current through the entire circuit. Using the known current (I) and the voltage drop across the RTD can now be used to calculate the RTD resistance (R_{RTD}). The voltage drop across the RTD does not

need to be directly measured since its value is $V_{source} - V1$, both of which are already known.

The assumption of a constant resistor holding is critical to the accuracy of the RTD resistance measurement. Store-bought carbon-film resistors of a certain value typically have a tolerance of ± 5% and can have TCRs of 150-500 ppm/°C. Therefore a 10,000 Ω carbon film resistor may actually be anywhere from 9500-10500 Ω and may change 5 Ω/°C. Because these resistors are directly in contact with the air around the hot spring and indirectly in contact with the ground near the hot spring, they could easily be warmed 10-15 °C above the temperature in the laboratory where they were calibrated. A 10 °C increase in the constant resistor temperature would result in a 50 Ω resistance increase that could cause the RTD hot spring temperature measurement to be undervalued by > 1 °C (assuming a RTD value ~1200 Ω). This environmentally-induced error is far too high considering the additional error sources and the design requirement to have a measurement accurate to ± 1 °C. Therefore, special high precision/low TCR 10,000 Ω resistors with a tolerance of 0.01% (± 1 Ω) and TCR of ± 10 ppm/°C (which is a resistance change of 1 Ω with a 10 °C increase in temperature) were utilized (Vishay Intertechnology, Inc. part number MR10210K000TAE66). With these resistors, a 10 °C increase in environment temperature would result in the hot spring temperature undervalued by only 0.1 °C.

The previous circuit discussion was for only one RTD. On the arrays, there are 15 RTDs available for simultaneous measurement which requires 15 high precision constant resistors that are placed on a different printed circuit board (Figure 3.16).

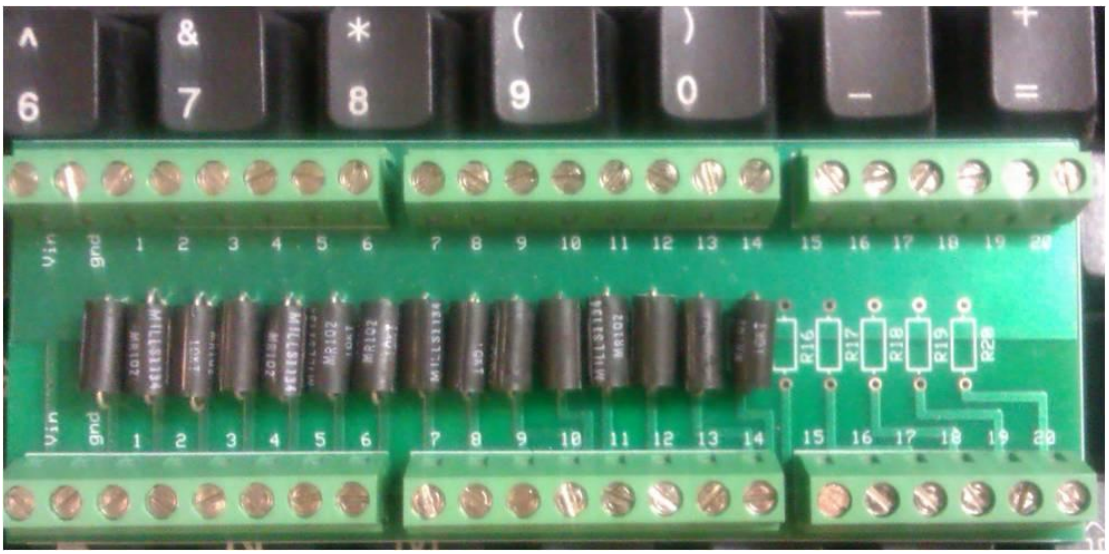

Figure 3.16: Printed circuit board for the high precision, low-TCR constant resistors required to determine the current in the measurement circuit. The keyboard in the background is provided for scale.

The data acquisition instrument used for these measurements must be capable of continuously monitoring 15 different voltage drops across the constant resistors and be able to supply a constant voltage input of 2 V. In fact, the voltage measurement across the constant resistor is a differential one (i.e., a voltage measurement must be taken on both sides of the resistor and then the difference calculated) so each of the RTD measurements needed two voltage inputs on the data acquisition instrument. Therefore, the data acquisition instrument required at least 30 analog voltage measurement input ports and at least one analog voltage output port. In addition, the instrument needed to be portable (for field transport) and able to be operated with a battery. The device chosen was a multifunction data acquisition device (Figure 3.17) from National Instruments (USB-6289) which had the most analog voltage input ports of any available product (32) along with other capabilities required by the conductivity sensor array (discussed in Chapter 4).

Figure 3.17: Photograph of the multifunction data acquisition device (USB-6289) from National Instruments.

The software chosen to interface with the data acquisition instrument was Laboratory Virtual Instrumentation Engineering Workbench (LabVIEW) from National Instruments. This is a visual programming language software commonly used for electronic experiment applications. The constant 2 V supply voltage and the voltage input port readouts can all be monitored through this software. The mathematical operations needed to calculate the circuit currents and RTD resistances were performed and the RTD resistances were then used in conjunction with the calibration curve formulas to calculate temperature readings (Figure 3.18). These data were then output to a text file along with the corresponding time stamp for each set of 15 temperature measurements. Data were sampled at a rate between 1 kHz and 1 Hz depending on the desired length of each measurement.

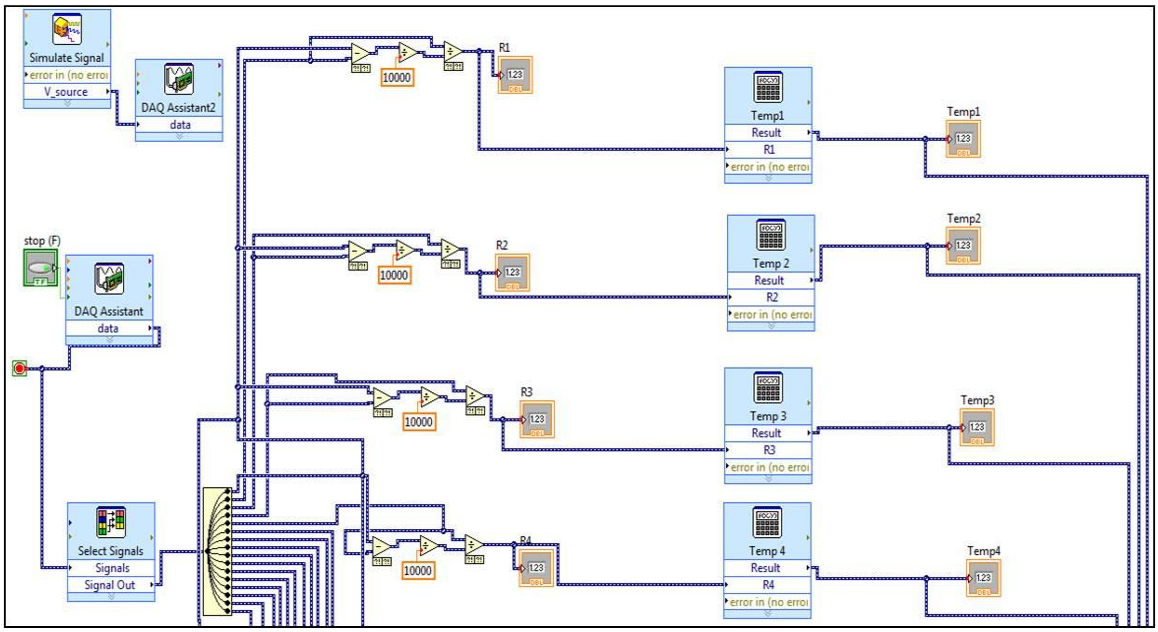

Figure 3.18: Screenshot from the LabVIEW software showing a portion of the temperature array measurement program.

3.7 Hot Spring Measurement Locations

Temperature measurements were taken at three different hydrothermal systems around the world. The first measurements were taken at the Rehai geothermal field near the city of Tengchong in Yunnan Province, China (Figure 3.19).

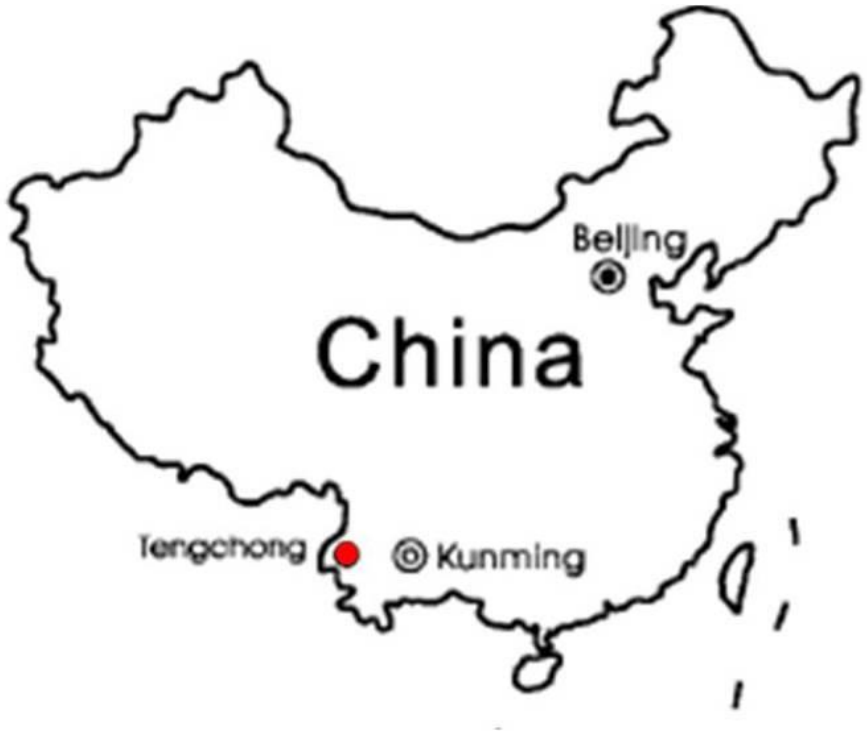

Figure 3.19: The hydrothermal systems are located in southwest China near the city of Tengchong in the Yunnan Province (red dot).

The heat source for the Rehai hydrothermal systems is thought to come from magma intrusion or 69 Ma Yanshanian granite (Zhang et al. 2008). Measurements were also taken over consecutive summers at numerous sites within Yellowstone National Park, U.S.A (Figure 3.20).

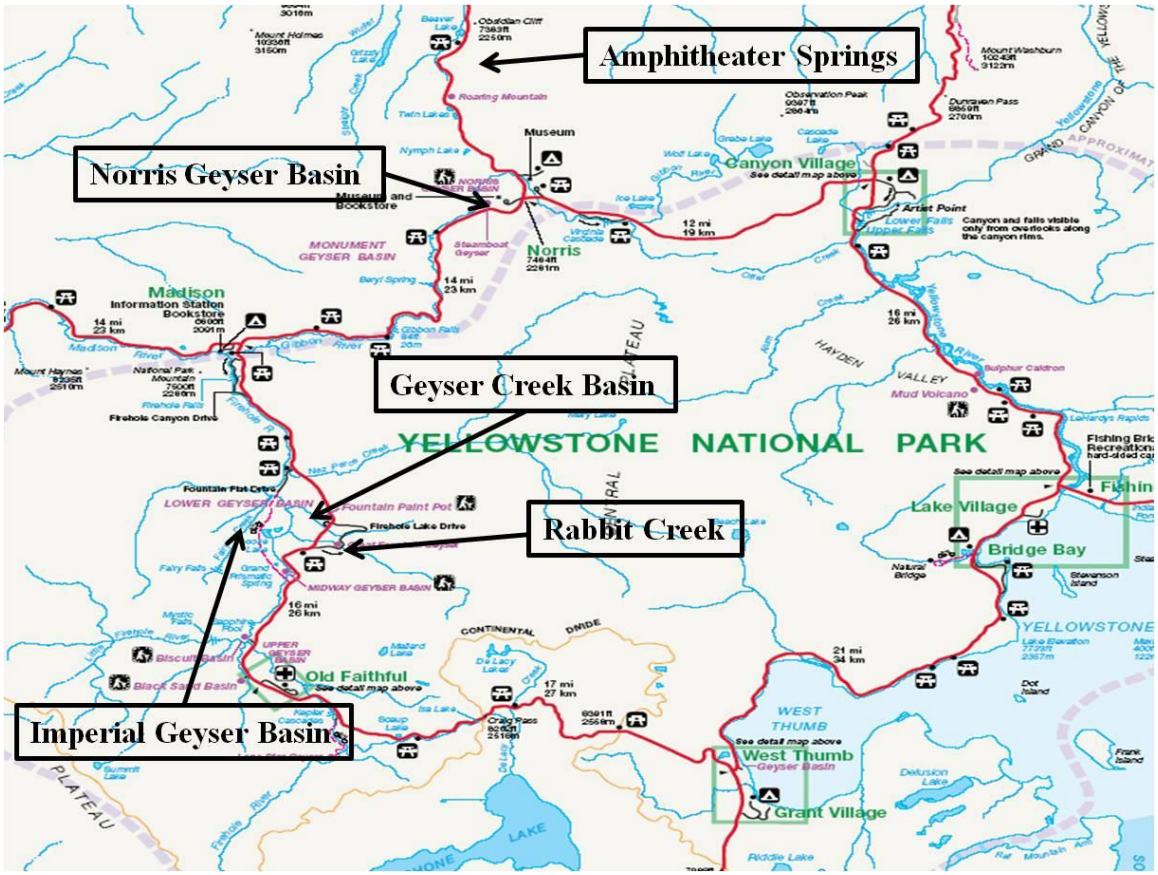

Figure 3.20: Map of Yellowstone National Park showing the location field sites referenced in this chapter.

Yellowstone National Park (YNP) hydrothermal systems are volcanically driven. Finally, measurements were taken at the Great Boiling Spring hydrothermal system in Gerlach, NV, U.S.A. The Great Boiling Spring system is located in the Great Basin region of the U.S.A. and the heat source comes from tectonic activity.

3.8 Hot Spring Data from China

The first time the sensor arrays were used was at the Rehai geothermal field in Yunnan Province, China. In one measurement at the hot spring named 'Geothermal Explosion Site', the temperature array was placed vertically into the hot spring channel through microbial mats and sediment at different equally spaced locations (Figure 3.21).

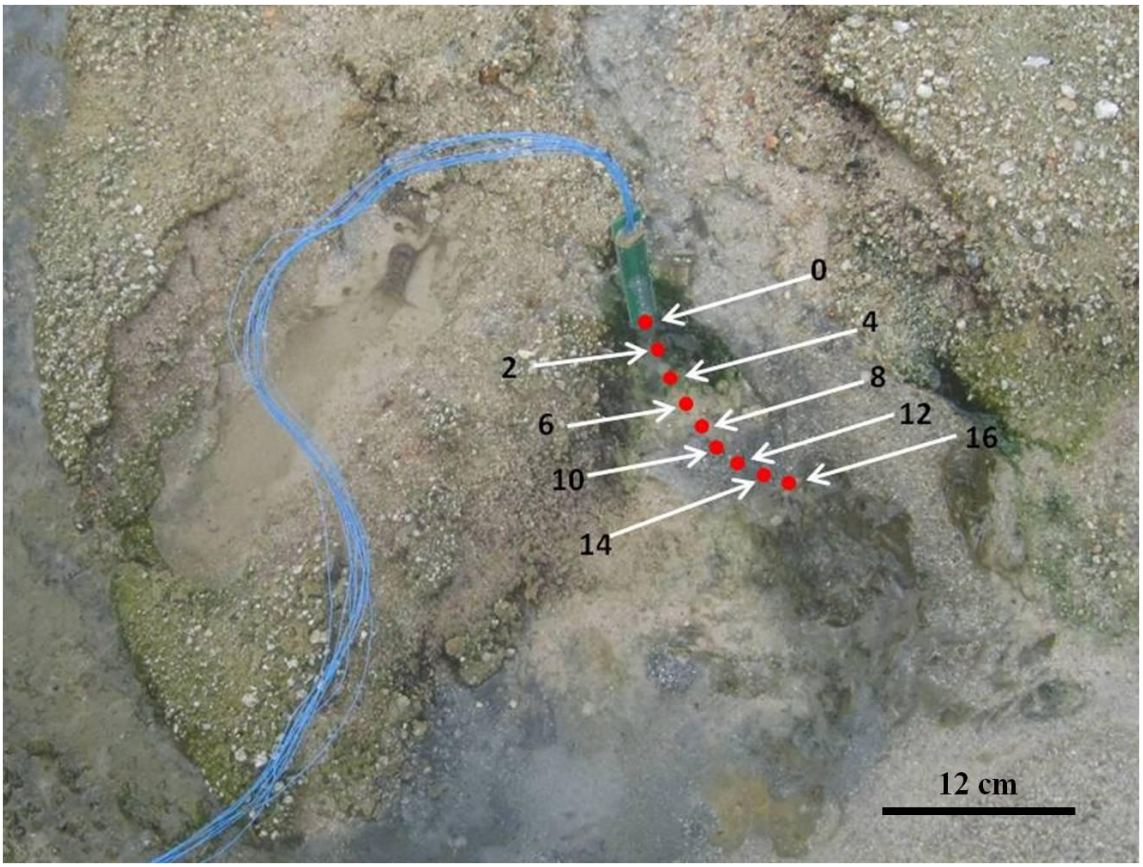

Figure 3.21: Photograph of the temperature array being placed vertically into the hot spring to a depth of about 4 cm at nine different locations.

At position 0, the array was placed through a photosynthetic mat. The mat disappears near position 4 and a different mat appears near position 14. There is a small bubbling fluid source at position 10. The plot of temperature across the feature as a function of depth is provided in Figure 3.22.

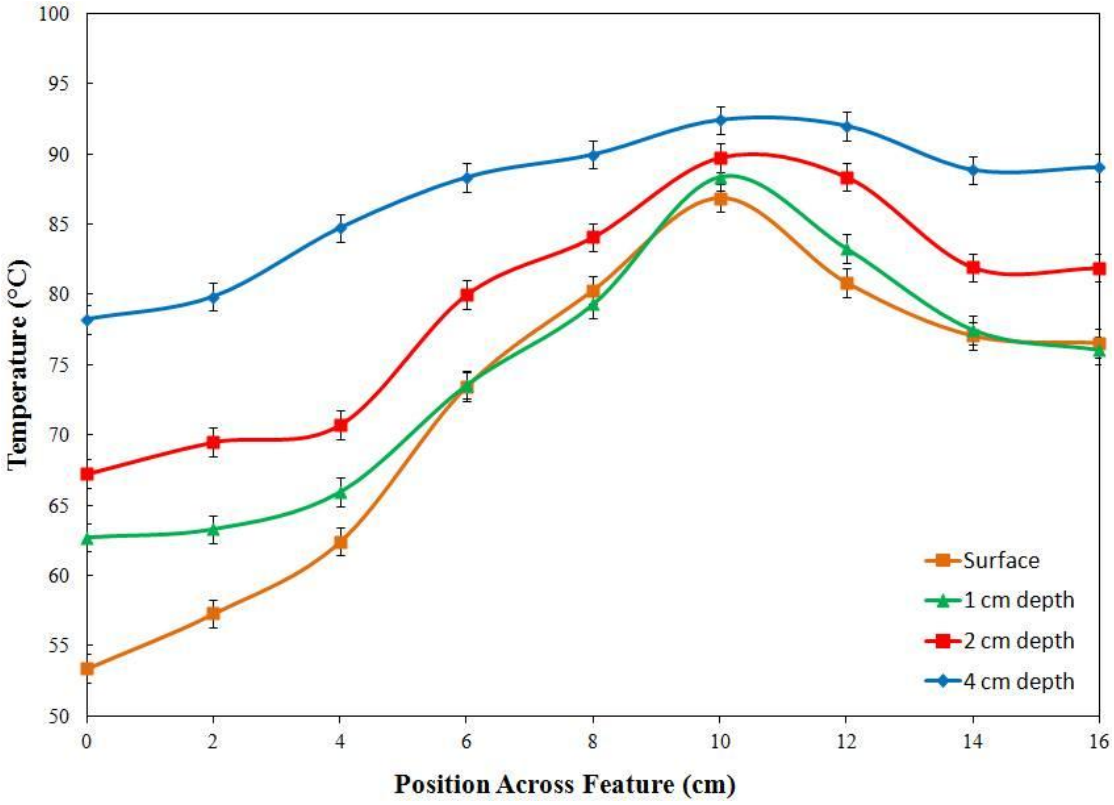

Figure 3.22: Plot of temperature at various depths along different spatial locations at the 'Geothermal Explosion Site' hot spring in Tengchong, China. Error bars on all temperature plots represent the uncertainty of ±1 °C due to sensor system noise and calibration error.

The array was only placed to a depth of ~4 cm, yet a considerable temperature gradient was observed from 4 cm depth to the surface. The plot shows decreasing temperature along the y-axis in order to have depth increasing lower on the graph. The temperature gradient (dT/dz) is largest where the microbial mats are found and the gradient is smallest at the bubbling fluid source.

All temperature measurement values given in this dissertation are time-averaged values from an approximate 2 Hz sampling frequency typically measured for one minute. Error bars on all temperature plots are ±1 °C and represent the measurement error due to sensor and instrument noise and calibration accuracy. These error bars do not express the

temporal variability of temperature over the measurement interval. The temporal variability as expressed by one standard deviation from the mean temperature is approximately 0.5 °C or less for all the reported values.

A number of important experiences were gained from this first foray into the field. Firstly, in order to be able to hike with the equipment to remote locations, a much smaller and lighter weight battery would be needed. For the data collection in China, a 12 V (~23 kg) car battery was used to supply power to the data acquisition device. For later field work, a 12 V ~3 kg scooter battery was used. The scooter battery was more than satisfactory for a single day of field work but required an overnight recharging cycle. Secondly, the wires connecting the array to the data acquisition device were too short. Thicker and longer wires were used in future experiments to limit the resistance contribution and allowed myself to remain farther away from the hot spring during testing. Finally, the most important materials and equipment for mending devices in the field was determined such that almost any electronic or mechanical problem could be fixed with a lightweight field-work 'survival pack' including such items as electrical tape, portable soldering gun, extra wire and RTDs, and a screw driver.

3.9 Hot Spring Data from Yellowstone National Park

Field data collection from Yellowstone National Park spanned two different field trips during the summers of 2011 and 2012. During the first summer trip (2011), an undergraduate student, Karl Schliep, assisted with sensor array testing and data collection. In one hot spring outflow channel at Upper Amphitheater Springs, there were two different colored photosynthetic communities observed on either side of the hot spring outflow channel. The immediate question to be addressed was: *why are there two*

different photosynthetic communities present in what seems to be one fluid reservoir? The image of the outflow channel and the temperature profile measured across the channel is provided in Figure 3.23.

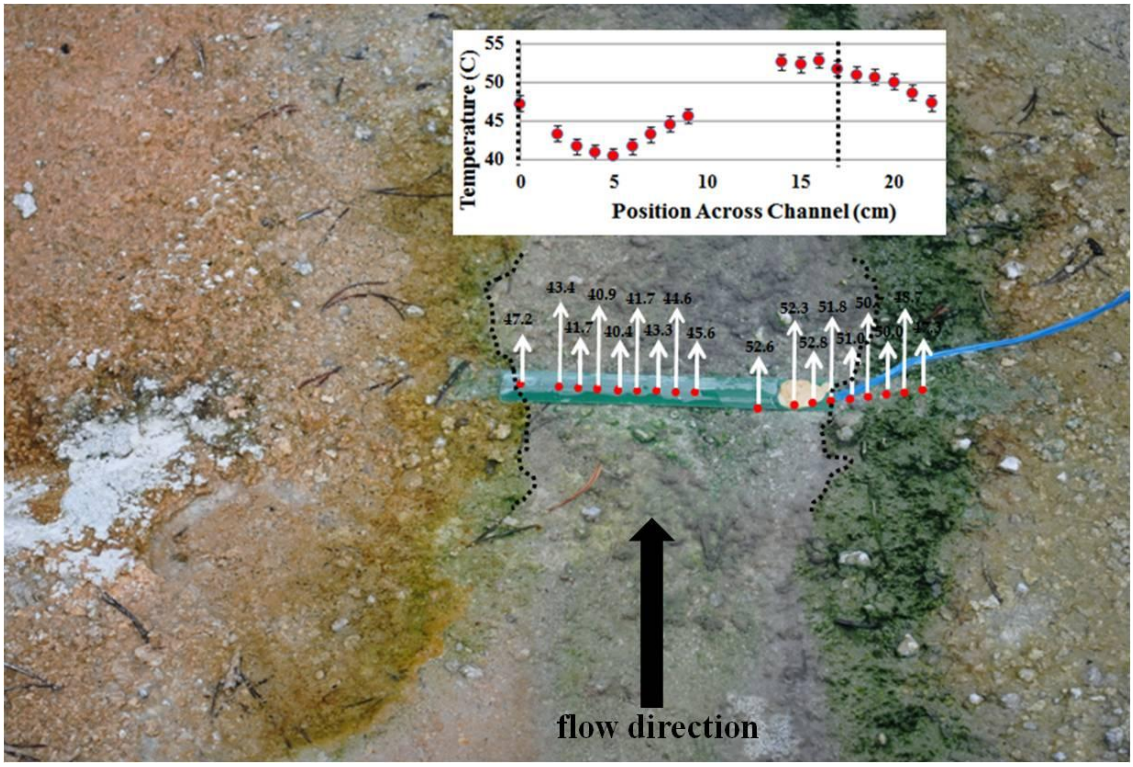

Figure 3.23: Photograph of a hot spring outflow channel where a yellowish photosynthetic community can be seen at the left hand side of the channel and a green community seen at the right. A plot of the temperature distribution across the channel is also provided. Dashed lines in the image and plot mark the approximate locations where the visually distinct photosynthetic communities appear. Error bars on all temperature plots represent the uncertainty of ±1 °C due to sensor system noise and calibration error. The length of the array is 18.5 cm for scale.

The temperature profile from right to left across the stream shows an increase from about 47 °C to the highest recorded temperature of ~53 °C near the transition from the clear, unpigmented substrate to the green photosynthetic community followed by a temperature decrease toward the center of the stream. Strangely, the temperature begins to increase again as the yellowish community transition edge is approached. Since the temperature in

the particular communities are similar, the most likely explanation is that there are in fact two sources of water, one near the green community edge and one to the left of the yellowish community. These two sources could have different chemistries which might explain why the different communities were found.

At other locations around the Upper Amphitheater Springs site, there are many small bubbling sources surrounded by chemoautotrophic yellow sulfur "streamers." The yellow streamers are, in turn, surrounded by dark purple photosynthetic mats. One such example is shown in Figure 3.24.

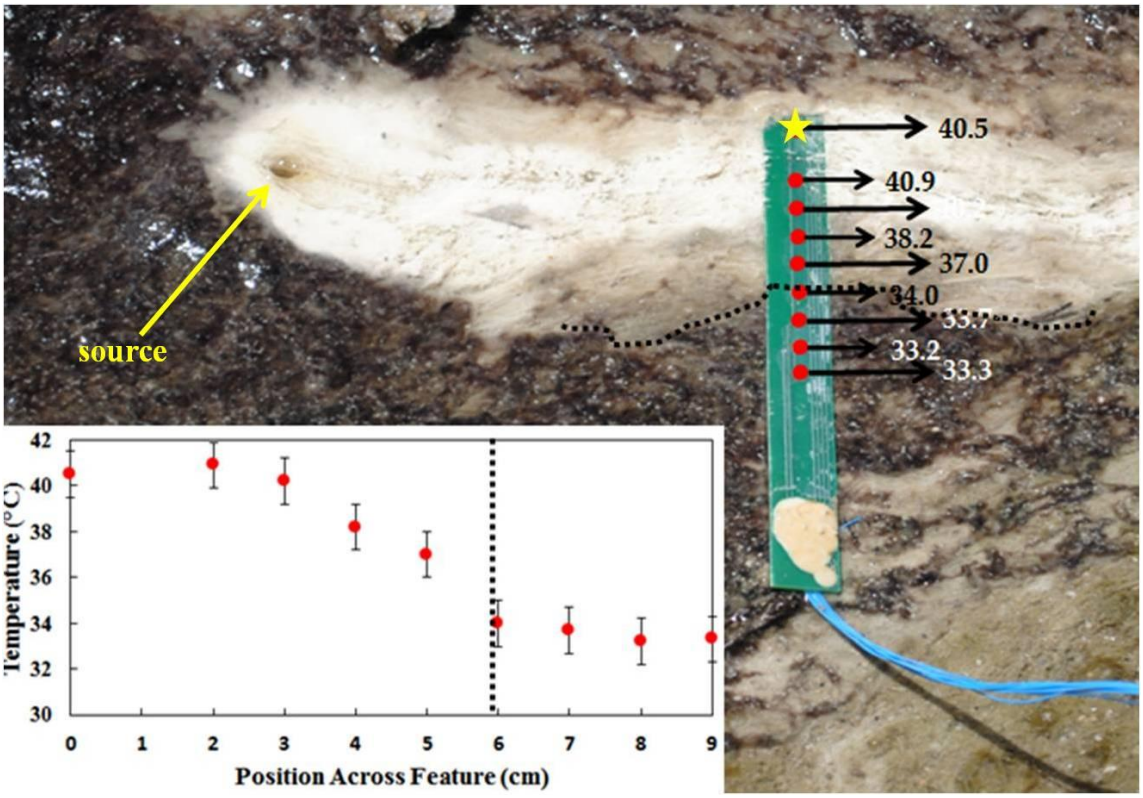

Figure 3.24: Photograph of a bubbling spring source surrounded by yellow sulfur streamers which are, in turn, surrounded by a purple photosynthetic mat community. A plot of the temperature distribution across one region of the photosynthetic transition zone (feature) is provided. The yellow star on the array signifies the zero position in the plot. The dashed line in the image and plot mark the approximate location where the visually purple mat appears. The length of the array is 18.5 cm for scale.

The temperature profile was measured at different locations in the vicinity of this bubbling source and one of the temperature plots is provided. Every location where the temperature was measured revealed that the dark purple mat appears only when the temperature dropped below ~34 °C. Therefore, based on the morphology of the flow channel and the temperature profile, temperature appears to govern the location of the transition to photosynthesis.

At a third location in the Upper Amphitheater Springs area, there is a hot spring with a graded mat at the edge of the source pool. The mat nearest the source pool is yellow, it transitions to a green mat, and then to a dark purple mat at increasing distances from the source pool over a span of < 20 cm (Figure 3.25).

Figure 3.25: Photograph of a hot spring source pool (at the left) and the transition to different photosynthetic communities with distance from the source pool. Black dashed lines approximate where the transitions to different microbial communities occur, red dots indicate the locations of temperature sensors. The yellow star marks the zero position for the next figure plot. The length of the array is 18.5 cm for scale.

The temperature measurement locations are not perfectly aligned across the pool, but the strong temperature gradient is clearly visible in the data and fairly linear (Figure 3.26). The colors of the microbial communities are labeled in the plot. Again, the dark purple mat shows up when the temperature drops below ~ 34 °C. What is not clear from these data is whether certain organisms appear because they out-compete other organisms within specific temperature ranges or whether organisms simply cannot exist at higher temperatures. Quite likely, both effects are occurring.

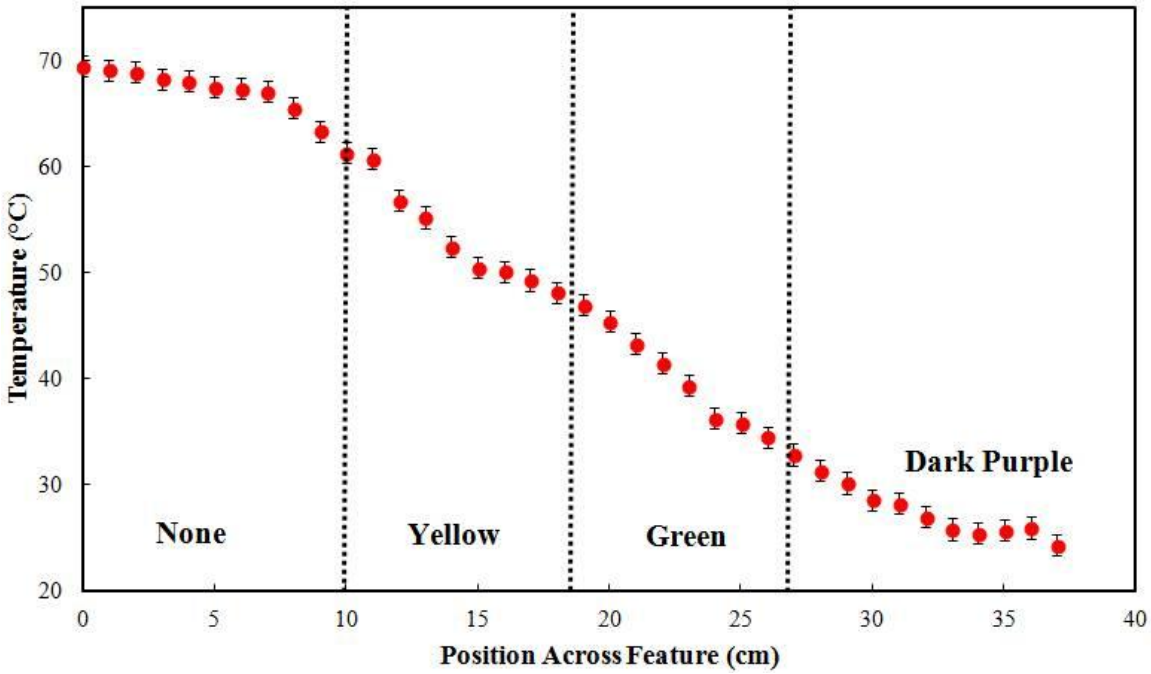

Figure 3.26: Plot of temperature as a function of distance away a source pool (at the left). The dashed lines mark the apparent boundaries of the different colored microbial communities.

At a location in Lower Amphitheater Springs there was an area where two streams converged to form a single stream (Figure 3.27).

Figure 3.27: Photograph of an area where two different hot spring outflow channels merge and a sharp photosynthetic boundary occurs. Arrows show the direction of flow from the different outflow channels. The length of the plastic box is 30 cm for scale.

One stream was visibly devoid of photosynthetic bacteria, while the other stream was filled with green photosynthetic cyanobacteria. Where the two streams converged, a sharp transition zone occurred between the regions where microbes were clearly visible and where they were not. This transition zone occurred approximately in the middle of the stream (Figure 3.28).

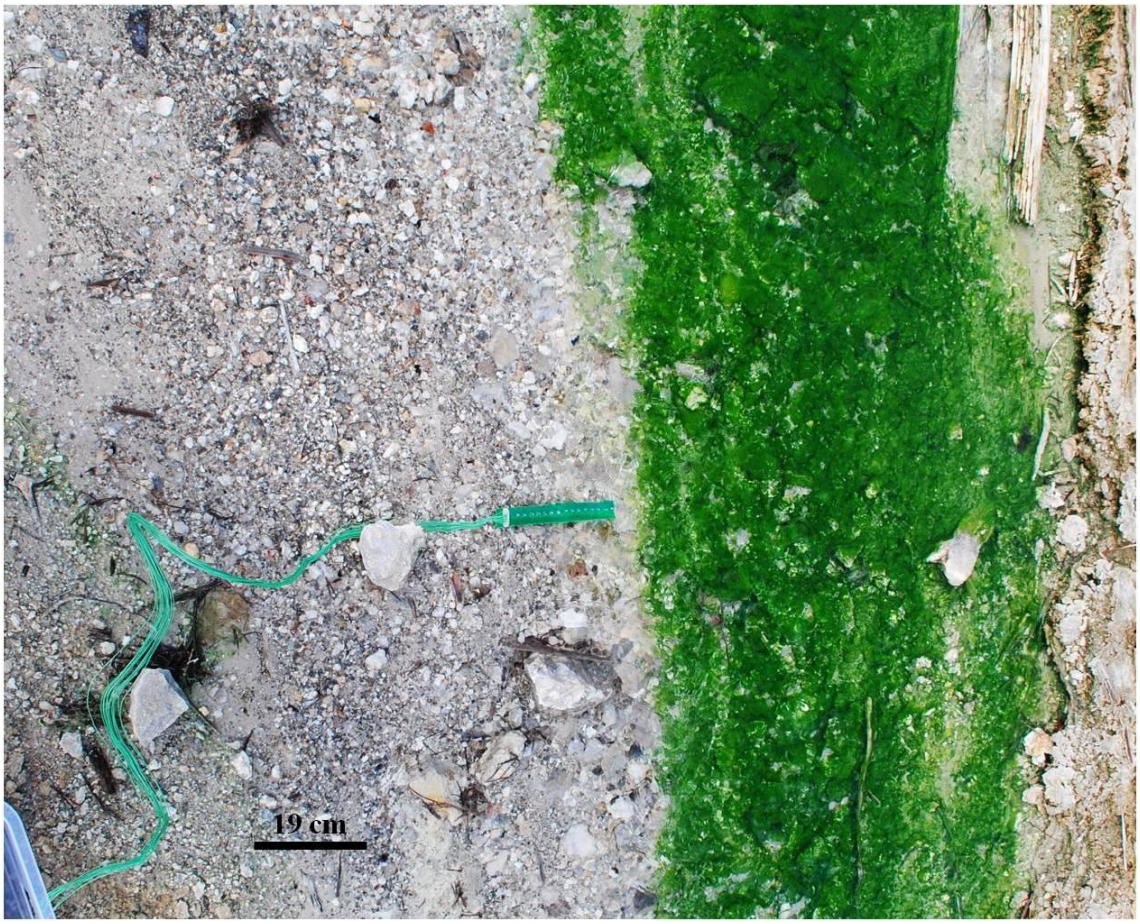

Figure 3.28: Photograph of a hot spring stream where two channels from different sources merged and a photosynthetic boundary appears sharply at about the center of the stream.

A temperature profile was measured across the converged stream (Figure 3.29). The data show that the green cyanobacteria appear at a temperature of ~50 °C. The temperature difference between the clear and green zones is ~15 °C. The pH in the clear and green regions was approximately the same at 2.35 and the conductivity showed only a small difference (~4100 μS/cm on the clear side of the stream and ~3600 μS/cm on the green side of the stream).

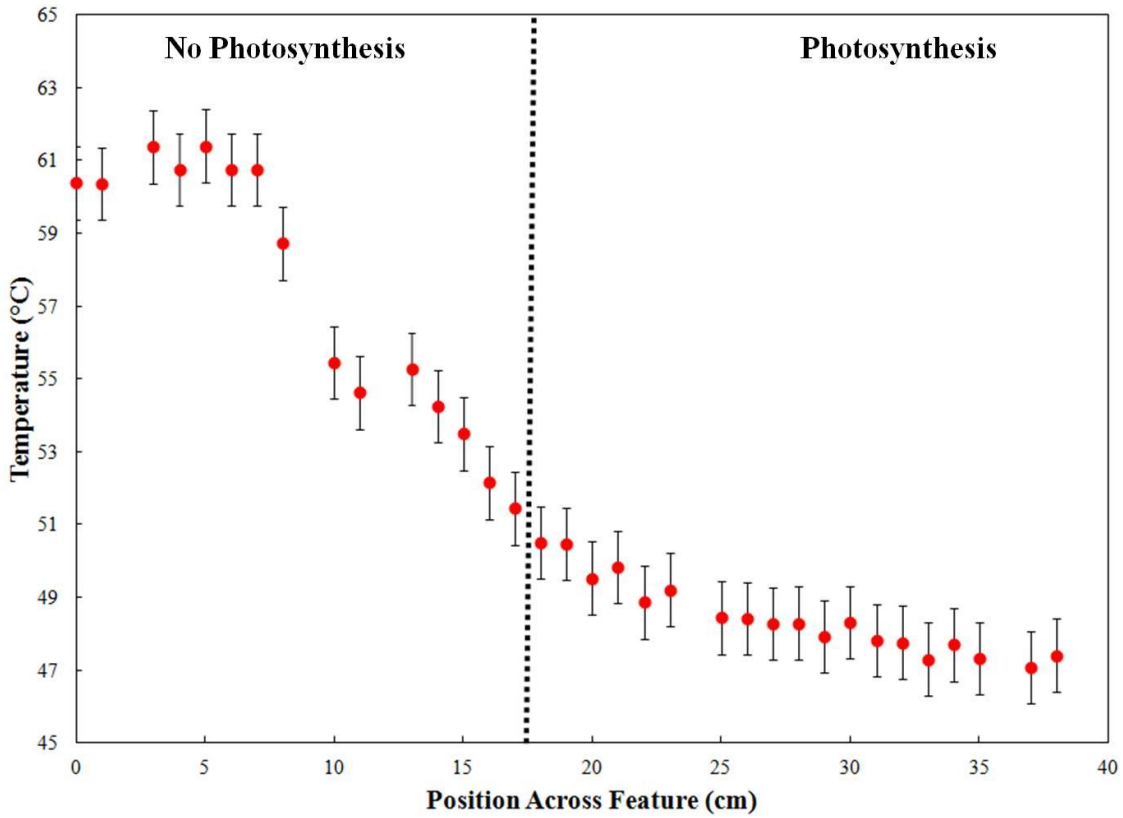

Figure 3.29: Plot of temperature across the stream below the confluence of two outflow channels. The clear side of the stream (no photosynthesis) is hotter than the green side (photosynthesis) of the stream. The dashed line marks the approximate transition to photosynthesis at this location.

At a second location in Lower Amphitheater Springs was an area where two outflow channels from different source pools merged. In one outflow channel, there is a thriving community of green photosynthetic cyanobacteria everywhere in the stream. In the other outflow channel, there appears to be no photosynthetic communities (Figure 3.30).

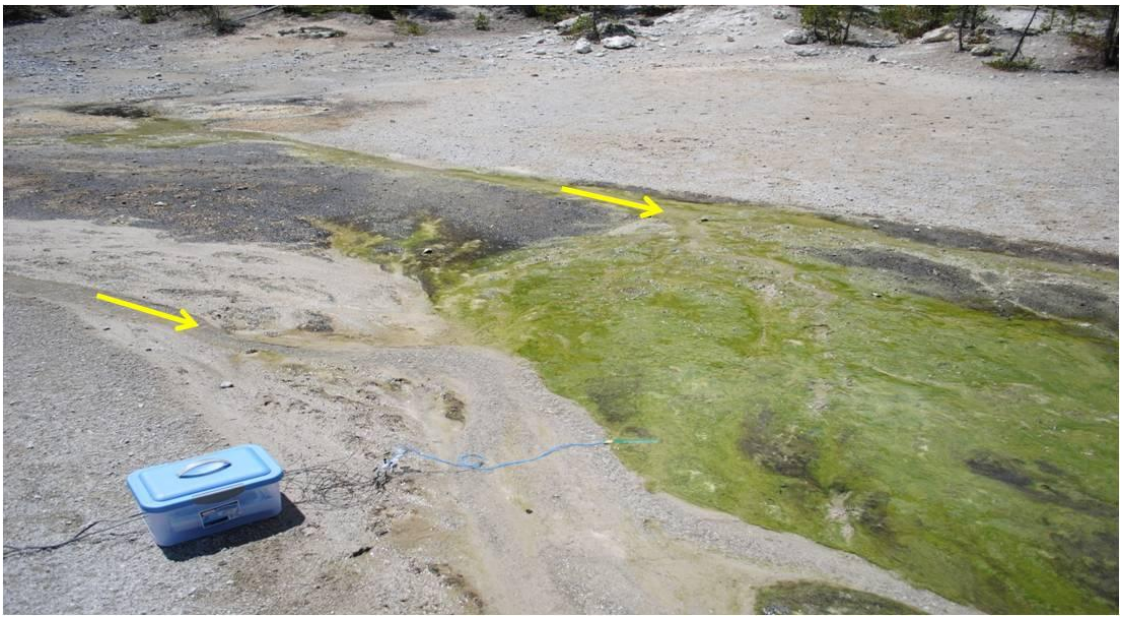

Figure 3.30: Photograph of two outflow channel merging (yellow arrows). In the upper channel the green photosynthetic community is clearly apparent. In the lower stream there is no visible community and where they merge a sharp boundary occurs. The length of the plastic box is 30 cm for scale.

Temperature was measured across the boundary where the two streams converge (Figure 3.31). The data clearly show there is no temperature gradient across the boundary zone. The conductivity and pH show little variation across this zone as well, therefore the cause for the sharp biological boundary remains elusive.

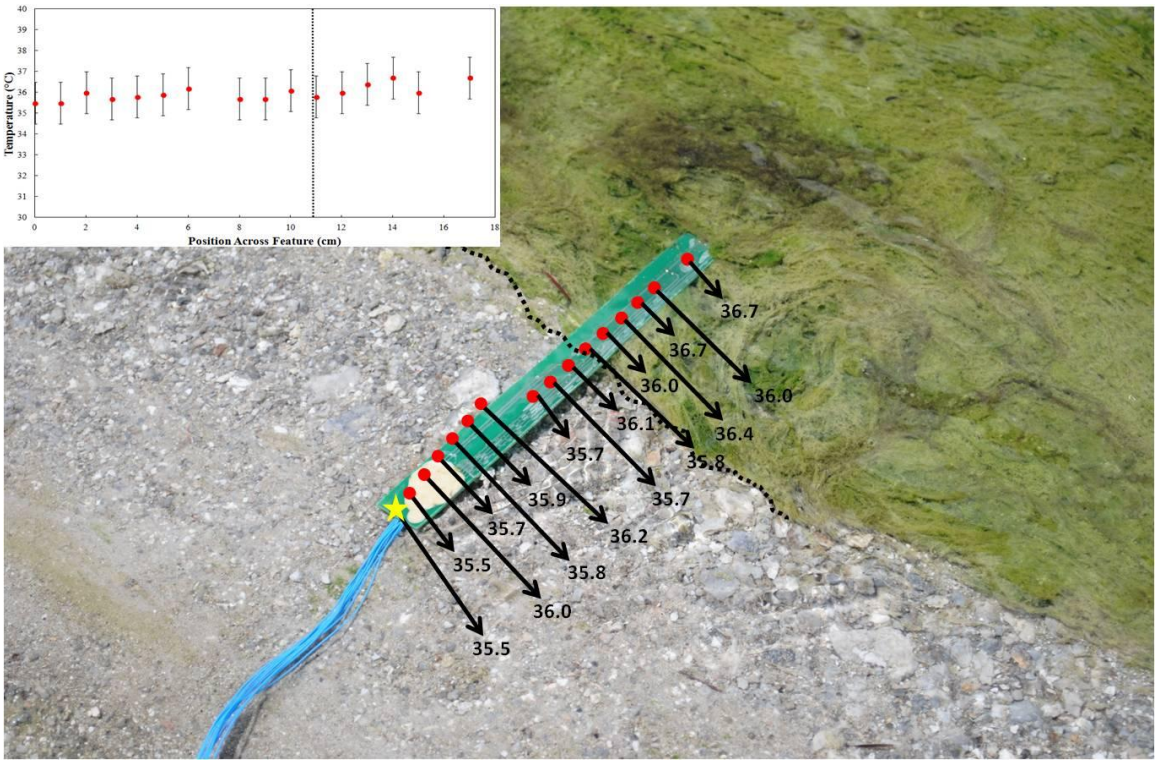

Figure 3.31: Photograph of the stream conversion zone where the photosynthetic mat sharply ends. The yellow star marks the zero position in the temperature plot. The black dashed line represents the approximate location where the transition to photosynthesis occurs. The length of the array is 18.5 cm for scale.

There are a number of deep source pools located at the Rabbit Creek field site in Yellowstone National Park. One of the unique capabilities of the sensors was that they were amenable to being lowered into the depths of the hot spring source pools (Figure 3.32).

Figure 3.32: Photograph of a temperature array connected to a fishing pole in order to measure temperature at depth in a hot spring source pool.

Figure 3.32 shows my undergraduate research assistant lowering a temperature array into the hot spring using a fishing pole. By holding the position of the fishing pole at a specific location, the depth of the array can be determined by measuring the amount of fishing line released. The sensor was bonded to a piece of wood in which two holes were drilled. The polyethylene fishing line was tied through the top hole. Metal weights were tied to the bottom hole. The data from one such measurement show temperature measurements at different depths (Figure 3.33). The small variation in temperature between the local bottom of the source pool and the surface indicate this particular hot spring is well mixed. Unfortunately, after a couple measurements, the epoxy bonding the array to the wood was corroded causing the array to separate from the wood.

Figure 3.33: Average temperature measurements averaged between depths from the bottom of the pool (at this particular location) to the surface.

A longer duration temperature measurement was carried out at a geyser hot spring in Imperial Geyser Basin in Yellowstone National Park (Figure 3.34).

Figure 3.34: Photograph of a geyser hot spring in Imperial Geyser Basin where the water level oscillates. The water periodically recedes below the edge of the source pool and becomes heated and then rises to a point at which the water overflows and runs down into the outflow channel (shown by black arrow).

At fairly regular intervals the geyser water level rises and spills over the edge of the source pool. Water then flows down the outflow channel (in the direction of the black arrow) and spills out over a wide expanse of ground. The outflow channel is covered by a yellow-orange photosynthetic community. A temperature array was placed in the outflow channel during a time when water was not flowing in the outflow channel. The array was placed in a region where phototrophic microbes could seen under the first 11 sensors (0-10), but not the last four sensors (11-14) which were closer to the center of the channel where the water should be hottest (Figure 3.35).

Figure 3.35: Close-up photograph of the temperature array in the outflow channel of a geyser in Imperial Geyser Basin. The length of the array is 18.5 cm for scale.

A time series set of pictures that show the water flowing down the outflow channel and immersing the sensor is provided in Figure 3.36.

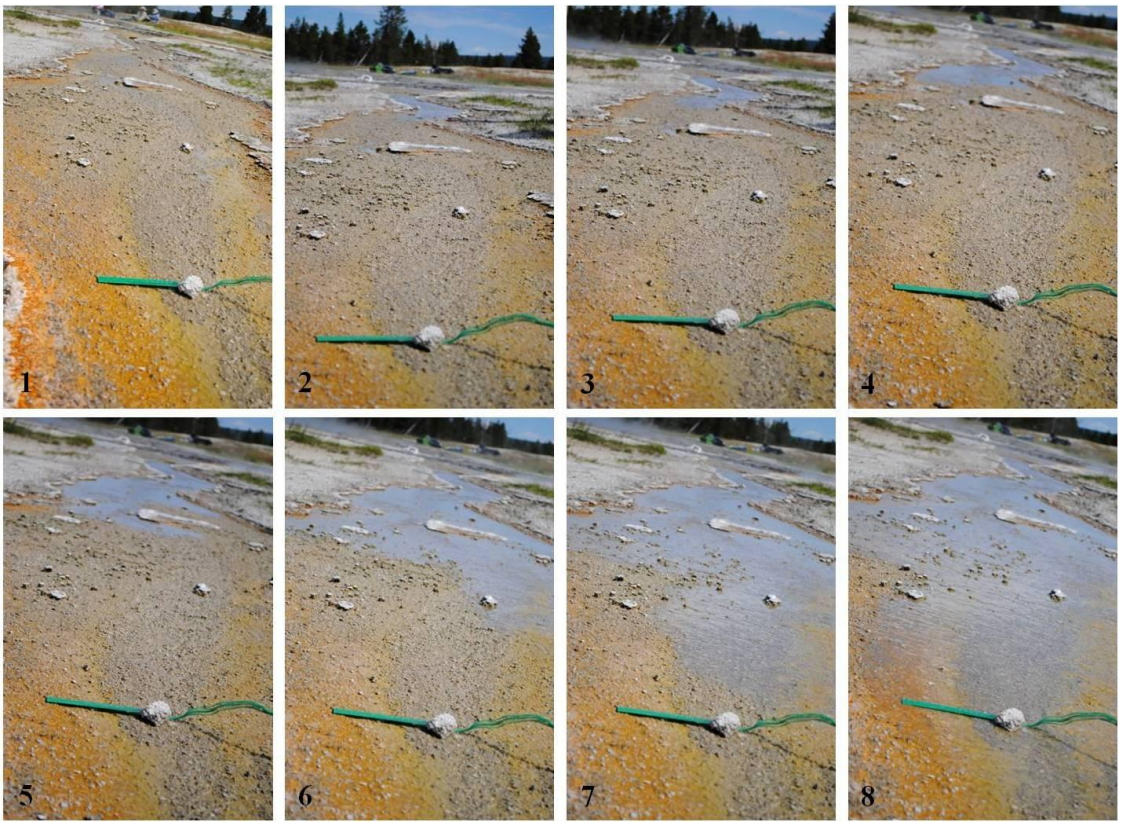

Figure 3.36: Time-series photographs showing the flow of water down the outflow channel. The numbers at the bottom left of each picture show the order of the picture series. Water begins flowing over the sensor at picture 8 approximately 10 minutes after the data started recording. The length of the array is 18.5 cm for scale.

The array data begin measuring the ground temperature and then, approximately 10 minutes later, the water temperature once water started flowing down the outflow channel and finally, it measures ground temperature again once the geyser activity stops and the water seeps into the ground (Figure 3.37).

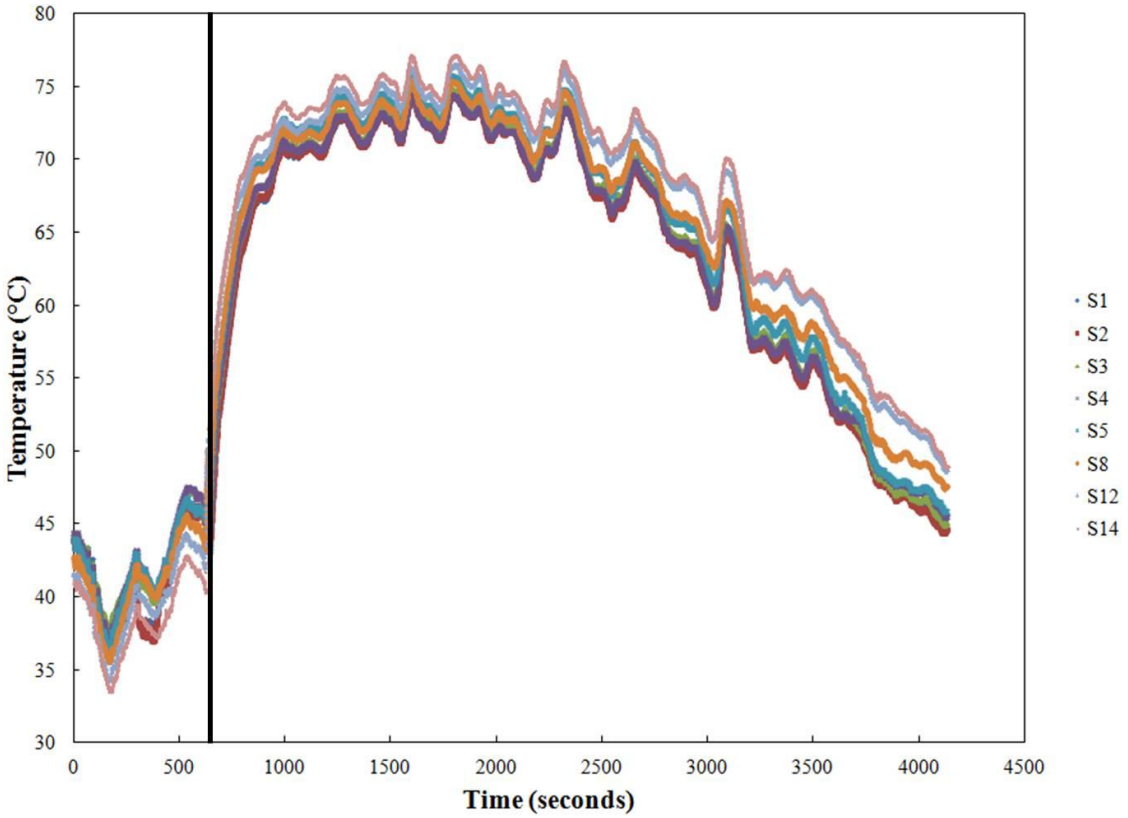

Figure 3.37: Plot of temperature over time for selected sensors in the temperature array. The black line designates when water begins flowing over the array.

The data show that initially, the ground temperature is cooling but then begins to heat up as the geyser source pool water level increases. It is interesting to note that the ground temperature increases by more than 10 °C from its coolest point before any water touches the sensor. This indicates that there may likely be a volume of space somewhere underneath the outflow channel that fills with water before the geyser erupts over the edges of the source pool and the heat from this water conducts through the ground and warms the sensor. In fact, if the chamber below the outflow channel is coupled to the source pool, then once the chamber is full, the source pool will rise and spill over the edge. There are a number of peaks and valleys in the temperature plot. These fluctuations can be seen in the geyser source pool where the activity briefly becomes more turbulent,

with vigorous bubbling, and then calms down even as the water level, on average, is rising. Additionally, the peak temperature recorded in the channel was 77.2 °C; however, this sensor (12) was close to the center of the channel and did not appear to have photosynthetic organisms underneath. The phototrophs disappeared somewhere around sensors 9 or 10 which recorded maximum temperatures of 75.5 °C and 76.5 °C, respectively. The literature (Brock 1978) places the upper temperature for photosynthesis at 75 °C, which is approximately the value recorded here (within error).

The data from these sites as well as data discussed in later chapters provide a strong indication that in most cases temperature plays a key role in determining where there is a transition to photosynthesis or transitions between visually-distinct photosynthetic communities in a hot spring. However, without having a number of other arrays measuring other chemical properties (e.g., pH or other dissolved chemical species) at small spatial scales, temperature cannot be said to be the only key parameter. Often times, as temperature changes, so do other parameters whose concentrations may be temperature dependent, so it can be said that if temperature is not the only factor in transitions to photosynthesis, it certainly may be a proxy for other important chemical concentration changes. As is so commonly found in the natural world, there are always outliers such as the example shown in Figure 3.30, where neither temperature, nor pH, nor conductivity could explain why the photosynthetic mat had such a sharp boundary at the intersection of the two outflow channels. In that case, it is possible there was some toxin in the clear stream that inhibited the green microbial community.

The transitions to photosynthesis and between adjacent photosynthetic communities were found, in almost all cases, to correspond to fairly linear temperature

gradients across the visible boundaries rather than step-like functions which might be assumed given the sudden appearance of photosynthetic microbes. Unfortunately, longer duration measurements were not made across the boundaries. It would be interesting to learn how quickly a particular community responds to change in temperature at these photosynthetic transition zones. As was seen in the outflow channel of the geyser at Imperial Geyser Basin – there are photosynthetic microbes that can adapt to a wide range of temperature (35 °C – 76 °C) and water flow conditions. The MEMS sensors provide the new capability to measure temperature fluctuations across these transition boundaries at smaller spatial scales than previously possible and over long periods of time and therefore can be used to address questions about the environmental-biological system dynamics such as: 1) *What is the rate at which these photosynthetic communities respond to temperature changes that may occur on a daily, weekly, or longer scale?* and 2) *What range of temperatures can a photosynthetic microbial community withstand from a short-duration pulse heating event?*

3.10 Long-term Temperature Monitoring Station

It is well understood that hot spring systems are dynamic. Source pools and outflow channels resulting from either volcanic or tectonic activity will change from year to year in terms of topography, water level, chemistry, and temperature. In fact, since these systems rely on meteoric water, they are strongly influenced by local weather patterns such as rainstorms and droughts and therefore can change on a daily basis. When researchers collect data from hot springs at a particular time on a particular day, they are making inferences about the geology, chemistry, and biology based on a snapshot in time. It is therefore important to move beyond this paradigm and begin understanding the role

of daily, weekly, monthly (and longer) weather and climate effects on these systems. YNP's National Park Service currently has a policy discouraging researchers from leaving scientific equipment at the hot springs for more than a day due to environmental preservation and human and animal safety concerns and is probably right to do so at this juncture in time. Fortunately, there are hot springs located on private land in Gerlach, NV in which the owner is agreeable to allowing equipment to be left for long periods of time. This allows us a test-bed for a long-term monitoring station where any 'kinks' related to environmental preservation and human and animal safety can be worked out so that these systems may be suitable for deployment at YNP in the future.

With the land owner's approval, a long-term temperature monitoring station was set up at the Great Boiling Spring hydrothermal system of the Great Basin hydrothermal system in Gerlach, NV. There are three pools connected to one another in this system (Figure 3.38). The westernmost (and smallest) pool is called Great Boiling Spring (GBS) which has its own source. To the east of GBS (but still connected to it at the surface through a small outflow channel), is the larger GBS16 pool (which also may have a shared source with GBS), and furthest to the east is another pool connected through an outflow channel to GBS16 with no source which people sometimes use as a natural hot tub.

Figure 3.38: Google satellite image of Great Boiling Spring hydrothermal system. Data are being collected from the GBS pool and from the Great Boiling Springs hot spring (GBS16) pool (Costa et al. 2009) along the edge near the bathing pool (yellow oval).

In the main source pool (GBS), 16 individual RTD sensors were placed at different locations (Figure 3.39).

Figure 3.39: Photographs of Great Boiling Spring hot spring (GBS), Gerlach, NV, from two different directions where the first long-term monitoring station was set up. The red dots represent the locations where 16 individual RTDs were placed in the hot spring. The numbers correspond to the sensor numbers provided in the following plot. Arrows pointing north are provided for orientation. The GBS pool is ~6.5 m in diameter.

The temperature sensors were the same commercial MEMS RTDs used previously. PTFE insulated wires were soldered to the RTD leads and the bonds were reinforced with epoxy (H77 – Epoxy Technologies). Each of the sensors was coated in Parylene-C for additional protection. Teflon weights were tied to the ends of some of the sensors to ensure they would sink and to hold them in place. Each of the sensor wires was soldered to a long multi-conductor cable encircling the hot spring. This cable was connected to an electronic

circuit of the same design as the one described above in order to monitor the resistance of the RTDs. The data were processed by a data acquisition device. The temperature data were recorded hourly and sent through satellite communications via an iridium modem. A large number of lithium ion batteries connected in parallel were used to provide the power for the long-term measurement system. The electronic circuit, data acquisition device, batteries, and modem were housed in a water-tight Pelican™ case. The Pelican case set up, termed the Behar's Environmental Networking, Telemetry, and Observation (BENTO) Box, was put together by postdoctoral researcher Andres Mora. Dr. Mora also performed all the programming of the electronics in the box which were used to process and send the temperature data. Data were post-processed and made available through a website. Hourly data for the 16 sensors, plotted over three months is provided in Figure 3.40.

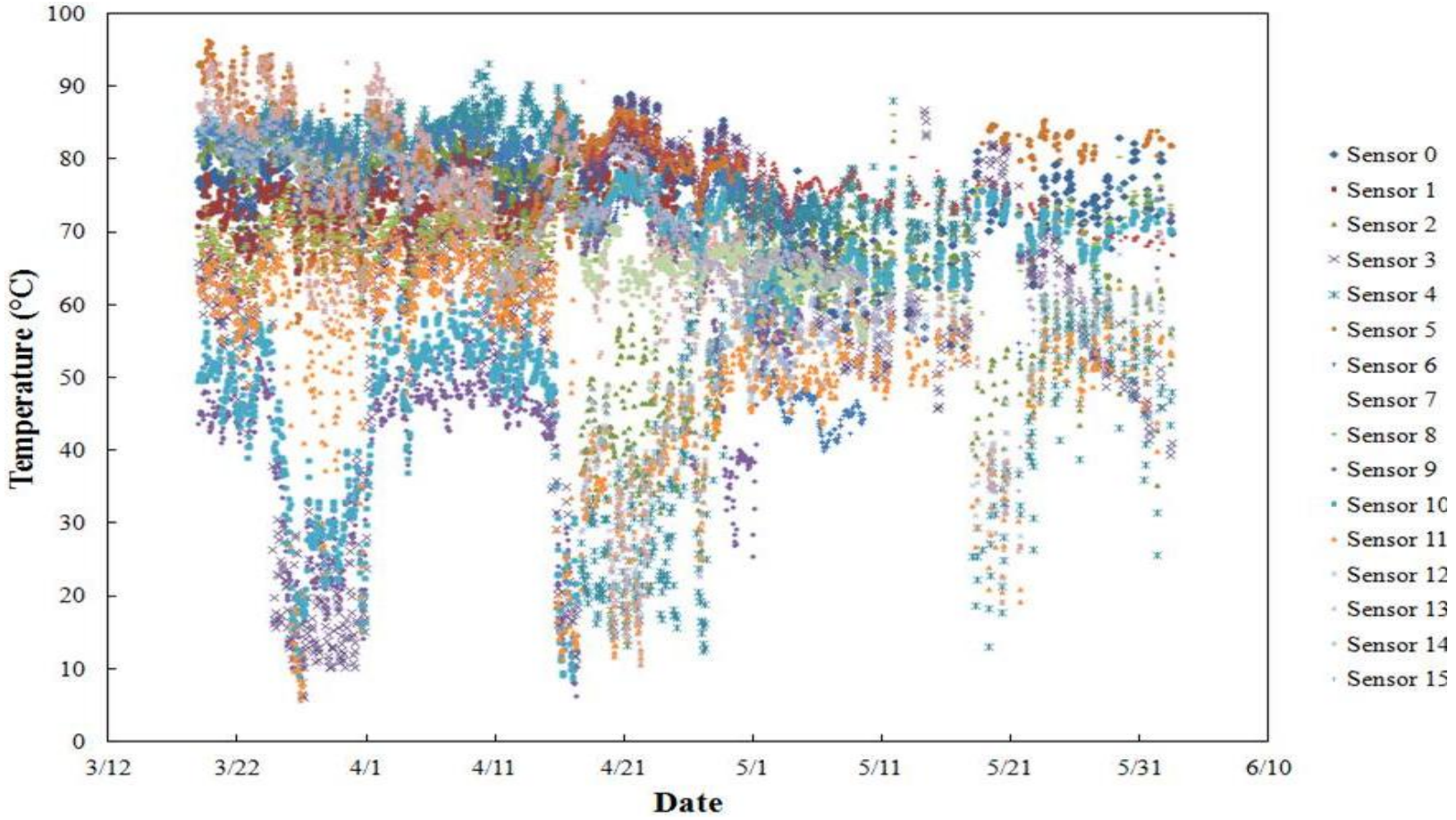

Figure 3.40: A plot of temperature as a function of time for the 16 RTDs over a 3 month period between March, 2012 and June, 2012 for the GBS pool.

The plot is a busy one but when all the sensors are plotted together, some interesting features are seen. There are three notable periods over five or more days, where a number of the sensors show extreme drops in temperature. When the first temperature drop was noticed near the end of March, 2012, it was originally presumed that weather may have damaged some of the sensor connections where they interface with the BENTO box. However, the sensor measurements returned to normal after several days. The second temperature drop that occurred on 4/18/2012 and, serendipitously, one of my colleagues was at the site and able to photograph what was happening at the pool (Figure 3.41).

Figure 3.41: (left) Photograph of the Great Boiling Spring pool after sensor installation. (right) Photograph of Great Boiling Spring pool on 4/18/12 showing receded water level. The GBS pool is ~6.5 m in diameter.

The pictures show that the water level in the pool had receded significantly, exposing a number of the sensors located in shallower portions of the pool (i.e., sensors 2, 3, 4, 9, 11, and 13) to the air. These sensors were no longer recording the water temperature, but rather the air temperature which explained the large temperature drop. Based on the temperature data, these drainage events are not all that uncommon with evidence for perhaps three events over a period of less than a few months. Most importantly, this data

provide the evidence for why long-term monitoring stations are important. When scientists study and report on the microorganisms living in these hot springs, the assumption is that the temperature and water conditions on the day that they are taken are representative of the environment that the microbes experience. However, as this example shows, microorganisms found around the edges of the hot spring pool in 65 °C water have to withstand periodic conditions of desiccation and large temperature drops of as much as 50 °C.

A second temperature monitoring station consisting of 14 sensors and a second BENTO box was set up around the far edge of the GBS16 (Figure 3.42).

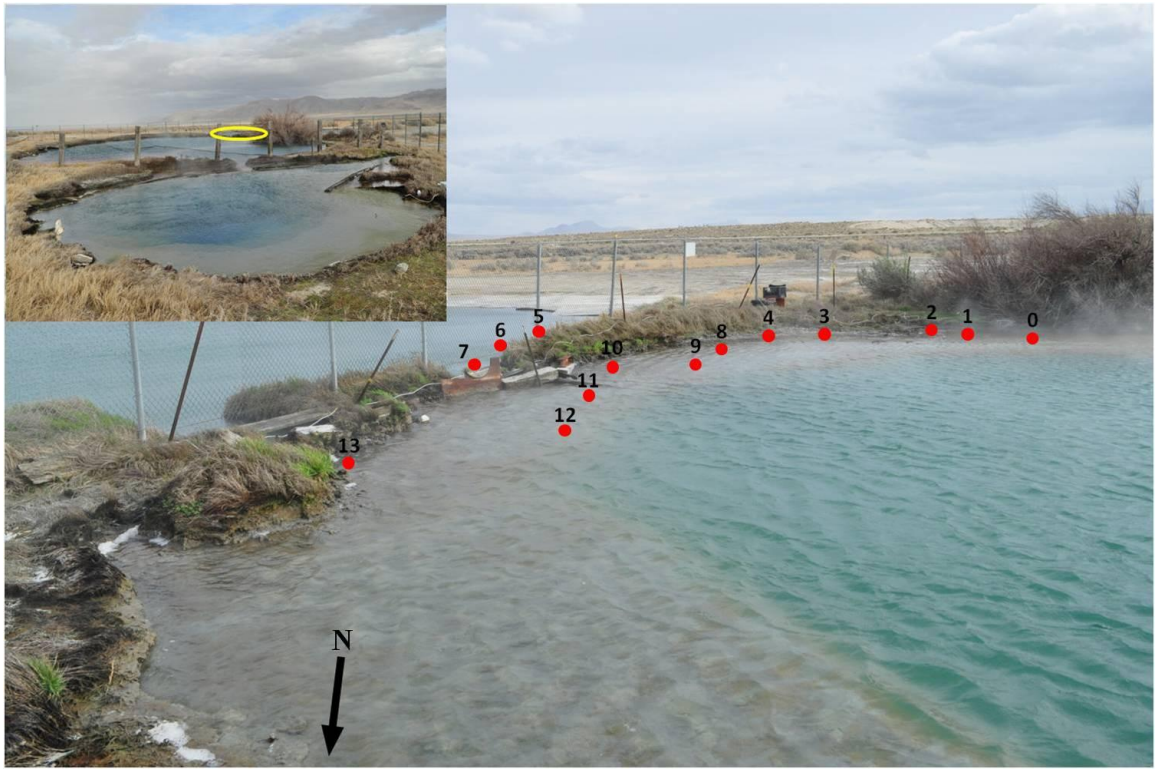

Figure 3.42: Photograph and location of the 14 RTDs located around GBS16 pool. The inset shows the location of the sensors relative to the GBS source pool. The yellow oval is the same oval from Figure 3.38 showing the satellite image. Arrow pointing north is provided for orientation. The GBS16 pool is ~25 m in diameter.

Three of the sensors were placed in the bathing pool adjacent to GBS16. The technique for wiring and bonding the sensors used in the second monitoring station was improved. A plot of the temperature for 11 working sensors over the past 10 months is provided in Figure 3.43. Although not as clear as in the previous (three month) plot, the drops in temperature experienced by sensors 0 and 4 (the shallowest sensors) match the approximate dates at which temperature drops were seen in the GBS pool, independently confirming those events.

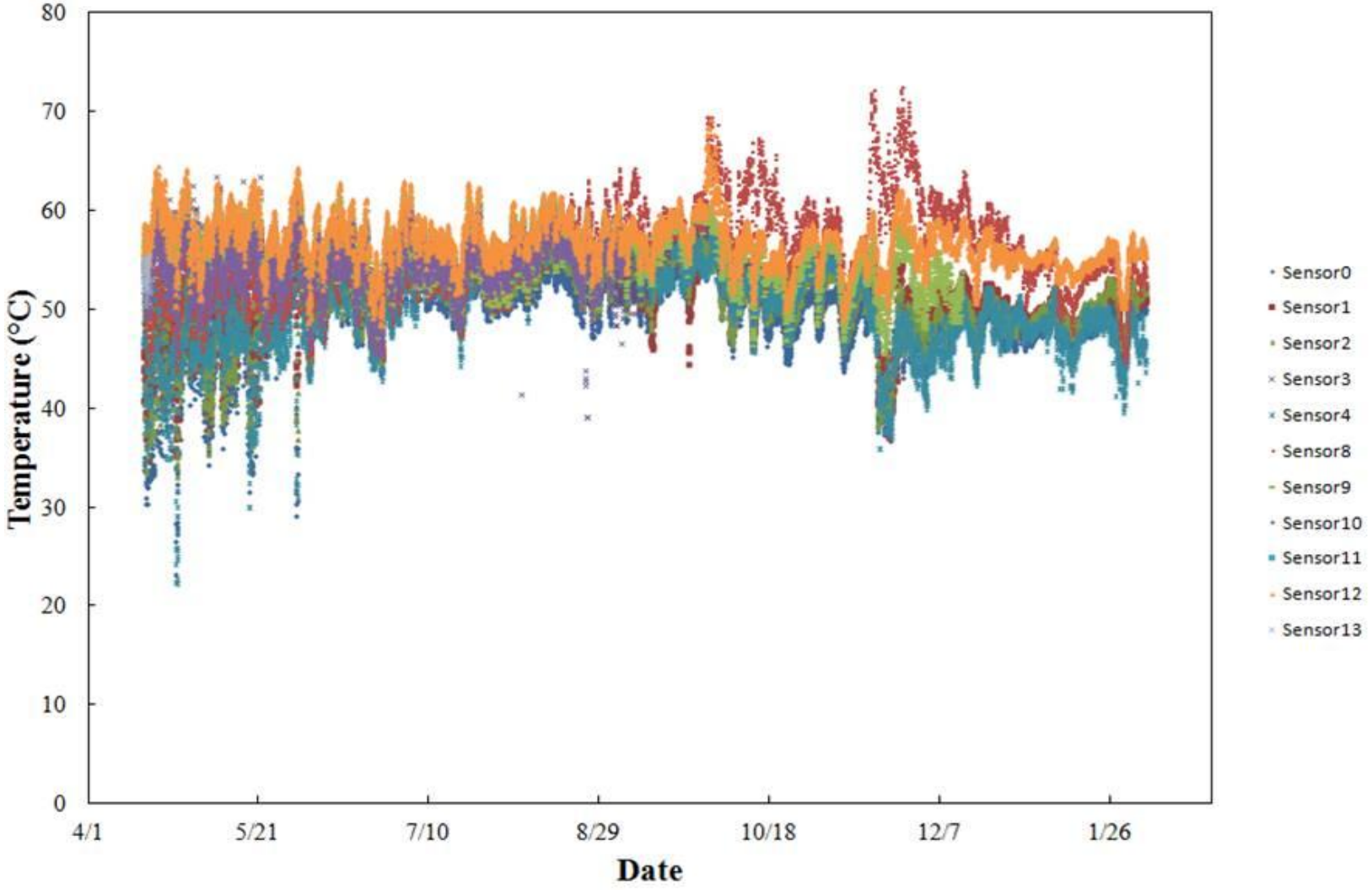

Figure 3.43: Temperature data for 11 RTDs located in GBS16 (adjacent to GBS) over the previous 10 month.

Unfortunately, over time a number of sensors began recording inaccurate data, which is why data from the first monitoring station is not provided after ~3 months. The improved wiring and epoxy methods employed for the sensors as well as improved solder connections to the multi-conductor cable leading to the BENTO box in the second monitoring station appears to have improved the lifetime of sensors in the hot spring system by as much as 9 months (and counting). Therefore, with additional improvements to the sensor wiring design, a near 100% yield of sensor data could be collected easily over 1 year.

There is a lot of time-varying structure seen in all of the sensors in these plots. Understanding the structure of these temperature plots may reveal important factors governing the dynamics of this system. A cursory examination of the time when the relative peaks and troughs appear did not appear to correlate with a specific time of day or wind speed profiles; however there are a number of other factors that have yet to be compared such as air temperature, other weather effects such as rain, and seasonal changes.

3.11 Conclusion

Various MEMS temperature sensor arrays were developed to measure temperature at spatial scales smaller than previously possible in the harsh environment of terrestrial hot springs. The temperature sensors were designed as resistance temperature detectors and the final version involved using a high TCR metal nickel deposited on a fused quartz substrate. An electronic circuit was developed in order to take 15 simultaneous measurements from each sensor in the array. A LabView program was

written in order to interface with the electronic circuit and to display *in-situ* temperature measurements in real-time.

The temperature arrays were tested and deployed at geothermal sites in Yunnan Province, China and in Yellowstone National Park, U.S.A.. The China data highlight the new capability that the temperature arrays can be placed in a vertical configuration into the floor of the hot spring to provide 2D plots of temperature at different locations and depths. The Yellowstone National Park data show that temperature may play a key role in the transition from non-photosynthesis to photosynthesis, and in transitions between photosynthetic communities. In some cases, the detailed temperature profiles indicate that transitions in the photosynthetic community are not associated with clear temeperature gradients, indicating that temperature is likely not the only parameter controlling these biological transitions. In addition, the temperature change measured across the photosynthetic boundaries is not a step function but rather an approximately linear one. Long-time-duration measurements are critically important for understanding the range of conditions in which the biology is exposed. These small size, robust, low power, and high resolution MEMS devices will provide researchers with the capability to create ‘movies’ instead of ‘photographs’ about the dynamic life of microorganisms and the hot spring environments. Temporal changes for both short-duration temperature shocks to the sytem and long-term daily, seasonal, and yearly changes can be monitored.

The temporal structure of the long-duration measurements may provide insight into the extraneous factors that most affect the dynamics of the hot spring systems. However, there are a number of additional challenges posed by long-duration measurements due to material degradation from the long exposure time to the harsh

environment, data recording and transmission, and other factors such as biofouling which are not discussed here, yet none of these issues seem insurmountable in the development of new technology and techniques for hydrothermal research.

CHAPTER 4: MEMS ELECTRICAL CONDUCTIVITY SENSOR ARRAYS

On the early Earth (> 1.5 billion years ago and < 3.5 billion years ago), as river water flowed across the landscape, it reacted with rock and soil, carrying large quantities of the most easily dissolved elements (e.g., sodium) and delivered them into the first oceans (Sverdrup et al. 2003) that already contained large amounts of chloride from volcanic outgassing (Maisonneuve 1982) and thus formed sodium chloride (NaCl) – perhaps the most widely recognized salt. In this way, the early oceans accumulated salt, but they also lost some through evaporative deposition (Knauth 2005). Today, the world's oceans contain approximately 3.5% by mass NaCl salt and most rivers emptying into them now carry lower concentrations of less soluble elements (e.g., calcium) gleaned from water-rock interactions and can form other salts (e.g., $CaCl_2$). These elements (along with several others) have been labeled as conservative constituents because their concentration ratios relative to one another do not change, even when the overall salt concentration changes. Conservative constituents are also typically unaffected by the presence of living organisms (Sverdrup et al. 2003).

Continental hydrothermal systems, of which the Yellowstone National Park hot springs are a subset, are the ultimate dynamic geochemical systems. In a similar process that made the oceans salty, water interacts with rock and delivers the leached chemical constituents to hot spring source pools and outflow channels. As the meteoric water percolates down through the permeable and fractured rock, it's heated as it comes into contact with higher temperature rock warmed through contact with magma. For the Yellowstone system, the rock is heated from being in contact with magma associated with the Yellowstone Supervolcano. In addition, the water is supplemented by anions due

to the influx of volcanic gases such as carbon dioxide (Fournier 1984) and is often under high pressure and thus becomes superheated before it makes its way back to the surface (Figure 4.1).

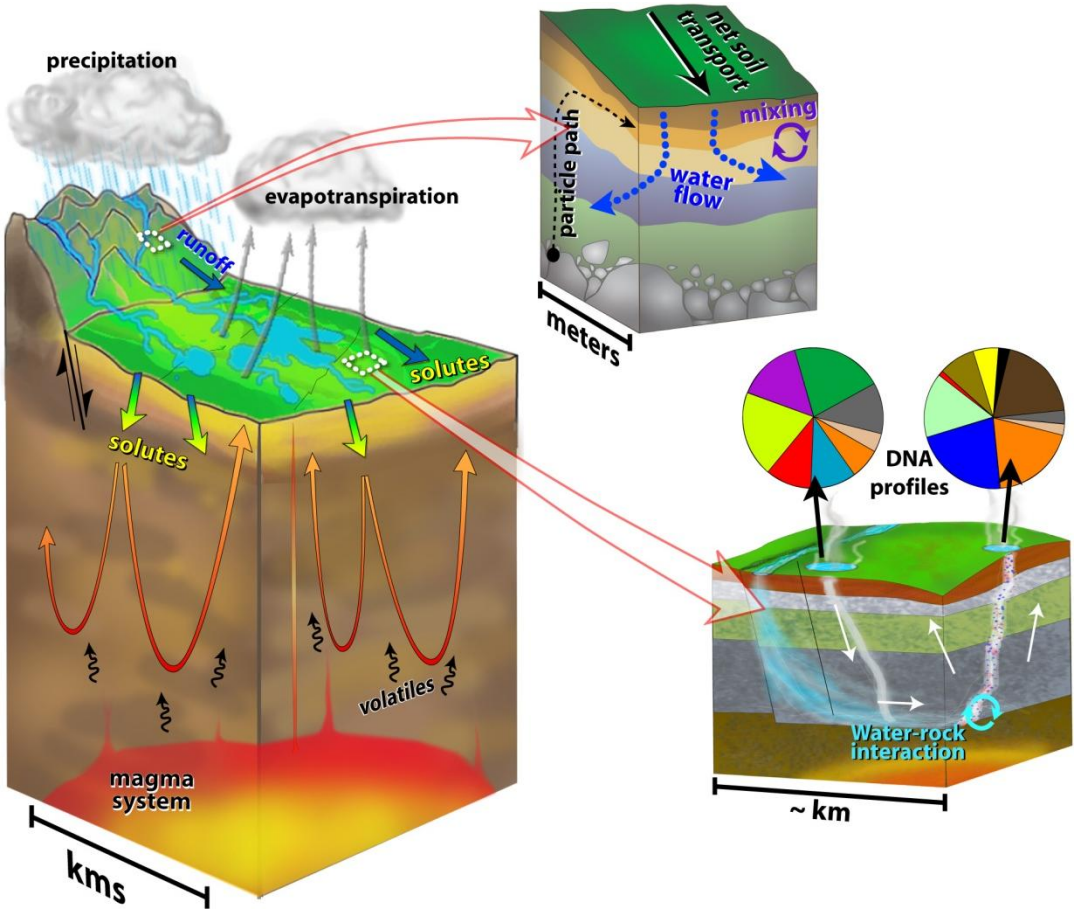

Figure 4.1: Illustration depicting the underlying processes responsible for the biogeochemical conditions found in the hot springs. (Credit: Ed Garnero and Everett Shock).

Compared to the slow and steady salinization of the oceans on a billion year time scale, the dynamic hydrothermal systems cycle water and chemicals much faster due to their small size, high temperature, and the influence of external effects such as the weather. The high fluid temperature increases the rate of chemical reactions and the solubility of some of the constituents. The hydrothermal waters contain both conservative constituents

and nonconservative constituents, and the specific chemistries of the hot springs at Yellowstone National Park can vary by orders of magnitude in concentration (Shock et al. 2010); there are equally large differences in the resident organisms of hot springs (Meyer-Dombard et al. 2005).

Quantifying the geochemistry of these hydrothermal systems is critical to understanding the biological ecosystems that thrive within them. In principle, the identification of all chemical species present in the hot spring and their associated concentrations could be carried out. However, in practice, identifying every chemical and its concentration might not even be possible given analytical constraints. Fortunately, researchers can make targeted measurements that provide a general picture of the hot spring chemistry and can use that information to choose which additional samples to take and measurements to make. The three most common geochemical measurements performed on hot springs are temperature, pH, and electrical conductivity. Temperature, as discussed in the previous chapter, provides information about the type of biological systems expected to be present (chemosynthetic or photosynthetic) as well as about chemical and biochemical reaction rates. The pH measurement specifically provides the activity (a measure of effective concentration) of hydrogen (H^+) ions present in a unit volume of water. Since H^+ ions are strongly reactive, the pH can provide information about the influence of chemical weathering in the hot spring. In addition, the pH is a strongly-dependent factor in how much biologically-available energy can be gained from various chemical reactions (Shock et al. 2005). Measurements of electrical conductivity are used quantify the number of ions in a volume of water. Conductivity is related to the amount of dissolved salt in solution. The specific measurement of salt concentration is

called salinity and is a complicated function of both of temperature and conductivity. Though salinity is the desired value, conductivity is an acceptable proxy for salinity and can be directly measured *in-situ*.

As mentioned in Chapter 3, transitions to photosynthesis in hot springs often have a dramatic appearance and can occur in <1 cm and drove the development of the temperature arrays. In the same way, the scientific question driving the development of the MEMS conductivity arrays is: *What role does changes in conductivity play in the transition to photosynthesis and transitions between photosynthetic communities?* This question is, perhaps, not a critical one, since it is known that conductivity likely does not play as important a role as temperature and pH do in these transitions (Cox et al. 2011); however, from an engineering standpoint the device design requirements for operation in the harsh hot spring environment are significantly more difficult. This is due to the fact that current must be passed between electrodes through the hot spring water and because of these measurement requirements, the electrodes must be exposed to the water and therefore cannot be protected with the chemically-inert Parylene-C polymer. Thus, a conductivity sensor array is the next step from a temperature array in terms of engineering difficulty, with the most difficult being a pH sensor array.

4.1 Electrical Conductivity Sensors

Electrical conductivity is a measure of how easily an electrical current passes through a material. The parameter describing how much the current flow is impeded is defined as the resistivity (see Chapter 3 for more discussion). Therefore, electrical conductivity is simply the reciprocal of resistivity.

The aim of an electrical conductivity sensor then, is to provide a source of current to be 'pushed' from one location to another (voltage) through the fluid. For a given amount of current, the resistance of the fluid can be measured by knowing how much 'push' is necessary through Ohm's Law (discussed in Chapter 3). In order to perform the most basic conductivity measurement, two electrodes are required. A known current is passed between the two electrodes and the voltage drop between them is measured, which provides a measure of resistance (Figure 4.2). As discussed in Chapter 3, resistance is a function of length of the resistor, or in this case, the separation between the two electrodes. The inverse of resistance is conductance (measured in units of Siemens, S) which is also a function of the electrode separation. Therefore, normalizing by the electrode separation provides a comparable quantity of resistivity or its inverse, conductivity.

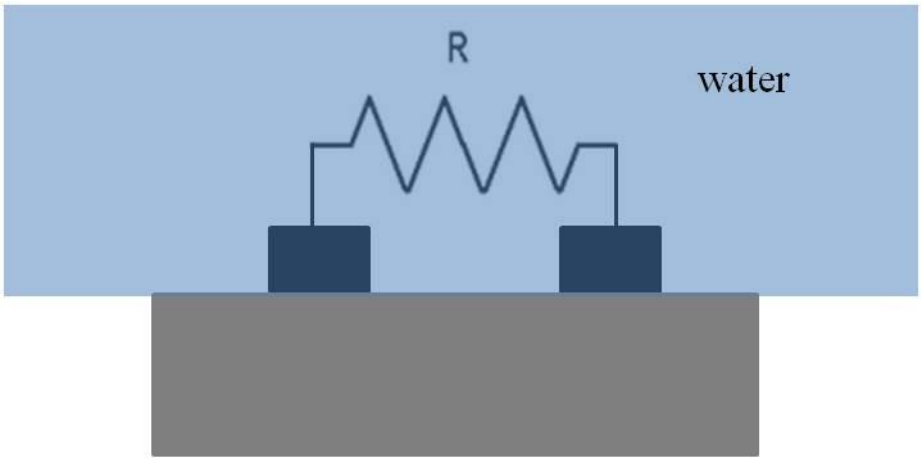

Figure 4.2: Schematic of the electrical conductivity measurement. Current is passed between the two black square electrodes. The ions work as charge carriers and the solution acts as a resistor, and the resistance value is inversely proportional to the number of ions between the electrodes.

While this basic conductivity measurement is simple, obtaining an accurate measurement with low error requires a more complicated knowledge of the electrical conductivity measurement. Since the measurement being taken is essentially resistance, any additional resistance contributions from the sensor itself and the interface between the sensor and the liquid decrease the accuracy of the measurement. In order to use a two-electrode sensor (two-point probe), the current must be passed through the same electrodes from which the voltage drop is measured. In practice, any two-point probe not only has two electrodes but also metal leads connecting those electrodes to the bond pads where the wires are soldered (Figure 4.3).

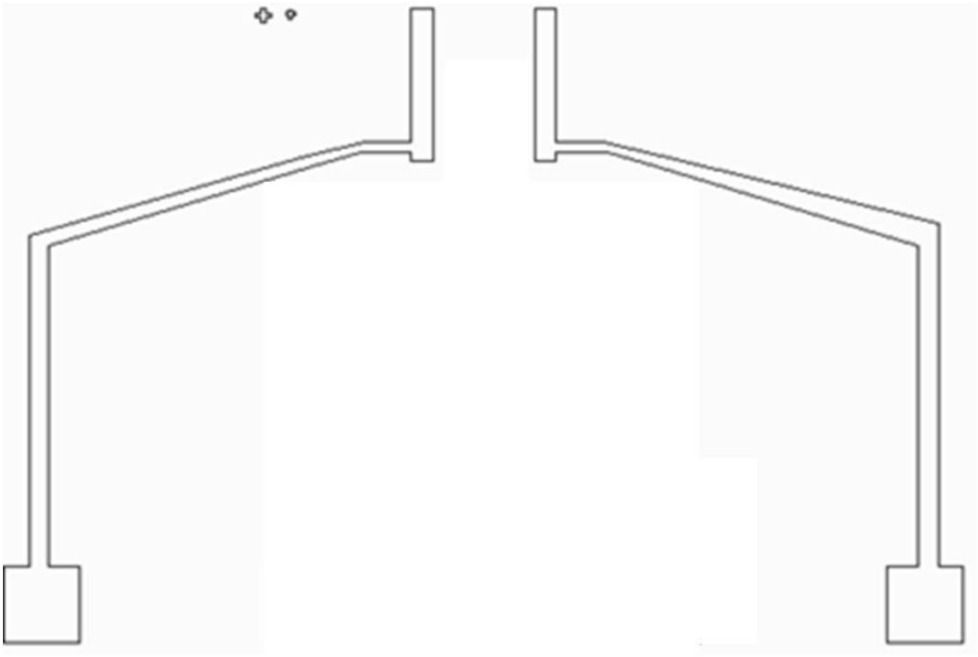

Figure 4.3: Schematic drawing of a two-point conductivity sensor. The electrodes are located at the top of the image and the square bond pads at the bottom with leads to connecting the bond pads to the electrodes. Measurement of both the current that is passed and the voltage drop is performed at the same electrodes and leads. The small shapes to the left of the electrodes are alignment marks for fabrication. Distance between the electrodes is ~1 cm.

The leads must be long enough such that any post-processing involving the soldering of wires or covering of the solder connections with epoxy does not affect the electrodes which should be as clean as possible. The bond pads are separated farther apart than seems necessary so that a resistance temperature detector (RTD) can be fabricated between the electrodes (discussed later in the chapter). However, the leads are fabricated of the same metal as the bond pads and electrodes and are sources of resistance to the current flow; therefore, the leads contribute to the total resistance measured by the sensor and thus affect the predicted value of the conductivity. For measurements of high conductivity (low resistance) solutions, these additional resistance sources will reduce accuracy. Additionally, since the leads are made of metal (platinum), they will increase in resistance with a temperature increase. Because they are placed directly in the hot spring, the heated leads provide more resistance than can be accounted for with calibrations at room temperature and will further reduce accuracy.

In order to reduce the effects of the resistance contribution from the leads, a four electrode sensor (four-point probe) can be used. In the four-point probe, the current is passed between the outer (force) electrodes and the voltage drop across the inner (sense) electrodes is measured (Figure 4.4).

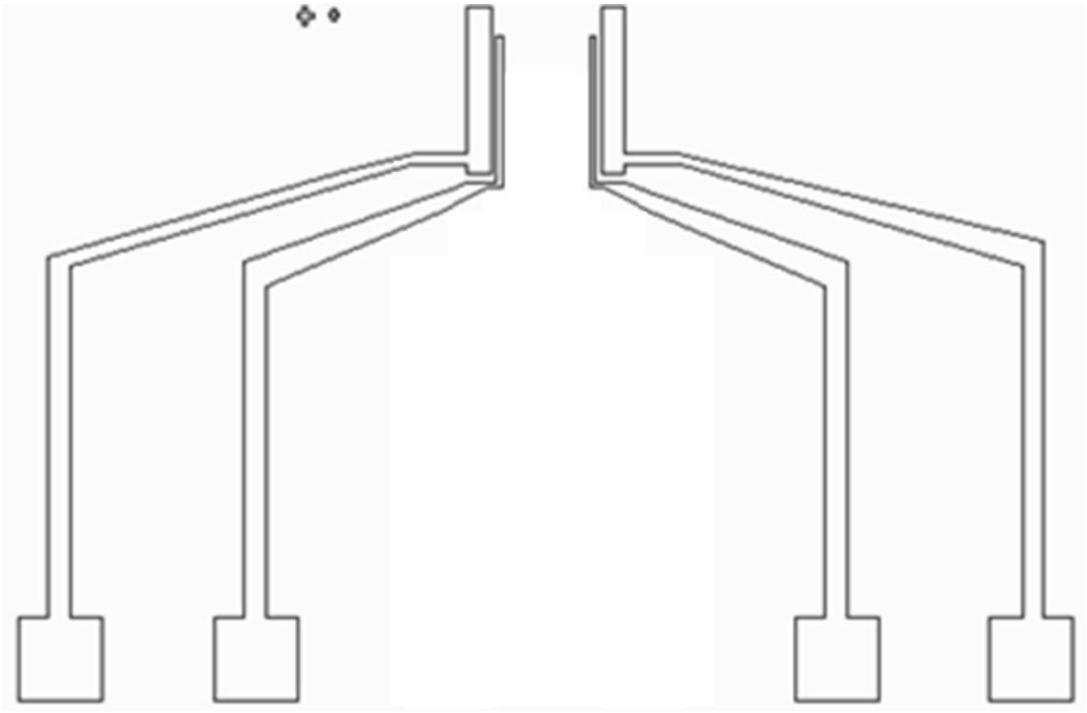

Figure 4.4: Schematic drawing of a four-point conductivity sensor. The electrodes are located at the top of the image and the square bond pads at the bottom with leads to connecting the bond pads to the electrodes. Current is passed between the outer electrodes and the voltage drop across the solution is measured at the inner electrodes. The small shapes to the left of the electrodes are alignment marks for fabrication. Distance between the outer electrodes is ~1 cm.

In order to measure the voltage drop across the sense electrodes a much smaller current can be used than is required to drive the force electrodes, thereby making the lead resistance contribution to the overall resistance (or conductivity) measurement negligible (Li and Meijer 2002).

There are additional physical effects at the electrode-solution interface that contribute resistance error in the measurement. For a given current, the smaller the electrode from which the current flows results in a larger the current density (current per unit area). Large current densities, especially when using direct current (DC), have the capability to separate molecules and actively create new molecular species such as

splitting the water molecule into hydrogen gas at the cathode and oxygen gas at the anode. Since the electrons supplied at one end of the electrode are being used in the electrolysis reaction and producing additional ions, the measurement of electron resistance through the solution is less accurate. There are two techniques employed to combat the potential for electrolysis. The first is to use a lower current density. Lower current density can be achieved by lowering the current utilized in the measurement and/or increasing the size of the electrodes. Using the lowest the current possible is always the best option, but it must large enough to be measured above the noise. The largest electrodes that are allowed by the measurement requirements should be used as well. In this case, the electrode size is restricted by the desire to make conductivity measurements at the centimeter scale in order to probe the photosynthetic transition zones. This effect also places design limits on how small conductivity sensors can be fabricated before current density becomes a major problem. The second technique employed to minimize electrolysis is to use an alternating current (AC). Alternating currents switch the direction at which electrons flow at a specific rate depending on the frequency of the current. Switching the current direction switches whether the electrode performs the anode or cathode reaction. Switching the electrode polarization maintains the original number of ions in the solution. However, using an AC current complicates the measurement since a simple battery cannot be used to generate the signal as was the case for the RTD measurement.

Another source of resistance error comes from the electrodes themselves. Metal ions of the electrode material will dissociate into the liquid solution and at the same time metal ions in the solution will deposit onto the surface of the electrode. At equilibrium,

the rate of dissociation and deposition will be equal, and although the net current is therefore zero, there is still charge transfer across the electrode-liquid interface. Therefore, inert electrodes such as platinum or gold are preferred since the number of atoms exchanged with the solution at equilibrium is very small and this effect can be neglected (He 2001).

The most critical source of resistance error is called polarization impedance. Polarization impedance arises from charged electrodes being placed in a solution of mobile ions and electrons. A positively charged electrode will attract negatively charged ions (and electrons) to the surface of the electrode. Similarly, a negatively charged electrode will attract positively charged ions. The presence of opposite charges at the electrode interface separated at a finite distance (even if very small) creates a capacitor. The capacitor created by the charged electrodes and ions at the surface of the electrode in solution is called the double layer capacitance (Figure 4.5).

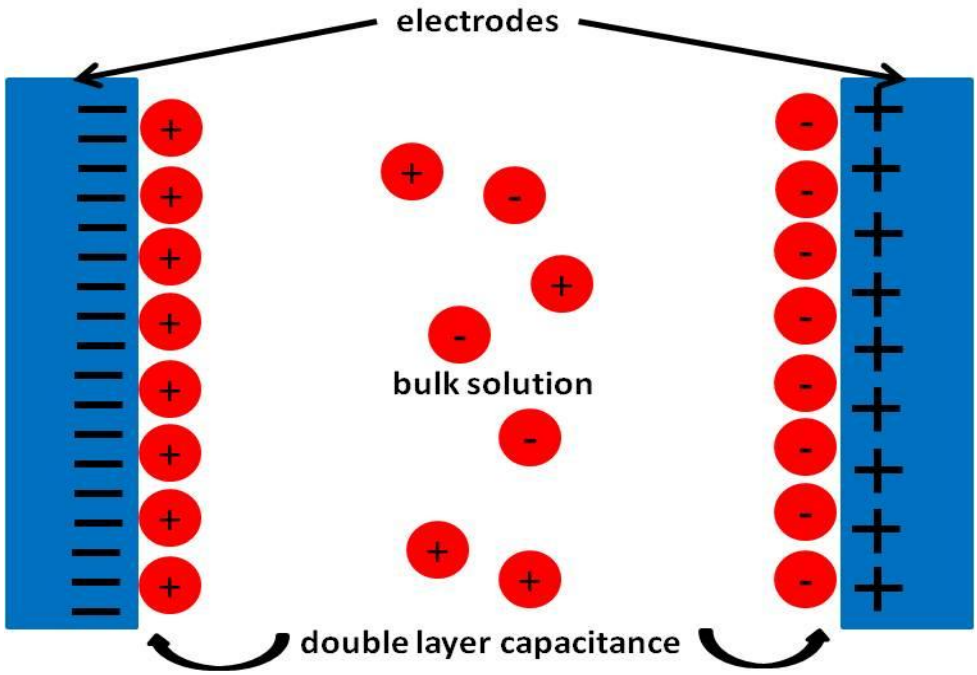

Figure 4.5: Schematic of charged electrodes in solution of mobile ions. Negative ions are attracted to positively charged electrodes and vice versa. The charge layer sets up the double layer capacitance.

The double layer capacitor acts like a capacitor in any electrical circuit. A low voltage applied to an electrode will attract the mobile ions in the solution and charge the capacitor. Once the voltage is increased enough such that the maximum number of charges is lined up near the electrodes, any increase in voltage will allow current to flow between the electrodes. Figure 4.5 and the explanation of the double layer are simplified in their descriptions. In reality, the double layer is much more complicated due to the complex interactions between ions, polar solvent molecules, and the electrode surfaces (Braunstein and Robbins 1971). As the AC voltage is increased and an AC current is passed between electrodes, chemical reactions driven in both directions will follow the current variation. If, for example, the AC current is sinusoidal, then a sinusoidal chemical concentration gradient will occur at the electrode-solution interface and propagate out

into the bulk solution. The resulting diffusion due to the varying concentration gradient creates a complex impedance (resistance) commonly described as the Faraday impedance (He 2001). The double layer capacitor and the Faraday impedance act in parallel and define the polarization impedance of the electrode (Figure 4.6).

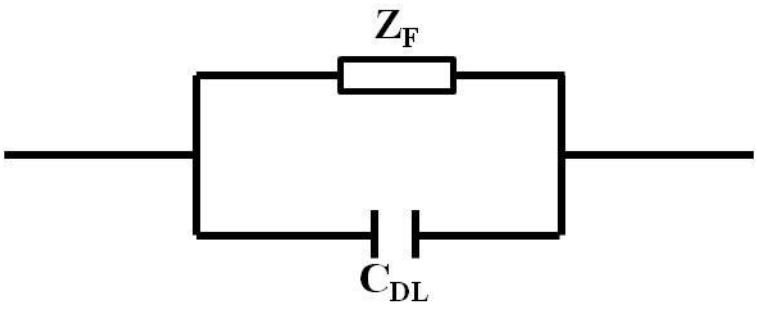

Figure 4.6: Electrical model of the electrode polarization impedance shows the Faraday impedance (Z_F) in parallel with the double layer capacitor (C_{DL}).

The electrical circuit model of the four-point probe in solution is shown in Figure 4.7, where the impedance (resistance) between the inner sense electrodes, R_{SOL}, is the solution resistance which is the targeted measurement.

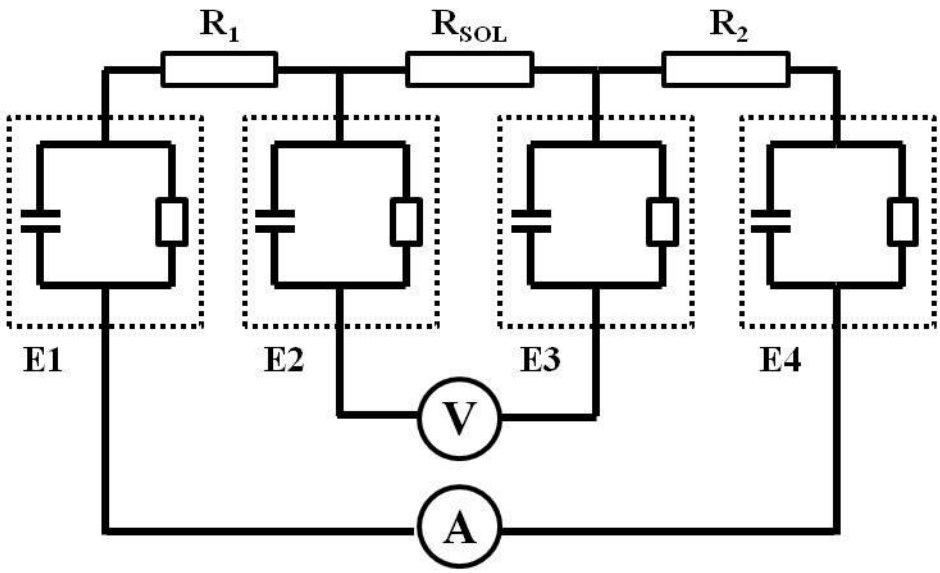

Figure 4.7: Electrical model of the four-point probe. The resistances of the liquid solution between the outer force electrodes and the inner sense electrodes are given as R_1 and R_2. The resistance between the inner sense electrodes is given as R_{SOL} and is the desired measurement of the solution resistance. The electrode polarization impedances are labeled as E1-E4. The voltage (*V*) is measured between the inner sense electrodes and the current (*A*) is passed between the outer force electrodes.

The polarization impedance is a strong function of the frequency of the AC current. Choosing a higher frequency AC signal will decrease the effects of both the Faraday impedance and double layer capacitive impedance and therefore reduce the resistance error contribution (Kordas et al. 1994) and improve measurement accuracy. However, generating a high frequency signal and reading the high frequency output makes the readout circuit more complex.

4.2 Electrical Conductivity Arrays

An electrical conductivity sensor array was designed such that conductivity measurements could be made at a scale similar to that of the temperature measurements from Chapter 3 (cm scale). Therefore, the spacing between each sensor was fixed at approximately 1 cm. Understanding the sources of resistance measurement error provided

more guidelines for the design of the each sensor. To reduce lead resistance effects, a four-point probe geometry was used. To minimize one aspect of the electrode impedance, the highly inert metal platinum was chosen for the interface with the liquid.

While measurement error concerns dictate that the electrodes have as large a surface area as possible to minimize current density, the error issues do not specify the geometry of the four-point probe in terms of electrode dimensions and spacing. However, the range of conductivity values expected to be measured in the hot spring provides some design criteria. For example, a liquid solution with low conductivity, equivalently has a high resistance per unit length (resistivity). A high resistance per unit length would ideally be measured by electrodes with a large separation so the resistance measured would not exceed that which is capable of detection by the readout circuitry. Conversely, a liquid solution with a high conductivity (low resistance per unit length) would require electrodes with a small separation so that the resistance signal would be measureable above the noise.

The electrodes size and spacing can be ideally determined through the analysis of the cell constant. The cell constant is a number that is divided by the solution conductivity to give the solution resistance (not resistivity):

$$R_{SOL} = \frac{\kappa_c}{\sigma} = \rho\kappa_c = \rho\frac{l_E}{A_E}, \qquad \text{(Eq. 4.1)}$$

where R_{SOL} is the solution resistance, κ_c is the cell constant, σ is the solution conductivity, ρ is the solution resistivity, l_E is the effective path length, and A_E is the effective area within the conductivity cell geometry. Probes with low cell constants (~0.1 cm^{-1}) are used for measurements of low conductivity. Probes with high cell constants (~10 cm^{-1}) are

used for measurements with high conductivity. Since most of the measurements of conductivity in Yellowstone National Park are generally high but still cover a wide range (100-8000 μS/cm) a cell constant of 6 cm^{-1} was selected. Following the work of He (2001), the four-point probe electrode geometry can be determined from the cell constant with the following formulas derived by Hahne and Grigull (1971):

$$K_{CF} = K_{CT} F_C \left(\frac{S_1 - 2S_2 - 2W_2}{S_1}\right), \quad \text{(Eq. 4.2)}$$

where K_{CF} is the four-point probe cell constant, K_{CT} is the two-point probe (outer electrodes only) cell constant, F_C is a non-dimensional potential distribution correction factor necessary when changing between two-point and four-point probe geometries, S_1 is the separation between the outer electrodes, S_2 is the separation between the outer and inner electrodes, and W_2 is the width of the inner electrodes (Figure 4.8).

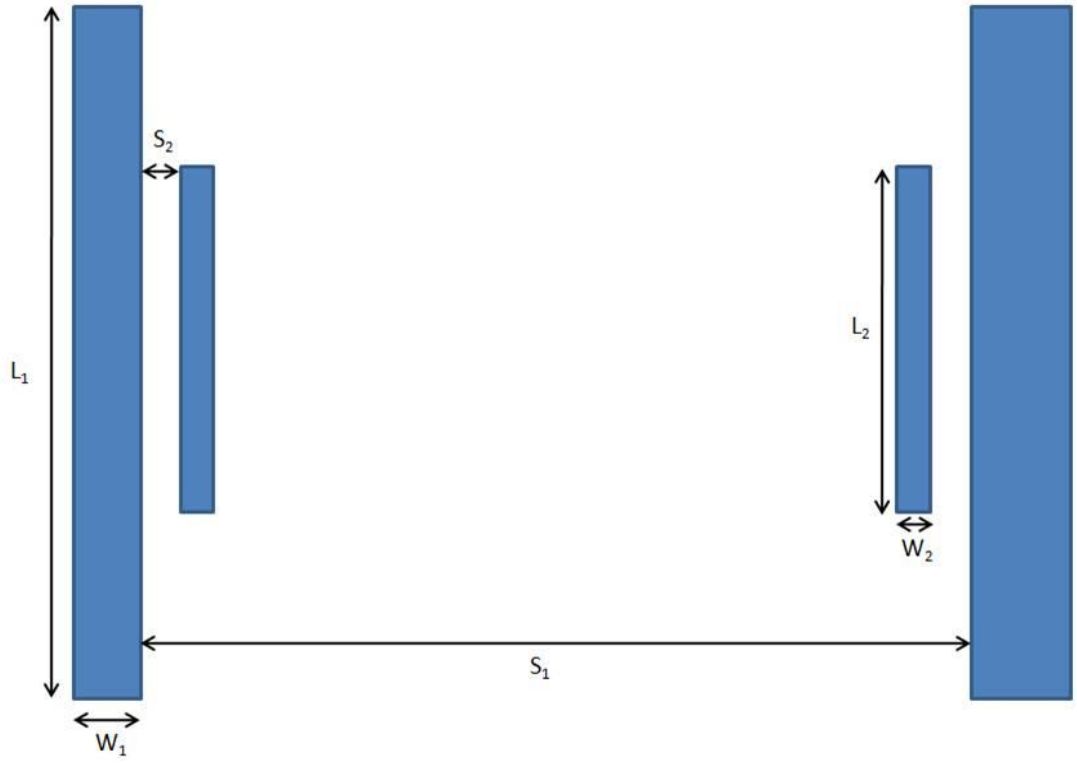

Figure 4.8: Schematic of the four-point probe electrode geometry and variables determined for a cell constant of 6 cm^{-1}.

The two-point probe cell constant K_{CT} can be determined via:

$$K_{CT} = \frac{2\theta(\gamma)}{L_1\theta((1-\gamma^2)^{\frac{1}{2}})}, \quad \text{(Eq. 4.3)}$$

where L_1 is the length of the outer electrode, γ is the non-dimensional ratio $S_1/(S_1+2W_1)$, and θ is given by:

$$\theta(\gamma) = \int_0^1 \frac{d\varepsilon}{[(1-\epsilon^2)(1-\gamma^2\epsilon^2)]^{\frac{1}{2}}}. \quad \text{(Eq. 4.4)}$$

The equations were modeled using Matlab® and the electrode geometry for a 6 cm^{-1} cell constant was chosen as L_1 = 1500 µm, W_1 = 215 µm, S_1 = 1000 µm, L_2 = 1000 µm, W_2 = 50 µm, and S_2 = 50 µm. These geometries were used in the design of the conductivity sensors.

Arrays of electrical conductivity sensors were fabricated on fused quartz substrates. Resistance temperature detectors (RTDs) were fabricated between the inner electrodes in order to determine temperature at the exact location of the conductivity measurement. Therefore, each sensor on the array incorporated six bond pads – two for the outer force electrodes, two for the inner sense electrodes, and two for the RTD. With six connections each, the maximum number of conductivity sensors that could be simultaneously read out using the data acquisition instrument described in Chapter 3 is five. If the RTDs are not used, the maximum number of sensors available for simultaneous measurement is eight. Eight was also the maximum number of sensors that could be fabricated in an array format on a 10 cm diameter wafer.

The fabrication flow process of the conductivity array is depicted schematically in cross-section in Figure 4.9.

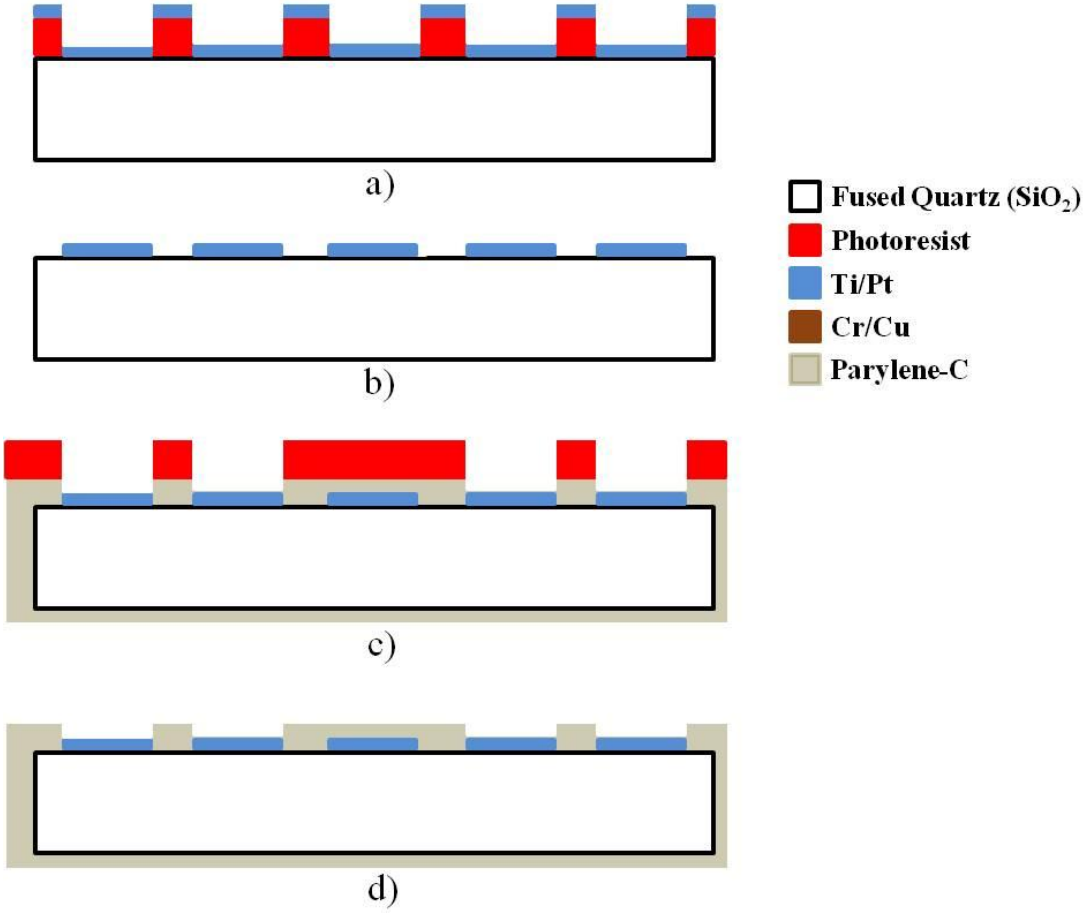

Figure 4.9: A schematic of the fabrication process flow for the conductivity array in cross-section. A layer of Ti/Pt is deposited and patterned on the wafer to create both the electrodes and the RTD in (a) and (b). Next a layer of Parylene-C is deposited over the entire wafer and selectively etched over the conductivity electrodes and bond pads (c) and (d). A platinum resistance temperature detector fabricated between the sense electrodes remains covered by the Parylene-C.

In the first step, a negative photoresist is deposited and the conductivity electrodes and meandering resistor geometry is patterned on top of a bare silicon (Si) wafer. Then, a 15 nm layer of titanium (Ti) is deposited followed by a 120 nm layer of platinum (Pt) using electron-beam evaporation. After metal deposition, the wafer is prepared for Parylene-C deposition. In order to create a strong bond between the Parylene-C and wafer, the wafer is immersed in an adhesion promoter wet bath of A-174 silane and isopropyl alcohol.

Following this step, the wafer is placed in the Parylene deposition chamber and undergoes a 5 μm thick deposition. The final step is to deposit and pattern positive photoresist over the electrodes and bond pads and remove the Parylene-C over top the electrodes bond pads using a dry O_2 plasma etch. The Parylene-C is not etched over top the RTD and therefore provides electrical insulation from the conductivity measurement processes as well as leakage protection.

As with the RTD arrays, following the fabrication of the conductivity arrays the wafers were diced to create separate arrays. Wires with PTFE insulation were soldered to the bond pads and a chemically-inert epoxy (H77 – Epoxy Technologies, Inc.) was used to strengthen the solder connections. Finally, Parylene-C deposition was performed on the arrays and wires. Since the electrodes must be exposed to the fluid, Kapton® tape was used to cover the electrodes during Parylene-C deposition. Following deposition, the tape was carefully removed and the electrodes were cleaned with a cotton swab and isopropyl alcohol. A picture of the completed sensor is provided in Figure 4.10.

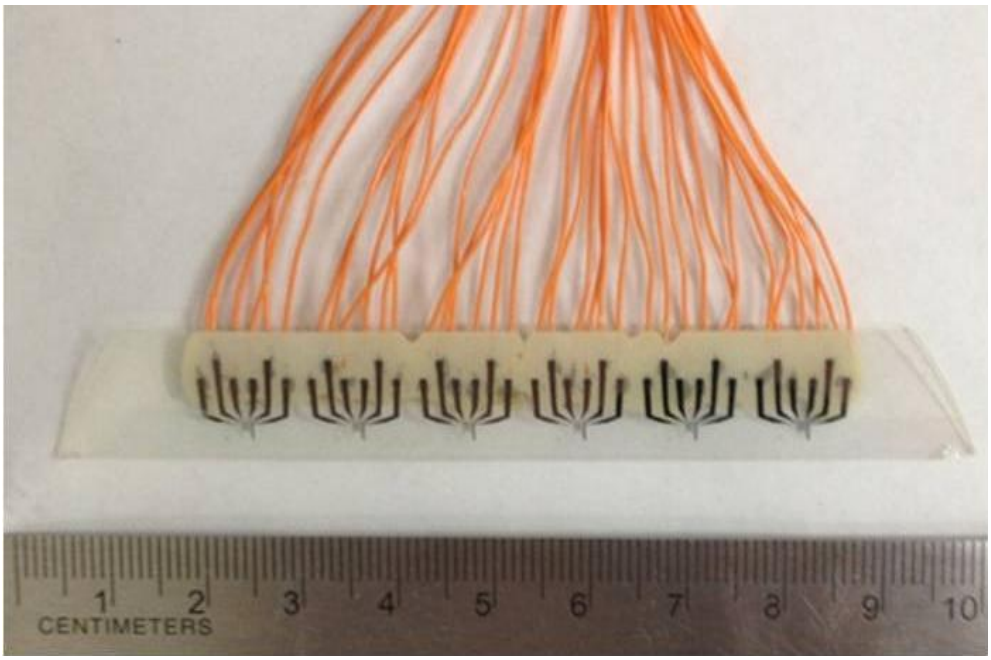

Figure 4.10: Photograph of a completed conductivity sensor array fabricated on fused quartz.

In fact, in the initial conductivity array fabrication, instead of platinum, nickel was used as the primary metal due to the fact that it has a higher TCR which would improve the sensitivity of the RTD that was fabricated in conjunction with conductivity sensor. Following the nickel deposition, a thin layer (15 nm) platinum was deposited on top of that as a protective coating for the electrodes exposed to the hot springs. The conductivity sensors were first tested in hot springs in Gerlach, NV, and after a day or two of testing, the electrodes were severely corroded (Figure 4.11) and the sensors were not working properly. Following this experience, all future conductivity sensor arrays were fabricated with platinum instead of nickel.

Figure 4.11: Photograph of the corroded electrode following operation for a few hours in a hot spring. One of the outer force electrodes is at the right of the image with the sense electrode located to its left. The non-corroded metal should appear black in this image as is seen at the bottom of the electrodes and in the meandering RTD to the left of the sense electrode which is covered by the transparent polymer Parylene-C. Epoxy covers a portion of the RTD in this image. The width of the outer right electrode is 215 μm.

The conductivity array sensors were calibrated with standard conductivity calibration solutions from Cole-Parmer, Inc. The standard conductivity solutions are specified to span a range from 84 μS/cm and 15,000 μS/cm at 25 °C. Calibration was performed at room temperature, close to the recommended 25 °C requirement. The solutions were poured into clean bowls and the sensors were submerged in the solution. The calibration curve for a five-sensor array based on nickel electrodes with the thin platinum cover layer is provided in Figure 4.12.

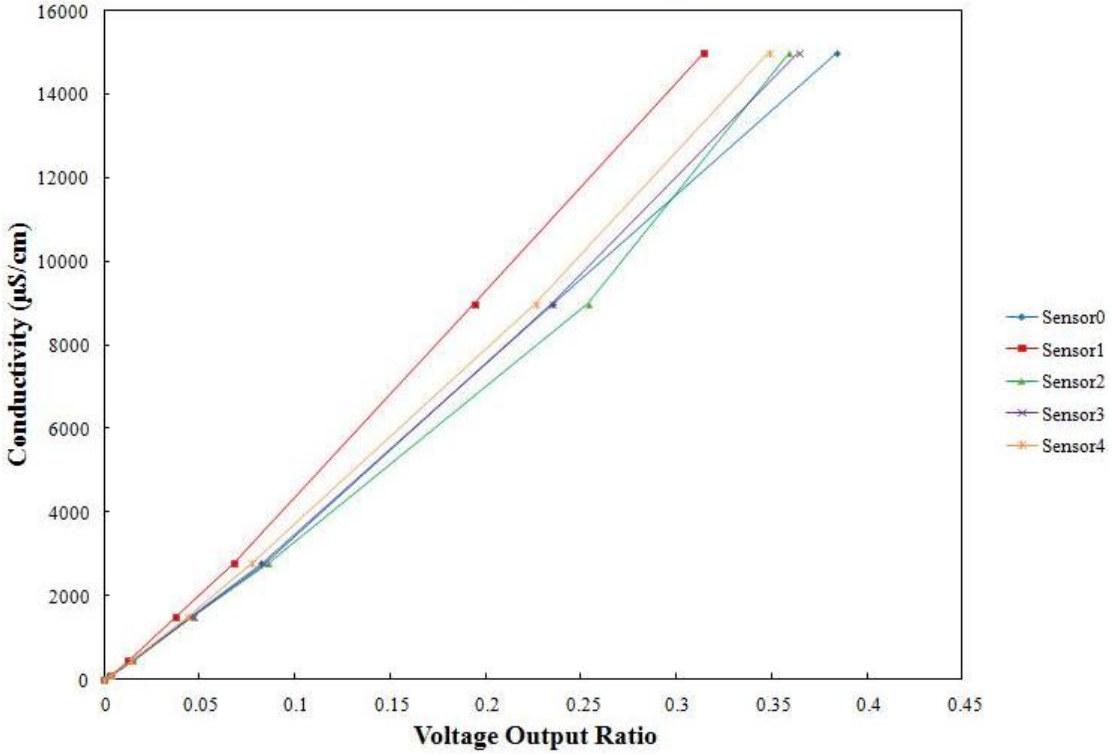

Figure 4.12: Calibration curve for the nickel-based electrode conductivity arrays used in Gerlach, NV.

The curves were not nearly as linear in conductivity as was expected, possibly due to the choice of a less stable metal (nickel) for the electrodes or due to the interaction between the nickel and the thin platinum layer over top. Nevertheless, equations were fit to the curves from each sensor and the sensors were deployed and tested at hot springs in Gerlach, NV.

Following the return from the hot springs at Gerlach, NV, the next batch of conductivity sensor arrays were fabricated using platinum instead of nickel and platinum. The calibration curves for these platinum five-sensor arrays (Figure 4.13) were much more linear and slightly more sensitive. In addition, all of the devices showed the same

responsivity to changes in conductivity. These platinum-only devices were deployed at Yellowstone National Park.

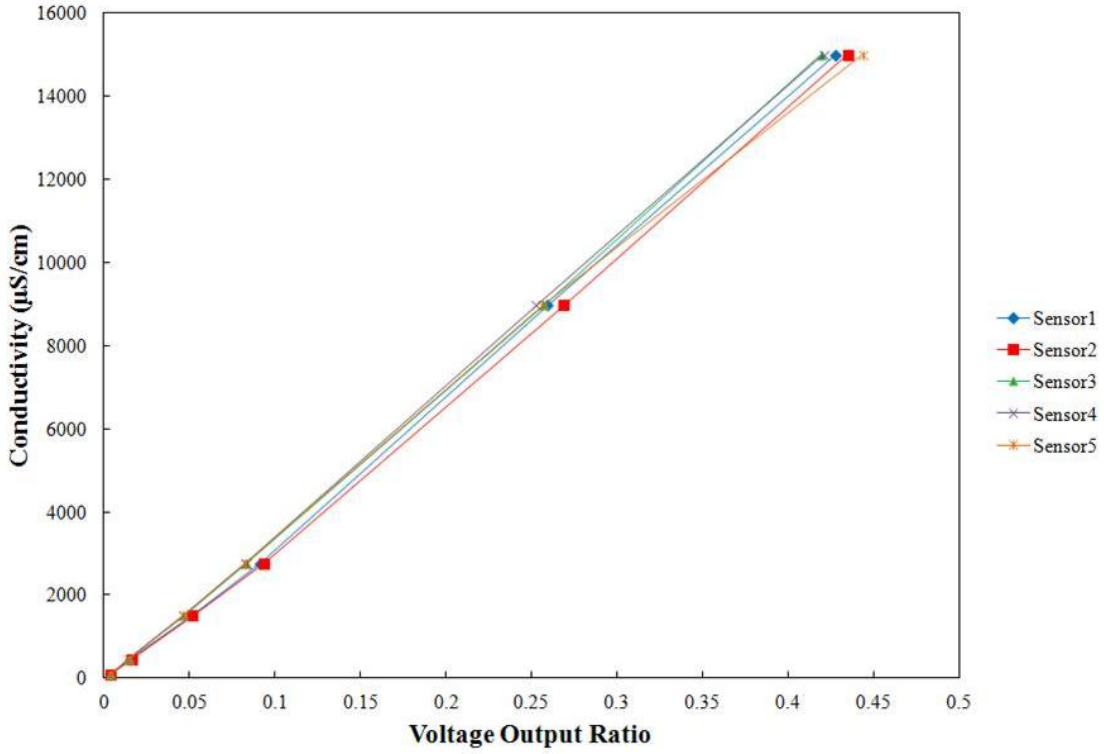

Figure 4.13: Calibration curve for the platinum-based electrode conductivity arrays used at Yellowstone National Park.

4.3 Electronic Read-Out

As mentioned earlier, the actual measurement from the solution is resistance. Again, using Ohm's Law, the resistance can be determined by knowing both the current through the solution and the voltage drop across the solution. The four-point probe incorporates two inner sense electrodes for directly measuring the voltage drop across the solution. The more difficult measurement is determining the current through the solution. The circuit layout and fabrication was carried out by a team of four undergraduate electrical engineering senior design students under my direction. The senior design team

chose the circuit based on the conductivity circuit example from Li and Meijer (2008). The circuit layout is provided in Figure 4.14.

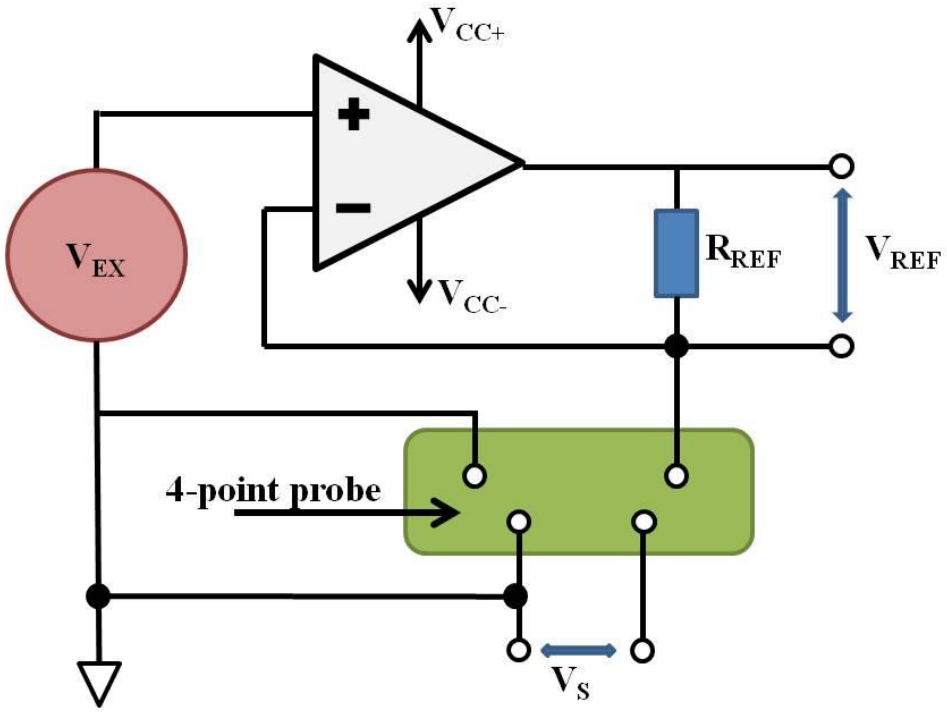

Figure 4.14: Circuit layout schematic for the conductivity measurement. The green shape represents the four-point probe. The sinusoidal excitation voltage V_{EX} is input to the outer force electrodes. The voltage drop (V_S) across the solution is measured at the inner sense electrodes. The current through the solution is determined by taking V_{REF} and dividing by the resistance R_{REF}. V_{CC+} and V_{CC-} are the voltage supplies to power the operational amplifier (triangle).

In this circuit, the input excitation signal (red circle) to one of the outer force electrodes of the four-point probe (green rectangle) is set by V_{EX} since a voltage of a specific amplitude and frequency is much easier to generate than the equivalent current. The V_{EX} signal is a 2 V peak-to-peak amplitude sinusoidal signal with a frequency of 1000 Hz generated by the data acquisition device described in Chapter 3. The operational amplifier (op-amp; white triangle) is set up in a non-inverting configuration. This means

the negative input pin of the op-amp will have exactly the same voltage as the positive input pin of the op-amp that is connected to V_{EX}. Therefore, the V_{EX} signal can be found at the rightmost outer force electrode and below the reference resistor R_{REF} (blue rectangle) in Figure 4.14. The voltage drop (V_S) across the solution of unknown resistance is measured by the inner sense electrodes. The same current that passes through the liquid solution will also be passed through the reference resistor R_{REF} since they are in series because an ideal op-amp will not allow current to flow to the negative input pin of the op-amp. In this way, the unknown resistance of the solution can be determined via Ohm's Law.

The Ohm's law equation determining the resistance can be expressed in terms of the resistance of the solution, R_{SOL}, the voltage drop across the solution V_{SOL}, and the current through the solution I_{SOL} and rewritten using the variables from Figure 4.14.

$$R_{SOL} = \frac{V_{SOL}}{I_{SOL}} = \frac{V_S}{\frac{V_{REF}}{R_{REF}}} = \frac{V_S R_{REF}}{V_{REF}}. \quad \text{(Eq. 4.5)}$$

Since conductance, C, is the inverse of resistance, it follows that the conductance equation is given by:

$$C_{SOL} = \frac{V_{REF}}{V_S R_{REF}}. \quad \text{(Eq. 4.6)}$$

In order to determine the conductivity of the solution, σ_{SOL}, Eq. 4.1 can be used, now knowing the solution resistance and the cell constant of the sensors, without using any calibration information. Therefore, the measurement of conductivity can be accomplished assuming the only contributions to the solution resistance come from the V_{REF}, V_S, and R_{REF} measurements and the cell constant, κ_C. However, a fairly complicated circuit is required in order to make these measurements, and each of the components in the circuit will contribute some tiny additional resistance component that will affect the

final output signal. Therefore, the previously mentioned calibration curves can be used to determine the conductivity. Wherever the resistance contributions come from in the circuit, the values of those contributions should remain constant. Therefore, since the output voltage ratio V_{REF}/V_S is proportional to the conductivity of the solution (multiplied by some unknown factor that includes all the resistance contributions of the circuit and the cell constant), we can use this voltage ratio in the calibration curve calculations. Since the calibration curves are linear, the conductivity equation is given by:

$$\sigma_{SOL} = G_m \frac{V_{REF}}{V_S} + B, \qquad \text{(Eq. 4.7)}$$

where B is the y-intercept of the calibration curve which is approximately zero since the voltage ratio is approximately zero when no conductivity is being measured (e.g., a measurement in air) and G_m is the unknown variable whose amplitude is constant and determined by the contributions from the resistances of all the circuit elements and the cell constant. The calibration equation can be used to directly measure the conductivity without knowing the resistance values or the cell constant.

The conductivity arrays were also capable of measuring temperature using a RTD fabricated between the sense electrodes. However, since temperature arrays were previously fabricated and with a desire to show the new capability to measure conductivity, the RTDs were not calibrated. Therefore all temperature measurements collected in the field are from the various temperature arrays.

One of the problems with the simultaneous operation of the conductivity sensors is that since all of the electrodes in the array are exposed to the water, there is an electrical path from one sensor's electrodes to an adjacent sensor's electrodes. And since the separation between the two outer electrodes of any sensor is almost the same as the

separation between electrodes of adjacent sensors, then there is sure to be electrical interference from one sensor's measurement on an adjacent sensor's measurement. Due to this possibility, the sensor readout circuitry was designed such that only one sensor was active at a time. This can be achieved using a multiplexer. A multiplexer is essentially a solid-state (non-mechanical) switch, which in this case, controlled which sensor received the input excitation signal and allowed the measurement of that particular sensor's voltage drops. Since there are 8 sensors, an 8-channel (8-input) multiplexer was required. However, since each sensor needs to output three different signals at one time (V_{REF}, V_S, and the voltage drop across the RTD), the circuit required three 8-channel multiplexers. The circuit layout was designed and built by the same senior design team and is shown in Figure 4.15

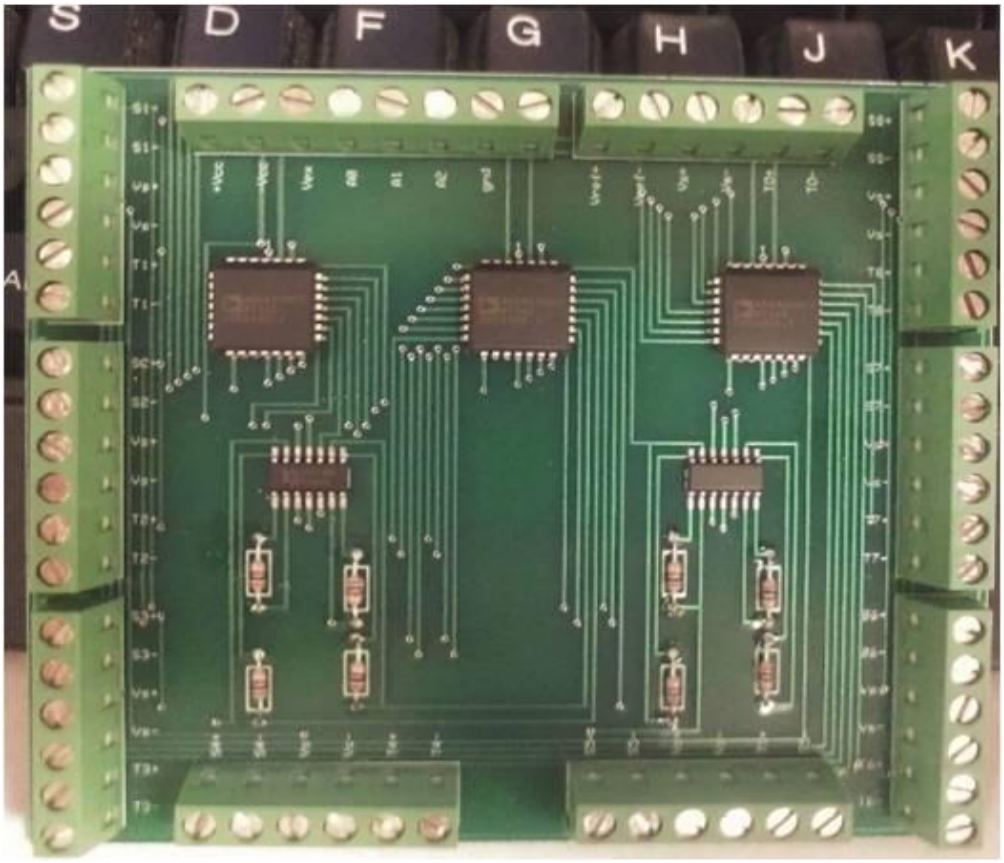

Figure 4.15: Photograph of printed circuit board built for making conductivity measurements. Around the outside of the board are screw terminal for the input wires from the conductivity array. The keyboard in the background is provided for scale.

Since multiplexers were used in the circuitry, the number of inputs to the data acquisition device was significantly reduced compared to that of the temperature array and therefore any number of conductivity sensors could be measured (8 sensors per 3 multiplexers) since the measurements are no longer simultaneous. However, the size of the fused quartz wafer (10 cm diameter) limited the maximum number of sensors in an array to eight (as did the number of multiplexers built on the printed circuit board). There were seven inputs to the data acquisition instrument from the printed circuit board (3 ground connections, V_{REF} output, V_S output, and two RTD outputs). There were six

outputs from the data acquisition instrument to the printed circuit board (two DC supply voltages for the op-amps, the sinusoidal AC excitation voltage, and three digital high/low outputs to control the multiplexers).

The software chosen to interface with the data acquisition instrument was LabView (see the software discussion in Chapter 3). This LabView program was created by the senior design students as well. The sinusoidal 2 V peak-to-peak excitation voltage was set through LabView. From the discussion above, a higher frequency excitation voltage will result in a lower resistance error in the measurement. So the highest frequency output (1000 Hz) allowed by the data acquisition device was used. The digital control to select the specific multiplexer output was setup so that each sensor in the array took five 1-second-long time-averaged measurements before the sensor was turned off and a new sensor was turned on. The mathematical operations needed to calculate the conductivity from the calibration curve equations were entered into LabView as well so that the conductivity values would be displayed on the computer screen during measurement. This allowed the sensor conductivity measurements to be directly compared to the commercial conductivity sensor brought to the field. These data were then output to a text file along with the corresponding time stamp.

4.4 Hot Spring Data from Gerlach, NV

The conductivity sensor array was first tested at hot springs located in the Great Basin region of the United States, specifically in the town of Gerlach, NV. The hot springs in this area are not driven by volcanic activity, but rather by heat generated from tectonic processes (Costa et al. 2009). These springs are generally very slightly alkaline (pH ~ 7.5). In one hot spring named Rick's Hot Creek, conductivity measurements were

made at different locations along the outflow channel, starting at the main source and moving downstream (Figure 4.16).

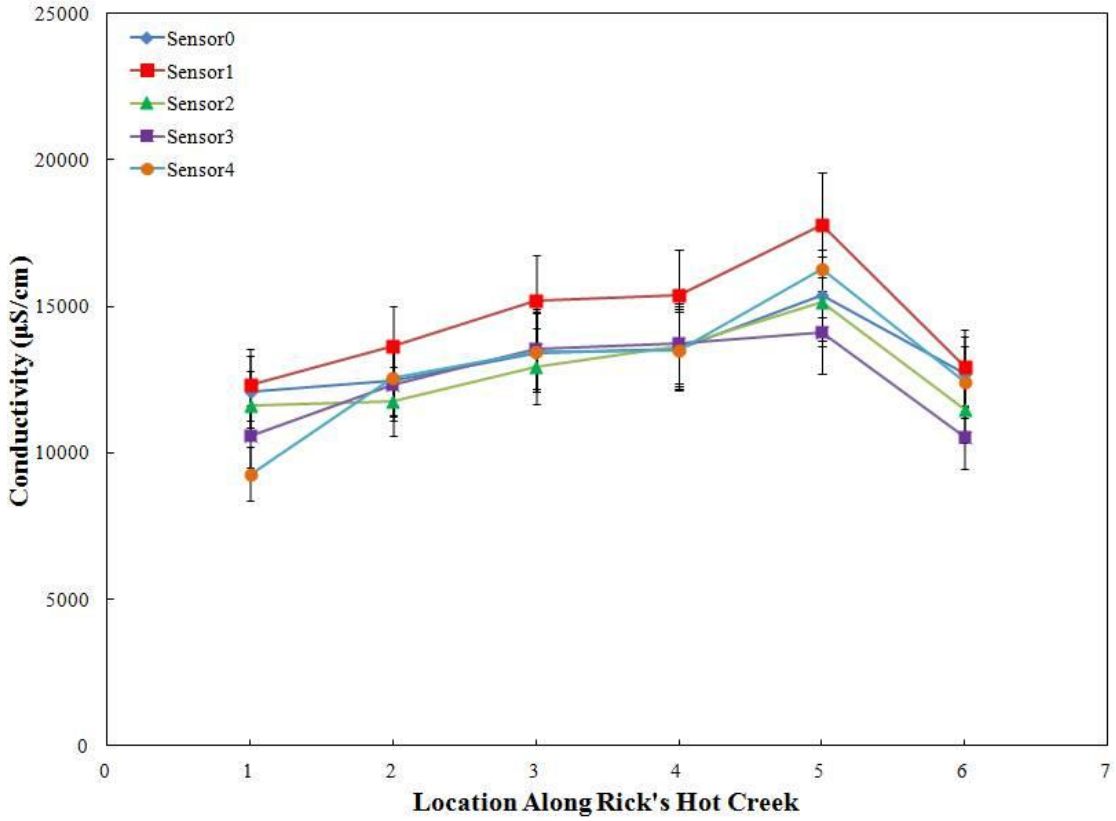

Figure 4.16: Conductivity measured by each sensor in the conductivity array at different locations downstream of the main source of Rick's Hot Creek. Locations are not equidistant. Error bars on all conductivity plots represent the uncertainty of 10% due to sensor system noise and calibration error.

The conductivity variance between the sensors was unexpected and somewhat dubious. A commercial conductivity sensor was also placed at these locations in order to compare data. Sensor 0 and sensor 2 match the commercial conductivity meter most closely. The variation of the other sensors could have been due to an incorrect calibration or to sensor damage. The temperature of this hot spring was extremely high with measurements of ~93 °C at the source and the high temperature could have contributed to the fast

corrosion of the nickel-platinum electrodes shown in Figure 4.11. Indeed, measurements conducted at other hot springs later in the day recorded values between 50,000 and 200,000 μS/cm, indicating that severe electrode damage had likely occurred.

All conductivity measurement values given in this dissertation are time-averaged values from an approximate 1 Hz sampling frequency typically measured for one minute. Error bars on the conductivity plots are 10% and represent the measurement error due to sensor and instrument noise and calibration accuracy. These error bars do not express the temporal variability of conductivity over the measurement interval. The temporal variability as expressed by one standard deviation from the mean conductivity is approximately 6% or less for all the reported values.

4.5 Hot Spring Data from Yellowstone National Park

Conductivity measurements were taken at a number of different regions within Yellowstone National Park. The combined data of temperature and conductivity from two hot springs at the Geyser Creek site will be presented in Chapter 5 and best highlights the utility of the conductivity array measurements. The conductivity measurements as stand-alone data are perhaps not especially interesting from a scientific standpoint; however, when paired with another measure such as temperature, the data become much more meaningful. For example, at one location at the Amphitheater Springs site, there is a bubbling hot spring source with high levels of sulfur. The sulfur precipitates out of solution as seen by the yellow deposits at the bottom of the channel. This hot spring outflow channel merges with another outflow channel filled with green photosynthetic bacteria (Figure 4.17).

Figure 4.17: Photograph of two hot spring outflow channels (yellow and green) merging. The length of the plastic box is 30 cm for scale.

Measurements of conductivity (red circles) and temperature (blue circles) were made across a region where the green bacteria are located next to the yellow sulfur precipitate (Figure 4.18).

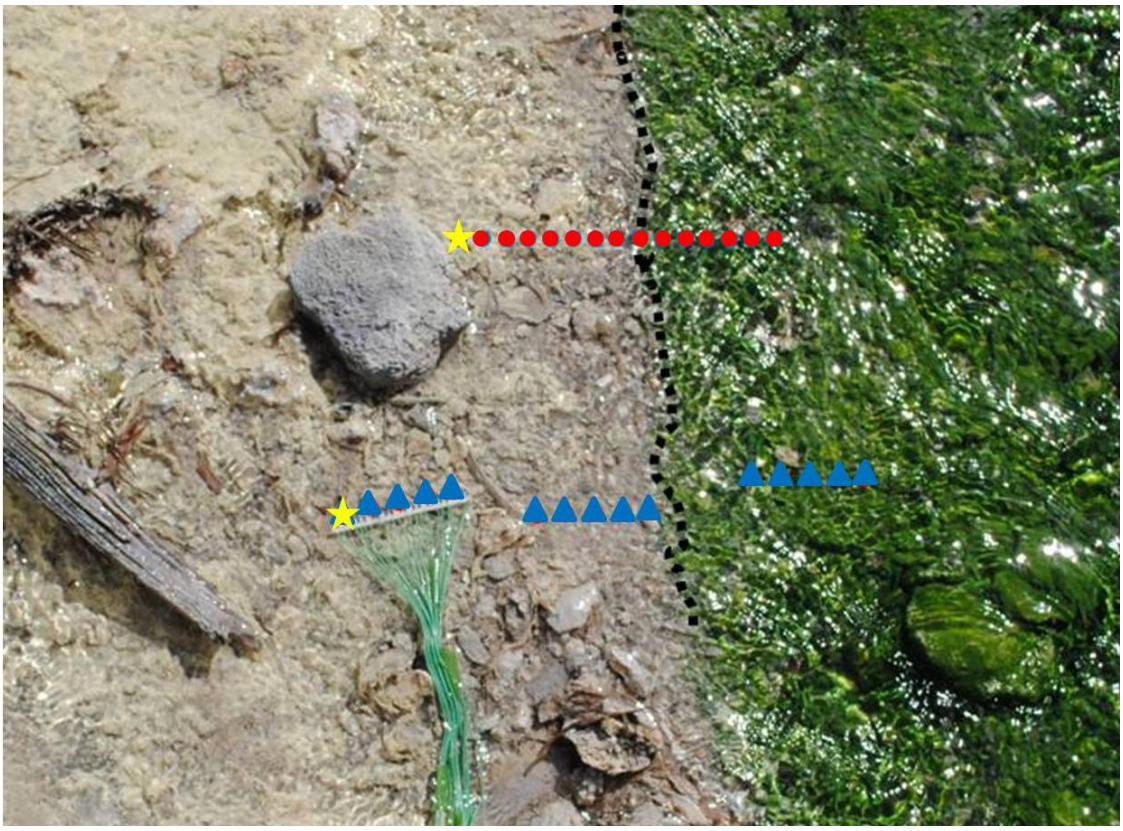

Figure 4.18: Photograph of boundary where two hot springs merge where green photosynthetic bacteria are juxtaposed with a region containing a yellow sulfur precipitate. Temperature (red circles) and conductivity (blue triangles) measurements were taken across the boundary. Yellow stars mark the zero positions for the next two figure plots. The long dimension of the conductivity array is ~6 cm for scale.

The plot of the temperature across the transition to photosynthesis is provided in Figure 4.19. As can be seen in the plot, the temperature remains relatively constant in the sulfur precipitate region at ≥ 70 °C.

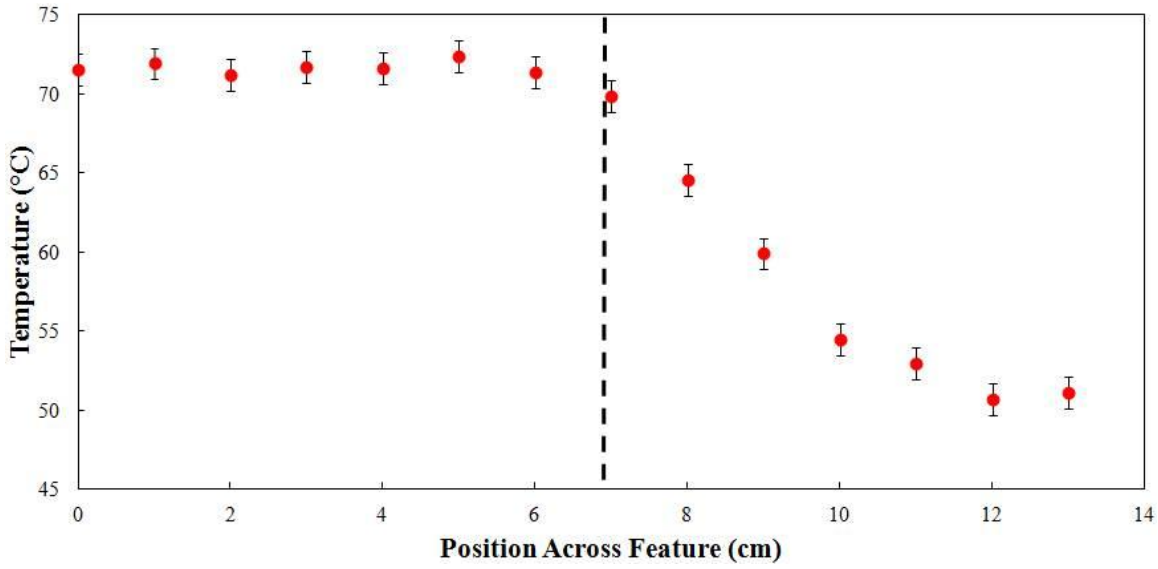

Figure 4.19: Plot of temperature across the photosynthetic transition zone. The sulfur region is at the left of the plot and the appearance of green bacteria occurs approximately where the dashed line appears and continues to the right of the line. The zero position corresponds to the yellow star in Figure 4.18. Error bars on all temperature plots represent the uncertainty of ±1 °C due to sensor system noise and calibration error.

The temperature at the sulfur source was ~73 °C. Once the temperature drops below 70 °C, the green photosynthetic bacteria suddenly appear. The microbial mat is continuous to the right of the image as the temperature drops to steady-state 50 °C. Numerous measurements in other sulfur precipitate regions show that as the temperature drops below 70 °C, the sulfur stops precipitating, or at least the yellow appearance to the channel is gone, regardless of whether a visible microbial community appears next to the precipitate zone or not.

In order to determine whether temperature is primarily responsible for the appearance of the green photosynthetic bacteria, measurements of other important parameters would ideally be made across the channel. A plot of the conductivity across the boundary is provided in Figure 4.20.

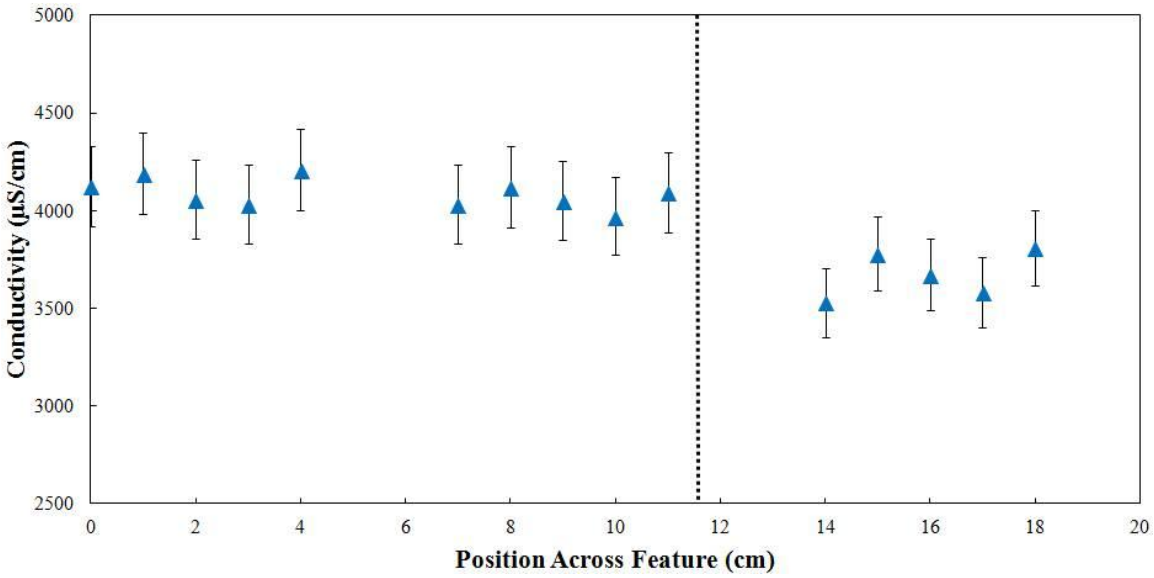

Figure 4.20: Plot of conductivity across the photosynthetic transition zone. The sulfur region is at the left of the plot and the appearance of bacteria occurs approximately where the dashed line appears and continues to the right of the line. The zero position corresponds to the yellow star in Figure 4.18.

As can be seen in the plot, the conductivity does not change noticeably across the transition zone suggesting the bulk ion chemistry is unlikely to be a factor in determining the appearance of the green photosynthetic bacteria. The 10% percent error in the conductivity is based on laboratory testing. Conductivity array data collected in the field were compared to a commercial conductivity meter at each location to verify the arrays were operating properly. While pH cannot be measured at small spatial scales across the transition zone as temperature and conductivity can, the pH on either side the zone can be measured by a commercial pH meter. The pH in the sulfur region was ~2.31 and in the green microbe region was ~2.38, and therefore pH is also not likely to be driving the transition to photosynthesis. Based on these data, temperature is likely responsible for the appearance of the photosynthetic community.

At another site in Norris Geyser Basin, oxidized iron (orange color) could be seen around a number of the hot spring source pools (Figure 4.21).

Figure 4.21: Photograph of a hot spring source pool in Norris Geyser Basin. The orange color around the pool is oxidized iron. The width of the source pool is ~1.5 m for scale.

The source pool had a temperature of ~89.1 °C, a conductivity of ~3640 µS/cm, and a pH of ~2.7. Whether the iron was being oxidized through biotic or abiotic processes, it was clear that oxidized iron was not present where water temperatures were highest (such as in the source pool and the outflow channel flowing from the source at the top of the image). Near the source pool in Figure 4.21 there were four small, shallow, but separate source pools (Figure 4.22). The temperature and conductivity were measured in each of the pools.

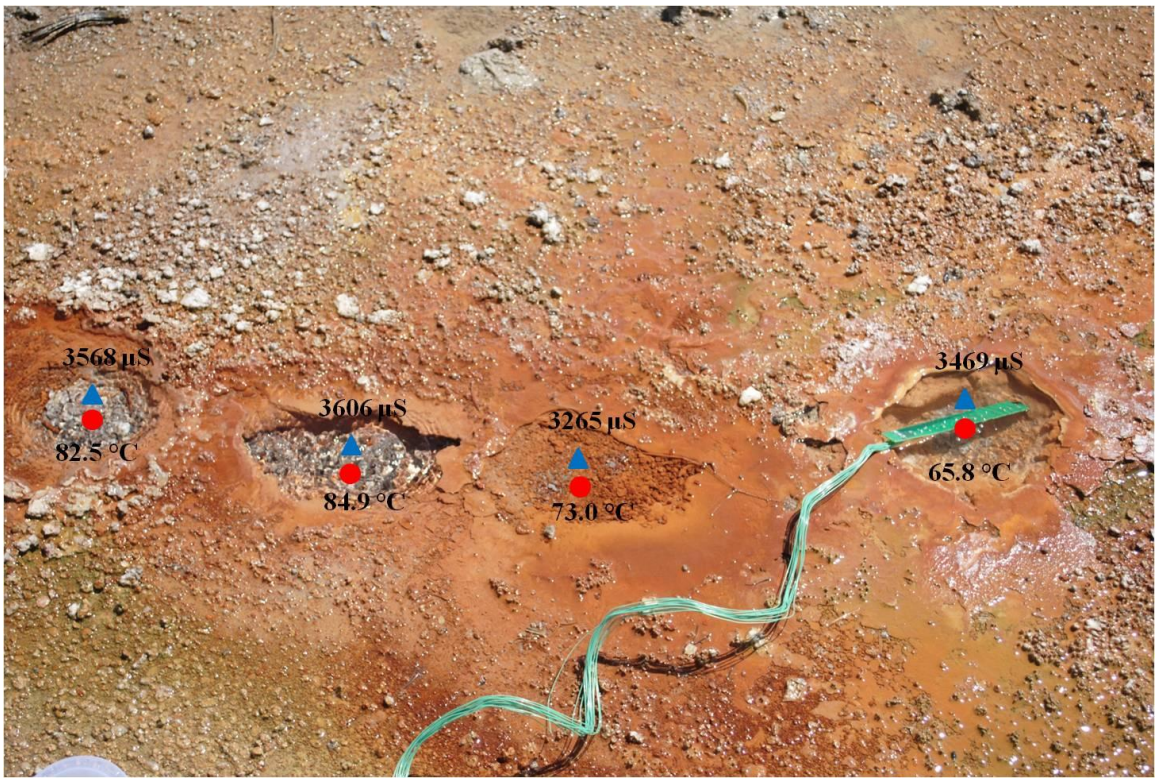

Figure 4.22: Measurements of temperature and conductivity in each of four small source pools at Norris Geyser Basin. The length of the array is 18.5 cm for scale.

Due to the small size and shallowness of each pool, it was not possible to use the commercial conductivity probe; however, the small size of the conductivity array and the individual four-point probes made measurement in these pools possible. The bottoms of the two leftmost pools are clear, but the two rightmost pools exhibit the orange color typical of oxidized iron. While the conductivity measurements show that bulk ion chemistry in the four pools is roughly the same (within error), the temperature measurements again suggest a link between the temperature of the water and the oxidation state of the iron. It should be noted that the depth of the pools are approximately similar (a few centimeters).

The conductivity sensor array data show that conductivity can be useful tool when used in conjunction with other measurements such as temperature as it assists with narrowing the parameter space in which the questions about the photosynthetic transition zones can be addressed. The next chapter will discuss how using the conductivity array led to a discovery about the increased utililty of the temperature array measurements as a mapping technique for other chemical parameters.

4.6 Current and Future Work

Currently (spring 2013), I am leading another senior design team in developing a new wireless conductivity measurement system. This project involves eliminating the necessarily long wires extending from the sensor array deployed in the water to the data acquisition device located on the bank of the hot spring. A harsh environment-tolerant box is being developed that can be deployed directly in the hot spring in which the electronics are placed and connected to the sensor array outside of the box through a water-tight electrical feed-thru. This new system would have the capability to wirelessly transmit the data to a transceiver located safely away from the hot spring. The system would record the data to a flash drive which would need to be retrieved periodically.

4.7 Conclusion

A MEMS electrical conductivity sensor array was developed to measure conductivity (as a proxy for bulk ion chemistry) in the harsh environment of hot springs. The MEMS conductivity sensor array is the first of its kind and measurements at the 1 cm scale cannot be otherwise made using existing commercial instruments due to their large size. Additionally, the MEMS conductivity arrays measurements may more accurately represent the conductivity at a specific location as compared to the commercial sensors

because the MEMS devices disturb the flow much less than the larger commercial instruments. The conductivity sensors were designed as four-point probes and the electrodes were fabricated using platinum in order to minimize measurement error and withstand corrosion in the hot springs. An electronic circuit was developed in order to take non-simultaneous measurements from each sensor in the array. A LabView program was written to interface with the electronic circuit and display *in-situ* conductivity measurements in real-time.

The conductivity arrays were first tested at hot springs in Gerlach, NV and electrode material design improvements were made based on the first field experiments. New arrays were brought to Yellowstone National Park and used to measure conductivity at various locations over a 6-day field excursion. The data show that conductivity, when paired with temperature, can provide insights into the transitions from non-photosynthetic to photosynthetic zones as well as into chemical reactions. Additionally, the small size of the four-point probe allows measurements in extremely shallow bodies of water, where existing commercial conductivity sensors cannot operate. The major reason for developing the conductivity array was advancing the capability of array-based hot spring sensors since the conductivity sensor measurement required exposing electrodes to the hot spring water and required more complicated circuitry in order to utitlize AC curents at higher frequencies. The success of the conductivity sensors paves the way for the development of a MEMS pH sensor and array. Future work involves developing the capability for wireless transmission and storage of data for long-term monitoring. Additional applications for the conductivity sensor include: 1) elucidating the dynamics of fluid exchange between surface and ground waters which can

be distinguished by their conductivity levels and 2) using the conductivity sensor in a platform for monitoring environments that are periodically underwater. In these systems, the conductivity sensor could be used a switch, which records zero conductivity when no fluid is present and records a measurable conductivity when submerged. A measurable conductivity reading could be used as a signal to turn on other sensors, which would conserve power and increase the experiment lifetime.

CHAPTER 5: MEASUREMENTS AT GEYSER CREEK BASIN

Temperature and conductivity sensor array measurements were taken over the course of one day at a site in Geyser Creek Basin, Yellowstone National Park. Hot springs within Geyser Creek Basin (Figure 5.1) are located in the central-west portion of the park and are known for having chemical compositions that can vary in pH between 2.5 and 8.5 (Raymahashay 1968).

Figure 5.1: Photograph of a hot spring in Geyser Creek Basin.

5.1 Data from Geyser Creek Hot Springs

Data were collected from an area of the basin where outflow channels from two different hot springs converge. One channel was acidic; it was approximately 1.5 m wide with a pH ~3.3. The other channel was alkaline, approximately 0.5 m wide with a pH of ~7.6. These two channels had different conductivity and temperature ranges. The acidic

channel had an average temperature of ~36 °C and a conductivity of ~900 µS/cm. The alkaline channel had an average temperature of ~60 °C and conductivity of ~4200 µS/cm. These values were all measured with standard pH/conductivity/temperature probes near the center of the channel, a few meters upstream from the mixing zone. There were no visibly identifiable microbial communities living in the acidic stream. A microbial community living in the alkaline stream was clearly identifiable by its dark brown pigment and filamentous shape (Figure 5.2).

Figure 5.2: Photograph of the microbial mat community found in the alkaline outflow channel. The temperature array is 2.4 cm by 18.5 cm.

The acidic and alkaline streams mixed together and merged into a single stream. Downstream of the mixing zone the temperature of the converged stream is ~47 °C, the conductivity is ~2000 µS/cm and the pH is ~6.5. A photo-mosaic of this region is

provided in Figure 5.3. The thin brown stick located on the dry ground between the two streams is approximately 1.2 m long and was included for scale. The alkaline stream microbial mat is clearly visible as the dark brown color of the alkaline stream prior to mixing with the acidic stream.

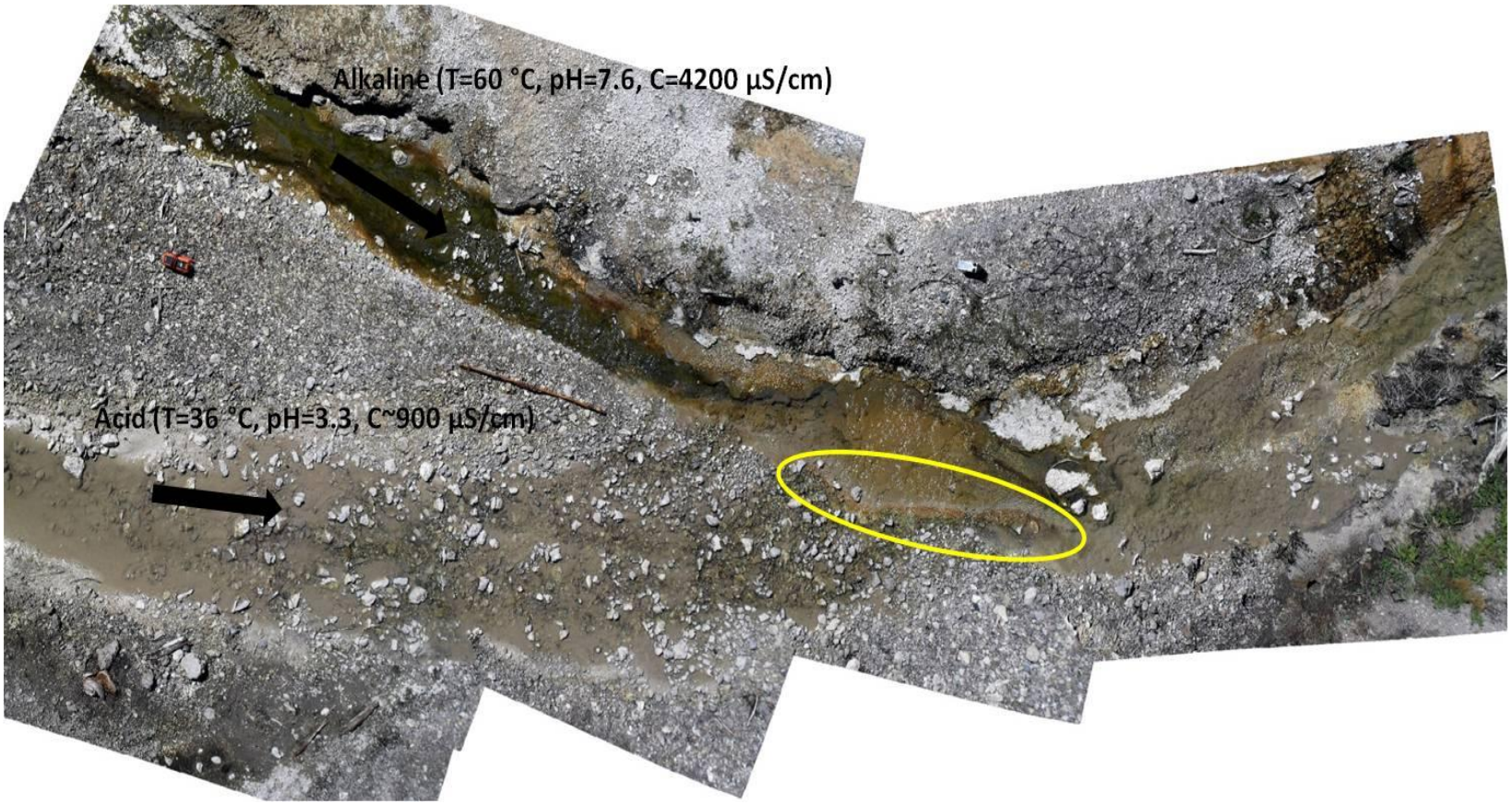

Figure 5.3: Photo-mosaic (courtesy of Andrew Dombard) of the acidic stream (bottom) and alkaline stream (top). A zoomed-in image of the region within the yellow oval is provided in Figure 5.4. A 1.2 m thin brown stick located between the two streams is provided for scale. Black arrows show the direction of the fluid flow in the two streams.

Where the two streams merge, several bands of different colors appear that are found nowhere else in either stream. These bands of color presumably represent different photosynthetic communities (or possibly no community in one case). Figure 5.4 shows an image of this region with dashed lines showing my interpretation of where the transitions to different communities occurred. The black arrows indicate the general direction of flow from the two streams before converging. The question of interest in this chapter is similar to one of the questions from Chapter 3: *Is temperature the key variable responsible for the transitions between the different photosynthetic communities in the mixing zone?* Answering this question is complicated by the fact that at small scales, each stream has variable pH and conductivity (and possibly other chemical parameters) as well.

Figure 5.4: Close-up photograph of the 'microbial striping zone' where the water from each of the two channels mixed. Black arrows show the approximate direction of flow for each stream before mixing. The sensor array at the right is 2.4 cm by 18.5 cm. The dashed lines indicate where the colored zones change.

At the right of Figure 5.4, from bottom to top of the photograph the zones of color are green (below the bottommost dashed line), orange, white, light brown, and brown (at the very top of the image). This region will be referred to as the 'microbial striping zone'. While the orange and light brown regions appear to be similar in color in this picture, those zones in other images (and in the field) look different. The white zone is similar enough in appearance to areas of the acidic hot spring where no noticeable microbial communities are present and therefore may not be a distinct microbial community, but possibly the lack of a pigmented community. At the left of the Figure 5.4, the dashed

lines approximate where the dark brown filamentous mat disappears with the onset of mixing between the alkaline and acidic streams.

Arrayed temperature measurements were made across the microbial striping zone (Figure 5.5, 5.6). The photograph in Figure 5.5 is oriented such that the fluid at the bottom of the photograph (green community) is more acidic than the fluid near the top of the photograph (light brown community).

Figure 5.5: Photograph of an 18.5 cm long temperature array placed across the microbial striping zone with dashed lines outlining four distinct color regions. The yellow star marks the zero position in the temperature plot.

The data show a show a strong temperature gradient across the boundaries of the different zones with the notable exception of the boundary between the green community and the

orange community where the temperature gradient is negligible within the error (Figure 5.6). The gradient is approximately linear across the orange-white boundary and the white-light brown boundary.

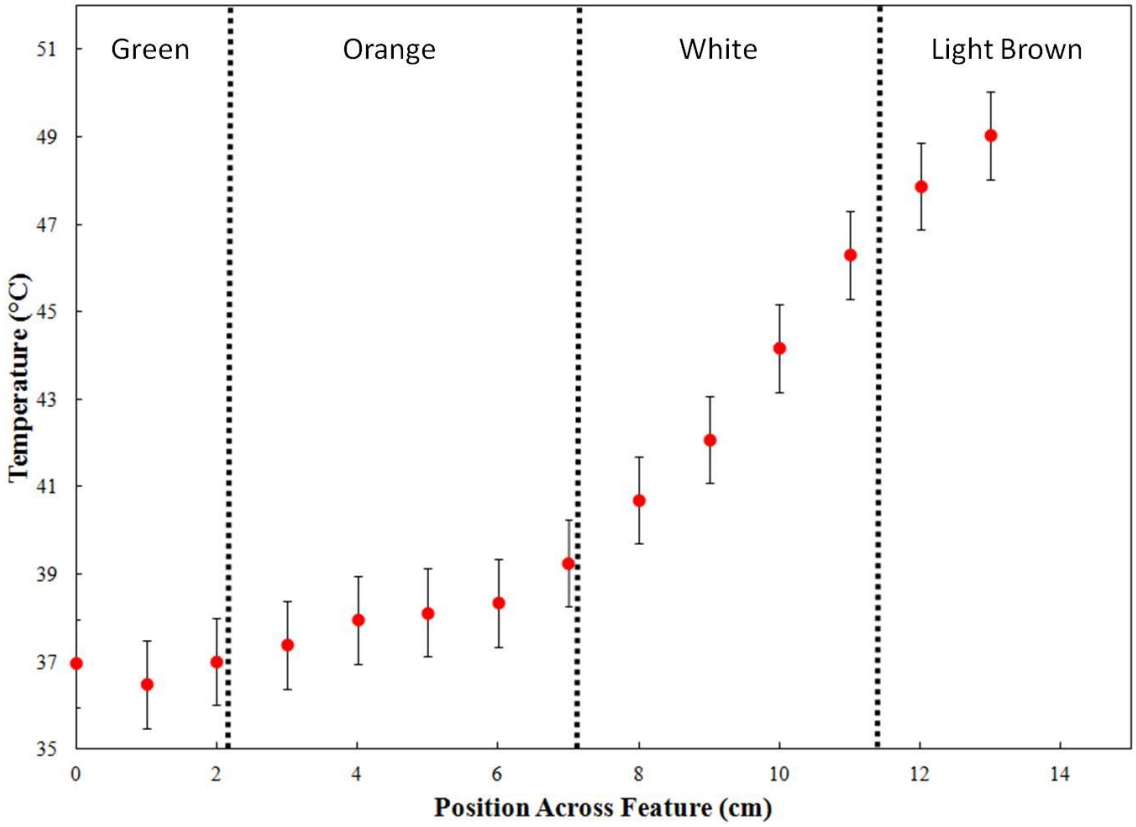

Figure 5.6: Plot of temperature across the microbial striping zone. Dashed lines approximate the locations where the transitions occur. Left on the plot is closer to the acidic stream. Error bars on all temperature plots represent the uncertainty of ±1 °C due to sensor system noise and calibration error.

In order to show another new capability of the array measurements, the area where the two streams merged were mapped in temperature and conductivity. A total of 750 temperature measurements and 90 conductivity measurements were taken over the course of a day.

Running out of time at the end of the day limited the number of conductivity measurements taken. The location and value of each measurement was overlaid on the photo-mosaic of the region in an ArcGIS® software program called ArcMap™ (Figure 5.7).

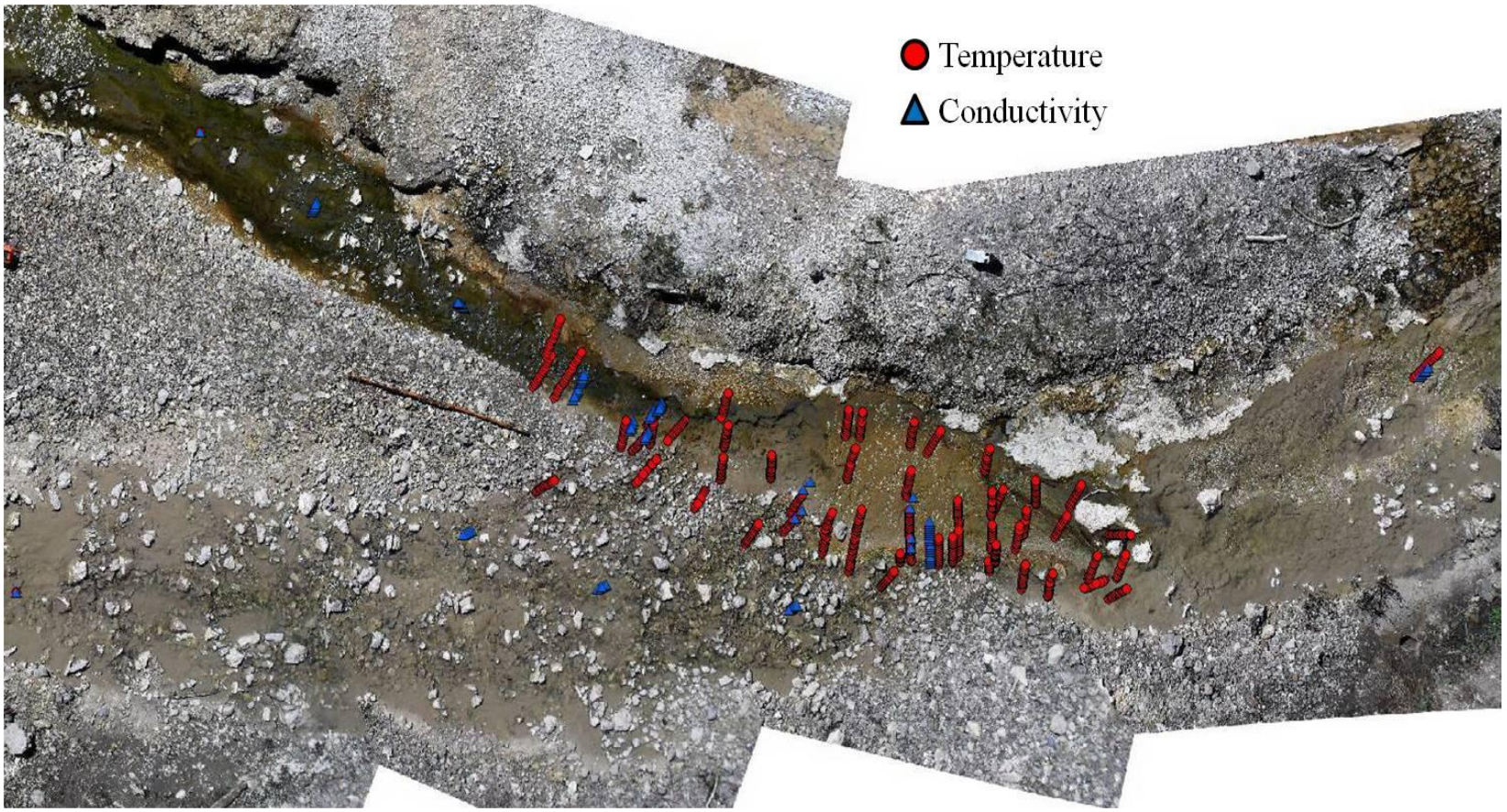

Figure 5.7: ArcMap™ image showing the photo-mosaic of the two streams and the temperature and conductivity measurement points over top. Red circles represent temperature measurements, blue triangles represent conductivity measurements. A 1.2 m thin brown stick located between the two streams is provided for scale.

Zooming into the mixing area, the location of the majority of the temperature and conductivity measurements can be seen more clearly in Figure 5.8.

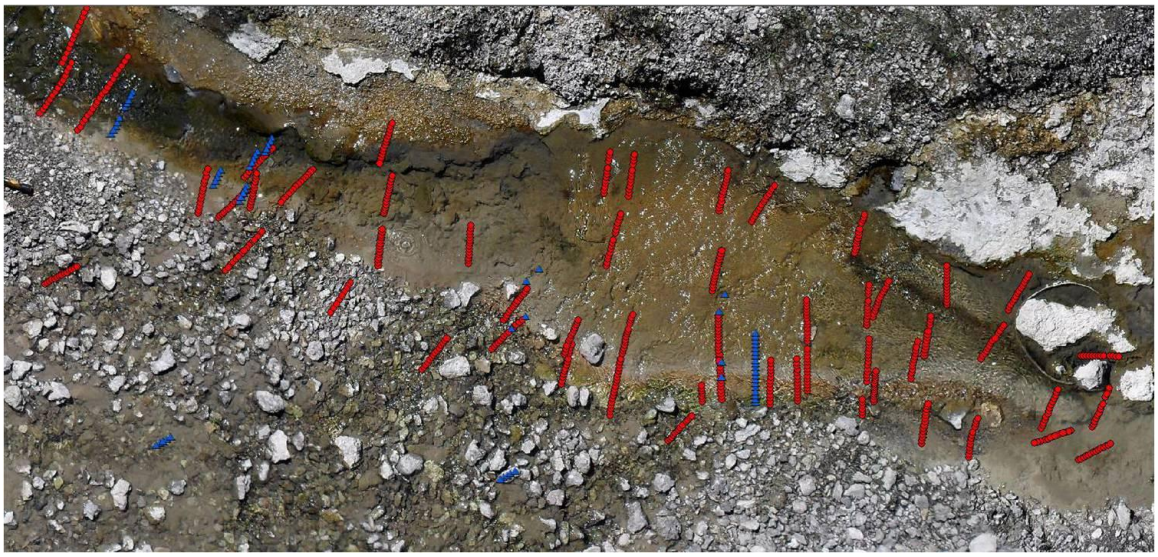

Figure 5.8: Close-up image showing the location of the temperature and conductivity measurements around the mixing zone. Red circles represent temperature measurements, blue triangles represent conductivity measurements.

Using the temperature data, a semi-transparent color map was created showing temperature across both streams (Figure 5.9). Values in between data points were interpolated using the inverse distance weighting technique. Inverse distance weighting interpolates values by giving more weight to actual values closest to the interpolated point and giving less weight to points farther away. While this interpolation technique created the most realistic looking color maps, it also created artifacts such as the linear orange-to-yellow transition at the right of the map. These generally occurred where distances between data points were greater than 50 cm.

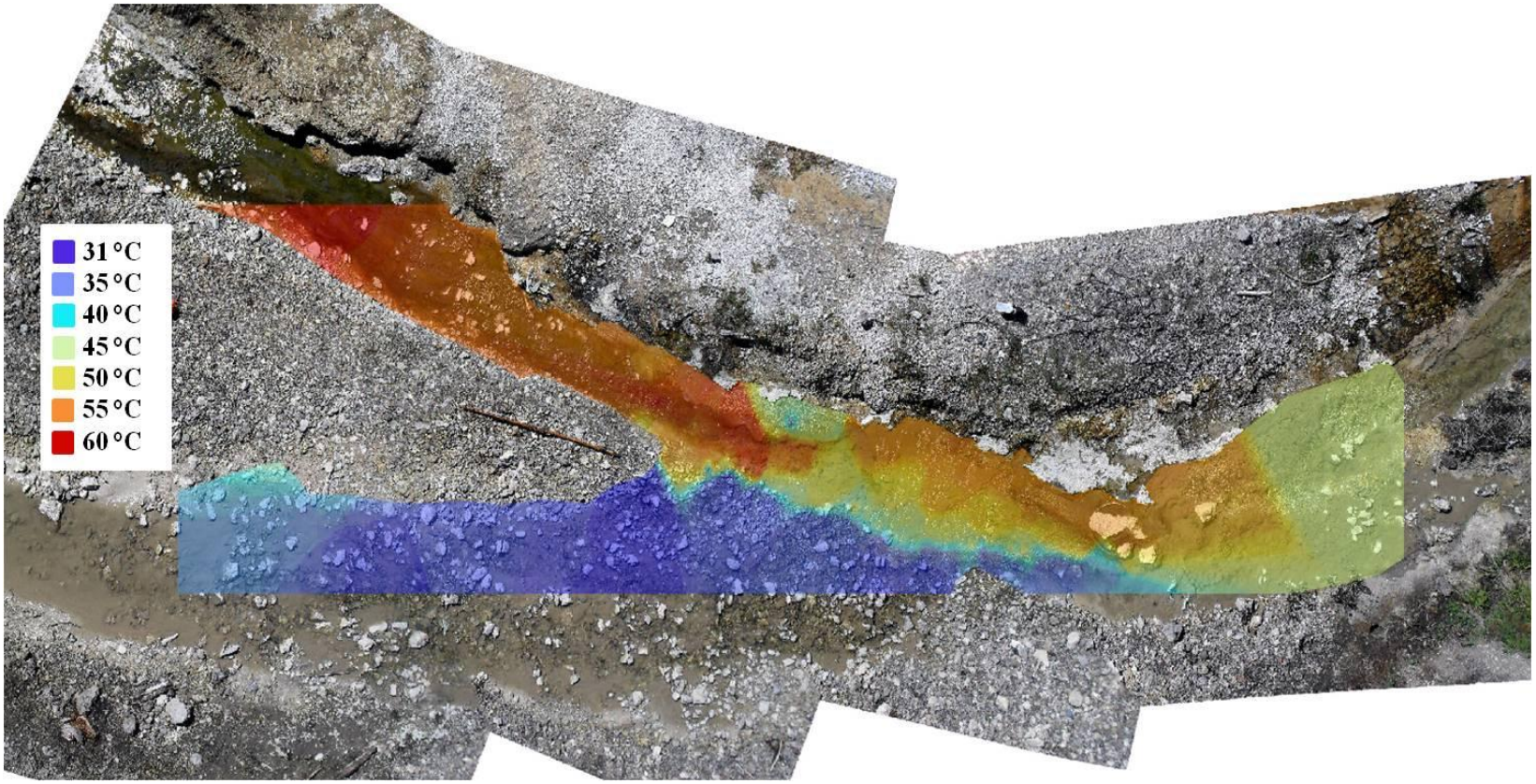

Figure 5.9: Temperature color map of the acidic and alkaline outflow channels created in ArcMap™. Temperatures range from 31 °C to 60 °C with blue representing cooler temperatures than red colors. The acidic stream is at the bottom of the image and the alkaline stream is at the top. A 1.2 m thin brown stick located between the two streams is provided for scale.

The blue colors in Figure 5.9 represent the coolest areas (minimum = 31.2 °C) and red colors represent the hottest (maximum = 59.9 °C). A close-up image of the mixing zone at the boundary of the two channels and a temperature color map overlaid on the image are provided in Figure 5.10.

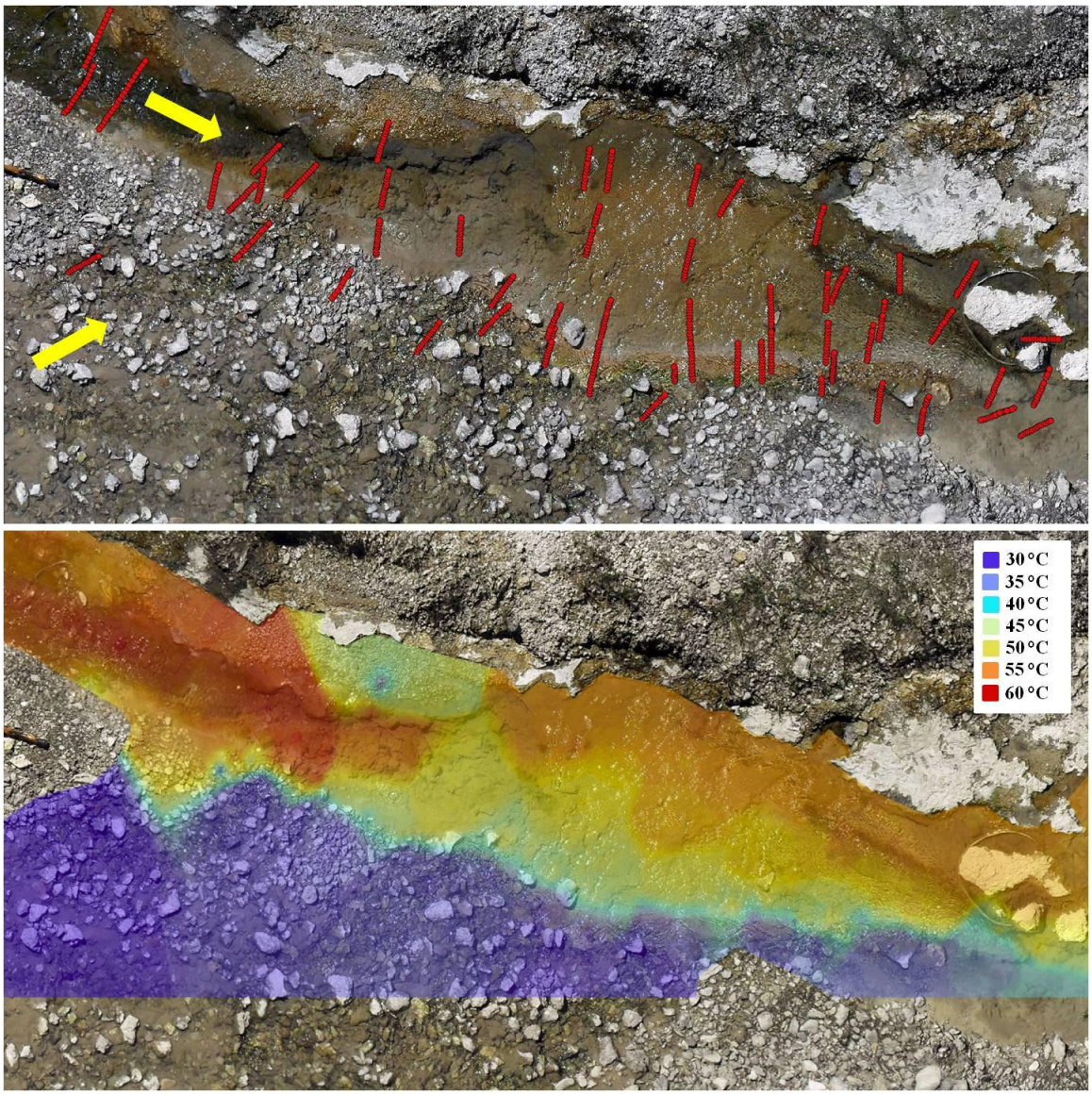

Figure 5.10: (top) Close-up image of the mixing zone where the two streams merge. Red circles represent temperature measurements. The acidic stream is flowing in the direction of the bottom left yellow arrow and the alkaline stream is flowing in the direction of the top left yellow arrow. (bottom) Close-up of the temperature color map overlaid on the image.

As seen in Figure 5.6, the color map does not distinguish between the green and orange striping zone – both are within the purple-to-blue color of the temperature scale. However, the aqua color above the purple zone traces the position of the white stripe

surprisingly accurately in both shape and width. The yellow (and light orange) zone above the aqua zone is large and corresponds spatially with the light brown microbial region fairly well, especially where the measurement density is high. The brown microbial zone also corresponds fairly well to the darker orange color where measurement density is high. Finally, the hottest region shown in red is found in the alkaline stream before mixing and transitions to the dark orange color at approximately the same location where the dark brown streamers end and mixing begins. As can be seen in these color maps, temperature is an extremely effective predictor of the location of the boundaries between most of these microbial communities, especially where the sampling density is highest. This provides strong evidence that temperature is probably a key factor governing the transitions between photosynthetic communities, but not necessarily the only one as evidenced by the inability of the map to distinguish the boundary between the orange-colored microbes and the green-colored microbes.

A similar map created in ArcMap™ was generated using conductivity sensor array data. The semi-transparent conductivity color map was generated from measurements indicated by the blue triangles in Figure 5.7 and is presented in Figure 5.11.

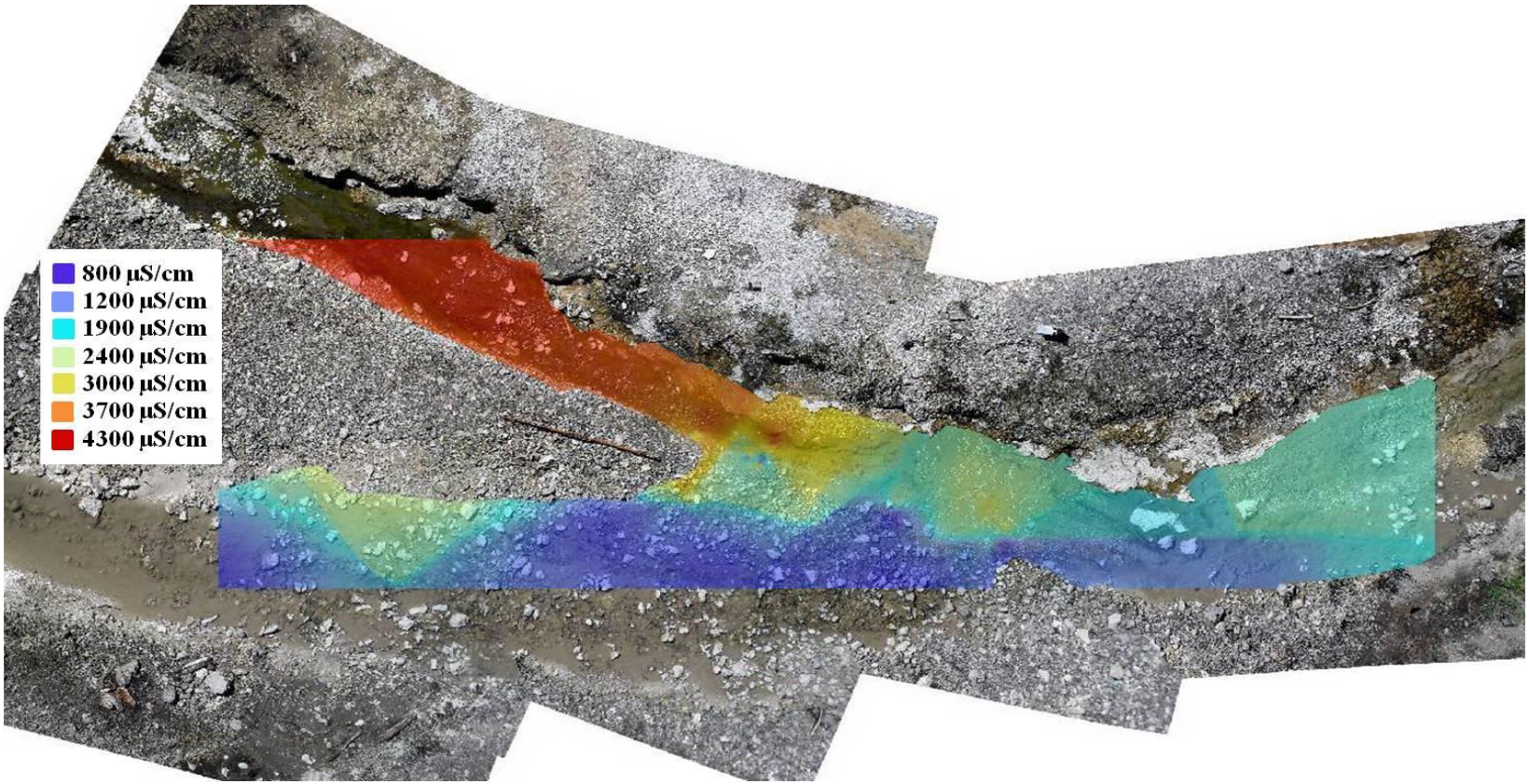

Figure 5.11: Conductivity color map of the acidic outflow channel (bottom of image) and alkaline outflow channel (top of image) created in ArcMap™ with blue colors that are lower conductivity than red colors. Conductivities range from 830 µS/cm to 4300 µS/cm. The acidic stream is at the bottom of the image and the alkaline stream is at the top. A 1.2 m thin brown stick located between the two streams is provided for scale.

The blue colors in Figure 5.11 represent the lowest conductivity areas (minimum = 833 μS/cm) and red colors represent the highest (maximum = 4300 μS/cm). Due to the much lower sampling resolution achieved with the conductivity measurements, the overall map contains more artifacts from the interpolation method. For example, there is a light green color region at the bottom left of the map in the acidic channel near the legend that shows much higher conductivity than the rest of the acidic channel. Clearly, the interpolated values were affected by the high conductivity values measured in the alkaline channel as the interpolation method did not recognize the land barrier between the acidic and alkaline channel as an interpolation boundary. A zoomed in image of the mixing zone along with the conductivity color map are provided in Figure 5.12.

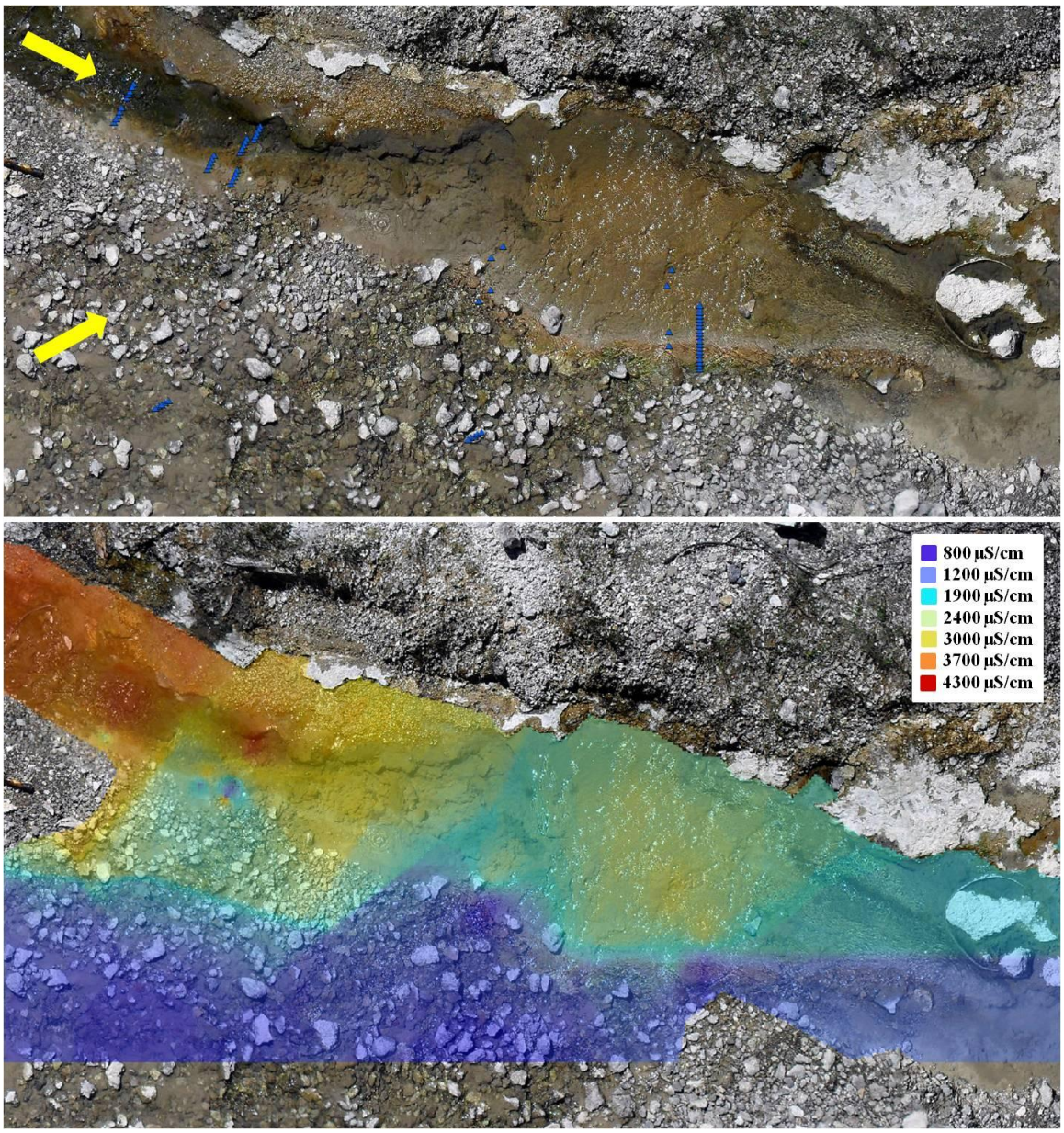

Figure 5.12: (top) Close-up image of the mixing zone between the alkaline and acidic channels. Blue triangles represent conductivity measurements. The acidic stream is flowing in the direction of the bottom left yellow arrow and the alkaline stream is flowing in the direction of the top left yellow arrow. (bottom) Close-up of the conductivity color map overlaid on the mixing zone.

The microbial striping zone is not nearly as well defined by the conductivity color map compared as it was by the temperature color map. One obvious possibility is that

conductivity has very little effect on where the transition zones occur between photosynthetic communities in this system. As seen in Chapter 4, there were a number of cases in other regions of Yellowstone National Park in which conductivity did not change (as temperature did) across photosynthetic boundaries. For the color maps to appear different also requires that conductivity must not be distributed in the same way as temperature. There are several reasons why the two properties might not have the same spatial (or temporal) distribution. First, the temperature and conductivity (and pH) differences between the two streams should cause both advective and diffusive mixing (Lester et al. 2012) of those properties. It is possible; however, that conductivity mixes over longer time scales than does the temperature, similar to the oceanic process of salt fingering (Kunze 2003). Second, the biological community uses the chemistry available in the hot springs as a nutrient and energy source, and could therefore affect the bulk ion concentration. Third, it is possible that low sampling density in the conductivity data causes the differences in the spatial distributions of conductivity and temperature because of the way in which the interpolation method handles the differences in spacing. In fact, a qualitative comparison of the two maps over areas where the conductivity and temperature sampling densities are both high seem to show that these areas correspond to the microbial striping features most accurately.

In order to test the third hypothesis about sample density and interpolation bias, the conductivity and temperature values were compared across the microbial striping zone in a region where both parameters were sampled close to one another in space. Figure 5.13 is a close up of a section of Figure 5.8 and highlights a excellent location for comparison of quite proximal measures of temperature and conductivity (within 5 cm).

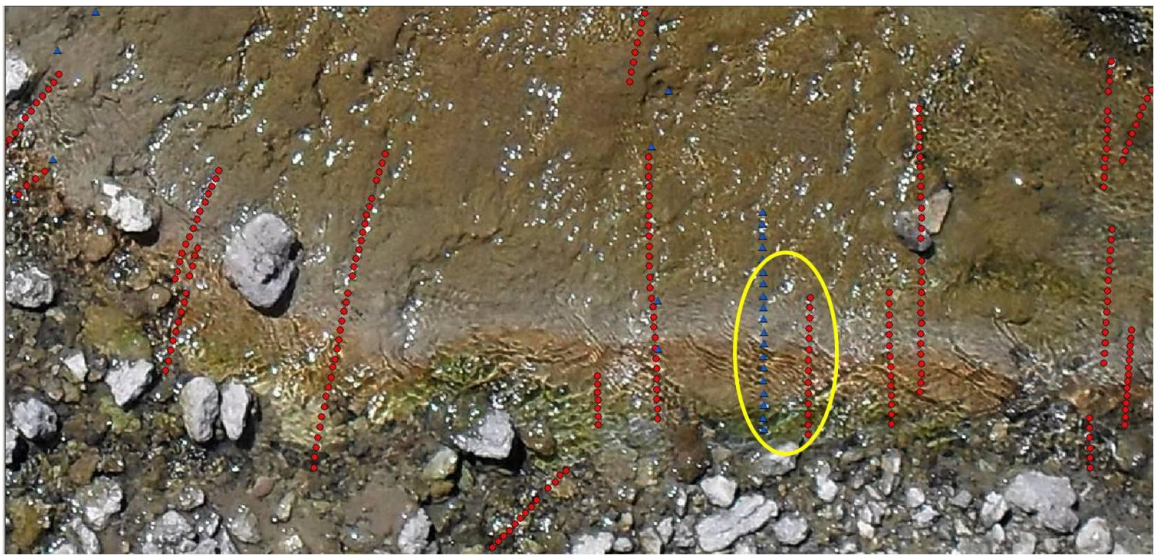

Figure 5.13: Image showing the microbial striping zone with the location of the temperature (red circles) and conductivity (blue triangles) measurements overlaid on it. The yellow oval shows the two sets of data to be compared. The two sets of data are separated by ~5 cm.

Figure 5.14 is the temperature and the conductivity data from the region highlighted by the yellow oval in Figure 5.13 plotted versus distance across the microbial striping feature.

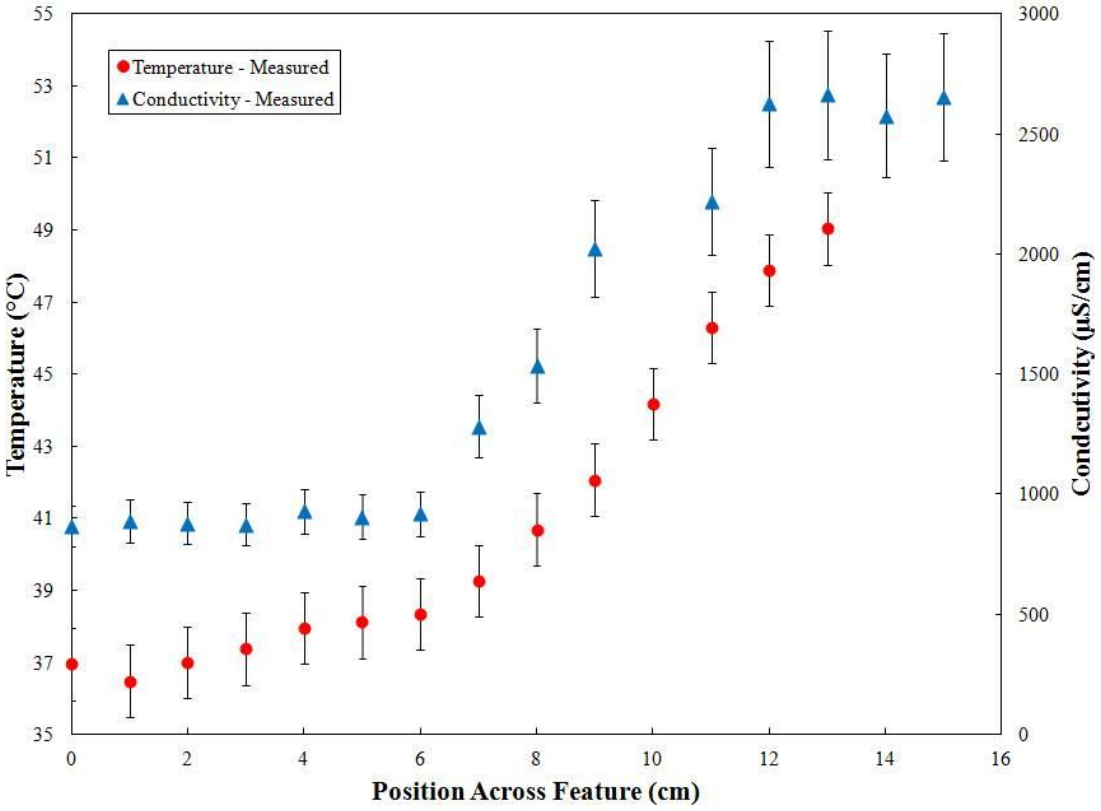

Figure 5.14: Plot of temperature and conductivity across the microbial striping zone. The zero position in this plot is located at the bottom of the image in Figure 5.13. Error bars on all conductivity measurements represent the uncertainty of 10% due to sensor system noise and calibration error.

The zero position in the plot represents where the temperature and conductivity measurements were taken beginning in the more acidic region of the mixing zone (green community). The temperature data is the same as that in Figure 5.6. The data indicate that conductivity and temperature show a similar pattern across the striping zone. Both sets of data start are relatively constant across the green and orange zones; both begin to increase at approximately the same location and perhaps also level out at a similar location.

Based on the likeness of the structure of the two plots, conductivity was modeled across the microbial striping zone using only temperature as a predictor. In order to do this, the streams are treated as two end member reservoirs of a specific temperature and

conductivity and the mixing zone as a linear combination of those end member reservoirs. Using this model the fractional contribution of the temperature (and conductivity) from each stream can be calculated. The end member values for the temperature and conductivity of the acidic reservoir are T_{acid} = 36.7 °C and C_{acid} = 890 μS/cm, respectively. The end member values for the temperature and conductivity of the alkaline reservoir are T_{alk} = 59.9 °C and C_{alk} = 4150 μS/cm, respectively. The temperature at any given location (T_{mix}) can be determined by:

$$T_{mix} = f_{acid}T_{acid} + f_{alk}T_{alk}, \quad \text{(Eq. 5.1)}$$

where f_{acid} and f_{alk} represent the fractional contribution of water from each of the reservoirs. The two fractions are unknown; therefore a second equation is required to determine their values. Since there is no contribution other than that from the two reservoirs, the two fractions should add to unity:

$$f_{acid} + f_{alk} = 1. \quad \text{(Eq. 5.2)}$$

Solving these two equations gives:

$$f_{acid} = \frac{T_{mix}-T_{alk}}{T_{acid}-T_{alk}}; \qquad f_{alk} = 1 - f_{acid}. \quad \text{(Eq. 5.3)}$$

Using this equation and inputting the temperature values measured across the microbial striping zone for the T_{mix} parameter gives the fractional contribution from each reservoir at that particular location. The same fractions can be used to determine the conductivity at those same locations:

$$C_{mix} = f_{acid}C_{acid} + f_{alk}C_{alk}, \quad \text{(Eq. 5.4)}$$

where C_{mix} is the conductivity at the T_{mix} location. The same temperature values from Figure 5.14 were used to determine the conductivity values and both are plotted in Figure 5.15:

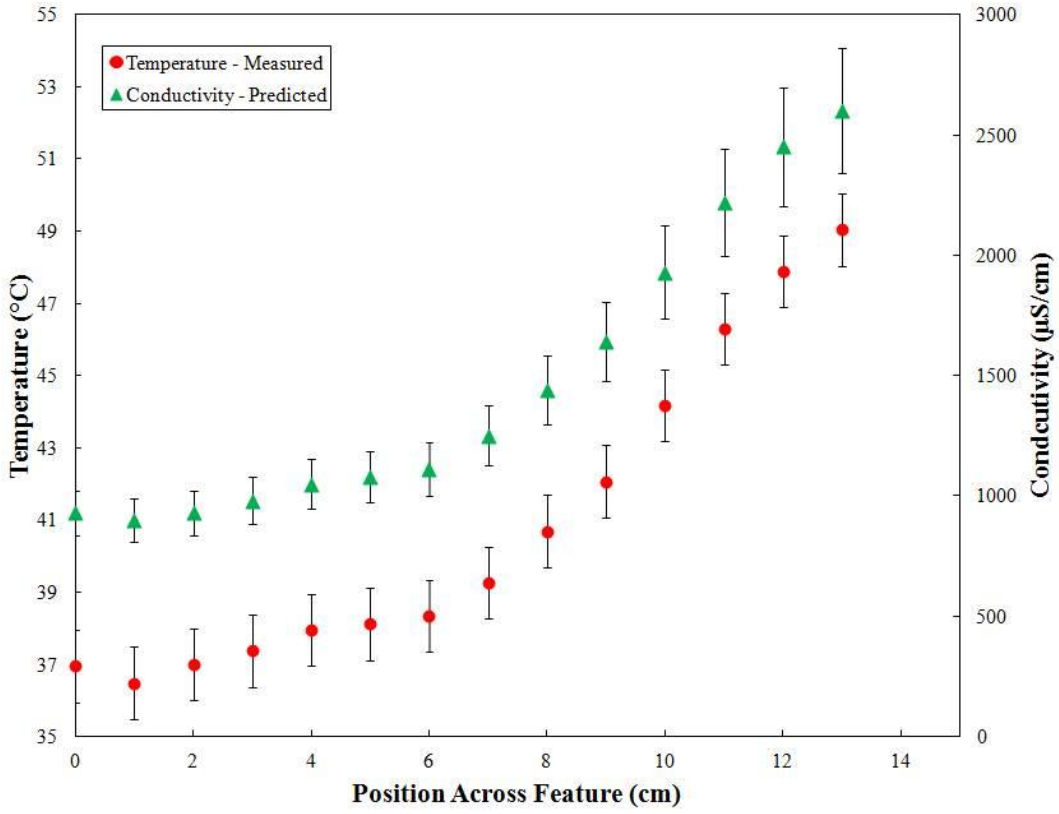

Figure 5.15: Plot of the measured temperature and conductivity predicted by the two-end member mixing model across the mixing zone.

The predicted conductivity data represent what would be measured if the temperature and conductivity mix in the same way. Error bars on the predicted conductivity values are ~11% and are the result of propagating the error from the temperature measurements (±1 °C) and the error from the reservoir conductivity measurements (10%) through the model equations. Finally, comparing the measured and predicted conductivity values across the mixing zone is provided in Figure 5.16.

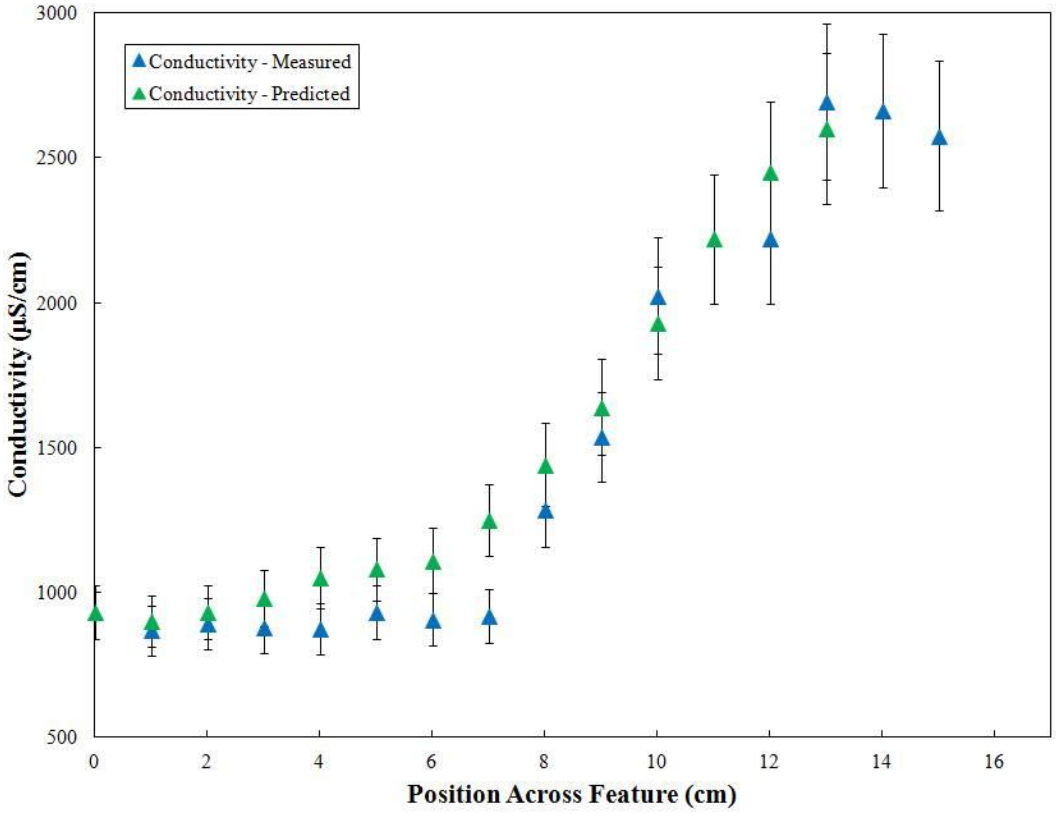

Figure 5.16: Plot of the measured and predicted conductivity across the mixing zone.

The predicted and measured conductivity values match each other (within error), except for one point at 7 cm. Based on these results, it appears a sampling and interpolation bias in the conductivity color map is the likely cause of the difference in spatial distributions for conductivity and temperature. This also implies that conductivity (bulk ion chemistry) is a conservative constituent within this hot spring system and is not noticeably affected by the presence of biology.

With the ability to predict the conductivity across the microbial striping zone using the temperature, a conductivity color map of the predicted conductivity was created based on the arrayed temperature data (Figure 5.17).

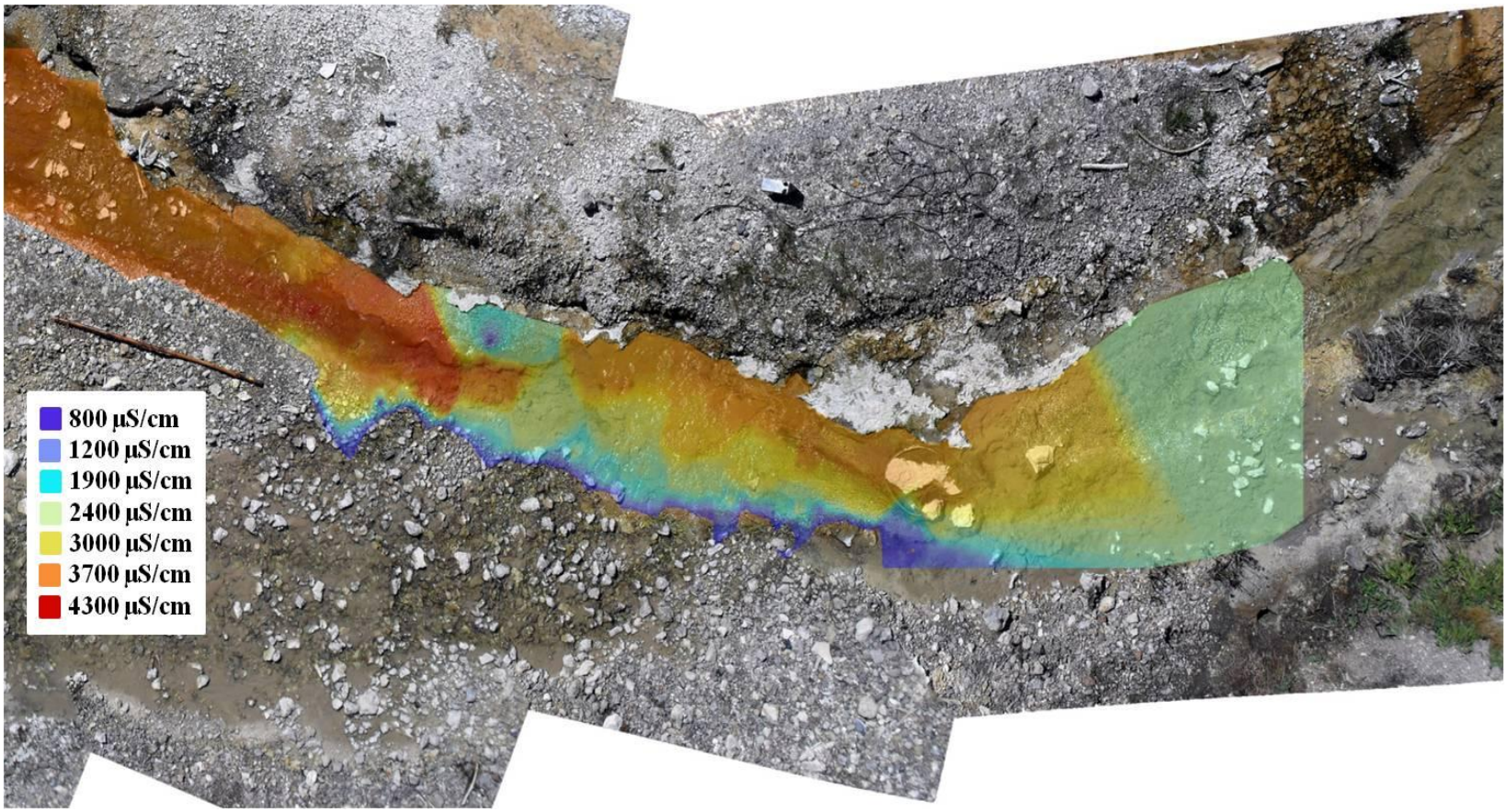

Figure 5.17: Predicted conductivity color map of the acidic outflow channel (bottom of image) and alkaline outflow channel (top of image) created in ArcMap™ with blue colors that are lower conductivity than red colors. Conductivities range from 810 µS/cm to 4200 µS/cm. A 1.2 m thin brown stick located between the two streams is provided for scale.

Assuming the previous method holds true everywhere in the mixing zone, this conductivity color map provides a more representative view of the conductivity distribution across the mixing zone. The predicted map provides conductivity information at a very high spatial resolution even though the actual conductivity data were sparse. The predicted conductivity map has been limited to areas where temperature measurements exist and therefore was not extrapolated upstream into the acidic outflow channel. Comparing this map to the measured conductivity map, the predicted map improves the prediction as to where the photosynthetic transitions occur and most noticeably predicts a higher conductivity in the light brown and brown photosynthetic zones.

As a way of comparing the measured and predicted conductivity values, a percent error color map was created, where percent error (*PE*) is given by:

$$PE = \frac{C_{pre} - C_{mea}}{C_{mea}} \times 100, \qquad \text{(Eq. 5.5)}$$

where C_{pre} is the predicted conductivity value, C_{mea} is the measured conductivity value. The absolute value of the percent error color map is provided in Figure 5.18.

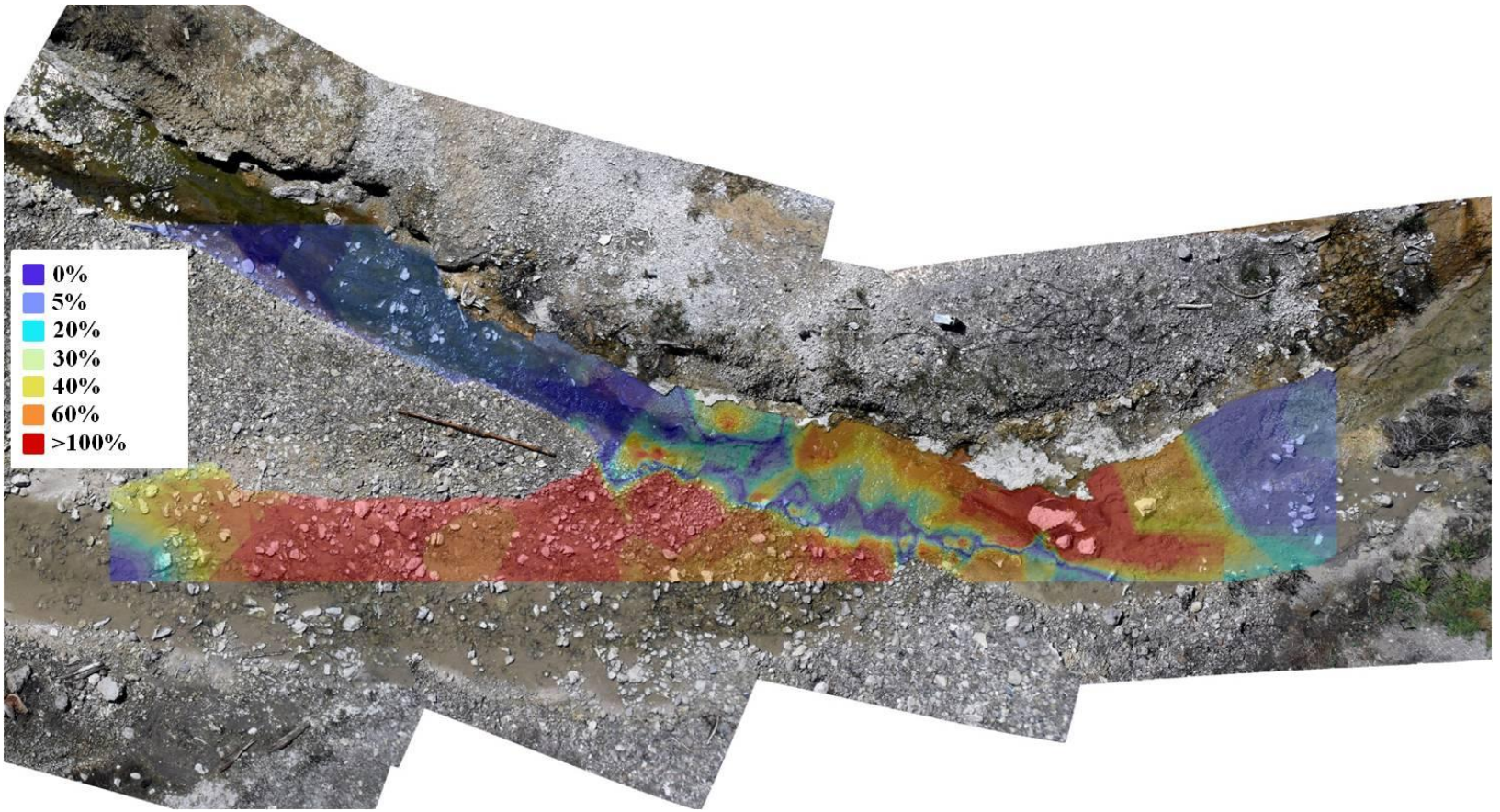

Figure 5.18: Percent error color map of the acidic and alkaline outflow channels created in ArcMap™. Blue colors are low error and red high error. The acidic stream is at the bottom of the image and the alkaline stream is at the top. Error ranges between ~0% and ~190%.

The dark blue colors in the map are low error and the error is highest in the red regions. At first glance, it appears the error is lowest for measurements in the alkaline stream and high in the acidic stream. There is also a region of apparently high error at a location downstream of the mixing zone. However, the conductivity sampling is somewhat sparse and therefore error will be high where there was no conductivity measured in the field as those values are, by necessity, interpolated from points relatively far away (>1 m). Therefore, in order to get a better understanding of how well the predicted conductivity values compare to the real conductivity values at the other measurement locations in the hot spring system, a zoomed-in percent error plot is provided that marks where the conductivity measurements were taken with blue triangles (Figure 5.19).

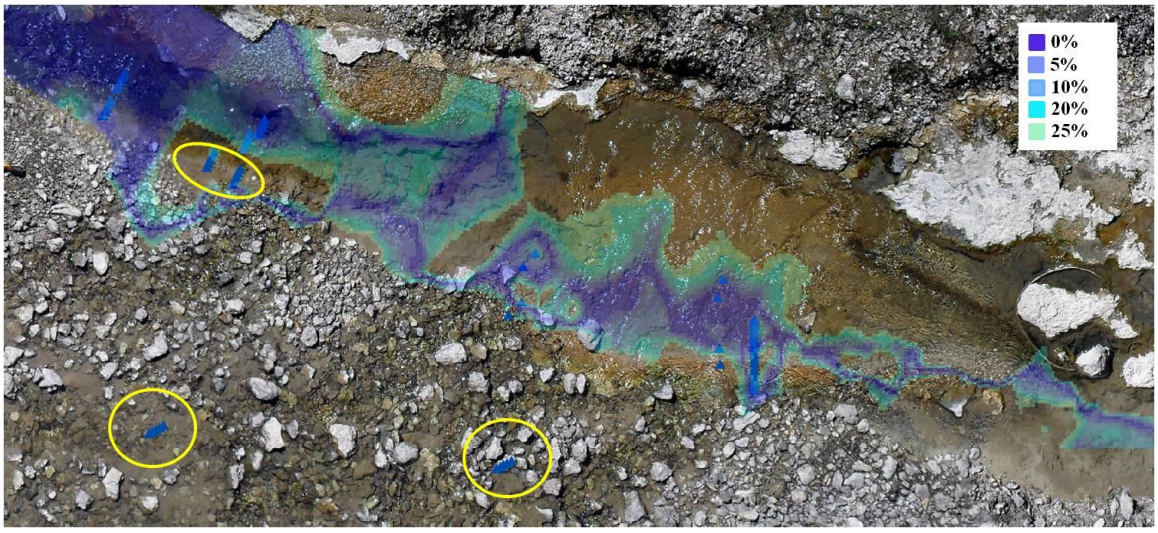

Figure 5.19: Close-up image of the percent error color map in the mixing zone. The blue triangles represent locations where the conductivity measurements were taken. The map highlights only areas where the percent error is below 30%. Yellow circles show conductivity measurements where the percent error > 30%.

Additionally, in Figure 5.19 the color map only shows locations where the percent error is below 30%. In all other areas, the percent error is > 30%. As can be seen in the image, the low percent

error regions are generally found where conductivity measurements were taken (blue triangles). However, there are three areas where there are conductivity measurements that have a percent error > 30%. Two of these areas, marked by yellow circles at the bottom of the figure, have high percent error values because no predicted conductivity existed at these locations (i.e., no temperature measurements were made). Therefore, for these two areas, the percent error would automatically be 100% and does not indicate an issue with the prediction technique. However, there is one location (yellow oval near the top of Figure 5.19) with high percent error despite the fact conductivity and temperature measurements were both collected. This area coincides with a location about 0.5 m downstream from the point where fluid from the acidic stream begins to mix with fluid from the alkaline stream. The measured temperature at this spot is high (53-58 °C) which suggests minimal mixing with the acidic stream (thus, the high predicted conductivity values). However, the measured conductivity at this location is in fact low, in the range of 1300-2000 μS/cm, suggesting mixing between the two streams. Visually, the dark brown streamer mat disappears in this region, which further suggests that there is mixing between the two channels at this location. The temperature measurements ~0.1 m downstream from this point show a large temperature gradient, indicative of mixing between the channels. The temperature gradient ~0.5 m upstream of this point, at the beginning of the mixing zone, appears to show mixing as well. Therefore, the temperature gradient at this location, for reasons unknown, does not appear to appropriately reflect the mixing conditions within this region.

While there is no pH array available for measurements across the microbial striping zone, individual pH measurements were made using a pH meter placed in the water in different locations within the microbial striping zone. The pH sensor is too large to define its location within a specific photosynthetic community (i.e., color zone); however, the pH sensor also

measures temperature data and these temperature data can be used to perform the same calculations on pH as were used to predict conductivity. Mixing fractions were calculated from the pH sensor's temperature data and the pH measurements of pH_{acid} = 3.6 and pH_{alk} = 7.6 for the end member reservoirs, respectively. Before carrying out the calculation, the pH values were converted to the H^+ ion concentration. The pH change as a function of mixing temperature is provided in Figure 5.20.

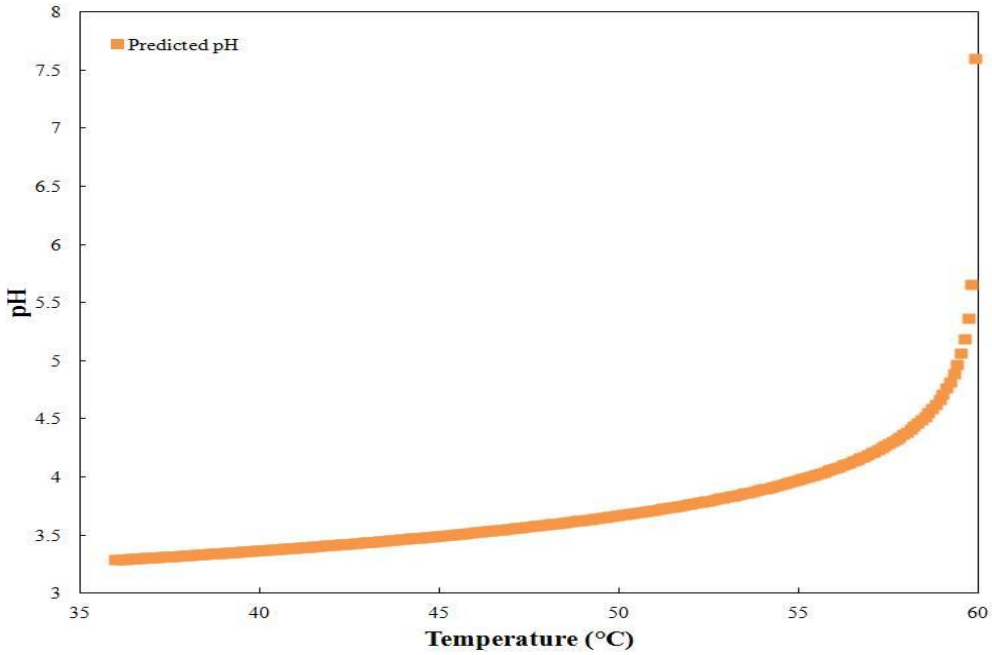

Figure 5.20: Predicted pH based on temperature values in the range of those measured in the acidic-alkaline hot spring system.

Since the model uses the concentration of the H^+ ion for mixing calculations, the ion concentration change with temperature is linear. The concentrations are changed back to pH, a log scale, for this plot. The shape of this plot is due to the fact that the H^+ concentration in the acidic stream is almost four orders of magnitude higher than in the alkaline stream, therefore during mixing the pH in the mixing zone is dominated by acidic stream contribution. The

measured pH data across the mixing zone compared to the predicted pH based on temperature is provided in Figure 5.21.

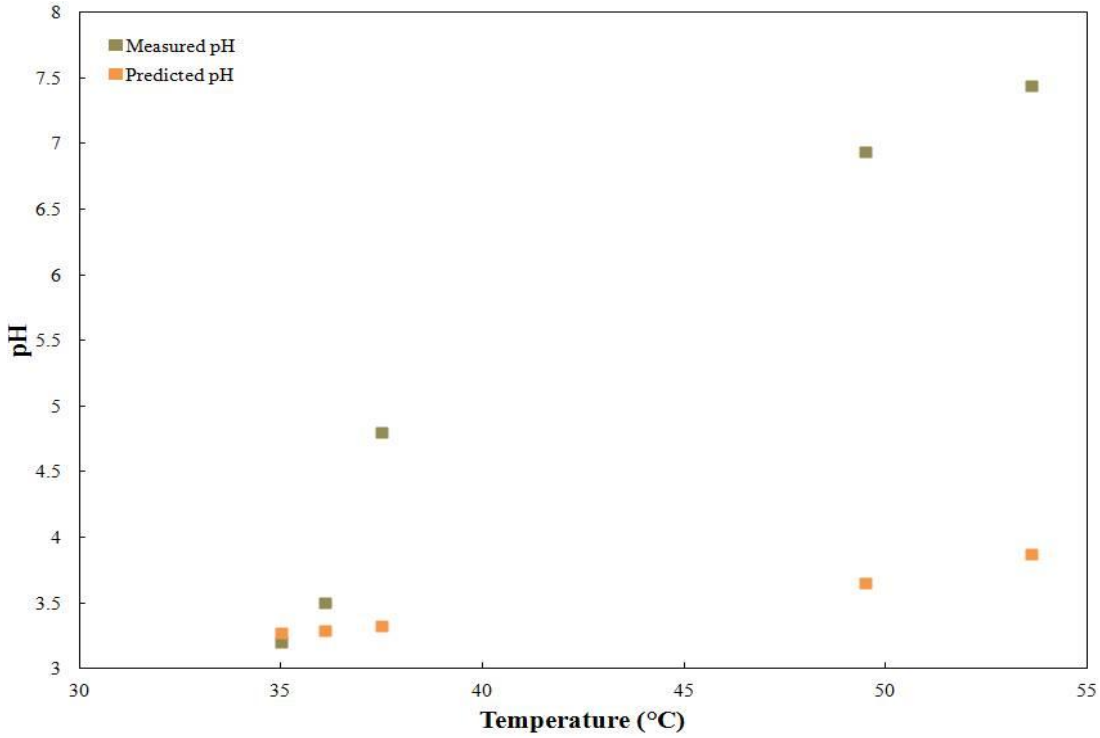

Figure 5.21: Measured and predicted pH values plotted as a function of temperature across the mixing zone. Error bars for the uncertainty in pH (0.01) are smaller than the data markers.

The pH measured in the microbial striping zone is considerably higher than is predicted by the model. Since this is a log scale plot, the difference between the measured and predicted values cannot be explained by errors in temperature or the uncertainty of the pH measurement (±0.01). While the pH is a function of the temperature of the water independent of the mixing physics, the decrease in pH is negligible compared to the difference between the measured and predicted values. Therefore, this difference indicates that pH is either governed by a different mixing mechanism or that pH is not a conservative constituent in the system and is being modified by the biological community within the microbial striping zone (or both). Using basic principles of chemistry, the pH of a solution formed by mixing two solutions of different pH is easily

determined when the molarity of the solutions (concentration per unit volume) and the fractional volumetric contribution of each are known. However, the pH can also be affected by chemical mixing processes such as buffering. Buffering involves the presence of a weak acid (or weak base) and its conjugate base (or conjugate acid) mixing with a strong base (or strong acid). In this system, the alkaline stream (weak base) may be buffered by bicarbonate (HCO_3^-) which is formed when carbon dioxide (CO_2) dissolves in water. The bicarbonate buffering agent works to maintain a higher pH than the physical mixing alone would predict and may be responsible in part for the measured results. Once more geochemical data is analyzed from the two hot springs, a more complex model incorporating the chemical effects of buffering could be applied to the model in order to determine what effect buffering may have on the system.

The measured and predicted pH discrepancy may also be biologically induced. It is well-known that pH is not always conserved in biological systems. For example, the pH in highly acidic lakes contaminated by strip-mining has been successfully increased by introducing sulfate reducing bacteria (Gyure et al. 1989). Additionally, photosynthetic bacteria (such as those in the microbial striping zone) will consume CO_2 (an acid when dissolved in water) during photosynthesis, functionally raising the pH of the system (Revsbech et al. 1983). Any pH discrepancy remaining after buffering is accounted for in the model may provide information as to how much the pH is modified in this system by the biology.

5.2 Conclusion

The utility of using MEMS sensor arrays in a Geyser Creek Basin hot spring system has been shown. The large number of temperature and conductivity measurements taken would not have been possible using existing commercial technology. The system studied involved the mixing zone where two chemically distinct hot spring outflow channels merged. One channel

was hot, alkaline, and had high conductivity, while the other was cool, acidic, and had low conductivity. In the mixing zone where the two streams merged, a zone of several distinct photosynthetic communities appears; these colored communities and are not found anywhere else in the two streams. A high resolution temperature color map was created in ArcMap™ using the high density temperature measurements collected with the MEMS sensor array. The spatial distribution of the various colored photosynthetic communities could be traced out based on the color (temperature zones) of the temperature map. In addition, a similar (albeit lower resolution) conductivity color map was created using the less dense conductivity array measurements.

Conductivity and temperature were compared across the microbial striping zone at approximately the same location and appeared to show the same trend. Therefore, the high-spatial resolution temperature data were used to predict the conductivity based on a mixing model that assumed each stream was an end member reservoir of known conductivity and temperature (and pH). Predicted conductivity values matched the measured conductivity values fairly well at most locations. Therefore, the temperature data was used to create a high resolution *predicted* conductivity color map. The percent error comparing measured conductivity to predicted conductivity was low except at one location where the temperature data appeared dubious. The ability to generate a high spatial resolution map of conductivity even though the measured data were sparse is a potentially powerful technique that could be utilized for other conservative constituents that are impossible to measure at those spatial scales.

Finally, pH was modeled in the same way across the microbial striping zone. Measured pH values varied dramatically from the predicted pH values according to the physical mixing model and buffering and/or biological influence was proposed as the moderating variable.

CHAPTER 6: THERMOELECTRIC COOL-FILM FLOW SENSOR

Flow sensors are extremely important for making a variety of different fluid dynamic measurements. Flow sensors are often used in measuring flow speed and direction and wall shear stress. Flow speed measurements are common for water monitoring purposes such as leak detection for pipes carrying potable water (Melani et al. 2008), industrial process control (Goetz et al. 2009) and flood monitoring (Castillo-Effer et al. 2004). One application of wall shear stress measurement involves measuring aerodynamic properties such as flow separation (and detachment) and drag. Flow separation and detachment measurements determine when a fluid detaches from a surface (e.g. airfoils or propeller blades) which creates vortices and can increase drag. These measurements are critical in the design of airplane wings and wind turbines (Buder et al. 2008). Shear stress sensors have also been developed for underwater vehicles (Xu et al. 2005) and on flexible substrates for *in-vivo* applications (Ai et al. 2009). The focus of this research involved developing a sensor capable of measuring shear stress (flow velocity) in two different types of harsh environments: hot spring hydrothermal systems and the human body.

As discussed in previous chapters, hot springs are considered a harsh environment due to the fact that the water temperature can be near boiling and may have a wide range of pH and salinity, which are corrosive to commercial-of-the-shelf instrumentation. In addition, the biology in the hot spring can grow on the sensor surface and cause measurement error and drift – a process called biofouling (Kerr et al. 1998). Flow measurements in the hot springs may provide information about water mixing and residence time. As discussed in Chapter 5, outflow channel mixing is an important aspect as microbial communities can appear at the intersection between two chemically different hot spring outflow channels or organisms thriving in one channel may disappear where that channel intersects with another. Flow speed and direction may help

determine to what degree streams are mixing, especially if a parameter such as temperature is not substantially different between the two streams. In addition, flow rates in the hot springs have been used to determine rates of change in chemical concentrations (Cox et al. 2011) and can be used to determine residence time (how long it takes for a parcel of water entering the system from the source pool to flow to the edge of the pool or through the length of an outflow channel) which may affect the redox state of the hot spring and therefore microbial community composition (Costa et al. 2009).

Sediment also plays a role in hot spring habitats. Microbial mats are made up of a matrix of microbes and silica grains precipitated from the water. The physical transport of sediment is expected to scale with excess shear stress exerted by water on a channel bed such that (Wolman and Miller 1960):

$$Q = k(\tau - \tau_c), \qquad \text{(Eq. 6.1)}$$

where Q is the rate of transport, k is a transported material specific constant, τ is the shear stress (per unit area), and τ_c is a critical shear stress (per unit area) required to initiate transport. While recent work has suggested that transport may be principally determined by sediment flux and not fluid discharge (Sklar and Dietrich 2001), this equation provides an approximate physical limit to the amount of sediment that can be carried by a fluid and is still widely used to infer erosion rates as well. Monitoring variables that control erosion and transport rates such as bed shear stress are important because these factors can influence the amount of energy, nutrients, and materials available to organisms living in the hot springs and influence the microbial community composition and structure.

The hot spring environment is quite different from that inside the human body; however, there are some similarities as well. The human body can also be considered a harsh environment. While blood is slightly alkaline and 0.9% salt by mass, the main factor making it a harsh environment for sensors is due to the fact that objects placed *in-vivo* may be determined by the body as foreign and attacked by antibodies. Antibodies and other proteins may bind to the device and corrode the sensor surface and cause biofouling issues as well. In addition, the human body may also be harmed by the sensor due to the introduction of toxic elements or molecules (Wisniewski et al. 2000). Materials that will not harm the body and won't cause an immune response are given the term biocompatible (Chow et al. 2010). Biocompatible materials are also desired for operation in hot springs as well, as these ecosystems can be sensitive to foreign elements and molecules and the scientists studying them try to cause as little stress to the organisms living there as possible. Furthermore, determining certain chemical and elemental concentrations in the hot springs are important and therefore sensor degradation and structural decomposition upstream of a measurement site may invalidate data collected downstream.

Just as shear stress measurements can elucidate flow properties within the hot spring, these same measurements are important for understanding blood flow in the human body. Atherosclerosis, the leading cause of death in the industrialized world, is a disease that primarily affects the outer edges of blood vessel bifurcations. In arteries, blood flows differently at bifurcations compared to more straight regions of the vessel (Rouhanizadeh 2007). Along the medial wall where the flow diverges, the shear stress is high (Figure 6.1).

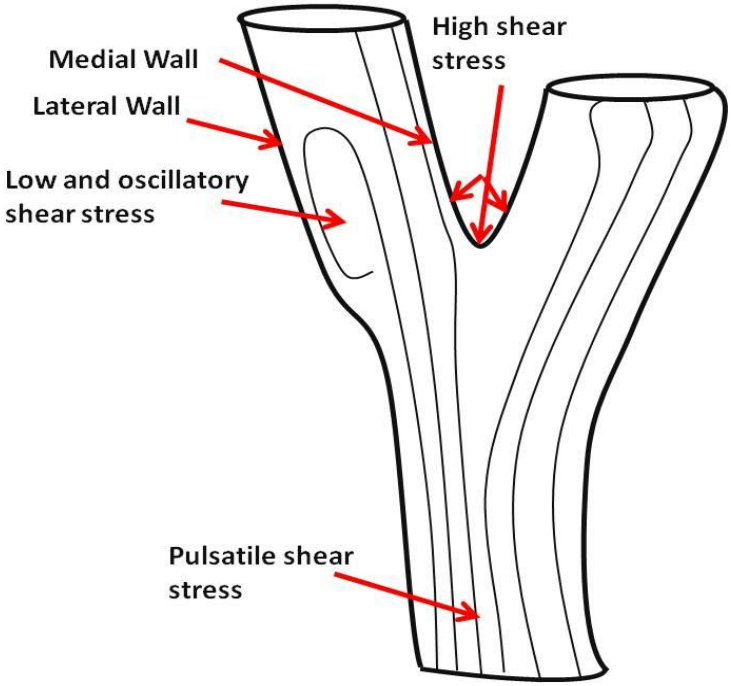

Figure 6.1: Schematic drawing of an arterial bifurcation with flow fields highlighting distinct regions of wall shear stress.

Along the lateral wall of the bifurcation, the flow is slow and oscillatory, which leads to a significantly lower amount of wall shear stress (Malek et al. 1999). This area of low shear stress can allow for the accumulation of plaque; forming lesions which can rupture and induce clotting of the vessel at the point of rupture or farther downstream. The build-up of plaque causes tell-tale changes in the local flow field, mainly low-shear stress upstream of the lesion, high shear-stress at the throat of the lesion, and oscillatory flow downstream (Cecchi et al. 2011) where more plaque can accumulate.

Therefore, the onset of atherosclerosis can be identified and studied by measurement of the shear-stress field.

Most of the available commercial flow sensors use mechanical or magnetic methods for measuring flow properties and, as such, these devices can be cumbersome and expensive. The

sensor size, power consumption, spatial and temporal resolution, and cost can all be improved by utilizing MEMS fabrication techniques (Rouhanizadeh et al. 2006). There are two main methods for MEMS shear stress (and flow speed) measurements. The first is a direct method involving a floating sensing element. Floating sensing elements involve structures that move or bend proportional to the shear stress (or flow speed). Two of the more common techniques for monitoring floating element movements are capacitive sensing or piezoresistance measurements on a cantilevered beam. With capacitive sensing, typically an electrode is placed at the free end of the cantilevered beam which will bend under fluid-induced shear stress and the variable distance between the beam electrode and a fixed-position electrode can be determined through a simple capacitive measurement (Jiang et al. 2005). Piezoresistive measurements involve fabricating the cantilevered beam from a piezoresistive material (e.g. polysilicon) that will change resistance as the beam is placed under stress due to bending from shear forces (Shajii et al. 1992) and can be monitored using Ohm's Law with a constant current input. However, the sensing elements of floating sensors can be fragile and easily broken and can be difficult to fabricate and package (Buder et al. 2007).

The second method for shear stress measurement is an indirect measurement. The most popular method of indirect flow detection uses thermal methods (although ultrasonic and electromagnetic methods are used as well). Typically, this is performed by injecting heat into the flow and using convection heat transfer principles to determine properties of the flow and is called thermal anemometry (Lin et al. 2004). The use of heat to determine flow dynamics as well as fabrication processes that permit relatively small and flat surfaces, results in very little flow perturbation which allows more accurate measurements. The most common thermal flow measurement method, anemometry, is based on convective cooling of a heated sensing element

as fluid flows over its surface. The heated sensing element is a resistor. When the resistor's temperature is higher than the surrounding fluid, heat energy is transferred to the moving fluid via convection, increasing the water temperature within a small boundary layer (Figure 6.2).

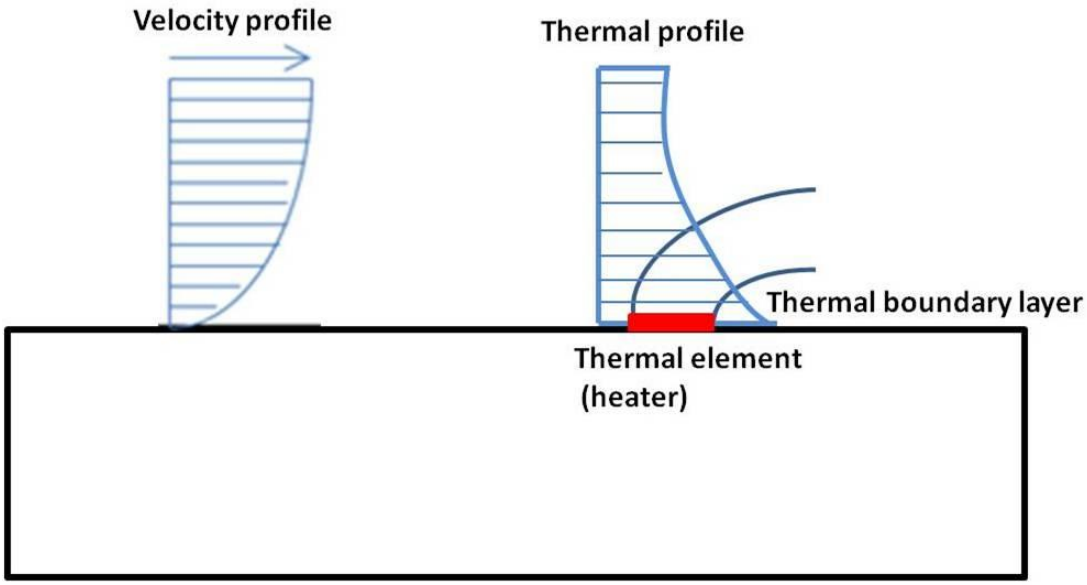

Figure 6.2: Schematic diagram showing a fluid moving across a plate with a heated sensing element on top. The velocity profile shows the shape of the velocity boundary layer and the thermal profile shows shape of the thermal boundary layer.

There are two different boundary layers of importance. The first boundary layer is the velocity boundary layer. This boundary layer signifies where the velocity gradient (magnitude of the velocity change with respect to distance above the surface) is non-zero. At the surface, the velocity is assumed to be zero due to the no-slip boundary condition. At the top of the velocity boundary layer the velocity is same as the free stream velocity (technically, the boundary layer is defined as stopping at a height where the velocity is 99% of the free stream value). The height of the velocity boundary layer increases moving away from the leading edge of the flow (Fox et al. 2004). The thermal boundary layer signifies where the temperature gradient (temperature change with respect to distance above the surface) is non-zero. At the surface, the temperature will

match that of the heated sensor. At the top of the thermal boundary layer the temperature matches that of the ambient environment (fluid temperature). While the two boundary layers need not be the same height, the majority of the heat transfer occurs within the velocity boundary layer.

By setting the heater to a constant temperature (constant resistance), which requires a variable current input, the total electrical power input (P_{in}) to this resistor is given by:

$$P_{in} = I^2 R, \quad \text{(Eq. 6.2)}$$

where the current input to the heated resistor is given by I and the resistance of the heated element is R. The convective heat transfer from the heated surface to the fluid depends on the flow characteristics in the viscous boundary region and is given by:

$$Q = hA(T - T_0), \quad \text{(Eq. 6.3)}$$

where Q is the heat energy transferred from the heated element to the fluid per unit time, h is the convective heat transfer coefficient, A is the surface area of the heated sensing element, T is the temperature of the heated sensing element and T_0 is the temperature of the ambient environment (fluid). The convective heat transfer coefficient carries the information about the velocity of the flow and its equation is generally given as:

$$h = a + bv^c, \quad \text{(Eq. 6.4)}$$

where v is the velocity of the flow, and a, b, and c are ambient specific, empirically determined constants affected by geometry and boundary layer dynamics and are characterized through calibration. If all of the heat energy generated by the resistor (per unit time) is transferred to the liquid via convection, then the variable Q becomes the power output, P_{out}. This means that heat transfer by other mechanisms (conduction and radiation) to the flow and the sensor substrate

must be negligible. For most non-zero flow speeds, heat conduction in the water will be much smaller than heat convection due to the low thermal conductivity coefficient of water. The conduction contribution should also remain relatively constant for a constant temperature fluid and will not vary with changing flow speed. Radiative heat transfer to the water and surroundings is also negligible due to the small surface area of the sensor and the small temperature difference between the resistor and ambient fluid (typically 10 °C). Heat conduction to the substrate beneath the heater is a much bigger issue and therefore MEMS anemometers often times incorporate vacuum cavities beneath the resistor to minimize this effect (Huang et al. 1996). Equating the power input and output gives:

$$P_{in} = P_{out} \rightarrow I^2R = hA(T - T_0), \qquad \text{(Eq. 6.5)}$$

and finally substituting Eq. 6.4 into Eq. 6.5 and solving for the velocity gives:

$$v = \left(\frac{I^2R}{bA\Delta T} - \frac{a}{b}\right)^{1/c}, \qquad \text{(Eq. 6.6)}$$

where ΔT is used in place of $(T\text{-}T_0)$ and Eq. 6.6 represents the final form of the convective heat transfer equation. The advantages of this sensing technique are simplicity in fabrication, robustness due to an absence of moving elements, high sensitivity, and the capability of measuring time-varying flows. The anemometer principle provides a sensitive and accurate method for measuring the flow velocity because the amount of heat convectively delivered to the flow is measured directly by the power input to the resistor. However, an anemometer alone cannot provide any information on flow direction.

There is a second thermal flow sensing principle called calorimetry which can be used to determine flow magnitude and direction (Dijkstra et al. 2008). Here the fluid is again heated up by a central resistor as with thermal anemometry. However, temperature sensors arranged

symmetrically upstream and downstream of the flow are used to determine the temperature change of the fluid (and thus speed) and the direction of the flow. A central resistor injects heat into the fluid, which increases the water temperature in a small boundary layer. The water is carried downstream in the direction of the flow where it passes over the downstream temperature sensor. The downstream temperature sensor, originally at ambient temperature, will now be convectively heated from the higher temperature water within the small boundary layer (Ashauer 1998). The upstream (opposite of flow direction) sensor measures the ambient temperature of the flow. The temperature sensors are typically temperature-sensitive resistors (often called thermistors) or thermopile junctions and are located very close to the central heater to increase sensitivity. Measuring flow velocity magnitude via the heat exchange between the heated fluid and the thermistors (calorimetry) is less sensitive than anemometry for high flow speeds (Elwenspoek 1999); when the heat is initially injected into the flow via the central heater, the finite amount of time the heat energy spends in the flow allows diffusion to occur where some amount of heat will escape the velocity boundary layer. Also, inefficiency in transferring the heat from the fluid to the thermistor adds to the loss. Keeping the thermistors near the central heater can improve sensitivity; however, it can also create additional measurement error due to heat passing conductively from the heater to the thermistors through the substrate.

The third thermal flow sensing principle is called thermal time of flight. In this method a pulse of heat is delivered to the flow through a centralized heater. When the pulse is delivered a clock timer begins. The heat is carried downstream where it flows over a temperature sensor which is convectively heated. When the temperature sensor (such as a thermistor) output registers a maximum in temperature (corresponding to the pulse peak), the time is recorded. By fabricating the thermistors at a known distance from the central resistor delivering the heat pulse,

the velocity can be determined by taking this distance and dividing by the amount of time it took for the pulse maximum to be registered at the downstream thermistor. By placing thermistors symmetrically around the heating source, the direction of the flow can be determined as well. Because the heat will diffuse in the water, more accurate results are obtained by setting the thermistors close to the heating element. However, as noted before, conduction through the substrate becomes an issue and limits how close the temperature sensors can get to the heater and the control and readout circuitry is significantly more complicated.

The thermal flow sensing techniques work very well in environments where the fluid temperature is not extremely high and the local temperature increase around the sensing element is not an issue. However, for heated sensing elements used in fluids near boiling temperature (e.g. some hot springs), the heat energy produced by the resistor can boil the water at its surface, creating a two-phase mixture with entirely different heat transfer properties than non-boiling water (Tong and Tong 1997). In the human body, prolonged localized heating may cause damage to cells or tissue. Dewhirst et al. (2003) reviewed research on cell damage in both mice and humans at prolonged exposures to elevated temperatures. They showed that a five-hour exposure of just 5.5 °C above ambient body temperature (~37 °C), killed almost 99.9% of cells in one experiment and for temperatures approximately 8 °C above ambient, almost 99.9% of cells were killed in less than one hour. Based on these *in-vivo* heating results and the issues with boiling water in the hot springs, the allowed temperature difference between the heated sensing element and the environment would be extremely limited. Since the sensitivity of an anemometer is proportional to the temperature difference between the heated resistor and the ambient fluid, the reduced temperature difference makes this technique much less sensitive.

Therefore, in order to measure fluid properties in these environments, a thermal anemometry flow sensor based on cooling the flow was investigated. A sensor incorporating the same heat transfer physics (Figure 6.3), but cools the hot fluid instead of heating it would be able to be used in any hot spring environment.

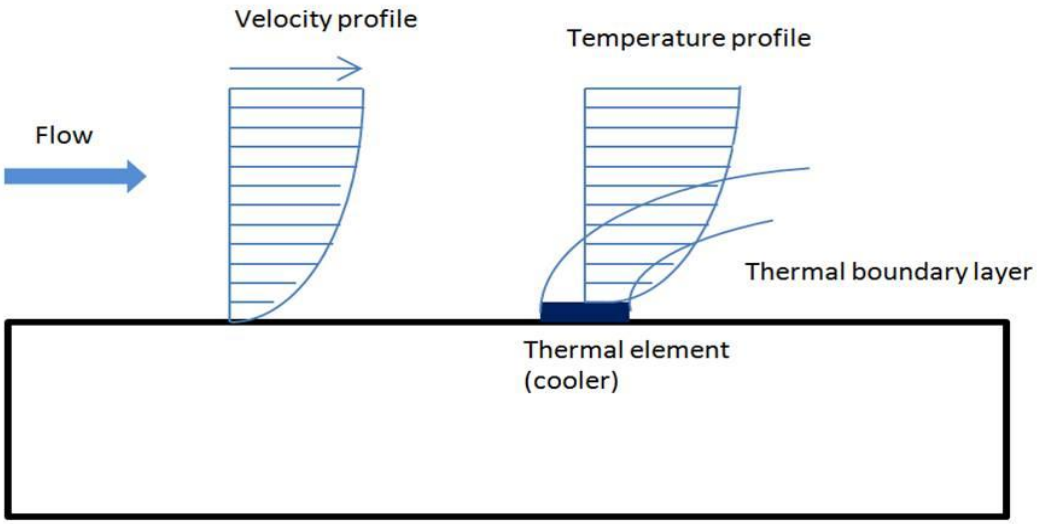

Figure 6.3: Schematic diagram showing a fluid moving across a plate with a cooled sensing element on top. The velocity profile shows the shape of the velocity boundary layer and the thermal profile shows shape of the thermal boundary layer.

In regard to the human body, it turns out that locally cooling tissue is less harmful at similar or significantly larger changes in temperature compared to heating (Hoffmann and Bischof 2002) and therefore provides a safer mechanism for in-vivo flow property measurements while at the same time allowing for increased measurement sensitivity due to a larger allowable temperature difference between the cooled film and ambient environment. The resistive element can be actively cooled through use of thermoelectric cooling.

Thermoelectric cooling is governed by the Peltier effect to turn electrical energy into thermal energy by pumping heat from one junction to another under a voltage differential (Figure 6.4).

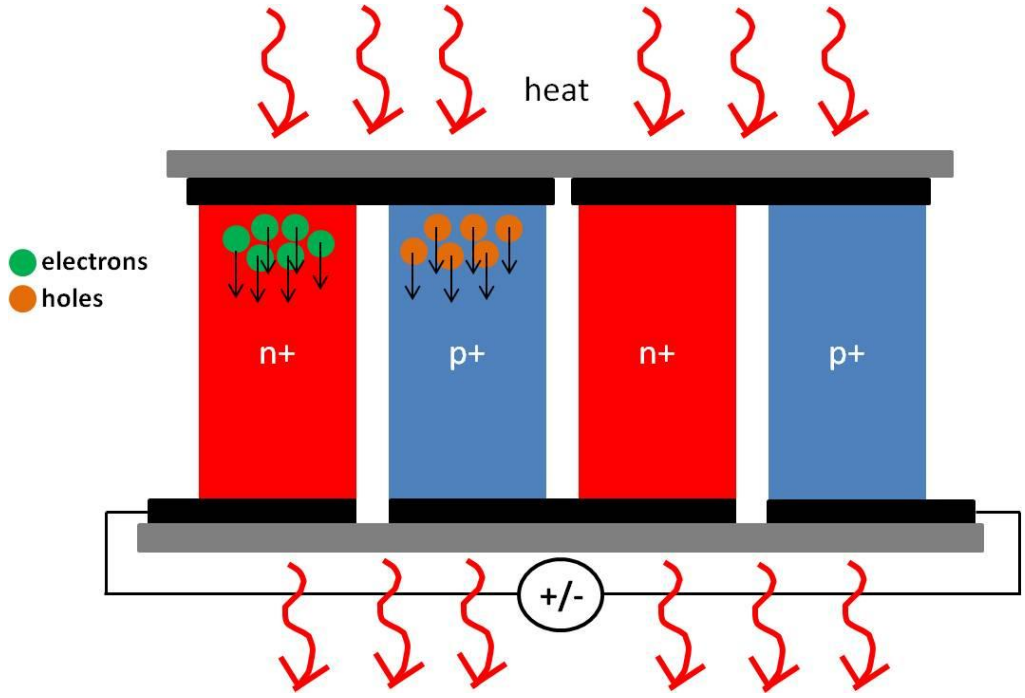

Figure 6.4: Schematic diagram showing how the Peltier cooling effect pumps heat from the top of the device to the bottom under an applied voltage. Red arrows represent the flow of heat.

The thermoelectric cooler consists of two junctions where different conducting materials, typically n-type and p-type semiconductors are electrically joined. One type of thermoelectric material employed in thermoelectric coolers is poly-crystalline silicon (polysilicon). Polysilicon that has been doped with an n-type (n^+) dopant such as phosphorus has excess electrons. Polysilicon doped with a p-type dopant (p^+) such as boron has excess holes. When a negative voltage is applied to the p-type material and a positive voltage applied to the n-type material at the same junction, the majority carriers (electrons in n-type and holes in p-type) will migrate toward the oppositely charged junction. The majority carriers carry heat away from one junction

and bring it to another. The junction from which the majority carriers move away from becomes cooler and the junction to which the carriers move toward becomes hotter (DiSalvo 1999). Heat carried to the hot side junction must be efficiently rejected to the environment or the hot carriers may diffuse back to the cold side. The maximum efficiency of a thermoelectric material is governed by its figure of merit, *zT*, and is given by:

$$zT = \frac{\alpha^2 T}{\rho\kappa}, \qquad \text{(Eq. 6.7)}$$

where α is the material specific Seebeck coefficient, T is temperature, ρ is the material electrical resistivity and κ is the material thermal conductivity (Snyder and Toberer 2008). Materials with higher figures of merit are better for cooling, but they tend to incorporate more exotic elements which is less desired for *in-vivo* applications and may be more difficult to work with in MEMS fabrication processes. In general, thermoelectric coolers are inefficient and are best suited for cooling smaller objects (such as micro-sensors) with a small temperature differential to avoid a large consumption of power (Hilbert et al. 1999).

6.1 Cool-film Flow Sensor Experiment Setup

In order to test the proposed flow sensing mechanism, a micro thermoelectric cooler was purchased from TE Technology, Inc. The cooler that was purchased was potted, meaning that the space in between the thermoelectric material junctions was filled with an electrically insulating water resistant material of low thermal conductivity (to prevent an electrical short and a thermal short between the hot and cold junctions due to moisture). Since the potting material is only water resistant and not water tight, the outer edges of the cooler were covered in an insulating low thermal conductivity waterproof marine epoxy (Figure 6.5).

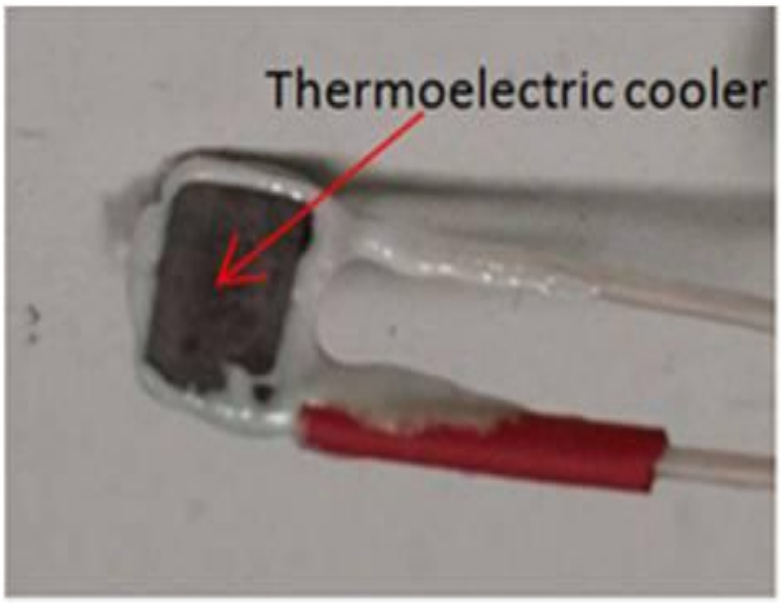

Figure 6.5: Image of a potted micro thermoelectric cooler (TE Technology, Inc.) with edges covered in waterproof marine epoxy. The cooler is approximately 3.4 mm length on a side.

The thermoelectric cooler was embedded in an electrically and thermally insulating transparent material called polydimethylsiloxane (PDMS). Only the cool side junction of the cooler was exposed to the water at the surface of the PDMS. Due to the thermally insulating nature of the PDMS, a hole was made through the PDMS to the hot side junction of the thermoelectric cooler, and a high thermally conductive silver epoxy (Epoxy Technology, Inc) was used to fill the hole and provide a larger area heat sink for the device. Normally, the small heat sink on the hot side of the cooler will lower the performance of the cooler under high power input and is therefore a critical aspect for *in-vivo* sensor design in order to maintain a small device size.

To operate the sensor, a small resistance temperature detector (RTD) was necessary to monitor the temperature of the cooled surface. A flexible micro RTD was fabricated and bonded to the top of the cooler so that temperature of the cold side junction could be measured. The

flexible RTD design is described in Yu et al. (2008) and the fabrication of the RTD was carried by out a colleague. The fabrication process for the flexible RTD is shown in Figure 6.6.

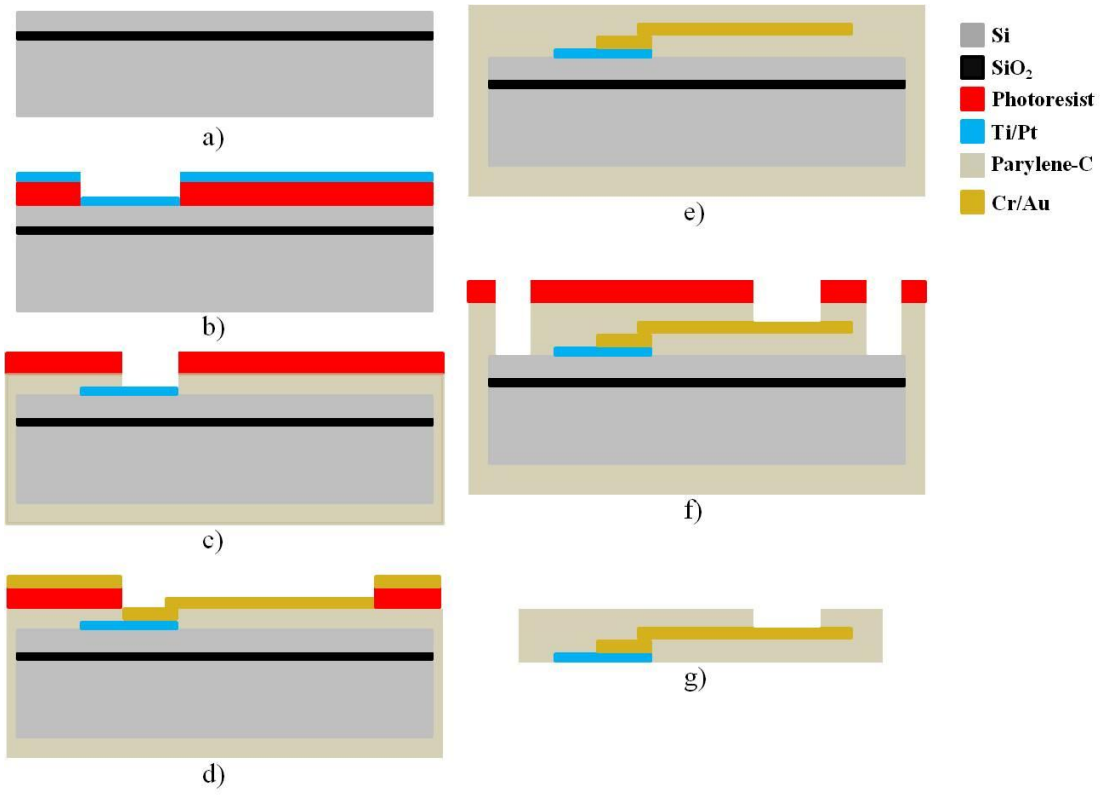

Figure 6.6: A schematic of the fabrication process flow for the flexible micro RTD in cross-section. (a) A layer of SiO_2 is thermally grown on the wafer and a layer of sacrificial amorphous Si is deposited overtop the SiO_2. (b) Photoresist is deposited and patterned and a layer of Ti/Pt is deposited and lifted off. (c) Parylene-C is deposited over the entire wafer and removed over an area of the Ti/Pt using a photoresist mask. (d) Photoresist is deposited and patterned and a layer of Cr/Au is deposited and lifted off over the Parylene-C opening. (e) A second layer of Parylene-C is deposited over the entire wafer. (f) The Parylene-C removed over an area of the Cr/Au and an area exposing the sacrificial Si. (g) Finally, the sacrificial Si is etched away underneath the Parylene-C, releasing the device.

The fabrication begins with a bare Si wafer. In the first step, 0.3 µm SiO_2 is thermally grown on the Si wafer, followed by a 1 µm electron-beam (e-beam) evaporation deposition of a sacrificial layer of amorphous Si. Next photoresist is deposited and patterned followed by an e-beam evaporation of 0.015 µm Ti and 0.06 µm Pt and liftoff in an acetone bath to form the RTD

resistive element. A 9 µm thick Parylene-C film is coated over the entire wafer and an opening is etched in the Parylene-C over the Pt resistor. Next, photoresist is deposited and patterned followed by an e-beam evaporation of 0.02 µm Cr and 0.6 µm Au to form the electrical leads and bond pads. Another 9 µm layer of Parylene-C is deposited over the entire device. The Parylene-C is opened over the Cr/Au at the bond pads and opened over two areas exposing the sacrificial Si. Finally, the layer of sacrificial Si is isotropically etched away using XeF_2 gas, releasing the micro RTD. The device substrate is now made of the electrically insulating, low-water-leakage, and flexible material Parylene-C. Figure 6.7 shows a magnified image of the RTD and a cross-section drawing. The exposed Pt and Parylene-C are both biocompatible materials. In addition, the epoxy and the wire used to make the electrical connection to the bond pads are biocompatible.

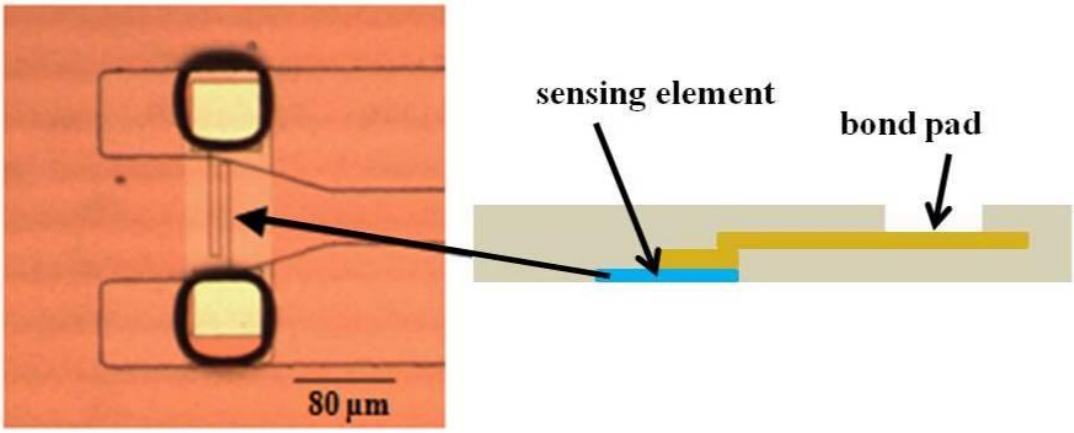

Figure 6.7: (left) Close-up image of the resistive sensing element on the micro RTD. (right) Schematic drawing of RTD in cross-section.

The micro RTD was bonded to the cold side junction of the PDMS-embedded thermoelectric cooler using a thin layer of photoresist (Figure 6.8). An acrylic channel (1.1 cm width x 1.1 cm height) was mounted on the PDMS substrate with the cooler and RTD positioned at the center of the channel.

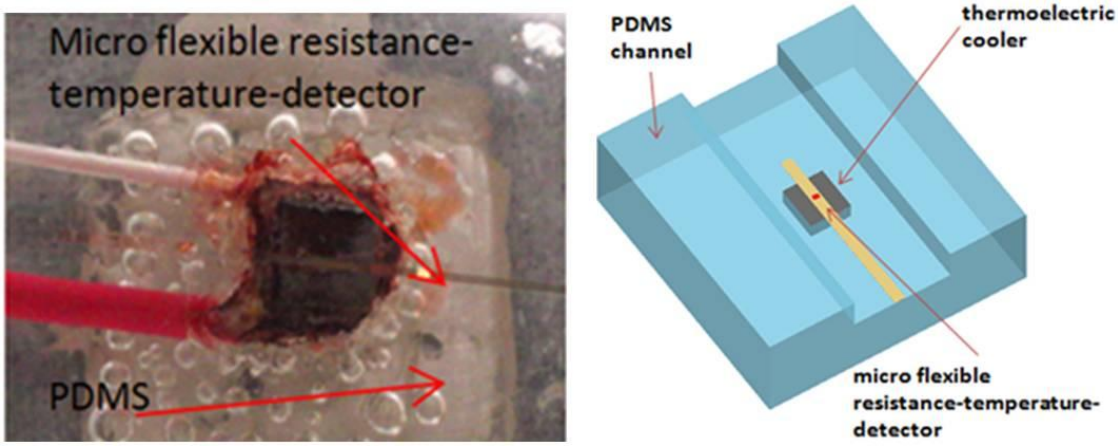

Figure 6.8: (left) Close-up image of the cooler with the micro RTD bonded to the cold-side junction. Bubbles are present in the PDMS due to non-vacuum curing. (right) Schematic drawing of the embedded cooler and RTD in a flow channel.

The acrylic flow channel was designed to be small enough in width and height to create higher flow speeds (higher shear stresses), but not so small that the flow over top the sensor would be affected by edge-effects from the side walls of the channel. The thermoelectric cooler wires were connected to a variable power source and the RTD wires were connected to a high-precision multimeter (Figure 6.9).

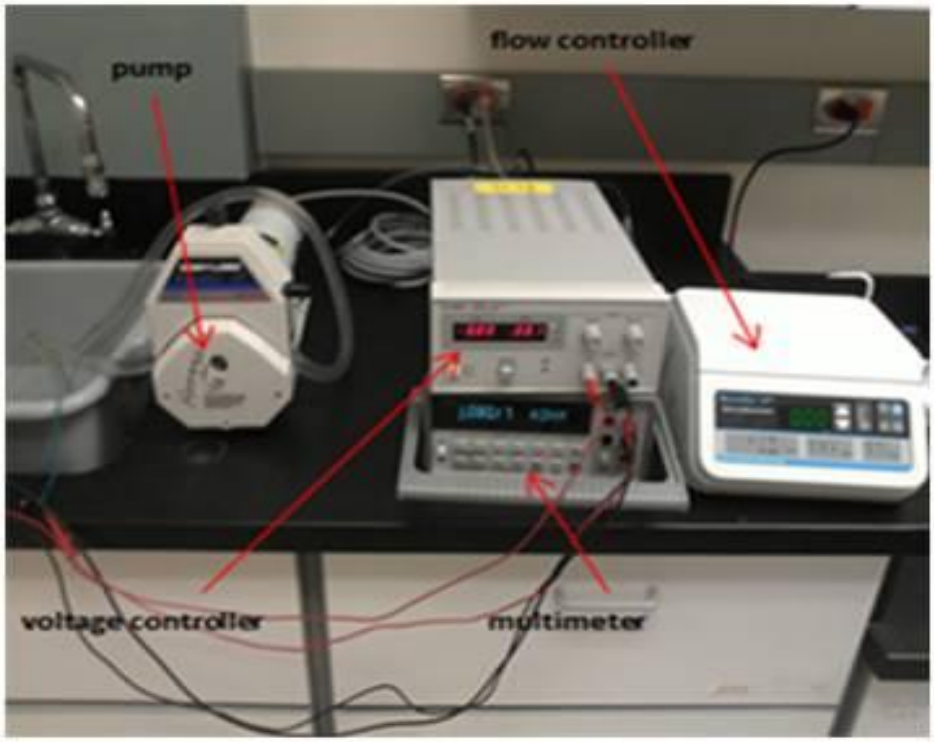

Figure 6.9: The flow channel with embedded sensor were placed entirely underwater. Flow speed was controlled by a peristaltic pump and flow controller. Power input to the thermoelectric cooler was monitored with the voltage controller and RTD resistance was monitored with a high-precision multimeter.

The flow rate through the channel was controlled by a flow controller and variable speed peristaltic pump (Cole-Parmer). The PDMS substrate and acrylic channel were submerged in room temperature water for testing. The cooler was connected to a voltage-controlled power supply and the micro RTD was connected to a high precision multimeter to monitor its resistance. In order to convert the resistance of the RTD to temperature, the temperature coefficient of resistance (TCR) was determined through calibration (Figure 6.10).

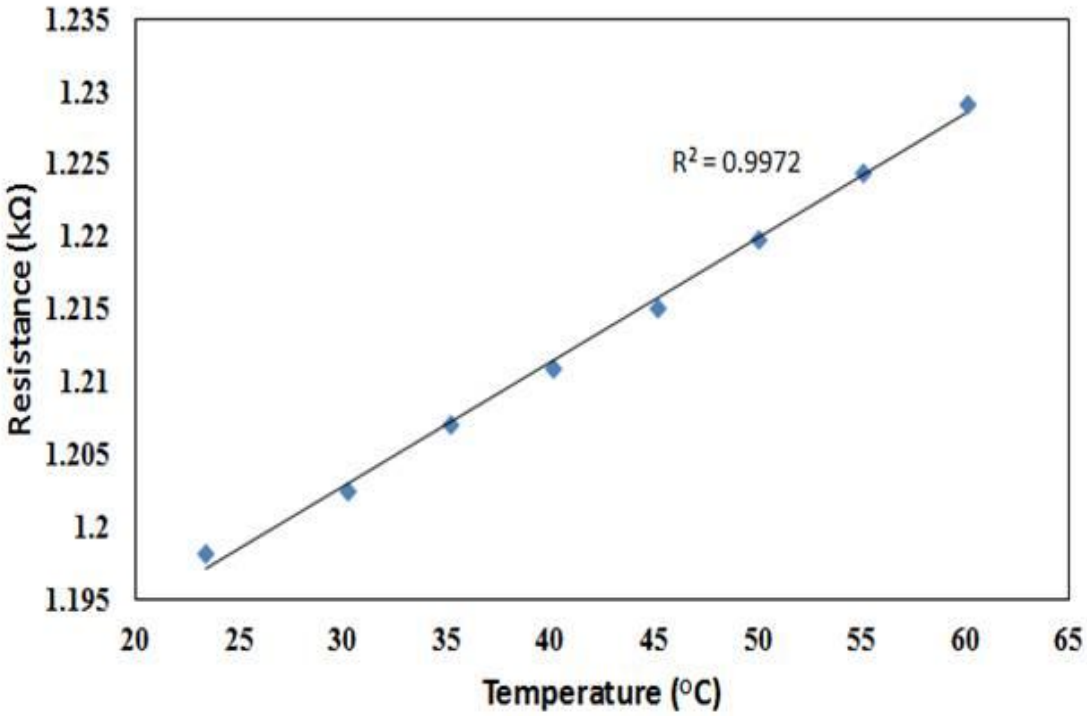

Figure 6.10: Temperature-resistance calibration curve for the micro RTD. The device TCR was ~1000 ppm/°C.

The RTD resistance was about 1200 Ω at room temperature and the TCR was approximately 1000 ppm/°C. The pump flow controller provided volumetric flow speed information which can be converted to a velocity using the channel geometry. The volumetric flow was converted to shear stress according to a complicated equation (Truskey et al. 2004) that takes into account channel geometry and is given by:

$$\tau = \mu Q \frac{\sum_{n=0}^{\infty} \frac{48}{(2n+1)^2 \pi^2 \cosh\left(\frac{(2n+1)\pi W}{2H}\right)}}{WH^2 - \sum_{n=0}^{\infty} \frac{96H^3}{(2n+1)^5 \pi^5 \cosh\left(\frac{(2n+1)\pi W}{2H}\right)} \exp\left(\frac{(2n+1)\pi W}{2H}\right)}, \qquad \text{(Eq. 6.8)}$$

where τ is the shear stress, μ is the viscosity of the water, Q is the volumetric flow rate, W is the width of the channel and H is the height of the channel.

6.2 Cool-film Flow Sensor Experiment Results

In the first test, the temperature of the RTD was maintained at 20 °C (around 5 °C below the ambient temperature) using the variable power supply. As the flow rate (and consequently, shear stress) over the RTD was increased from 0-0.5 L/min (0-0.06 dyne/cm^2), the power needed to maintain a constant temperature was increased from 5-110 mW. The data show an approximate linear response of power with increasing shear stress (Figure 6.11).

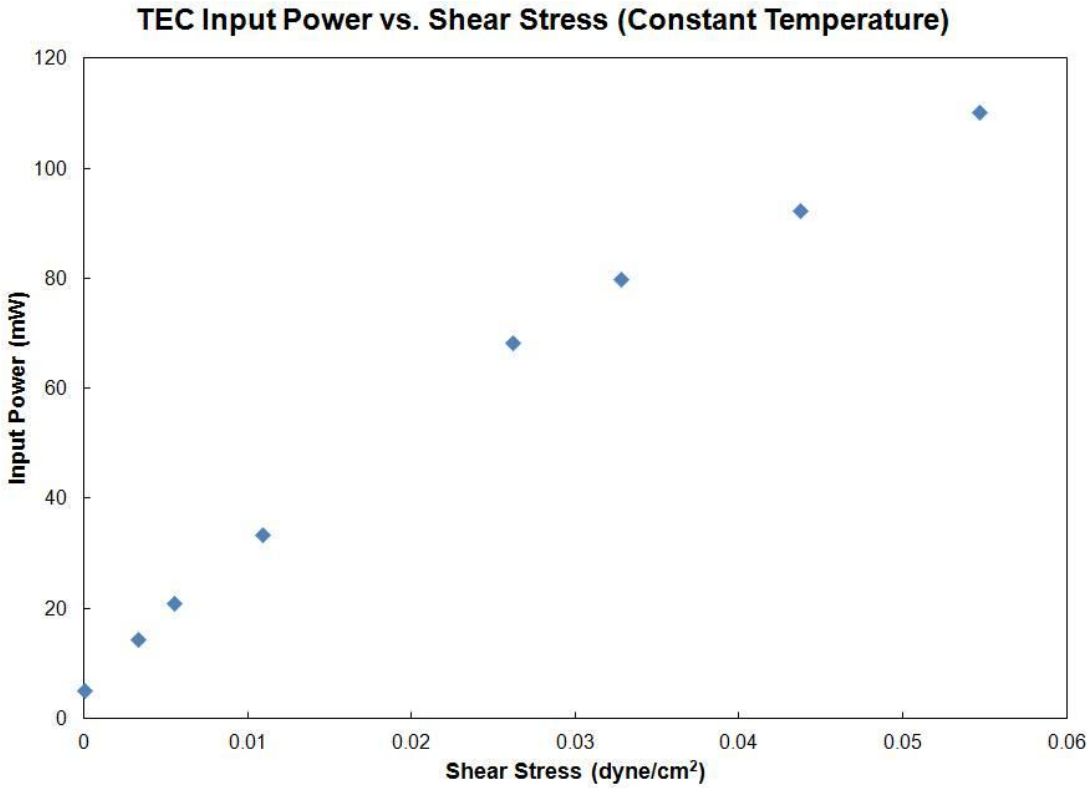

Figure 6.11: Plot showing the increase of power input to the thermoelectric cooler required to maintain a constant RTD temperature for increasing wall shear stress (flow speed).

In the second test, the power input to the thermoelectric cooler was maintained at a constant value of 47 mW. As the flow rate over the RTD was increased, the RTD temperature increased. The temperature increased linearly in the low shear stress domain (0-0.04 dyne/cm^2), and gradually saturated at higher wall shear stresses (Figure 6.12).

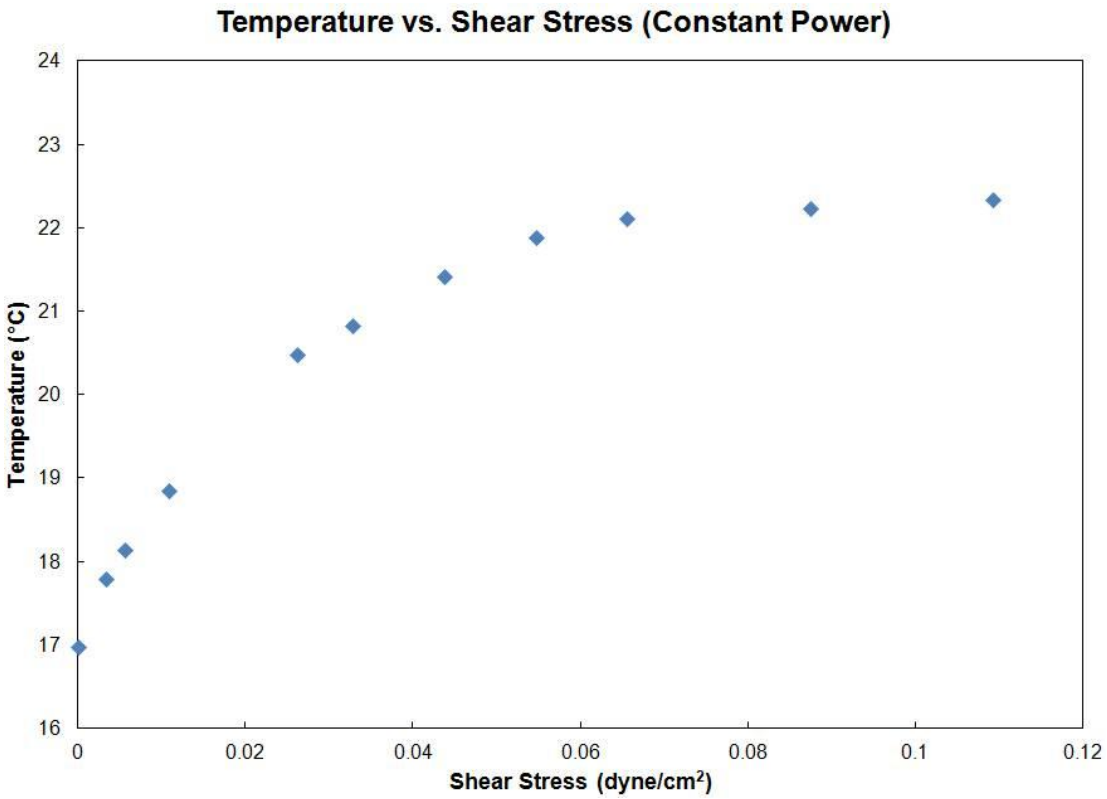

Figure 6.12: Plot showing the increase of RTD temperature (at constant power input) for increasing wall shear stress (flow speed).

The plot begins to saturate in the higher shear stress regime because the temperature of the thermoelectric cooler approaches that of the ambient environment which decreases the heat transfer from the fluid to the cooler. The combined data show that wall shear stress (or flow speed) can be measured using a thermoelectrically cooled RTD.

A three-dimensional model of the experiment was created in Comsol Multiphysics® to verify the proposed sensing mechanism (Figure 6.13).

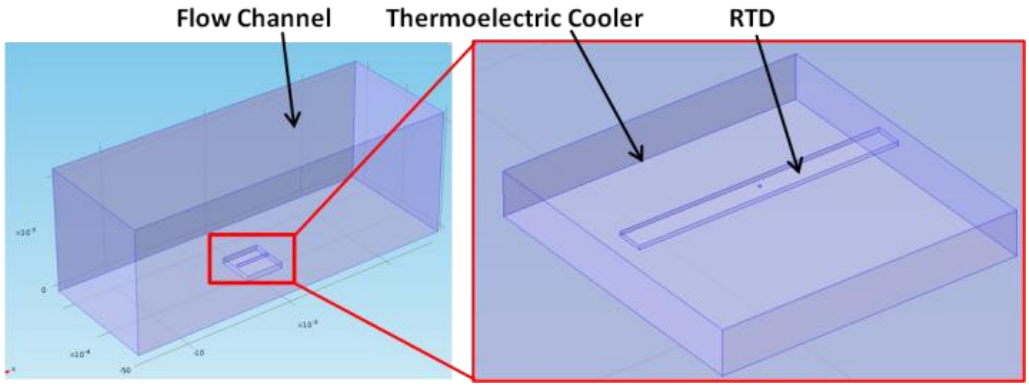

Figure 6.13: Screenshot image of Comsol® 3D model of a cooled RTD in flow channel.

The channel dimensions and approximate size and shape of the thermoelectric cooler and RTD were used in the model. The channel was modeled as water at room temperature. The cooler was modeled as a ceramic box with the top surface maintained at a constant temperature (approximately 10 °C below ambient). The RTD was modeled as a Parylene-C substrate with a thin platinum layer on top. The photoresist bond layer between the RTD and cooler was modeled as a thin resistive layer of 1 µm thick. The water was flowed at different velocities over the sensor which was cooled from below by the top surface of the ceramic box. The temperature in the platinum layer was output at different flow rates corresponding to those used in the experiment. The comparison between the experiment data at constant power and the model (Figure 6.14) show relatively similar changes in RTD temperature with increasing shear stress.

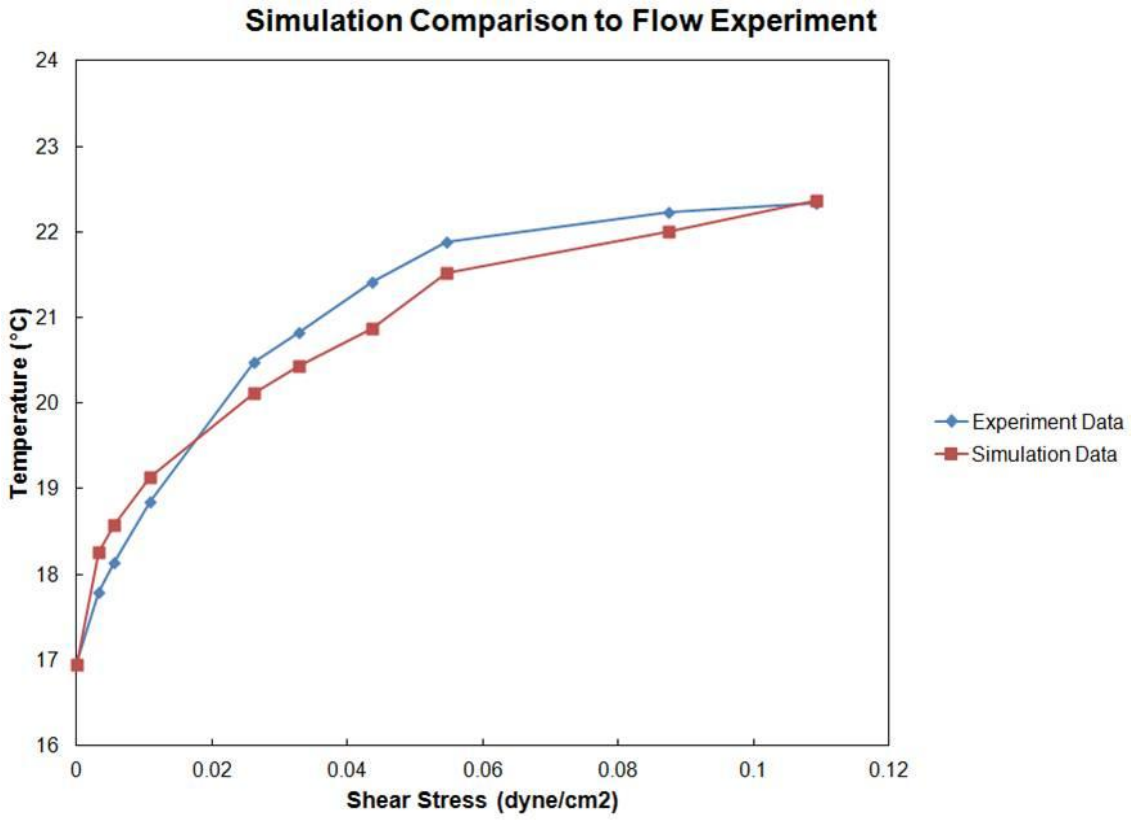

Figure 6.14: Plot comparing the change in RTD temperature with increasing shear stress (flow speed).

The major difference between the model and the experiment was that for the experiment, the cooler was set at a constant power input of 47 mW, whereas the model could not simulate a constant power input to cooler surface that matched physical reality. Instead, the model cooler (ceramic box) surface (underneath the RTD) was set to a constant temperature such that the initial temperature of the simulated RTD matched that of the RTD in the experiment.

6.3 Conclusion

A sensor was developed to measure flow properties in fluids with near-boiling temperatures or conditions where the amount of localized heating of the fluid by an anemometer was a major constraint such as in the human body. Instead of using a heated resistor set to a

temperature above the ambient environment, a RTD was cooled below the ambient temperature by a micro thermoelectric cooler. The results show that a thermoelectrically-cooled RTD can be used to measure wall shear stress (or flow speed) based on thermal convection principles. Channel size and flow rate were limited by the cooler size and peristaltic pump, respectively, so significantly higher shear stress measurements were not possible that might better match flow properties in a hot spring or artery. Future sensor design work should focus on fabricating an integrated RTD with a micro thermoelectric cooler. The integrated cooler and sensor must have a means to prevent electrical and thermal shorting by the liquid penetration between the hot and cold junctions. The materials that will be exposed to the fluid should ideally be biocompatible for hot spring use and must be biocompatible for *in-vivo* use. Finally the heat sink connected to the hot side junction of the cooler must be optimized for improved heat rejection (to lower the hot side temperature) in order to prevent possible cell damage during *in-vivo* applications. A lower hot side junction temperature would also increase the efficiency of the thermoelectric cooler and will result in lower power consumption.

CHAPTER 7: CONCLUSION

This dissertation explored the development of MEMS sensors and the corresponding electronic systems for measurements to characterize an aspect of harsh environments (e.g. ionizing radiation) and operation within a harsh environment (e.g. temperature sensor arrays). A multitude of sensors were developed incorporating very different physical mechanisms for measurement. Two different novel ionizing radiation dosimeter technologies were developed, taking advantage of the charge trapping capabilities of wide band gap electrically insulating materials. A novel shear stress flow sensor was developed that utilized thermoelectric cooling of a micro temperature detector in order to operate in a heat-sensitive or near-boiling temperature environment. Finally, arrays of temperature and electrical conductivity sensors were fabricated that utilized mature sensing technology in a new way. These devices were used to collect data at the centimeter scale in hot springs in order to determine what chemical or physical parameter(s) may be driving the onset of photosynthesis in hot spring outflow channels. In addition, the temperature sensors were incorporated in a long-term hot spring temperature monitoring station to study short and long-period environmental changes.

The key premise for developing the MEMS Earth and space exploration sensor systems was based on the increasing need for instruments that can perform macro scale functions at the micro scale. While MEMS sensor systems may not be able to match the resolution or precision of their larger predecessors at this current stage, the unique capabilities of smaller size, lower weight, lower power, lower cost, and often increased robustness fit specialized needs within enterprises such as space exploration and remote field-based scientific study. As shown with the temperature and electrical conductivity array data, the small device size and ability to batch fabricate multiple sensors in an array configuration allowed for measurements at a small scale

that could not otherwise be interrogated by larger commercial instruments, and in this case elucidated that temperature is a key parameter (in most cases) driving the transition to photosynthesis in hot spring environments. The small scale measurements at Geyser Creek allowed for the discovery of a technique for predicting and tracing conservative constituent concentrations in the hot springs (e.g., bulk ion chemistry through electrical conductivity) using the temperature data alone. The temperature mapping provides a new capability for visualizing the entire hot spring as a dynamic environment, replacing the single measurement at a single snapshot in time technique. In addition, the temperature map data may be used to predict other, as of yet unidentified, conservative constituents at spatial scales that would normally be impossible or unreliable using bulk water sampling techniques. The limitation of this technique, of course, is that temperature (and the conservative constituents) must be controlled by the mixing fluid and not other means such as evaporative cooling which dominates in shallow regions at the end of the outflow channel and along the edges.

The low cost of fabricating a large number of single function sensors enabled the instrumentation of a hot spring to study temperature fluctuations over a long period of time (months). The data show that this particular hot spring periodically drains and refills, exposing organisms living near the edges of the source pool to periods of dramatic changes in temperature and desiccation. While a number of the temperature sensors in the first monitoring station used to instrument Great Boiling Spring hot spring failed, a second set of sensors in GBS16 hot spring fared much better, indicating changes to the way the sensors were wired was successful, and with future improvements, the sensor yield could be 100%. In addition, strategically located conductivity sensors placed around the hot spring in the future could indicate when meteoric water (e.g. rain) infiltrates the system and dilutes the water conductivity.

The knowledge gained from both the array and long-term data provides a tantalizing look at the future of remote access field-research. While this current sensor capability could be useful in a number of other fields, the development of new sensors and systems will be the focus of the remainder of this chapter. Currently, the engineering research already exists to continue with future development of a suite of different MEMS chemical sensors such as pH (or dissolved oxygen or dissolved hydrogen). These sensors can be developed in both individual and array formats and can be deployed and tested at the Great Boiling Springs hot spring instrumentation test bed in Gerlach, NV.

7.1 pH Sensor Development

Sensing pH using commercial instruments requires a measurement of the activity of hydrogen ions in solution. The most common technique for measuring pH involves an ion selective electrode. The ion selective electrode (ISE) works by measuring the voltage difference between two electrodes (typically made of silver/silver chloride [Ag/AgCl]) within two separate solutions. The reference electrode and potassium chloride (KCl) reference solution provide a stable potential independent of the pH of ambient fluid. The sensing electrode, also contained in a KCl solution, undergoes a potential change based on the pH of the ambient fluid due to the diffusion of sodium ions across a glass membrane separating the sensing electrode/solution and the ambient fluid. The amount of sodium ion diffusion is proportional to the pH of the ambient fluid. MEMS technology is not ideally suited to minimizing the ISE due to the structure of the ISE electrode and the requirement for the KCl solution and the difficult-to-fabricate Ag/AgCl electrode.

A second pH sensing technique using solid-state fabrication techniques was developed by Bergveld (1970). This ion-sensitive field-effect transistor (ISFET) sensor works similar to the

metal-oxide-semiconductor field-effect transistor (MOSFET) device described in Chapter 2. As with the effects of ionizing radiation changing the threshold voltage of the MOSFET, the total charge contribution of the hydrogen ions in solution on a hydrogen ion-sensitive insulator material will modify the threshold voltage of the ISFET (Bergveld, 2002). The entire pH sensing system still requires a stable reference electrode paired with the ISFET device to complete the measurement. A Ag/AgCl reference electrode has been incorporated with an ISFET device and was shown to operate as an ocean-based pH sensor (Shitashima, 2010), however, the reference electrode was added separately to the ISFET and not fabricated during the same process and requires an electrolyte solution to operate. Wong and White (1989) showed that a platinum pseudo-reference electrode in conjunction with two FETs, one that is sensitive to the hydrogen ion concentration (and possibly other non-hydrogen ions) and one that is not sensitive to the hydrogen ion concentration (but sensitive to everything else that the first FET is also sensitive), would eliminate the need for the difficult-to-fabricate and implement Ag/AgCl reference electrode system. The platinum electrode measures the electrical potential of the ambient fluid of unknown pH. The non-pH-sensitive ISFET is called the reference ISFET (REFET) and Parylene-C and Teflon® have been used successfully as non-pH-sensitive coatings overtop the ISFET structure (Bergveld, 2002). The difference between the outputs of the two FETs is proportional to the pH. Using the differential ISFET design with a platinum electrode allows for the devices to be batch fabricated in a MEMS process.

There are a number of different materials that have been researched as the hydrogen ion-sensitive gate insulator of the ISFET. Bergveld's (2002) ISFET review compared a number of different materials and it appears that tantalum oxide (Ta_2O_5) has the best qualities in terms of

sensitivity and linearity over a wide range of pH values and a small response to other ions in solution such as sodium chloride (Figure 7.1).

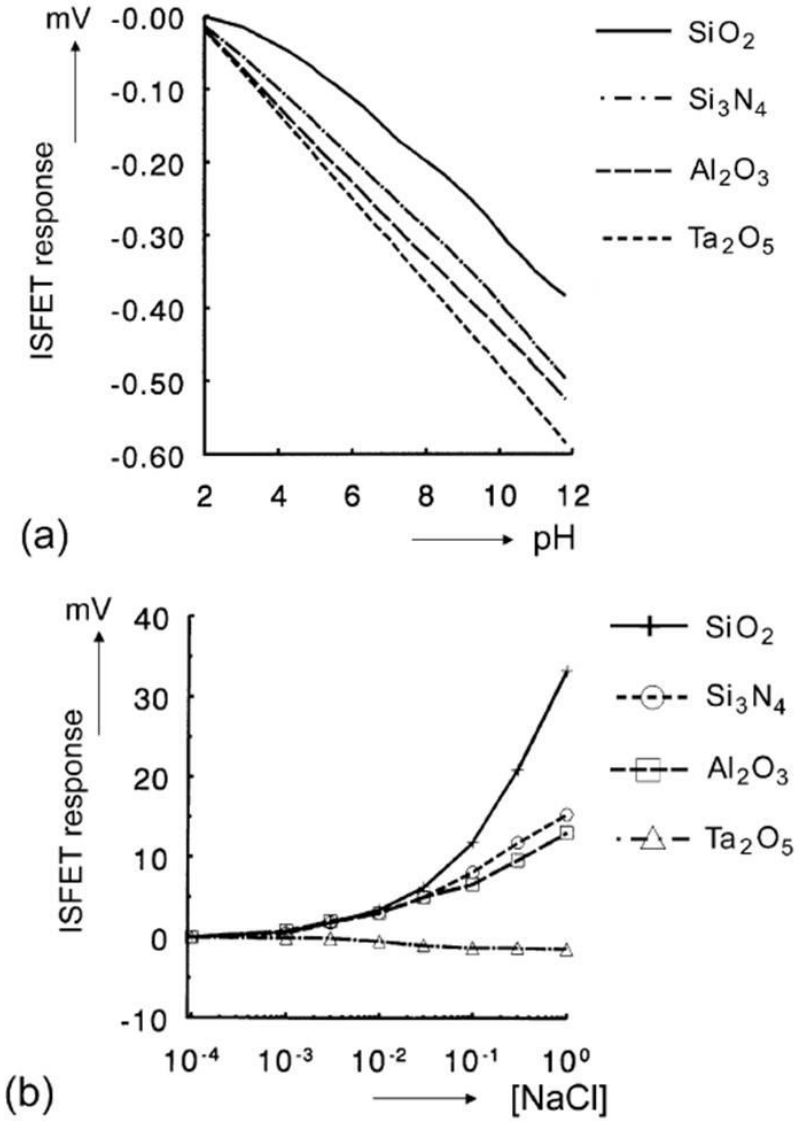

Figure 7.1: Plots from Bergveld (2002). (a) ISFET response as a function of increasing pH. (b) ISFET response as a function of increasing salt content.

In addition, the Ta_2O_5 ISFET sensitivity is a function of the quality of the film, both in terms of surface roughness (Chao and Hsiao, 2000) and annealing temperature (Bahari et al. 2010). Schematic drawings of the proposed ISFET devices are provided in Figure 7.2.

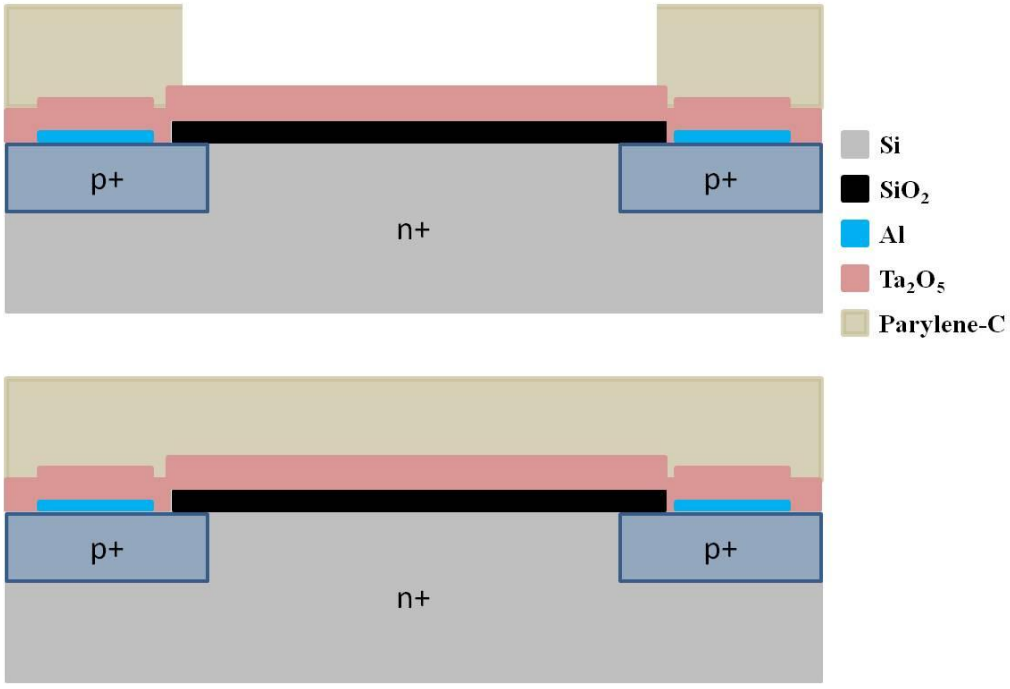

Figure 7.2: Schematic drawing of the pH-sensitive ISFET (top) and the non-pH-sensitive REFET (bottom).

Besides linearity, drift is the biggest issue affecting the long-term capability of a pH sensor. Drift is defined as the tendency of a sensor to measure a slow and steady change in pH measurement over time of a solution maintained at a constant pH. The drift is thought to be the result of a time-dependent change in the threshold voltage due to the hydration of the gate insulator surface when exposed to an aqueous solution over time (Jamasb, 1998). The drift of the pH sensor (in time) can be compensated by integrated hardware and software techniques (Chen and Chan 2008) or through *in-situ* re-calibration using a microfluidic system attached to the pH sensor (Le Bris and Birot 1997). Due to the large size and difficulty of incorporating a

microfluidic system, the hardware and software compensation technique, which can also account for nonlinear temperature effects, is likely the best option for the long-term monitoring of multiple pH ISFET sensors.

Because the temperature, conductivity, and pH sensors can be fabricated simultaneously using MEMS processing, the three sensors can be integrated onto a single chip, providing data from those key parameters at a single location. The batch fabrication of devices allows for the instrumentation of a hot spring at multiple locations. In addition, each of these individual sensors requires very little space so small spatial scale arrays can be fabricated as well. Finally, hot-film anemometers could be easily included on the chip to provide information about shear stress and flow speed, and could be utilized satisfactorily at temperature below 80 °C. The cool-film anemometers, useful for near-boiling water discussed in Chapter 6, require more complicated fabrication techniques but could eventually replace the hot-film anemometer as well.

7.2 Biofouling

Another major hurdle to long-term sensor measurement in natural aqueous environments is biofouling. Biofouling is the attachment and growth of organisms on a surface. While temperature measurements may be less affected by biofouling (provided the heat from the fluid can conduct through the biofilm), both conductivity and pH measurements have exposed electrodes where biofouling can occur, which can cause electrode corrosion and increased error, loss of sensitivity, and measurement drift.

The description of the microbial attachment mechanisms are well described in the review article from Al-Juboori and Yusaf (2012) and summarized here. The attachment of microbes and growth of biofilm starts with hydrodynamic forces bringing proteins and microorganisms near the substrate. There are three ways in which an organism can adhere to a surface. The first way

involves physio-chemical interactions such as van der Waals or electrostatic double layer interactions. The other two ways involve ligand-receptor interactions and sticky interactions from, for example, microbial appendages. Once a microbial layer is adhered to the surface, additional microbes attach to those layers via cohesion (Figure 7.3).

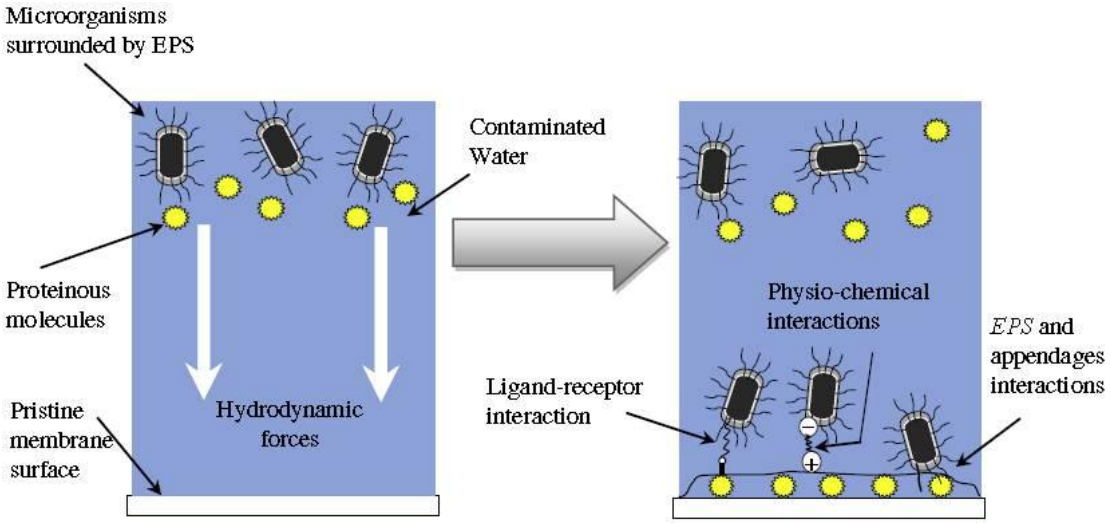

Figure 7.3: Schematic depiction of microbial adhesion to a material surface in aqueous solution from Al-Juboori and Yusaf (2012).

There is no universal method for the prevention of biofouling. Organisms have evolved a number of techniques to make them very difficult to remove from a substrate. One such example is a layer that some organisms have developed around their body called Extra-cellar Polymeric Substances (EPS) which can protect them from biocides and toxins (Flemming, 2002). When using sensors, the materials that are exposed to the fluid (e.g.,` platinum electrodes) are already determined by the sensing method and therefore anti-biofouling techniques that make microbial adhesion difficult such as surface modification are difficult to apply. Generally, biofilm removal from sensors has been researched in the areas of physical removal of the biofilm or use of some sort of chemical agent. An example of physical removal involves using acoustic waves to detach

the organisms (Mott et al. 1998). The difficulty with this technique, of course, is that there will be a number of individual sensors located within the hot spring and will be stationary for long durations, so any technique such as acoustic wave removal would require an additional acoustic wave generating device in conjunction with each sensor. While, incorporating a MEMS acoustic transducer with each sensor may be possible (Zhu et al. 2009), the fabrication processes become much more complicated and the electronics used in the field to operate the system become more involved and expensive. There are a number of chemical agents used in anti-biofouling processes and include chlorine or sodium hypochlorite or ozone. However, these chemicals would need to be poured into the hot spring near the sensor and will not only kill microorganisms on the sensor but also a large number of organisms in the surrounding environment which is highly undesirable and therefore not a legitimate possibility.

Two potential biofouling techniques for the removal of biofilm on the sensors are heat generation and copper. Heat generation has been shown to kill microbes (Davies et al. 2009), but it was not viewed as a viable solution due to the amount of energy required to heat the water in large systems. In addition, the microbes living in the hot springs are often thermophilic or hyperthermophilic, therefore a high sensor surface temperature (100-120 °C) may be periodically required to prevent biofouling. However, due to the small size of the MEMS devices and the extremely simple fabrication steps needed to create a heating element (resistor) near the sensor surface, thermal treatments to the sensor should still be considered since the power consumption may be low for the long-duration battery-powered devices. The other potential option would utilize copper, which has been shown to be an effective biocide (Hausman et al. 2010). Since copper can be easily deposited with electron-beam evaporation during fabrication of the sensors, the biofouling effects of a ring of electrically isolated copper around the sensor should be

investigated. The copper only needs to prevent growth of biofilms over the area covered by the sensor electrodes and therefore a small amount of copper may be enough to keep the sensor surface clean while not affecting nearby microbial communities.

7.3 Conclusion

MEMS devices stand to play an increasingly important role in remote scientific investigations. The previous chapters highlighted the mechanism by which many of these sensors operate and their potential regarding new techniques for measuring geochemical properties at small spatial scales. In addition to the current suite of sensors developed in this dissertation, the development of a pH ISFET sensor was described as the next important step for future studies of hot springs, especially for long-term monitoring. Measurement drift and biofouling remain as the most critical issues affecting long-term *in-situ* aqueous measurements.

REFERENCES

Abdolvand, R., Amini, B.V., and Ayazi, F. 2007. Sub-micro-gravity in-plane accelerometers with reduced capacitive gaps and extra seismic mass. *Journal of Microelectromechanical Systems* 16(5): 1036-1043.

Ahmad, N.R., Marks, G., and Mohiuddin, M. High-dose preoperative radiation for cancer of the rectum: Impact of radiation dose on patterns of failure and survival. *International Journal of Radiation Oncology*Biology*Physics* 27(4): 773-778.

Aigner, R., Huynh, N.-H., Handtmann, M., and Marksteiner, S. 2005. Behavior of BAW devices at high power levels. *IEEE International Microwave Symposium Digest*: 429-432.

Ai, L., Yu, H., Dai, W., Hale, S.L., Kloner, R.A., and Tsiai, H.K. 2009. Real-time intravascular shear stress in the rabbit abdominal aorta. *IEEE Transactions on Biomedical Engineering* 56(6): 1755-1764.

Al-Juboori, R.A., and Yusaf, T. 2012. Biofouling in RO system: Mechanisms, monitoring, and controlling. *Desalinization* 302: 1-23.

Amend, J.P. and Shock, E.L. 2001. Energetics of overall metabolic reactions of thermophilic and hyperthermophilic Archaea and Bacteria. *FEMS Microbiology Reviews* 25: 175-243.

Ashauer, M., Glosch, H., Hedrich, F., Hey, N., Sandmaier, H., and Lang, W. 1998. Thermal flow sensor for liquids and gases. *The Eleventh Annual International Workshop on Micro Electro Mechanical Systems*: 351–355.

Bahari, N., Zain, A.M., Abdullah, A.Z., Sheng, D.B.C., and Othman, M. 2010. Study on pH sensing properties of RF magnetron sputtered tantalum pentoxide (Ta2O5) thin film. *IEEE International Conference on Semiconductor Electronics*: 76-78.

Baker, D.N., Braby, L.A., Curtis, S., Jokipii, J.R., Lewis, W.S., Miller, J., Schimmerling, W., Singer, H., Strachan, L., Townsend, L.W., Turner, R.E., Zurbuchen, T.H. 2007. Space radiation hazards and the vision for space exploration: A report on the October 2005 Wintergreen Conference. *Space Weather* 5(2): 1-4.

Ballato, A. 1995. Piezoelectricity: Old effect, new thrusts. *IEEE Transactions on Ultrasonics, Ferroelectrics, and Frequency Control* 42(5): 916-926.

Barnaby, H. 2006. Total-ionizing-dose effects in modern CMOS technologies. *IEEE Transactions on Nuclear Science* 53(6): 3103-3121.

Barns, S.M., Fundyga, R.E., Jeffries, M.W., and Pace, N.R. 1994. Remarkable archaeal diversity detected in a Yellowstone National Park hot spring environment. *Proceedings of the National Academy of Sciences* 91: 1609-1613.

Belser, R.B. and Hicklin, W.H. 1959. Temperature coefficients of resistance of metallic films in the temperature range 25° to 600°C. *Journal of Applied Physics* 30(3): 313-322.

Bergveld, P. 1970. Development of an ion-sensitive solid-state device for neurophysiological measurements. *IEEE Transactions on Biomedical Engineering* 17(1): 70-71.

Bergveld, P. 2002. Thirty years of ISFETOLOGY: What happened in the past 30 years and what may happen in the next 30 years. *Sensors and Actuators B: Chemical* 88(1): 1-20.

Beyer, G., Mann, G., Pursley, J., Espenhahn, E., Fraisse, C., Godfrey, D., Oldham, M., Carrea, T., Bolick, N., and Scarantino, C. 2008. An implantable MOSFET dosimeter for the measurement of radiation dose in tissue during cancer therapy. *IEEE Sensors Journal* 8(1): 38–51.

Braunstein, J., and Robbins, G.D. 1971. Electrolytic conductance measurements and capacitive balance. *Journal of Chemical Education* 48(1): 52-59.

Brock, T.D. 1978. *Thermophilic Microorganisms and Life at High Temperatures.* New York: Springer-Verlag.

Buder, U., Berns, A., Petz, R., Nitsche, W., and Obermeier, E. 2008. AeroMEMS wall hot-wire anemometer on polyimide substrate featuring top side or bottom side bond pads," *IEEE Sensors Journal* 7(8): 1095–1101.

Castillo-Effer, M., Qunitela, D.H., Moreno, W., Jordan, R., and Westhoff, W. 2004. Wireless sensor networks for flash-flood alerting. *IEEE International Conference on Devices, Circuits, and Systems*: 142-146.

Cecchi, E., Giglioli, C., Valente, S., Lazzeri, C., Gensini, R., Abbate, R., and Mannini, L. 2011. Role of hemodynamic shear stress in cardiovascular disease. *Atherosclerosis* 214: 249-256.

Charles, M. 2001. UNSCEAR Report 2000: Sources and effects of ionizing radiation. *Journal of Radiological Protection* 21(1): 83-86.

Chen, D.Y, and Chan, P.K. 2008. An intelligent ISFET sensory system with temperature and drift compensation for long-term monitoring. *IEEE Sensors Journal* 8(12): 1948-1959.

Chou, J.C., and Hsiao, C.N. 2000. Comparison of the pH sensitivity of different surfaces on tantalum pentoxide. *Sensors and Actuators B: Chemical* 65(1-3): 237-238.

Chow, E.Y., Chlebowski, A.L., and Irazoqui, P.P. 2010. A miniature-implantable RF-wireless active glaucoma intraocular pressure monitor. *IEEE Transactions on Biomedical Circuits and Systems* 4(6): 340-349.

Clark, K., Boldt, J., Greeley, R., Hand, K., Jun, I., Lock, R., Pappalardo, R., Van Houten, T., and Yan, T. 2011. Return to Europa: Overview of the Jupiter Europa orbiter mission. *Advances in Space Research* 48(4): 629-650.

Clayton, W.A. 1988. Thin-film platinum for appliance temperature control. *IEEE Transactions on Industry Applications* 24(2): 332-336.

Coksun, C., Look, D.C., Farlow, G.C., and Sizelove, J.R. 2004. Radiation hardness of ZnO at low temperatures. *Semiconductor Science and Technology* 19: 752-754.

Costa, K.C., Navarro, J.B., Shock, E.L., Zhang, C.L., Soukup, D., and Hedlund, B.P. 2009. Microbiology and geochemistry of great boiling and mud hot springs in the United States Great Basin. *Extremophiles* 13: 447-459.

Cox, A., Shock, E.L., and Havig, J.R. 2011. The transition to microbial photosynthesis in hot spring ecosystems. *Chemical Geology* 280: 344-351.

Cucinotta, F.A., Manuel, F.K., Jones, J., Iszard, G., Murrey, J., Djojonegro, B., and Wear, M. 2001. Space radiation and cataracts in astronauts. *Radiation Research* 156(6): 460-466.

Dalgarno, A. and McElroy, M.B. 1966. Twilight effects of solar ionizing radiation. *Planetary and Space Science* 14(12): 1321-1329.

Davies, C.M., Roser, D.J., Feitz, A.J., and Ashbolt, N.J. 2009. Solar radiation disinfection of drinking water at temperate latitudes: Inactivation rates for an optimized reactor configuration. *Water Resources* 43(3): 643-652.

de Rooij, N.F., Gautsch, S., Briand, D., Marxer, C., Mileti, G., Noell, W., Shea, H., Staufer, U., and van der Schoot, B. 2009. MEMS for space. *IEEE International Conference on Solid-State Sensors, Actuators, and Microsystems*: 2449-2452.

Denlinger, E.J. 1969. Radiation from microstrip resonators. *IEEE Transactions on Microwave Theory and Techniques* 17(4): 235-236.

Dewhirst, M., Viglianti, B., Lora-Michiels, M., Hanson, M., and Hoopes, P. 2003. Basic principles of thermal dosimetry and thermal thresholds for tissue damage from hyperthermia**.** *International Journal of Hyperthermia* 19: 267-294.

Dijkstra, M., Lammerink, T.S.J., de Boer, M.J., Berenschot, J.W., Wiegerink, R.J., Elwenspoek, M.C. 2008. Low-drift U-shaped thermopile flow sensor. *IEEE Sensors Conference*: 66-69.

DiSalvo, F.J. 1999. Thermoelectric cooling and power generation. *Science* 285(5428): 703-706.

Dun, H., Pan, P., White, F.R., and Douse, R.W. 1981. Mechanisms of plasma-enhanced silicon nitride deposition using SiH4/N2 mixture. *Journal of the Electrochemical Society* 128(7): 1555-1563.

Eden, R. and Eden, G. 1984. *Impedance Microbiology*. Letchworth: Research Studies Press.

Elwenspoek, M. Thermal flow micro sensors, *1999. International Semiconductor Conference* 2: 423–435.

Estrada, H.V. 1990. Linearization of the temperature dependence of the silicon's resistivity for its use as a thermistor. *Proceedings of the IEEE Southeastcon* 3: 1095-1099.

Fan, L.-S., Tai, Y.-C., and Muller, R.S. 1988. IC-processed electrostatic micro-motors. *International Electron Devices Meeting*: 666-669.

Ferrari, P., Corrao, N., and Rauly, D. 2007. Miniaturized circular patch antenna with capacitors loading. *IEEE Microwaves and Optoelectronics Conference*: 86-89.

Flemming, H.-C. 2002. Biofouling in water systems – cases, causes, and countermeasures. *Applied Microbiology and Biotechnology* 59(6): 629-640.

Fournier, R.O. 1984. Geochemistry and dynamics of the Yellowstone National Park hydrothermal system. *Annual Review of Earth and Planetary Sciences* 17: 13-53.

Fox, R.W., McDonald, A.T., and Pritchard, P.J. 2004. *Introduction to Fluid Mechanics*. Hoboken: John Wiley & Sons, Inc.

Futron Corporation. 2002. Space transportation costs: Trends in price per pound to orbit 1990-2000. *Futron Corporation*: 1-8.

Gaucher, E.A., Kratzer, J.T., and Randall, R.N. 2010. Deep phylogeny-how a tree can help characterize early life on Earth. *Cold Spring Harbor Perspectives in Biology* 2(1): a002238.

Georgiou, J. 2008. An ultra-compact, low-power reference circuit/dosimeter for space environments. *IEEE Transactions on Nuclear Science* 55(4): 2385-2388.

Goetz, M., Messner, S., Ashauer, M., and Zengerle, R. 2009. Precise dosage system for controlled liquid delivery based on fast MEMS based flow sensor. *IEEE International Conference on Solid-State Sensors, Actuators, and Microsystems*: 1261-1264.

Gopalan, M.S. 2010. Experimental study of MOS capacitors as wireless radiation dose sensors. Master's Thesis, Arizona State University.

Gross, A.J., Hwang, G.S., Huang, B., Yang, H., Ghafouri, N., Kim, H., Peterson, R.L, Uher, C., Kaviany, M., and Najafi, K. 2011. Multistage planar thermoelectric microcoolers. *Journal of Microelectromechanical Systems* 20(5): 1201-1210.

Gyure, R.A., Konopka, A., Brooks, A., and Doemel, W. 1989. Microbial sulfate reduction in acidic (pH 3) strip-mine lakes. *FEMS Microbiology Ecology* 73(3): 193-202.

Hahne, E., and Grigull, U. 1971. Shape factor and shape resistance for steady multidimensional heat conduction. *International Journal of Heat and Mass Transfer* 18: 751-767.

Hausman, R., Gullinkala, T., and Escobar, I.C. 2010. Development of copper-charged propylene feedspacers for biofouling control. *Journal of Membrane Science* 358(1-2): 114-121.

He, D. 2001. Theory, fabrication and characterization of micromachined electrolytic solution conductivity sensors. Ph.D. dissertation, University of Illinois at Urbana-Champaign.

He, D., Shannon, M.A., and Miller, N.R. 2005. Micromachined silicon electrolytic conductivity probes with integrated temperature sensor. *IEEE Sensors Journal* 5(6): 1185-1196.

Hilbert, C., Nelson, R., Reed, J., Lunceford, B., Somadder, A., Hu, K., and Goshal, U. 1999. Thermoelectric MEMS coolers. *International Conference on Thermoelectrics*: 117-122.

Hijazi, Y.S., Vlasov, Y.A., and Larkins, G.L., Jr. 2003. Design of a superconducting MEM shunt switch for RF applications. *IEEE Transactions on Applied Superconductivity* 13(2): 696-699.

Hoffmann, N., and Bischoff, J. 2002. The cryobiology of cryosurgical injury. *Urology* 60: 40-49.

Hopkins, P.E., Reinke, C.M., Su, M.F., Olsson, R.H., Shaner, E.A., Leseman, Z.C., Serrano, J.R., Phinney, L.M., El-Kady, I. 2011. Reduction in the thermal conductivity of single crystalline silicon by phononic crystal patterning. *Nano Letters* 11(1): 107-112.

Huang, J.-B., Tung, S., Ho, C.-M., Liu, C., and Tai, Y.-C. 1996. Improved micro thermal shear-stress sensor. *IEEE Transactions on Instrumentation and Measurement* 45(2): 570-574.

Hughes, R.C. 1984. The origin of interfacial charging in irradiated silicon nitiride capacitors. *Journal of Applied Physics* 56(4): 1044-1050.

Jamasb, S., Collins, S.D., and Smith, R.L. 1998. A physical model for the threshold voltage instability in Si_3N_4-gate H+-sensitive FET's (pH-ISFET's). *IEEE Transactions on Electron Devices* 45(6): 1239-1245.

Jamneala, T., Bradley, P., Koelle, U., and Chien, A. 2008. Modified mason model for bulk acoustic wave resonators. *IEEE Ultrasonics, Ferroelectrics, and Frequency Control* 55(9): 2025-2029.

Jiang, Z., Modi, V., and Farmer, K. 2005. A microfabricated wall shear-stress sensor with capacitive sensing. *Journal of Microelectromechanical Systems* 14: 167-175.

Johnson, J.P.L., and Whipple, K.X. 2010. Evaluating the controls of shear stress, sediment supply, alluvial cover, and channel morphology on experimental bedrock incision rate. *Journal of Geophysical Research* 115(F2): 1-21.

Jorgensen, A.M., Patamia, S.E., and Gassend, B. 2007. Passive radiation shielding considerations for the proposed space elevator. *Acta Astronautica* 60(3): 198-209.

Kelleher, A., Lane, W., and Adams, L. 1995. A design solution to increasing the sensitivity of pMOS dosimeters: The stacked RADFET approach. *IEEE Transactions on Nuclear Science* 42(1): 48-51.

Kerr, A., Cowling, M.J., Beveridge, C.M., Smith, M.J., Parr, A.C.S., Head, R.M., Davenport, J., and Hodgekiess, T. 1998. The early stages of marine biofouling and its effects on two types of optical sensors. *Environmental International* 24(3): 331-343.

Knauth, L.P. 2005. Temperature and salinity history of the Precambrian ocean: implications for the course of microbial evolution. *Palaeogeography, Palaeoclimatology, Palaeoecology* 219(1-2): 53-69.

Knauth, L.P., and Lowe, D.R. 2003. High Archaean climactic temperature inferred from oxygen isotope geochemistry of cherts in the 3.5 Ga Swaziland Supergroup, South Africa. *Bulletin of the Geological Society of America* 115(5): 566-580.

Koev, T. 2006. Microcantilever biosensors with Chitosan for the detection of nucleic acids and Dopamine. *Master's Thesis*, University of Maryland, College Park, MD.

Kordas, N., Manoli, Y., Mokwa, W., and Rospert, M. 1994. A CMOS-compatible monolithic conductivity sensor with integrated electrodes. *Sensors and Actuators A* 43(1-3): 31-37.

Kulah, H. and Najafi, K. 2008. Energy scavenging from low-frequency vibrations by using frequency up-conversion for wireless sensor applications. *IEEE Sensors Journal* 8(3): 261-268.

Kunze, E. 2003. A review of oceanic salt-fingering theory. *Progress in Oceanography* 56(3-4): 399-417.

Lacy, F. 2011. Evaluating the resistivity-temperature relationship for RTDs and other conductors. *IEEE Sensors Journal* 11(5): 1208-1213.

Larson III, J., Bradley, P.D., Wartenberg, S., and Ruby, R.C. 2000. Modified Butterworth-Van Dyke circuit for FBAR resonators and automated measurement system. *IEEE Ultrasonics Symposium* 1: 863-868.

Le Bris, N., and Birot, D. 1997. Automated pH-ISFET measurements under hydrostatic pressure for marine monitoring application. *Analytical Chimica Acta* 356: 205-215.

Lester, D.R., Ord, A., and Hobbs, B.E. 2012. The mechanics of hydrothermal systems: II. Fluid mixing and chemical reactions. *Ore Geology Reviews* 49: 45-71.

Li, M.J., Brown, A.D., Kutyrev, A.S., Moseley, H.S., Mikula, V. 2010. JWST microshutter array system and beyond. *Proceedings of the International Society for Optics and Photonics* 7594: 1-9.

Li, X. and Meijer, M. 2002. A low-cost and accurate interface for conductivity sensors. *IEEE Instrumentation and Measurement Technology Conference* 1: 765-768.

Li, X. and Meijer, M. 2005. A low-cost and accurate interface for four-electrode conductivity sensors. *IEEE Transactions on Instrumentation and Measurement* 54(6): 2433-2437.

Li, X. and Meijer, M. 2008. A high-performance interface for grounded conductivity sensors. *Measurement Science and Technology* 19: 115202-115208.

Lin, Q., Jiang, F.K., Wang, X.Q., Wang, Y., Zhu, Z, Han, G., Tai, Y.-C., Lew, J., and Ho, C.-M. 2004. Experiments and simulations of MEMS thermal sensors for wall shear-stress measurements in aerodynamic control applications. *Journal of Micromechanics and Microengineering* 14: 1640-1649.

Livermore, C., Forte, A.R., Lyszczarz, T., Umans, S.D., Ayon, A.A., and Lang, J.H. 2004. A high-power MEMS electric induction motor. *Journal of Microelectromechanical Systems* 13(3): 465-471.

Lo, C.C. and Fedder, G.K. 2007. On-Chip high quality factor CMOS-MEMS silicon-fin resonators. *IEEE International Conference on Solid-State Sensors, Actuators, and Microsystems*: 2449-2452.

Loloee, R., Askeland, P.A., Ghosh, R.N. 2007. Dissolved oxygen sensing in a flow stream using Molybdenum Chloride optical indicators. *IEEE Sensors Conference*: 1404-1407.

Maisonneuve, J. 1982. The composition of the Precambrian ocean waters. *Sedimentary Geology* 31(1): 1-11.

Malek, A., Alper, S., and Izumo, S. 1999. Hemodynamic shear stress and its role in atherosclerosis. *The Journal of the American Medical Association* 282: 2087-2088.

Martin, L.M., Marples, B., Coffey, M., Lawler, M., Lynch, T.H., Hollywood, D., and Marignol, L. 2010. DNA mismatch repair and the DNA damage response to ionizing radiation: Making sense of apparently conflicting data. *Cancer Treatment Reviews* 36(7): 518-527.

Mehregany, M., Zorman, C.A., Rajan, N., and Wu, C.H. 1998. Silicon carbide MEMS for harsh environments. *Proceedings of the IEEE* 86(8): 1594-1609.

Melani, M., Bertini, L., De Marinis, M., Lange, P., D'Ascoli, F., and Fanucci, L. 2008. Hot wire anemometric MEMS sensor for water flow monitoring. *IEEE Conference on Design, Automation, and Test in Europe* 1: 342-347.

Messenger, G.C. 1992. A summary review of displacement damage from high energy radiation in silicon semiconductors and semiconductor devices. *IEEE Transactions on Nuclear Science* 39(3): 468-473.

Meyer-Dombard, D.R., Shock, E.L., and Amend, J.P. 2005. Archaeal and bacterial communities in geochemically diverse hot springs of Yellowstone National Park. *Geobiology* 3: 211-227.

Mimoun, D., Lognonné, P., Banerdt, W.B., Hurst, K., Deraucourt, S., Gagnepain-Beyneix, J., Pike, T., Calcutt, S., Bierwirth, M., Roll, R., Zweifel, P., Mance, D., Robert, O., Nébut, T., Tillier, S., Laudet, P., Kerjean, L., Perez, R., Giardini, D., Christenssen, U., Garcia, R. 2012. The InSight SEIS experiment. *The 43rd Lunar and Planetary Science Conference* 1493: 1-2.

Mott, I.E.C., Stickler, D.J., Coakley, W.T., and Bott, T.R. The removal of bacterial biofilm from water-filled tubes using axially propagated ultrasound. *Journal of Applied Microbiology* 84: 509-514.

National Research Council of the National Academies of Science. 2009. Radioisotope power systems: An imperative for maintaining U.S. leadership in space exploration. *The National Academies Press*: Washington, D.C.: 1-68

Olthuis, W., Streekstra, W., and Bergveld, P. 1995. Theoretical and experimental determination of cell constants of planar-interdigitated electrolyte conductivity sensors. *Sensors and Actuators B* 24(1-3): 252-256.

Orbital Sciences Corporation. 2006. Taurus launch system payload user's guide. *Orbital Sciences Corporation*: 1-82.

Ozgur, U., Alivov, Y.A., Liu, C., Teke, A., Reshchikov, M.A., Dogan, S., Avrutin, V., Cho, S.-J., and Morkoc, H. 2005. A comprehensive review of ZnO materials and devices. *Journal of Applied Physics* 98(4): 041301-041301-103.

Phlips, B.F., Wulf, E.A., Johnson, W.N., Kurfess, J.D., and Novikova, E.I. 2004. Development of a silicon gamma ray spectrometer. *IEEE Transactions on Nuclear Science* 51(5): 2438-2442.

Pollack, A. 1988. New generation of tiny motors challenges science to find a uses. *The New York Times*. Technology section: 1.

Qiu, X. 2011. Environmental sensing applications of zinc oxide based film bulk acoustic resonator. Ph.D. dissertation, Arizona State University.

Qiu, X., Zhu, J., Oiler, J., Yu, C., Wang, Z., and Yu, H. 2009. Film bulk acoustic-wave resonator based ultraviolet sensor. *Applied Physics Letters* 94(15): 151917-151917-3.

Raymahashay, B. 1968. A geochemical study of rock alteration by hot springs in the Paint Pot Hill area, Yellowstone Park. *Geochimica et Cosmochimica Acta* 32(5): 499-522.

Revsbech, N.P., Jorgensen, B.B., Blackburn, T.H., and Cohen, Y. 1983. Microelectrode studies of the photosynthesis and O_2, H_2S, and pH profiles of a microbial mat. Limnology and Oceanography 28(6): 1062-1074.

Rouhanizadeh, M. 2007. Interfacing fluid shear stress with vascular oxidative stress: Application of nano and micro sensors. Ph.D. dissertation, University of Southern California.

Rouhanizadeh, M.,Soundararajan, G., Lo, R., Arcas, D., Browand, F., and Hsiai, T.K. 2006. MEMS sensors to resolve spatial variations in shear stress in a 3-D blood vessel bifurcation model. *IEEE Sensors Journal* 6(1): 78–88.

Ruby, R.C., Bradley, P., Oshmyansky, Y., Chien, A., and Larson, III, J.D. 2001. Thin film bulk acoustic resonators (FBAR) for wireless applications. *IEEE Ultrasonics Symposium* 1: 813-821.

Schwank, J.R., Shaneyfelt, M.R., Fleetwood, D.M., Felix, J.A., Dodd, P.E., Paillet, P., and Ferlet-Cavrois, V. 2008. Radiation effects in MOS oxides. *IEEE Transactions on Nuclear Science* 55(4): 1833-1853.

Shajii, J., Ng, K.Y., and Schmidt, M.A. 1992. A microfabricated floating-element shear stress sensor using wafer-bonding technology. *Journal of Microelectromechanical Systems* 1(2): 89-94.

Shalaby, M.M., Zhongde, W., Chow, L.L.-W., Jensen, B.D., Volakis, J.L., Kurabayashi, K., and Saitou, K. 2009. Robust design of RF-MEMS cantilever switches using contact physics modeling. IEEE *Transactions on Industrial Electronics* 56(4): 1012-1021.

Shitashima, K. 2010. Evolution of compact electrochemical in-situ pH-pCO_2 sensor using ISFET-pH electrode. *Oceans 2010*: 1-4.

Shock, E.L., Holland, M., Meyer-Dombard, D.R., and Amend, J.P. 2005. "Geochemical sources of energy for microbial metabolism in hydrothermal ecosystems: Obsidian Pool, Yellowstone National Park, USA," In *Geothermal Biology and Chemistry in Yellowstone National Park*. Edited by W. Inskeep and T. McDermott. Bozeman: Montana State University Publications.

Shock, E.L., Holland, M., Meyer-Dombard, D.R., Amend, J.P., Osburn, G.R., and Fischer, T.P. 2010. Quantifying inorganic sources of geochemical energy in hydrothermal ecosystems, Yellowstone National Park, USA. *Geochemica et Cosmochimica Acta* 74(14): 4005-4043.

Singh, A. Film thickness and grain size diameter dependence on temperature coefficient of resistance of thin metal films. *Journal of Applied Physics* 45(4): 1908-1909.

Sklar, L.S., and Dietrich, W.E. 2001. Sediment and rock strength controls on river incision into bedrock. *Geology* 29: 1087-1090.

Snow, E.H., Grove, A.S., and Fitzgerald, D.J. 1967. Effects of ionizing radiation on oxidized silicon surfaces and planar devices. *Proceedings of the IEEE* 55(7): 1168-1185.

Snyder, G.F., and Toberer, E.S. 2008. Complex thermoelectric materials. *Nature Materials* 7: 105-114.

Sohgawa, M., Huang, Y.-M., Yamashita, K., Kanashima, T., Noda, M., Okuyama, M., and Noma, H. 2007. Fabrication and characterization of silicon-polymer beam structures for cantilever-type tactile sensors. *IEEE International Conference on Solid-State Sensors, Actuators, and Microsystems*: 1461-1464.

Son, C., and Ziaie, B. 2006. A micromachined electret-based transponder for in situ radiation measurement. *IEEE Electron Device Letters* 27(11): 884-886.

Son C., and Ziaie, B. 2008. A wireless implantable passive microdosimeter for radiation oncology. *IEEE Transactions in Biomedical Eng*ineering 55(6): 1772-1775.

Space Exploration Technologies Corporation (Space-X). 2009. Falcon 9 launch vehicle payload user's guide. *Space Exploration Technologies Corporation*: 1-65.

Summers, G.P., Burke, E.A., and Xapsos, M.A. 1994. Displacement damage analogs to ionizing radiation. *Radiation Measurements* 24(1): 1-8.

Suzuki, H., Kojima, N., Sugama, A., and Fujita, S. 1991. Micromachined Clark oxygen electrode. *IEEE International Conference on Solid-State Sensors, Actuators, and Microsystems*: 339-342.

Sverdrup, K.A., Duxbury, and A.C., Duxbury, A.B. 2003. *An Introduction to the World's Oceans* (7th Edition). New York: McGraw-Hill.

Temple-Boyer, P., Rossi, C., Saint-Etienne, E., and Scheid, E. 1998. Residual stress in low pressure chemical vapor deposition SiNx films deposited from silane and ammonia. *Journal of Vacuum Science & Technology A* 16(4): 2003-2007.

Tong, L.S., and Tang, Y.S. 1997. *Boiling Heat Transfer and Two-Phase Flow* (2nd Edition). Washington: Taylor & Francis.

Tortonese, M. 1997. Cantilevers and tips for atomic force microscopy. *IEEE Engineering in Medicine and Biology Magazine* 16(2): 28-33.

Trietley, H.L. 1986. *Transducers in mechanical and electronic design*. New York City: Marcel Dekker, Inc.

Truskey, G., Yuan, F., and Katz, D. 2004. *Transport Phenomena in Biological Systems*. Upper Saddle River: Pearson Prentice Hall.

Tsu, D.V., Lucovsky, G., Mantini, M.J. 1986. Local atomic structure in thin films of silicon nitride and silicon diimide produced by remote plasma-enhanced chemical-vapor deposition. Physical Review B 33(10): 7069-7076.

United Launch Alliance. "Launch Vehicles." United Launch Alliance. http://www.ulalaunch.com/site/pages/About_Overview.shtml

Wapelhorst, E., Hauschild, J.-P., and Muller, J. 2007. A one-chip solution of a mass spectrometer. *IEEE International Conference on Solid-State Sensors, Actuators, and Microsystems*: 2015-2018.

White, R.J. and Averner, M. 2001. Humans in space. *Nature* 409: 1115-1118.

Williams, K.R. and Muller, R.S. 1996. Etch rates for micromachining processing. *Journal of Microelectromechanical Systems* 5(4): 256-269.

Wisniewski, N., Moussy, F., and Reichert, W.M. 2000. Characterization of implantable biosensor membrane fouling. *Journal of Analytical Chemistry* 366(6-7): 611-621.

Wolman, M.G., and Miller, J.P. 1960. Magnitude and frequency of forces in geomorphic processes. *The Journal of Geology* 68(1): 54-74.

Wong, H.-S., and White, H.M. 1989. A CMOS-integrated 'ISFET-operational amplifier' chemical sensor employing differential sensing. *IEEE Transactions on Electron Devices* 36(3): 479-487.

Xu, X.G., Bednarz, B., and Paganetti, H. 2008. A review of dosimetry studies on external-beam radiation treatment with respect to second cancer induction. *Physics in Medicine and Biology* 53(13): R193-R241.

Xu, Y., Lin, Q., Lin, G., Katragadda, R.B., Jiang, F., Tung, S., and Tai, Y.-C. 2005. Micromachined thermal shear-stress sensor for underwater applications. *Journal of Microelectromechanical Systems* 14(5): 1023-1030.

Yamashita, A., Dotani, T., Bautz, M., Crew, G., Ezuka, H., Gendreau, K., Kotani, T., Mitsuda, K., Otani, C., Rasmussen, A., Ricker, G., and Tsunemi, H. 1997. Radiation damage to charge coupled devices in the space environment. *IEEE Transactions on Nuclear Science* 44(3): 847-853.

Yang, H., Yu, Z., Li, X., and Wang, Y. 2005. A novel pull-in accelerometer based on cantilever beam mass structure. *Proceedings of the IEEE Sensors* 1: 644-647.

Yasseen, A.A., Wu, C.H., Zorman, C.A., Mehregany, M. 2000. Fabrication and testing of surface micromachined polycrystalline SiC micromotors. *IEEE Electron Device Letters* 21(4): 164-166.

Young-Min, K., Chang-Taeg, S., Duk-Soo, E., Sung-Gen, P., Chan-Seop, J., and Jong-Hyun, L. 2003. Characteristics of cantilever beam fabricated by silicon micromachining for flow sensing application. *Proceedings of the IEEE Sensors* 1: 642-646.

Yu, H., Ai, L., Rouhanizadeh, M., Patel, D., Kim, E.S., and Hsiai, T.K.2008. Flexible polymer sensors for in vivo intravascular shear stress analysis. *Journal of Microelectromechanical Systems* 17: 1178-1186.

Zastawny, T.H., Kruszewski, M., and Olinski, R. 1998. Ionizing radiation and hydrogen peroxide induced oxidative DNA base damage in two L5178Y cell lines. *Free Radical Biology and Medicine* 24(7-8): 1250-1255.

Zhang H., and Kim, E.S. 2005. Micromachined acoustic resonant mass sensor *Journal of Microelectromechanical Systems* 14(4): 699-706.

Zhang, G., Liu, C.-Q., Liu, H., Jin, Z., Han, G., and Li, L. 2008. Geochemistry of the Rehai and Ruidian geothermal waters, Yunnan Province, China. *Geothermics* 37: 73-83.

Zhou, J.W.L., Chan, H.-Y., To, T.K.H., Lai, K.W.C., and Li, W.J. 2004. Polymer MEMS actuators for underwater micromanipulation. *IEEE/ASME Transactions on Mechatronics* 9(2): 334-342.

Zhu, J., Qui, X., Oiler, J., Yu, C., Wang, Z., Lee, C., Hsiai, T.K., Kim, E.S., and Yu, H. 2009. Localized cell lysis by self focused acoustic transducer. *IEEE International Conference on Solid-State Sensors, Actuators, and Microsystems*: 608-61